



University
of Glasgow

Maclean, Catherine Elaine (2012) *Towards Molecular Machine Functionalised Biological and Biomimetic Systems*. PhD thesis
<http://theses.gla.ac.uk/3277/>

Copyright and moral rights for this thesis are retained by the author

A copy can be downloaded for personal non-commercial research or study, without prior permission or charge

This thesis cannot be reproduced or quoted extensively from without first obtaining permission in writing from the Author

The content must not be changed in any way or sold commercially in any format or medium without the formal permission of the Author

When referring to this work, full bibliographic details including the author, title, awarding institution and date of the thesis must be given.

Towards Molecular Machine Functionalised Biological
And Biomimetic Systems.

Catherine Elaine Maclean

Thesis is submitted in part fulfilment of the requirements for the
Degree of Doctor of Philosophy



School of Chemistry
College of Science and Engineering
February 2012

Abstract.

Overall this thesis describes the study of the ability of the tetracationic cyclophane CBPQT⁴⁺ to form inclusion complexes with electron-rich moieties such as tetrathiafulvalene (TTF) and dioxynaphthalene. These complexes are strengthened by π -stacking and charge transfer interactions, which give rise to coloured complexes. The complexes are fully reversible and can be decomplexed by the addition of a stimulus that can be chemical, electrochemical, and thermal. In addition we have exploited the ability of ferrocene to form inclusion complexes with cyclodextrins in aqueous media. The host-guest interactions that occur between these molecules were investigated using a number of techniques such as UV-Vis, fluorescence, NMR spectroscopy and cyclic voltammetry. Isothermal titration calorimetry (ITC) was also used to measure the K_a of the complexes.

Chapter two describes the synthesis of naphthalene and ferrocene functionalised dihydroimidazophenanthridines (DIPs). These materials were synthesised in order to create DNA intercalating agents that could undergo further host-guest interactions with either CBPQT⁴⁺ or β -cyclodextrin. These interactions were studied using ITC in a number of aqueous buffers with calf thymus DNA and the synthetic Dickerson dodecamer D-DNA. Additionally, the host-guest interactions for the naphthalene functionalised DIP with CBPQT⁴⁺ were studied using UV-Vis, fluorescence and NMR spectroscopy. The cytotoxic nature of the functionalised DIPs were investigated using MDCK epithelial cell culture experiments.

Chapter three describes the synthesis and analysis of silane and disulfides modified with chosen electron rich substrates for the production of functionalised surfaces where self-assembled monolayers were produced on either glass or gold surfaces. These functionalised surfaces were then utilised in cell adhesion experiments with MDCK cells where

the modulation of adhesion was attempted by the formation of pseudo-rotaxanes with either CBPQT⁴⁺ or β -cyclodextrin and by changing the oxidation state of the functional group in the case of ferrocene.

Chapter four describes the synthesis of functionalised diacetylenes for the formation of polydiacetylene liposomes in aqueous conditions. The liposomes successfully formed were analysed by DLS. UV-Vis spectroscopy and cyclic voltammetry were used to investigate the dual response chromophoric sensing applications of these materials.

Chapter five describes the synthesis of functionalised surfactant compounds for the formation of mixed micelles in aqueous conditions with sodium dodecyl sulfate (SDS). The interactions between the surfactant and CBPQT⁴⁺ were measured by ITC, NMR, UV-Vis, and fluorescence spectroscopy.

Chapter six describes the modification of the protein BSA with a naphthalene functionalised chloroacetate. The modified protein was analysed by ITC, MALDI TOF, UV-Vis, and fluorescence spectroscopy in order to identify the degree of functionalisation that had occurred and whether complexation was possible with CBPQT⁴⁺.

Chapter seven describes the synthesis of a naphthalene, and two ferrocene functionalised biotin conjugates with a view to investigate the interactions with avidin proteins. The interactions were measured by ITC and UV-Vis spectroscopy. The effect of changing the chain length on binding to neutravidin and β -cyclodextrin was studied in the ferrocene biotin conjugates where the interactions were assessed using ITC, cyclic voltammetry, and NMR spectroscopy. The interactions between the naphthalene based conjugate and CBPQT⁴⁺ was measured by UV-Vis and fluorescence spectroscopy.

Acknowledgements.

I would like to thank my supervisors Prof. G. Cooke, Prof A Cooper, Dr M. Riehle and Dr B. O Smith for all their help, patience and expertise over the past four years whilst I was working on my PhD.

I would like to thank the past and present members of the Cooke group, in particular Dr S Caldwell and Dr B Fitzpatrick for all their help throughout. I would like to thank the members of the cell engineering department for all their help expertise and patience.

I would like to show my appreciation to Dr C Richmond and Mr A G Boulay for their work with the DIP compound. Many thanks to Mr T Carpy for his work with the SAMs.

I would also like to thank Mrs M Nutley, Mr. J. Tweedie, Ms I. Freer, and Mr D. Adams for their continual help with ITC, Mass Spec and NMR work.

Most of all I would like to thank my family and friends for their continual support over the past four years and beyond.

I would like to thank the University of Glasgow and The Kelvin-Smith Scholarship for funding.

Declaration:

I hereby declare that the substance of this thesis has not been submitted, nor is currently submitted in candidature for any other degree. Portions of the work described herein have been published elsewhere and are listed below.

I also declare that the work presented in this thesis is the result of my own investigations and where the work of other investigators has been used, this has been fully acknowledged within the text.

Catherine Elaine Maclean.

Glossary

DNA	Deoxyribose nucleic acid
D-DNA	Dickerson dodecamer DNA with sequence. d(CGCGAATTCGCG) ₂
DMAP	4-Dimethylaminopyridine.
EDCI	1-(3-Dimethylaminopropyl)-3-ethyl carbodiimide.
ECM	Extracellular Matrix
FAB	Fast Atom Bombardment.
MDCK	Madin Derby Canine Kidney Epithelial cells
NOBA	Nitro benzyl alcohol.
TTF	Tetrathiafulvalene
CBPQT ⁴⁺	Tetracationic cyclophane cyclobis(paraquat- <i>p</i> -phenylene)
MALDI	Matrix assisted laser desorption ionisation.
EPR	Electron Paramagnetic Resonance
SPR	Surface Plasmon Resonance
NMR	Nuclear Magnetic Resonance
ITC	Isothermal Titration Calorimetry
DLS	Dynamic Light Scattering
CV	Cyclic Voltammetry
DIP	Dihydrimidazophenanthridine
IP	Imidazophenanthridine
POM	Polyoxometallate crystals

SAM	Self-assembled Monolayer
Fc	Ferrocene
CR	Colorimetric Response
SDS	Sodium Dodecyl sulfate
Cp	Cyclopentadiene
HABA	4'-Hydroxy azobenzene-2-carboxylic acid
N _A	Neutravidin
A _v	Avidin
PBS	Phosphate buffered saline
BSA	Bovine Serum Albumin
PIPES	Piperazine-1,4-bis(ethanesulfonic acid)
MOPS	3-(<i>N</i> -morpholino) propane sulfonic acid
ITO	Indium Tin Oxide
FTIR	Fourier Transform Infrared Spectroscopy
PDI	Polydispersity Index
RGD	Tripeptide chain with Arginine, Glycine, Aspartic acid
NBS	N-bromosuccinimide
CMC	Critical micelle concentration

Contents Page

1.	Introduction.	1
1.1.	Supramolecular Chemistry.	1
1.2.	Intermolecular Interactions.	2
1.2.1.	Electrostatic Interactions.	4
1.2.2.	Van der Waals Forces.	4
1.2.3.	Ion-Dipole Interactions.	4
1.2.4.	Dipole- Dipole Interactions.	5
1.2.5.	Hydrophobic Interactions.	6
1.2.6.	Hydrogen Bonding Interactions.	6
1.2.7.	π - π Stacking Interactions.	8
1.2.8.	Self Assembly and Other Factors for Complexation.	9
1.2.8.1.	Self Assembly.	9
1.2.8.2.	The Chelate Effect.	10
1.2.8.3.	Preorganisation.	10
1.3.	Molecular Architectures.	11
1.4.	Key Functional Supramolecular Groups used in this study	15
1.4.1.	Cyclobis(paraquat- <i>p</i> -phenylene) (CBPQT ⁴⁺).	15
1.4.2.	Tetrathiafulvalene as redox active guests for CBPQT ⁴⁺ .	21
1.4.3.	Cyclodextrins.	23
1.4.4.	Ferrocene as a redox active guest.	25
1.5.	Molecular Machines.	32
1.6.	Sensors and Biosensors.	33
1.7.	Cells and their adhesion properties.	35
1.8.	Analytical Techniques used in this research programme.	46
1.8.1.	Isothermal titration calorimetry.	46
1.8.2.	Cyclic Voltammetry.	49
1.8.3.	Dynamic Light Scattering.	53
1.8.4.	UV-Vis, Fluorescence spectroscopy.	56

2.	Functionalised Dihydroimidazophenthridine Intercalating Agents.	58
2.1.	Dihydroimidazophenanthridines and Imidazophenanthridines.	59
2.1.1.	Synthesis of Dihydroimidazophenanthridines and Imidazophenanthridines.	59
2.1.2.	Intercalative and Cytotoxic Properties of DIP and IP compounds.	63
2.1.3.	Microtubule Formation with Polyoxometallate (POM) Crystals.	65
2.2.	Aims and Objectives.	70
2.3.	Results and Discussion.	71
2.3.1.	Synthesis of the naphthalene amine 5a.	71
2.3.2.	Synthesis of the ferrocene amine 25a.	75
2.3.3.	Analysis of the functionalised Dihydro Imidazo Phenanthridines.	78
2.3.3.1.	UV-Vis Spectroscopy of Naphthalene DIP (23) and CBPQT ⁴⁺ (61).	79
2.3.3.2.	¹ H NMR spectroscopic studies.	80
2.3.4.	DNA Interactions with the DIP compounds.	82
2.3.4.1.	ITC experiments with Calf Thymus DNA.	82
2.3.4.2.	ITC experiments with a synthetic dodecamer DNA.	89
2.3.5.	Cell Culture Studies.	93
2.3.5.1.	Cell Injection studies.	93
2.3.5.2.	Cell toxicity studies.	98
2.3.6.	Microtubule Formation from Anionic Polyoxometallate crystals and Cationic DIPs.	105
2.4.	Conclusions and Future Work.	110
2.4.1.	Conclusions.	110
2.4.2.	Future Work.	111

3.	Functionalised Self Assembled Monolayers for Cell Adhesion Studies.	112
3.1.	Introduction.	113
3.2.	Aims and Objectives.	120
3.2.1.	Modified Silanes.	120
3.2.2.	Modified Disulfides.	121
3.3.	Results and Discussion.	122
3.3.1.	Synthesis of functionalised Silanes.	122
3.3.1.1.	Ferrocene silane synthesis.	122
3.3.1.2.	Naphthalene silane synthesis.	123
3.3.2.	Monolayer formation of 18 on Glass Surfaces.	124
3.3.3.	Synthesis and analysis of thiotic acid functionalised electron rich moieties.	127
3.3.3.1.	Synthesis of ferrocene disulfide.	127
3.3.3.2.	Synthesis of tetrathiafulvalene disulfide.	127
3.3.4.	Immobilisation of naphthalene disulfide 16 onto gold.	130
3.3.5	Cell Engineering experiments.	137
3.4.	Conclusions and Future Work.	142
3.4.1.	Conclusions.	142
3.4.2.	Future Work.	143
4.	Pseudorotaxane modification of Diacetylene Liposomes.	144
4.1.	Introduction.	145
4.2.	Aims and Objectives.	153
4.3.	Results and Discussion.	154
4.3.1.	Synthesis of functional diacetylene monomers.	154
4.3.2.	Liposome formation and analysis.	156
4.4.	Conclusions and Future Work.	164
4.4.1.	Conclusions.	164
4.4.2.	Future Work.	165

5.	Pseudorotaxanes as tunable micelles.	166
5.1.	Introduction.	167
5.2.	Aims and Objectives.	174
5.3.	Results and Discussion.	175
5.3.1.	Synthesis of functionalised trimethylammonium bromide surfactants.	175
5.3.1.1.	Synthesis of naphthalene based surfactant (9).	175
5.3.1.2.	Synthesis of TTF hexan-1-one-6-Trimethyl ammonium bromide.	176
5.3.2.	Complexation of 9 with CBPQT ⁴⁺ .	177
5.3.2.1.	Isothermal Titration Calorimetry of compound 9 with CBPQT ⁴⁺ .	177
5.3.2.2.	¹ H NMR study with CBPQT ⁴⁺ .	180
5.3.2.3.	UV-Vis and Fluorescence Spectroscopy.	181
5.3.3.	Micelle formation and analysis.	183
5.3.3.1.	¹ H NMR titration studies of Naphthalene trimethylammonium bromide 9 with SDS.	183
5.3.3.2.	Fluorescence Spectroscopy Titration Studies.	185
5.4.	Conclusions and Future Work.	189
5.4.1.	Conclusions.	189
5.4.2.	Future Work.	189
6.	Modification of BSA via Pseudorotaxane Formation.	190
6.1	Introduction.	191
6.2	Pseudorotaxane protein modification Aims and Objectives.	198
6.3	Results and Discussion.	199
6.3.1	Attempted Synthesis of 1-Azidopropyl-3-maleimide (43) for click Chemistry.	199
6.3.2	Synthesis of 1-(2,2,2-chloroacetyloxyethoxy), -5-(2,2-hydroxy ethoxy ethoxy) naphthalene (19a).	200

6.3.3	Modification of BSA with 1-(2,2,2-chloroacetyloxyethoxy), -5-(2,2-hydroxy ethoxy ethoxy) naphthalene (19a).	200
6.3.4.	Analysis of the modified BSA.	202
6.3.4.1	MALDI TOF analysis.	203
6.3.4.2	Investigation of binding to CBPQT ⁴⁺ by ITC.	204
6.3.4.3	UV-Vis Spectroscopy.	206
6.3.4.4	Fluorescence Spectroscopy.	208
6.4	Conclusions and Future Work.	211
6.4.1	Conclusions.	211
6.4.2	Future Work.	211
7	Functionalised Biotin Compounds and their implementation as pseudorotaxane based bioconjugates.	212
7.1	Introduction.	213
7.2	Aims and Objectives.	220
7.3	Results and Discussion.	222
7.3.1	Synthesis of biotinylated ferrocene compounds 28 and 29 .	222
7.3.2	Analysis of the biotinylated conjugates.	223
7.3.2.1	UV-Vis Spectroscopy.	223
7.3.2.2	ITC experiments.	227
7.3.2.3	Cyclic Voltammetry.	236
7.3.2.4	¹ H NMR studies with β -cyclodextrin.	239
7.4.	Conclusions and Future Work.	241
7.4.1.	Conclusions.	241
7.4.2	Future Work.	242
8.	Experimental.	243
8.1	General Experimental and Materials.	244
8.2	Synthesis.	245
9.	References.	291

10. Appendices.	297
Appendix 1.	
Experimental Procedures for the synthesis of the functionalised DIPs 23 and 30 .	297
Appendix 2.	
Standard procedures for using analytical equipment.	300
Appendix 3.	
Cell Culture Protocols.	302
Appendix 4.	
Glass cleaning with Caro's Acid.	307
Appendix 5.	
Monochromatic images from antibody cell staining experiments in § 3.3.4 .	308
Publications.	310

Table of Figures.

Figure 1.1	Schematic diagram of host – guest binding.	2
Figure 1.2	Schematic diagram showing Fischer's lock and key principle.	3
Figure 1.3	Hydrogen bonding found between the nucleoside base pairs of DNA.	3
Figure 1.4	Shows the different types of electrostatic interaction.	4
Figure 1.5	The binding of Na ⁺ within the cavity of [18]-Crown-6.	5
Figure 1.6	Dipole-Dipole Interactions. a) Singular Dipole Interactions. b) Opposing Dipole Interactions.	5
Figure 1.7	Schematic Representation of the Hydrophobic Effect.	6
Figure 1.8	The Donor-Acceptor Interactions found in Hydrogen Bonding.	7
Figure 1.9	The Different Possible Angles for H-bonding.	7
Figure 1.10	π - π Stacking Interactions. a) Edge to Face π Stacking. b) Face to Face π Stacking.	8
Figure 1.11	Illustration of DNA.	9
Figure 1.12	Binding of Ni ²⁺ complexes. a) [Ni(NH ₃) ₆] ²⁺ . b) [Ni(en) ₃] ²⁺ . *en = ethylenediamine.	10
Figure 1.13	The Binding of a Metal Cation to a) a spherand b) a crown ether.	11
Figure 1.14	Illustration of a) A [2]-Rotaxane b) A [2]-Catenane.	12
Figure 1.15	Motions found in a) [2]-Rotaxanes b) [2]-Catenanes.	12
Figure 1.16	Formation of Pseudorotaxane then Capping of the ends.	13
Figure 1.17	Formation by Clipping.	13
Figure 1.18	Formation by Ring Slippage.	14
Figure 1.19	Clipping to form Catenanes a) One ring Preformed. b) Clipping of both rings.	14
Figure 1.20	'Mobius Strip' Ring Slippage in Catenanes.	15
Figure 1.21	Structure of CBPQT ⁴⁺ with the α , β , and benzyl Hydrogens' labelled.	15
Figure 1.22	Structure of [2]-Rotaxane. The CBPQT ⁴⁺ ring in blue, the axle in red.	16
Figure 1.23	X-ray crystal structure of the [2]-Rotaxane 1. The axle in red folds around the CBPQT ⁴⁺ bead shown in blue.	16
Figure 1.24	A) Basic structure of the pseudorotaxane and B) The X-Ray crystal structure.	18
Figure 1.25	X-ray structure of TTF in the cavity of CBPQT ⁴⁺ .	20
Figure 1.26	CV of CBPQT ⁴⁺ 4PF ₆ ⁻ 0.5 mM solution in 0.1 M TABPF ₆ /MeCN at 25°C.	20
Figure 1.27	EPR spectrum for the CBPQT radical.	21

Figure 1.28	The three forms of TTF. TTF(0), TTF ^{••} , and TTF ²⁺ .	21
Figure 1.29	Cyclic voltammogram for TTF (black) in the presence of CBPQT ⁴⁺ and 1,5-DN-[38]-C10 (red).	23
Figure 1.30	Structure of a cyclodextrin. n = number of glucose units that make up the structure.	24
Figure 1.31	The complexation of Sodium with N-ferrocenylmethylaza-18-crown-6.	27
Figure 1.32	Illustration of the inclusion complexes of ferrocene and α , β and γ - Cyclodextrins.	28
Figure 1.33	Complexation/Decomplexation process required for the oxidation of ferrocene cyclodextrin inclusion complexes.	28
Figure 1.34	Cyclic Voltammogram of ferrocene with the complex of ferrocene with β -cyclodextrin overlaid.	29
Figure 1.35	¹ H NMR shifts observed for the ferrocene derivative with cyclodextrins.	30
Figure 1.36	Structure of a cucurbituril. n = number of glycoluril units that make up the structure.	30
Figure 1.37	¹ H NMR spectra of ferrocene derivative (A) in the absence and in the presence of (B) 0.5 equiv and (C) 1.1 equiv of CB7.	31
Figure 1.38	Structure of tetracationic macrobicyclic molecule in its native conformation.	33
Figure 1.39	Chromophoric switching of the macrobicyclic molecule with the addition of TTF.	34
Figure 1.40	Schematic Illustration of a biosensor.	34
Figure 1.41	Cartoon of cell adhesion to the ECM via focal adhesions.	36
Figure 1.42	The growth and migration of BCE cells on a surface after the application of an electrical potential where the time in minutes after the voltage pulse is indicated.	39
Figure 1.43	Summary of the influence of drugs on the motility of BCE cells after the application of a voltage pulse of -1.2V for 30s.	40
Figure 1.44	Redox process to form the benzoquinone from the hydroquinone followed by Diels alder reaction to create biologically active SAMs for Swiss 3T3 fibroblast cell migration.	41
Figure 1.45	Production and activation of surfaces for the migration and growth of cells with an electroactive substrate.	42
Figure 1.46	The effects of anti-motility drugs on the migration of Swiss 3T3 fibroblasts after the application of an electrical potential.	43
Figure 1.47	Structure of E [*] -RGD.	43
Figure 1.48	Structure of RGD-Cp.	44

Figure 1.49	Release of cells then remigration across surface after addition of RGD-Cp.	45
Figure 1.50	Schematic of ITC instrument showing the layout the sample and reference cells, insulating shield and injection syringe.	47
Figure 1.51	Typical binding curve produced by an ITC experiment.	48
Figure 1.52	Triangular sweeping of the electrical potential.	51
Figure 1.53	CV wave for the reversible redox process for Fe ²⁺ to Fe ³⁺ .	52
Figure 1.54	Schematic diagram of a cyclic voltammetry experimental setup.	53
Figure 1.55	Schematic diagram of a typical DLS experimental setup.	55
Figure 1.56	Schematic diagram of a UV-Vis experiment.	56
Figure 1.57	Schematic of a fluorescence experiment.	57
Figure 2.1	General structures of derivatised phenanthridine derivatives. a) Dihydro-imidazo-phenanthridine. b) Imidazo-phenanthridine.	59
Figure 2.2	a) Generalised structure of a reduced BCPA b) Pseudobase of a BCPA c) Pseudobase of a DIP.	60
Figure 2.3	Numbered general DIP structure with the N1 and N2 postions labelled in blue.	61
Figure 2.4	An example of ITC data for binding of a DIP ligand to salmon testes DNA.	64
Figure 2.5	Time-lapse images of a single tube emerging from a crystal.	66
Figure 2.6	Size control of a growing tube by altering the available concentration of cations at points (a), (b), (c), and (d). The estimated concentrations at each point are shown in the lower section.	67
Figure 2.7	Motifs formed by controlling the tube growth direction.	68
Figure 2.8	Manual breakage of tube to causes branching then manipulation growth.	68
Figure 2.9	Two microtubes merging to form a larger tube.	68
Figure 2.10	POM microtube injected with fluorescein isothiocyanate dye.	69
Figure 2.11	Final DIP products.	70
Figure 2.12	Functionalised DIPs 23 and 30 .	78
Figure 2.13	UV-Vis data from the complex of 23 and 61 at room temperature with baseline correction. Concentration 10 ⁻³ M in water.	80
Figure 2.14	¹ H NMR spectra recorded for A) 23 B) 61 C) Complex of 23/61 in D ₂ O.	81
Figure 2.15	ITC Data for experiment with water as the solvent. A is the raw data recorded. B is analysed DIP injected into CT-DNA. C is CBPQT injected into DIP/CT-DNA. D is CBPQT injected into CT-DNA.	83
Figure 2.16	The ITC data for 23 with CT-DNA in PBS. A) 23 into CT-DNA. B) CBPQT into 23 /CT-DNA. C) CBPQT into CT-DNA. D) 23 into CBPQT/CT-DNA.	85

Figure 2.17	The raw ITC data recorded for Phosphate, MOPS, and Water.	88
Figure 2.18	Raw ITC data for experiments ran in PIPES buffer.	89
Figure 2.19	Raw ITC data of 23 and CBPQT ⁴⁺ with D-DNA.	91
Figure 2.20	Analysed ITC experiments with D-DNA. A) 23 into D-DNA. B) CBPQT ⁴⁺ into D-DNA. C) 23 /CBPQT ⁴⁺ into D-DNA.	92
Figure 2.21	Naphthalene trimethylammonium bromide (9).	93
Figure 2.22	Fluorescence of Naphthalene trimethylammonium bromide with CBPQT ⁴⁺ (61) Ex = 295nm at room temperature. 10 ⁻⁵ M in water.	94
Figure 2.23	Fluorescence of 23 with and without CBPQT ⁴⁺ at room temperature. Excitation wavelengths of 295 nm and 365 nm. Concentration 10 ⁻⁵ M	95
Figure 2.24	Fluorescence of 30 with 63 compared to 23 . Ex 365 nm.	95
Figure 2.25	Illustration of the microsyringe within its holder.	96
Figure 2.26	Illustration of Syringe at search plane over a cell	97
Figure 2.27	Illustration of the movement of the needle from the search plane to cell injection then return to search plane.	97
Figure 2.28	Live/Dead Stain Components: Hoechst 33342 and Propidium Iodide.	99
Figure 2.29	Live Dead stained cells after treatment with 23 and 30 . Blue the nuclei of stained Live cells stained with Hoechst 33342 and red are the nuclei of dead cells stained with propidium iodide.	100
Figure 2.30	Live Dead stained cells after treatment with DIP substrates. Blue the nuclei of stained Live cells stained with Hoechst 33342 and red are the nuclei of dead cells stained with Propidium Iodide.	101
Figure 2.31	MTT staining agent and its metabolite.	102
Figure 2.32	Layout of the DIP treatments for MTT in 24 well plate.	103
Figure 2.33	Layout of the DIP treatments for MTT in 96 well plates A and B.	103
Figure 2.34	Microtubule growth of Naphthalene DIP/ CBPQT ⁴⁺ 4Cl ⁻ with POM Keggin net crystal over time.	108
Figure 2.35	Growth of CBPQT ⁴⁺ POM microtube which is halted by addition of 23 .	109
Figure 3.1	Illustration of the selective adhesion to the surface with CA-RGD present.	113
Figure 3.2	SPR sensorgrams that show that CA-RGD binds to 1% benzene sulfonamide, but fails to bind to 100% triethylene glycol SAMs.	114
Figure 3.3	Illustration of the effect of CA-RGD concentration on cell adhesion to the surface.	115
Figure 3.4	CHO cell adhesion mediated by CA-RGD on 1% benzenesulfonamide (C) and 1% Ac-GRGDSC (D). Cells failed to adhere to benzenesulfonamide monolayers (B).	115

Figure 3.5	Structure of GPTMS.	116
Figure 3.6	Illustration of the functionalised ITO glass surface.	117
Figure 3.7	E coli viability on the functionalised surfaces vs the time treated with WCl_6 /PWA with PMB.	118
Figure 3.8	Bactericidal activity of the surface vs Controls of PMB and PMB-free experiments.	119
Figure 3.9	Silane Target Molecules.	121
Figure 3.10	Target Molecules for Functionalised Disulfide Synthesis.	121
Figure 3.11	Naphthalene Silane SAM on glass.	124
Figure 3.12	The Average Contact Angles measured in triplicate for cleaned glass coverslips and cleaned coverslips treated with the naphthalene silane 18 .	125
Figure 3.13	Phase contrast images of MDCK cells grown on Naphthalene silane functionalised glass slides with and without CBPQT ⁴⁺ present. X10 optical zoom.	126
Figure 3.14	Structure of the Naphthalene disulfide 16 .	130
Figure 3.15	Resistivity measured for the formation of the Butyl disulfide SAM onto the gold surface at room temperature.	131
Figure 3.16	Resistivity measured for the 1:1 butyl - naphthalene disulfide SAM onto the gold surface at room temperature.	132
Figure 3.17	Resistivity measured for the formation of the naphthalene disulfide SAM onto the gold surface at room temperature.	132
Figure 3.18	Resistivity measured at room temperature for the addition of CBPQT onto the gold surface.	133
Figure 3.19	EPR of CBPQT ^{2(+.)} diradical formed by the addition of either zinc or copper.	134
Figure 3.20	The addition of CBPQT ⁴⁺ to the butyl and naphthalene SAMs in acetonitrile at room temperature.	135
Figure 3.21	Resistivity for SAMs treated with CBPQT ²⁺ at room temperature A) butyl disulfide SAM. B) naphthalene disulfide SAM.	136
Figure 3.22	Coomassie Blue staining of MDCK cells on the disulfide SAMs with and without β -cyclodextrin added. X10 optical zoom.	139
Figure 3.23	MDCK images stained for Actin (red), Tubulin (green) and with DAPI (blue). 40x optical zoom.	141
Figure 4.1	Illustration of a liposome.	145
Figure 4.2	1,4-addition ene-yne polymerisation of diacetylene chains.	146
Figure 4.3	A schematic representation of the possible interactions that can be incorporated into colorimetric polydiacetylene sensors.	147
Figure 4.4	Structure of sialic acid diacetylene.	148
Figure 4.5	Structure of Gangliosides G_{T1b} , and G_{M1} .	149

Figure 4.6	A) UV-Vis spectra for cholera toxin addition over time. B) Graph of the colorimetric response plotted % vs time.	150
Figure 4.7	Structure of the derivatised Azobenzene diacetylenes.	151
Figure 4.8	Schematic of reversibility of the functionalised polydiacetylene films.	152
Figure 4.9	Functionalised diacetylene target molecules.	153
Figure 4.10	Illustration of general liposome formation procedure.	156
Figure 4.11	UV-Vis of polydiacetylene liposomes.	157
Figure 4.12	Structure of the β -cyclodextrin polymer.	158
Figure 4.13	UV-Vis of FcDA liposome with β -cyclodextrin polymer.	159
Figure 4.14	UV-Vis of PCDA liposome with β -cyclodextrin polymer.	160
Figure 4.15	UV-Vis of the liposomes with 3×10^{-2} M of β -cyclodextrin polymer added.	160
Figure 4.16	DLS data recorded for FcDA liposome.	162
Figure 4.17	CVs of A) FcDA liposome (red) with β -cyclodextrin (blue) B) 100% PCDA liposome.	163
Figure 5.1	Illustration of a typical surfactant molecule.	167
Figure 5.2	Illustration of A) Micelle structure. B) Reversed micelle structure.	168
Figure 5.3	A) Structure of CTAB molecule and illustrations of B) Micelle and C) Reversed micelle.	169
Figure 5.4	Comparison of tandem mass spectra at m/z 10 000 for regular micelles in 200 mM ammonium acetate (A), reverse micelles in H_2O (B), and reverse micelles incorporating myoglobin in 10 mM ammonium acetate (C).	170
Figure 5.5	Schematic illustration of the round trip of PB-PEO micelles between the [BMIM] [PF6] and water layers, accompanied by experimental images at each temperature.	172
Figure 5.6	Hydrodynamic radius of the PB-PEO micelles in three different solutions (1 wt %) by DLS at ambient temperature.	173
Figure 5.7	Napthalene trimethylammonium bromide (9) and Tetrathiafulvalene trimethylammonium bromide (45).	174
Figure 5.8	ITC data for 9 with CBPQT ⁴⁺ in water.	179
Figure 5.9	Stacked ¹ H NMRs of NapMe ₃ N ⁺ (red), CBPQT ⁴⁺ (blue) and the 1:1 complex (green).	181
Figure 5.10	A) UV-Vis spectrum of 9 + 61 10^{-3} M. B) Fluorescence spectra recorded for 9 + 61 10^{-5} M. All measurements recorded at room temperature in water.	182
Figure 5.11	¹ H NMR spectra of 9 with increasing aliquots of SDS.	184

Figure 5.12	Graph showing the change in the fluorescence at $\lambda_{Ex}= 295\text{nm}$. $\lambda_{Em} = 329 \text{ nm}$ of 9 as a function of SDS concentration. Recorded in H_2O at 25°C .	186
Figure 5.13	Partial ^1H NMR spectra of: (a) 9 + 61 in D_2O . (b) 9 + 61 + SDS (supernatant), (c) 9 recorded in D_2O ; (d) precipitate from 9 + 61 + SDS in $\text{d}_6\text{-DMSO}$ $\sim 10^{-4} \text{ M}$ at 40°C .	187
Figure 6.1	Immobilisation of CP1c onto polystyrene-maleimide surface.	193
Figure 6.2	The structure of N-(ferrocenyl) iodoacetamide.	195
Figure 6.3	Structure of A) Fc-glutathione, B) Fc-cysteine.	196
Figure 6.4	CV of Fc-glutathione (0.4 mM) and glucose (32.5 mM) in 50 mM potassium phosphate buffer in the (a) absence, (b) presence of glucose oxidase ($40 \mu\text{M}$).	197
Figure 6.5	Naphthalene chloroacetate target molecule.	198
Figure 6.6	Structure of the modification per amino group on the protein BSA.	203
Figure 6.7	MALDI TOF results for m-BSA 45 and BSA.	204
Figure 6.8	Raw ITC data for CBPQT $^{4+}$ with BSA and m-BSA.	205
Figure 6.9	Analysed data for CBPQT $^{4+}$ into m-BSA.	206
Figure 6.10	UV-Vis spectrum for the addition of CBPQT $^{4+}$ to m-BSA at room temperature.	207
Figure 6.11	UV-Vis spectrum for the addition of CBPQT $^{4+}$ to BSA at room temperature.	208
Figure 6.12	Fluorescence emission spectra of BSA upon addition of A) CBPQT $^{4+}$ B) H_2O (1- $\text{Ex}=282\text{nm}$, 2- $\text{Ex}=295\text{nm}$). All measurements were carried out at room temperature.	209
Figure 6.13	Fluorescence emission spectra of M-BSA upon addition of A) CBPQT $^{4+}$ B) H_2O (1- $\text{Ex}=282\text{nm}$, 2- $\text{Ex}=295\text{nm}$). All measurements were carried out at room temperature.	210
Figure 7.1	Structure of Biotin.	213
Figure 7.2	Modified HABA derivatives with their binding constants K_a .	214
Figure 7.3	SAMs with biotin that is released by the application of an electrical potential.	216
Figure 7.4	SPR data for the SAMs before and after addition of an electrical potential.	216
Figure 7.5	Structure of the naphthalene biotin conjugate.	217
Figure 7.6	UV-Vis recorded in water/ethanol 70:30. avidin + CBPQT (grey); Plus Naphthalene biotin (purple); Plus TTF (green).	218
Figure 7.7	Heat vs time plot of A) naphthalene biotin into avidin. B) CBPQT $^{4+}$ into naphthalene biotin / avidin complex. C) CBPQT $^{4+}$ into avidin.	219
Figure 7.8	Functionalised biotin conjugates for investigation.	221

Figure 7.9	Illustrative schematic of the complexation of the functionalised biotins to avidin with additional complexation of a guest molecule.	221
Figure 7.10	Changes in the absorbance at 500nm with increasing equivalents of 28 to HABA-Neutravidin complex.	224
Figure 7.11	Changes in absorbance at 500nm with increasing equivalents of 29 to the HABA –Neutravidin complex.	224
Figure 7.12	UV-Vis of naphthalene biotin into HABA/avidin. Black = avidin 10^{-5} M. Red = avidin with 4eq HABA. Blue = upon addition of 4eq of 22 into the HABA/avidin complex.	225
Figure 7.13	UV-Vis spectrum of 22 with CBPQT ⁴⁺ . Red line = 22 (10^{-4} M). Blue line = 22 + CBPQT ⁴⁺ Recorded at room temperature in water.	226
Figure 7.14	Fluorescence emission spectrum of 22 with CBPQT ⁴⁺ . Black line = 22 (10^{-5} M). Grey line = 22 + CBPQT ⁴⁺ .	226
Figure 7.15	Fluorescence emission spectrum of 22 with avidin. Black line = 22 (10^{-5} M). Grey line = 22 + avidin.	227
Figure 7.16	Raw ITC data collected for compound 28 with Neutravidin and β -cyclodextrin.	229
Figure 7.17	ITC data for the titration of 28 into Neutravidin solution.	230
Figure 7.18	ITC titration data for A) 29 into neutravidin. B) addition of β -cyclodextrin to 29 / neutravidin. C) β -cyclodextrin into 29 .	233
Figure 7.19	ITC graphs of A) 22 into avidin. B) 22 into Neutravidin. C) CBPQT ⁴⁺ into 22 .	235
Figure 7.20	CV of compound 28 with increasing equivalents of β -cyclodextrin.	237
Figure 7.21	CV of compound 29 with increasing equivalents of β -cyclodextrin.	237
Figure 7.22	Spectra of the ferrocene SC biotin 28 with β -cyclodextrin added.	240
Figure 7.23	Spectra of the ferrocene LC biotin 29 with β -cyclodextrin added.	240

Table of Schemes.

Scheme 1.1	Naphthalene templated synthesis of CBPQT ⁴⁺ .	19
Scheme 1.2	Complexation switching by redox oxidation reduction processes for TTF.	23
Scheme 1.3	Conversion of Ferrocene to Ferrocenium.	25
Scheme 2.1	Formation DIP from 5-(2-bromoethyl) phenanthridinium salt.	61
Scheme 2.2	Formation IP from 5-(2-bromoethyl) phenanthridinium salt.	61
Scheme 2.3	Alkylation of 1,5-Dihydroxynaphthalene.	71
Scheme 2.4	EDCI couplings to the alkylated naphthalene.	72
Scheme 2.5	Methods for amine synthesis via nitrile formation.	73

Scheme 2.6	Retro-Michael reaction for the cleavage of the acrylonitrile.	74
Scheme 2.7	Tosylation reaction scheme.	74
Scheme 2.8	EDCI couplings to ferrocene carboxylic acid.	75
Scheme 2.9	Amine formation via acid chloride formation.	76
Scheme 2.10	Ferrocene acetonitrile reduction.	77
Scheme 2.11	Nap-DIP complex with CBPQT ⁴⁺ then displacement with TTF.	79
Scheme 3.1	Attempted formation of Ferrocene based silane.	122
Scheme 3.2	Synthesis of the naphthalene silane 18 from the diol 2 .	123
Scheme 3.3	EDCI coupling of ferrocene amine 25a with thiotic acid.	127
Scheme 3.4	TTF alcohol synthesis from the starting zincate compound.	128
Scheme 3.5	Reaction scheme for the synthesis of TTF disulfide 49 starting from TTF.	129
Scheme 4.1	Synthesis of functionalised ferrocene diacetylene via the PDA acid chloride.	154
Scheme 4.2	Synthetic scheme for the synthesis of the ferrocene diacetylene monomer 33 .	155
Scheme 4.3	Synthetic scheme for the synthesis of the naphthalene diacetylene 7 .	156
Scheme 5.1	Synthesis of the naphthalene compound 9 .	175
Scheme 5.2	The synthesis of compound 54 from TTF.	176
Scheme 5.3	Pseudorotaxane formation of compound 9 with CBPQT ⁴⁺ 61 .	177
Scheme 6.1	Reaction scheme to produce a naphthalene maleimide for protein modification.	198
Scheme 6.2	Synthesis of azido propyl maleimide from bromo propylamine	199
Scheme 6.3	Synthesis of 19a from diol 2 .	200
Scheme 6.4	Modification of BSA with compound 19a.	200
Scheme 6.5	Reaction mechanism SATA with BSA.	202
Scheme 6.6	Deprotection of the thiol followed by addition of a chloroacetate.	202
Scheme 7.1	Synthesis of ferrocene biotin compounds 28 and 29 from ferrocene amine 25a .	222

Table of Tables

Table 2.1	Functionalised amines used to synthesise DIP compounds.	62
Table 2.2	IC ₅₀ and K _a values for key phenathridine based ligands.	63
Table 2.3	ITC data parameters recorded for key ligands with Salmon Testes DNA.	65
Table 2.4	Thermodynamic data recorded for ITC titrations in water.	82
Table 2.5	pH of the aqueous solutions used.	84

Table 2.6	Thermodynamic data recorded for ITC titration experiments in PBS.	86
Table 2.7	Solvent Vs Concentration of Component.	87
Table 2.8	Experimental details of the 23 and CBPQT ⁴⁺ with D-DNA.	90
Table 2.9	Thermodynamic data recorded for the interaction between 23 , CBPQT ⁴⁺ and D-DNA.	91
Table 2.10	Concentrations of DIP treatment from volumes of 0.5 mM DIP to 1 ml wells.	98
Table 2.11	MTT treatment materials with the letters denoting treatment label.	102
Table 2.12	Average Percentage viabilities for several runs.	104
Table 2.13	Structure of POM crystal, DIPs and guest molecules used in experiments.	106
Table 2.14	Experiments with POM and substrates for microtube formation.	107
Table 3.1	Concentrations of ferrocene and butyl disulfide.	137
Table 4.1	Critical Temperatures for the azobenzene polydiacetylene films.	152
Table 4.2	DLS measurements for the liposomes formed.	161
Table 5.1	Experimental details of for the ITC of the naphthalene trimethylammonium bromide with CBPQT ⁴⁺ .	178
Table 5.2	Thermodynamic data from the titration of CBPQT ⁴⁺ 4Cl ⁻ into NapMe ₃ N ⁺ Br ⁻ 9 .	178
Table 5.3	¹ H NMR Shifts of CBPQT ⁴⁺ and NapMe ₃ N ⁺ upon complexation.	180
Table 5.4	Positions of key protons on the naphthalene trimethylammonium bromide 9 with increasing amounts of SDS.	183
Table 5.5	Shifts exhibited for 9 with SDS equivalents. Change in shift relative to 0eq SDS recorded in brackets.	185
Table 6.1	Bioactivity of m-PEG-rhG-CSF versus native G-CSF in murine myeloblastic NFS-60 cell line.	195
Table 6.2	CV data recorded for the ferrocene conjugates. 50mM potassium phosphate pH 7.4 at 298K vs SCE.	196
Table 6.3	Thermodynamic data recorded for CBPQT ⁴⁺ with the naphthalene modified BSA.	205
Table 7.1	Experimental details for 28 , Neutravidin, and β-cyclodextrin.	228
Table 7.2	Thermodynamic data recorded for titration of 28 into neutravidin.	229
Table 7.3	Experimental details for 29 , neutravidin, and β-cyclodextrin.	231
Table 7.4	Thermodynamic data recorded for the ITC of 29 with neutravidin and β-CD.	232
Table 7.5	Thermodynamic data recorded for ITC titration experiments of 22 with avidin, neutravidin and CBPQT ⁴⁺ .	234

Table 7.6	Intensity and $E^{1/2}$ of CVs collected for compound 28 and β -cyclodextrin.	238
Table 7.7	Intensity and $E^{1/2}$ of CVs collected for compound 29 and β -cyclodextrin.	238

Table of Equations

Equation 1.1	The Hammett Equation.	25
Equation 1.2	Derivised equation from Gibbs Free Energy and the Nernst Equation.	26
Equation 1.3	Derivation of Gibbs Free Energy and the Nernst Equation to yield Equation 1.2.	26
Equation 1.4	Free Energy Equation.	46
Equation 1.5	Calculation for heat capacity.	46
Equation 1.6	Nernst Equation.	49
Equation 1.7	Butler-Volmer Equation.	50
Equation 1.8	Fick's Law.	50
Equation 1.9		52
Equation 1.10		52
Equation 1.11	Stokes-Einstein equation.	54
Equation 1.12		54
Equation 1.13		54
Equation 1.14		54
Equation 1.15		54
Equation 1.16	Beer-Lambert Law.	56
Equation 1.17		57
Equation 2.1	Formula for calculating the concentration of the D-DNA from the absorption at 260nm.	90
Equation 4.1	Formulae for calculating the Colorimetric Response of Polydiacetylene Sensor	150
Equation 4.2	Formulae for calculating the Colorimetric Response	158

1. Introduction.

1.1 Supramolecular Chemistry.

“Chemistry beyond the molecule”^[1].

Supramolecular chemistry is the study of molecular assemblies made of two or more discrete molecular subunits that are held together via non-covalent binding interactions. It is defined as a highly interdisciplinary field that covers the chemical, physical, and biological features of complex molecular assemblies that are held together and organised by intermolecular bonding interactions.^[2] These assemblies are made of two or more discrete molecular subunits that can assemble to create a more complex system via reversible binding interactions, such as hydrogen bonding, hydrophobic effects, and van der Waals interactions. Examples of naturally occurring supramolecular structures include DNA, tobacco mosaic virus, and chlorophyll in plant leaves.

In 1987 Charles J. Pedersen and Donald J. Cram, and Jean-Marie Lehn won the Nobel Prize for chemistry for their work within the area of supramolecular chemistry. Jean-Marie Lehn described supramolecular chemistry as:

“the chemistry of the intermolecular bond covering the structures and functions of the entities formed by association of two or more chemical species.”^[3]

He described these interactions as the basis for the highly specific recognition processes found in biology such as found in substrate binding to a receptor protein. Donald J Cram, Lehn’s fellow Nobel laureate, defined host-guest complexes as:

“Complexes are composed of two or more molecules or ions held together in unique structural relationships by electrostatic forces other than those of full covalent bonds.” “High structural organization is usually produced only through multiple binding sites.” “A host-guest relationship involves a complimentary stereo-electronic arrangement of binding sites in host and guest.”^[4]

1.2 Intermolecular Interactions.

Host-guest complexes involve reversible binding of a substrate to a receptor using non-covalent interactions such as hydrogen bonding, electrostatic interactions and, π - π stacking interactions. A diagrammatic illustration is shown in Figure 1.1.

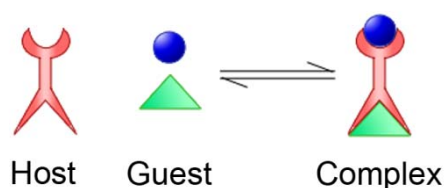


Figure 1.1. Schematic diagram of host – guest binding.

In 1894 Fischer hypothesised the lock and key principle for the visualisation of substrate-enzyme interactions. The principle describes the complementary nature of the host-guest binding site, which is dependent on size, shape and position of host to guest in the complex. The binding site must be both sterically and electronically complementary to the substrate requiring to bind. A schematic of the Fischer lock and key concept is shown in Figure 1.2.^{[5] [6]}

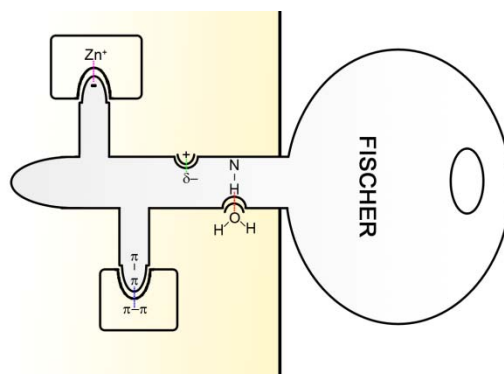


Figure 1.2. Schematic diagram showing Fischer's lock and key principle.^{[5] [6]}

Examples include the complementary association of the two strands in DNA, where hydrogen bonding and π -stacking occur between the nucleobases, adenine and thymine and guanine and cytosine respectively as shown in Figure 1.3.

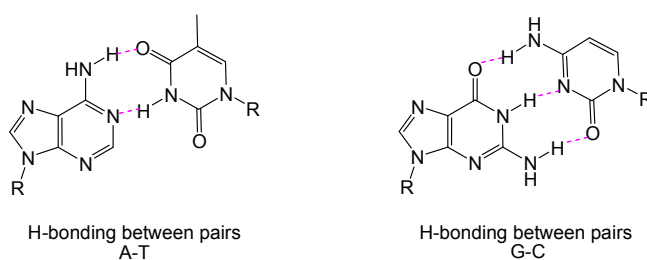


Figure 1.3. Hydrogen bonding found between the nucleoside base pairs of DNA.

Non-covalent interactions are weaker forces than covalent interactions with a strength in the range of 2 kJmol^{-1} to 250 kJmol^{-1} compared 350 kJmol^{-1} for covalent bonding. Each interaction has different ranges in strength.

1.2.1 Electrostatic Interactions.

Electrostatic interactions are high strength interactions based on the Coulombic attraction between opposite charges. They can be found in ionic bonding complexes, between dipoles, and through the attraction of lone pairs in highly electronegative atoms to electron rich atoms in another molecule. Hydrogen bonding is a specific type of electrostatic interaction found in supramolecular chemistry.^{[5] [6] [7]} The different types of interaction are shown in Figure 1.4.

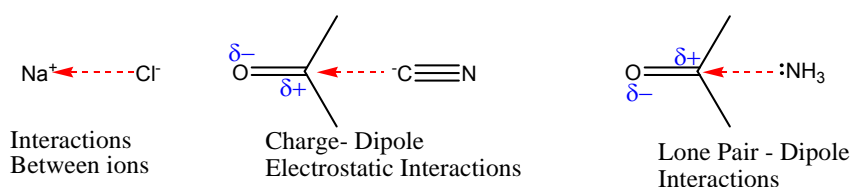


Figure 1.4. Shows the different types of electrostatic interaction.

1.2.2 Van der Waals Forces.

van der Waals forces, are general weak interactions that are typically $<5 \text{ kJmol}^{-1}$ in strength. An electron cloud can be polarised by its proximity to an adjacent nucleus causing a weak, temporary electrostatic interaction. van der Waals forces are not used for the design of supramolecular structures due to the unspecific and low strength of these interactions.^{[5] [6]}

1.2.3 Ion-Dipole Interactions.

Ion-dipole interactions are strong, and relatively directional, with interactions of between $50\text{-}200 \text{ kJmol}^{-1}$. The strongest interactions occur when suitable alignment of the dipole and charge is present. They are

found in the binding of metal cations to crown ethers, where the oxygen lone pairs are attracted to the positive charge of metal cation. An example of ion-dipole interactions can be seen in Figure 1.5. [5] [6]

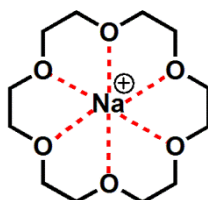


Figure 1.5. The binding of Na^+ within the cavity of [18]-Crown-6.

1.2.4 Dipole-Dipole Interactions.

Dipole-dipole interactions require the alignment of dipoles, which can result in an attractive force in the range of $5\text{-}50 \text{ kJmol}^{-1}$. Alignment can be of a single pair of poles or opposing alignments of dipoles. Opposing alignments of dipoles give the strongest interactions. Figure 1.6 shows both single and opposing dipole interactions. [5] [6]



Figure 1.6. Dipole-Dipole Interactions. a) Singular Dipole Interactions.
b) Opposing Dipole Interactions.

1.2.5 Hydrophobic Interactions.

Hydrophobic interactions are the specific driving force for non-polar species to associate together in aqueous solutions. As the species associate together there is an increase in entropy as water molecules become more disordered. There is also an increase in enthalpy as the hydrogen bonding between water molecules becomes stronger. The schematic below in Figure 1.7 shows the expulsion of water from a hydrophobic centre, as a result of binding from a general hydrophobic species. [5] [6]

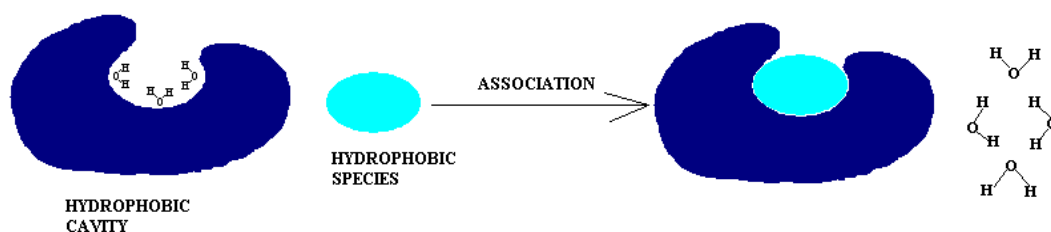


Figure 1.7. Schematic Representation of the Hydrophobic Effect.

1.2.6 Hydrogen Bonding Interactions.

Hydrogen bonding is an important type of intermolecular interaction found between hydrogen atoms attached to a highly electronegative atom that can be N, O, P, and a halogen, and the non-bonding electron pair on another electronegative atom, which can also be N, O, P, and a halogen. They are highly specific directional electrostatic forces, which are precise and can have a wide range of strengths, varying from 4–12 kJmol⁻¹ for weak bonds up to 60-120 kJmol⁻¹ for strong hydrogen bonds. Hydrogen bonding is utilised in biological systems including enzymes and DNA. They are found in receptors where coordination of neutral organic species such as amides and short chain alcohols to amino acids at the active site occur. The bonding in the donor

complex is highly polarised with the donor atom being δ^- and the hydrogen atom is δ^+ , as shown in Figure 1.8.

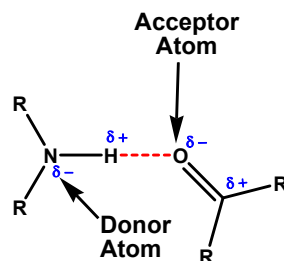


Figure 1.8. The Donor-Acceptor Interactions found in Hydrogen Bonding.

Hydrogen bonding can be spread over multiple atoms and have a number of different angles in relation to the position of the hydrogen to the acceptor atom. The more linear the hydrogen bond the stronger the bond: angles of $175-180^\circ$ have strengths of between $60-120 \text{ kJmol}^{-1}$, angles of $130-180^\circ$ tend to have strengths of $16-60 \text{ kJmol}^{-1}$ and the weakest interactions of $<12 \text{ kJmol}^{-1}$ tend to occur when the angle of H-bonding is between $90-150^\circ$. Bond distances can vary between $1.2-3.2 \text{ \AA}$ for H-A and $2.2-4.0 \text{ \AA}$ for D-H, where the closer the atoms, the stronger the interaction. Hydrogen bonding angles are shown in Figure 1.9. [5] [6]

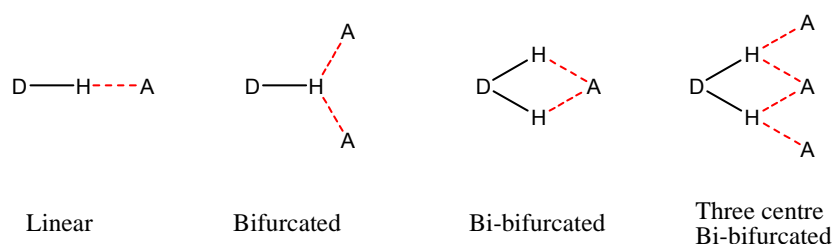


Figure 1.9. The Different Possible Angles for H-bonding.

1.2.7 π - π Stacking Interactions.

π - π stacking interactions are the weak electrostatic interaction between aromatic rings. The strength of these interactions ranges from 0-50 kJmol^{-1} . There are two types of π stacking interactions, they are face-to-face and edge-to-face. Face-to-face π -stacking is the interaction between the electron clouds of the aromatic rings where the clouds are parallel to each other. Face-to-face π stacking is found between the nucleobases in DNA. Edge-to-face π stacking is where there is an interaction between an electron deficient hydrogen of one aromatic ring to the electron rich π cloud of another aromatic ring. Crystallisation of edge to face aromatic rings yields a herringbone distribution pattern. Edge-to-face and face-to-face alignment structures are shown below in Figure 1.10.^{[5] [6]}

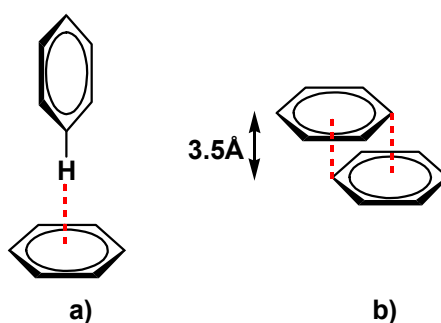


Figure 1.10. π - π Stacking Interactions. a) Edge to Face π Stacking.
b) Face to Face π Stacking.

1.2.8 Self Assembly and Other Factors for Complexation.

1.2.8.1 Self Assembly.

When two or more components aggregate spontaneously and reversibly together to give a non-covalently bound complex, using intermolecular forces to hold the complex together. Coordination of substrates can give appropriate alignment for covalent interactions to occur between individual substrates to form a macrocycle *in situ* of complexation.^{[5] [6]} An example of a self-assembled structure is the double helix found in DNA. The two strands are held together by a combination of hydrophobic interactions, hydrogen bonding and π -stacking between the nitrogen base pairs attached to the phosphate backbone. An illustration of the conformation shape of DNA is shown in Figure 1.11.^[8]

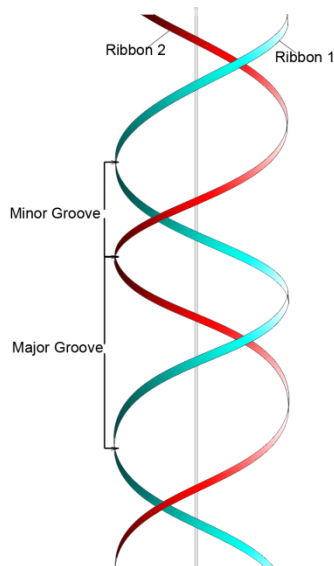


Figure 1.11. Illustration of DNA. ^[8]

1.2.8.2 The Chelate Effect.

The chelate effect is where the stability of a complex increases with the number of binding sites on a guest in comparison to the equivalent monodentate ligand bound to the same substrate. For example the chelation of ethylenediamine to Ni^{2+} is 10^8 times stronger than the chelation of ammonia to Ni^{2+} , due to the enhanced stability of the complex. As shown in Figure 1.12.^{[5] [6]}

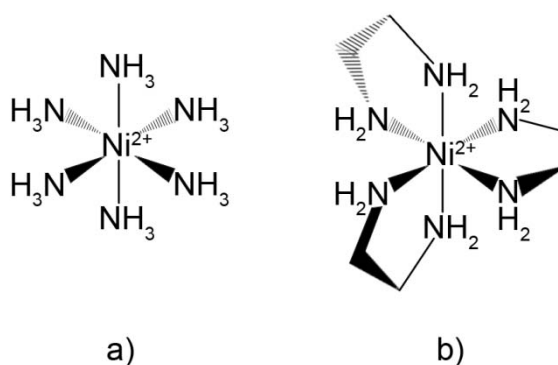


Figure 1.12. Binding of Ni^{2+} complexes. a) $[\text{Ni}(\text{NH}_3)_6]^{2+}$. b) $[\text{Ni}(\text{en})_3]^{2+}$.
*en = ethylenediamine

1.2.8.3 Pre-organisation.

Pre-organisation is where the host is in a conformation that requires very little or no rearrangement to bind the substrate. Pre-organised structures exhibit slower binding kinetics compared to less pre-organised structures, however, binding tends to be stronger in pre-organised complexes, such that the spherand binds up to 10^{10} times more strongly than the equivalent crown ether. This is exemplified in Figure 1.13.^{[5] [6]}

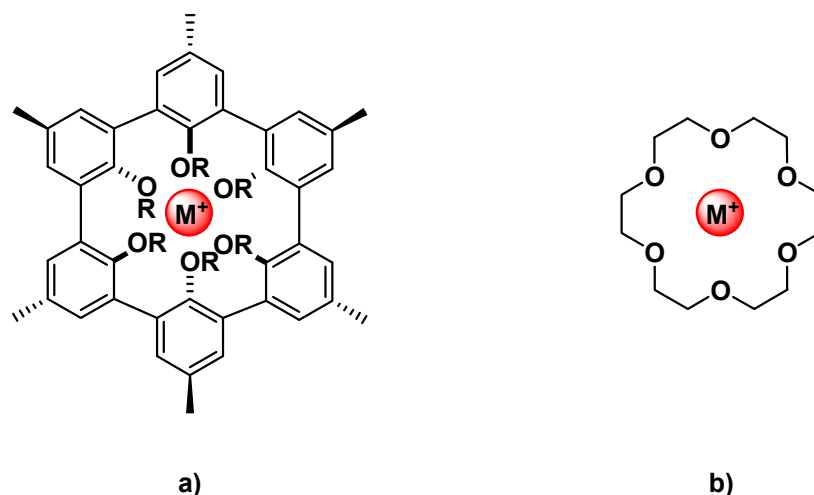


Figure 1.13. The Binding of a Metal Cation to a) a spherand b) a crown ether.

1.3 Molecular Architectures.

Rotaxanes and catenanes are interconnected structures, where the components are joined together by mechanical bonds, and cannot be separated without breaking covalent bonds. Rotaxanes are constructed from an axle with one or more rings threaded onto it. The ends of the axle have large bulky stopper groups which stop the ring from unthreading. The axle typically has two or more intermolecular binding sites at which interaction with the macrocycle can occur. Catenanes, consist of two or more interlocked macrocyclic rings. Catenanes also typically have two or more binding sites for interactions to occur. Figure 1.14 shows the basic form of these structures. Naming of these structures comes from the number of interlocked components, thus, the rotaxane and catenane of Figure 1.14 are [2]-rotaxane and [2]-catenane structures. It is possible to have more than two components in these structures and the names change accordingly. Pseudorotaxanes are similar to rotaxanes, where a macrocycle is threaded onto an axle. However, with pseudorotaxanes there are no stopper groups on the axle and the macrocycle can freely associate and dissociate from the thread.

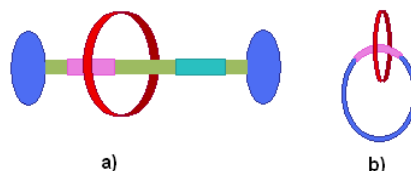


Figure 1.14. Illustration of a) A [2]-Rotaxane b) A [2]-Catenane.

These architectures have gained interest in recent years due to their potential uses as molecular machines and devices. Movement within these molecules can occur freely without cleavage of covalent bonds. The motions found within a rotaxane can occur in two ways, where the macrocycle moves in relation to the axle either by lateral shuttling from one site on the axle to another, or rotation around one site with no lateral movement observed.^[7] Movement within a catenane can be described by the motion of one ring relative to the other and can also be designated by lateral shuttling around the ring or pirouetting around a particular point on the ring. These motions are shown diagrammatically in Figure 1.15.

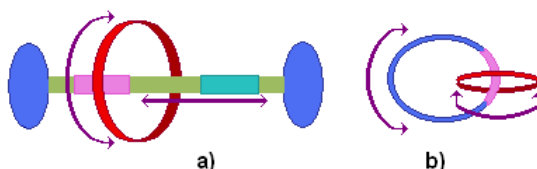


Figure 1.15. Motions found in a) [2]-Rotaxanes b) [2]-Catenanes.

The structure of these architectures can be modified in such a way that a variety of properties can be incorporated, such as fluorescence, electrochemical potential, and optical activity. The strength of non-covalent interactions found within each construct can be tuned, and so the degree of movement can be controlled. Rotaxanes can be synthesised by a number of methods. One method is via the formation of a pseudorotaxane intermediate that is then stoppered at each end prior to the macrocycle dethreading. This method generally does not have a great yield as dethreading of the macrocycle can occur rapidly at equilibrium,

and the macrocycle is not always trapped on the axle at time of stoppering. Figure 1.16 shows a schematic of this principle.

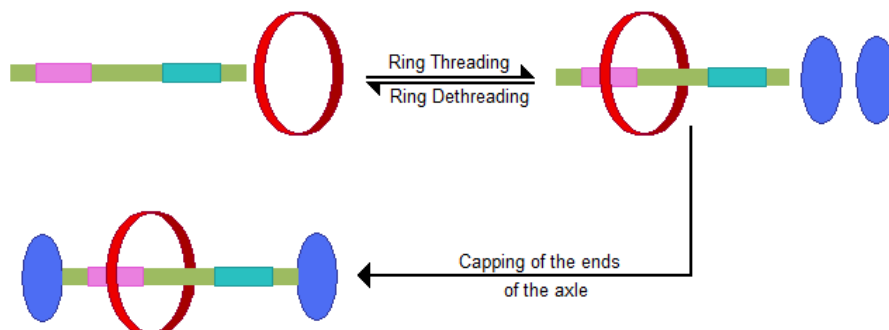


Figure 1.16. Formation of Pseudorotaxane then Capping of the ends.

The second method, clipping, utilises the intermolecular interactions formed between the macrocycle and the axle. Two halves of a ring orientate themselves around the preformed axle at a binding site where they then join together to form the complete macrocycle. The ring cannot then dethread due to the bulky stoppers on the ends of the axle. This method is shown schematically in Figure 1.17.

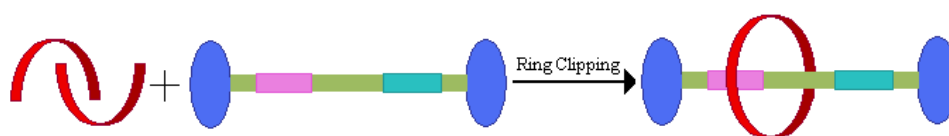


Figure 1.17. Formation by Clipping.

Rotaxanes can also be formed by ring slippage reactions. The bulky stopper groups are first attached to the axle, and then the intact ring is slipped onto the axle in a high temperature reaction. The stability of the components at the high temperatures required makes this method of rotaxane formation not always appropriate. Figure 1.18 illustrates this process.

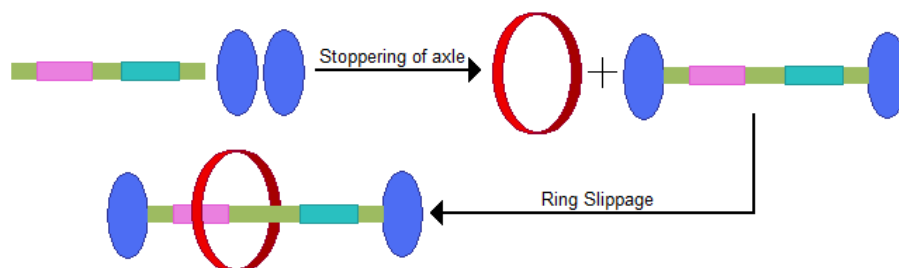


Figure 1.18. Formation by Ring Slippage.

Catenanes can be made in a similar way to rotaxanes. They can be formed by the clipping of two halves of one ring around a point on a second preformed macrocycle, where intermolecular interactions hold both halves of the ring in the correct orientation for joining together. Clipping together of both rings can also occur where all four halves of the rings are held together in the correct orientation for formation of the required catenane. This synthesis can be metal mediated or by simply using intermolecular interactions. Figure 1.19 shows the potential clipping methods.



Figure 1.19. Clipping to form Catenanes a) One ring Preformed b) Clipping of both rings.

Ring slippage in catenanes is rare, but can occur with metal-ligand complexes, where an intermediate in which the ligand metal centres change. The ligands loop back to their original metal centre, interlocking the two rings and the catenane is formed. This method is referred to as Mobius strip ring slippage and is illustrated in Figure 1.20.

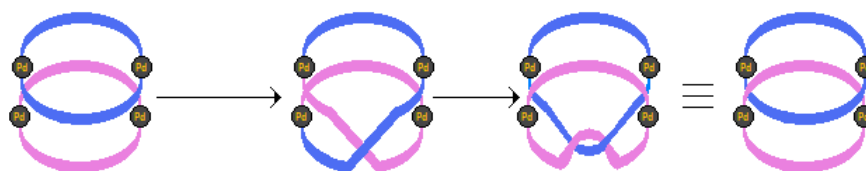


Figure 1.20. 'Mobius Strip' Ring Slippage in Catenanes.

1.4 Key Functional Supramolecular Groups used in this study.

1.4.1 Cyclobis(paraquat-*p*-phenylene) (CBPQT⁴⁺).

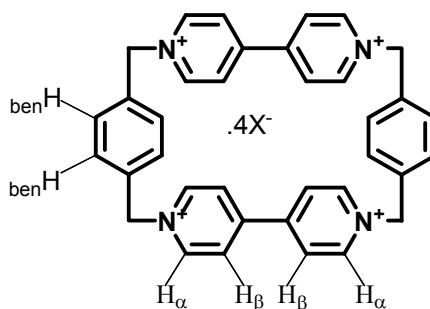


Figure 1.21. Structure of CBPQT⁴⁺ with the α , β , and benzyl hydrogens labelled.

The electron deficient cyclophane CBPQT⁴⁺, shown above in Figure 1.21, has been shown to interact with a number of π -electron rich substrates such that inclusion complexes are formed within the cavity of the CBPQT⁴⁺. The inclusion complexes are stabilised by a number of molecular recognition interactions including charge transfer, π - π stacking and hydrogen bonding interactions.^[9] As a direct result of the charge transfer interactions these complexes are highly coloured, where complexes with hydroquinone are red, dioxynaphthalene are purple and tetrathiafulvalene (TTF) are green. The inclusion complexes are fully reversible and the switching from complexed to uncomplexed can be induced by the addition of a stimulus. The stimulus used can vary from thermal to chemical or electrochemical.

Examples include the formation of a pseudorotaxane with a hydroquinone functionalised axle.^[10] It has been observed that this complex has a strong red colour from the interaction between the CBPQT⁴⁺ the hydroquinone group. X-ray crystal structures showed that the hydroquinone group was found in the center of the cavity and interacted with the CBPQT⁴⁺ through 'T-type' edge-face π -stacking interactions in addition to the charge transfer interactions. It was also found that for the rotaxane used, the thread folded back upon itself where the aromatic groups in the chain performed additional π -stacking interactions with CBPQT⁴⁺ resulting a highly stable complex.^[10] The structure of the [2]-rotaxane is shown in Figure 1.22. The X-ray crystal structure produced is shown in Figure 1.23.^[10]

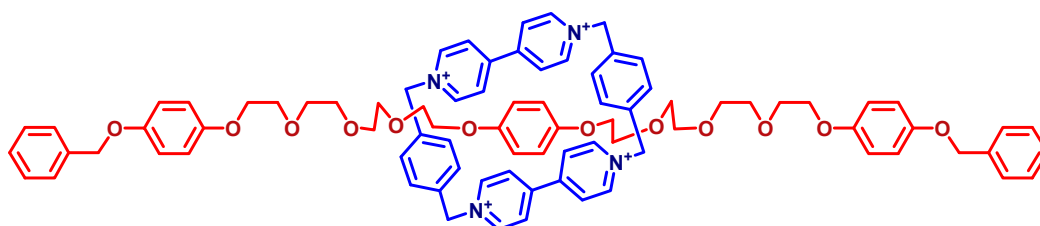


Figure 1.22. Structure of [2]-Rotaxane. The CBPQT⁴⁺ ring in blue, the axle in red.

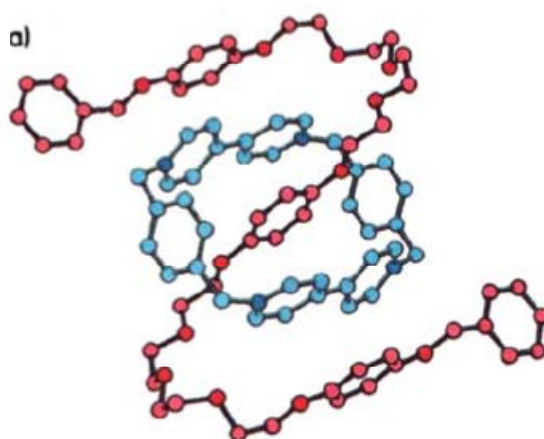


Figure 1.23. X-ray crystal structure of the [2]-Rotaxane 1. The axle in red folds around the CBPQT⁴⁺ bead shown in blue.^[10]

Similarly, the inclusion complex formed between CBPQT⁴⁺ and 1,5-dioxynaphthalene systems have been thoroughly investigated.^{[9, 11] [12]} It has been found by X-ray crystallography, that the naphthalene is threaded centrosymmetrically through the cavity of CBPQT⁴⁺ and is positioned with interplanar separations of ~3.5Å between the π- donor and π-acceptors. An example of this sort complex is shown in Figure 1.24, where the pseudorotaxane comprises of a 1,5-naphthalenediyl axle threaded through the cavity of CBPQT⁴⁺.

The naphthalene group undergoes π-π interactions with the electron deficient bipyridyl groups of the CBPQT⁴⁺. It can be observed that the thread has an *anti* geometry associated with the conformation of the ethyleneglycol chains. Hydrogen bonding interactions between the ethylene glycol oxygens and the H_α on the bipyridyl rings aid the stabilisation of the complex. The PF₆⁻ counter ions can also form hydrogen bonding with the H_{2/6} protons on the naphthalene moiety, the bipyridinium H_β protons, and the ethylene glycol chains. However this does not always occur in the X-Ray structure and is dependent upon the additional functionality present.^[11]

The changes in the ¹H NMR spectrum upon complexation, are particularly defined due to the prominent shifts of the naphthalene aromatic protons. In particular, the H_{4/8} protons that perform C-H—π interactions with the CBPQT⁴⁺ can be found in the region of δ 2.1-2.9ppm, in the complexed form, while in the un-complexed form are found within the range of 6.8-7.9ppm.^{[12] [13] [14]} The complex can be reversed by the addition of a competitor compound such as TTF,^[12] by application of heat,^[15] and by reduction of CBPQT⁴⁺ to its radical form, CBPQT^{•2+}.

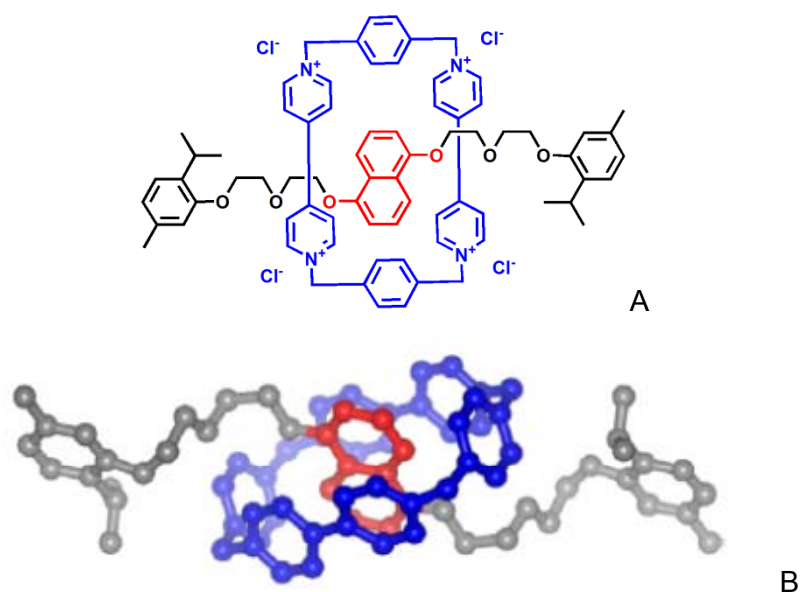
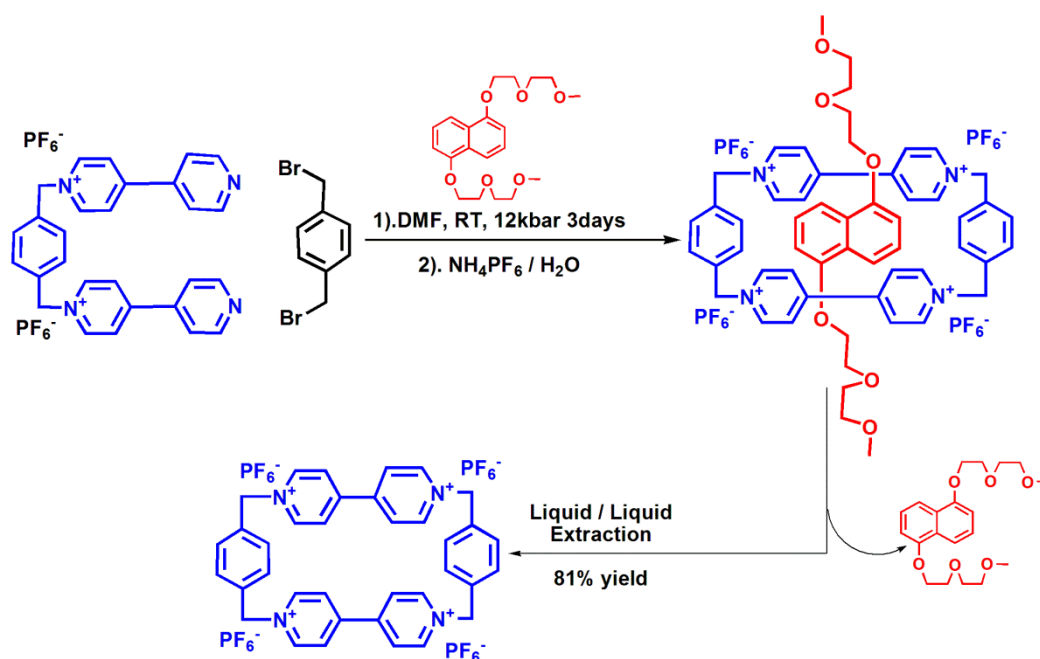


Figure 1.24. A) Basic structure of the pseudorotaxane and B) The X-ray crystal structure. Hydrogen atoms, solvent molecules, and counterions are omitted for the sake of clarity. The DNP unit is colored red, the CBPQT⁴⁺ ring blue, and the remainder gray.^[11]

It has also been found that the reversible interactions between CBPQT⁴⁺ and 1,5-dialkoxynaphthalene are optimal for use in the templated synthesis of CBPQT⁴⁺ from 1,1'-[1,4-phenylenebis(methylene)] bis(4,4'-bipyridinium) bis(hexafluorophosphate) and 1,4-bis(bromomethyl) benzene where the yields have been published as, up to 81%.^[9] The stability of the complex is higher than that of the complex between CBPQT⁴⁺ and hydroquinone.^[9] The complex is fully reversible and the naphthalene template is easily removed by liquid/liquid extraction. The reaction scheme for this process is shown in Scheme 1.1 .^[9]



Scheme 1.1. Naphthalene templated synthesis of CBPQT⁴⁺.

The interactions between TTF and CBPQT⁴⁺ have been found to be strong whereby TTF can competitively enter the cavity of CBPQT⁴⁺, displacing groups such as 1,5-dioxynaphthalene to give a strong dark green colour from the charge transfer interactions in water. From the X-ray crystal structure it has been observed that the TTF inserts at an angle that has the long axis of the centrally located TTF at an angle of 66° to the N⁺---N⁺ vector.^[16] This orientation maximises the π -stacking interactions between the two components and as a result it forms a tightly bound complex.^[9] The X-ray crystal structure is shown in Figure 1.25.^[16] It has been shown that TTF can be removed from the cavity of CBPQT⁴⁺ by the oxidation to TTF^{•+} and/ or TTF²⁺. The complex reformed by the reduction back to the neutral TTF. The oxidation reduction process can be carried by both chemical and electrochemical means.^{[15] [17]}



Figure 1.25. X-ray structure of TTF in the cavity of CBPQT⁴⁺. The TTF unit is coloured green, the CBPQT⁴⁺ blue. Hydrogen atoms, solvent molecules, and counterions are omitted for the sake of clarity. ^[16]

CBPQT⁴⁺ can itself undergo redox processes where there are two sets of redox waves formed in the cyclic voltammogram that are fully reversible. Each redox wave represents a 2x 1e⁻ reduction of the paraquat moieties. The first reduction wave at E₁ = -283 mV converts the cyclophane into the diradical species. The second reduction at E₂ = -709mV forms the neutral compound. The cyclic voltammogram is shown in Figure 1.26. ^[18]

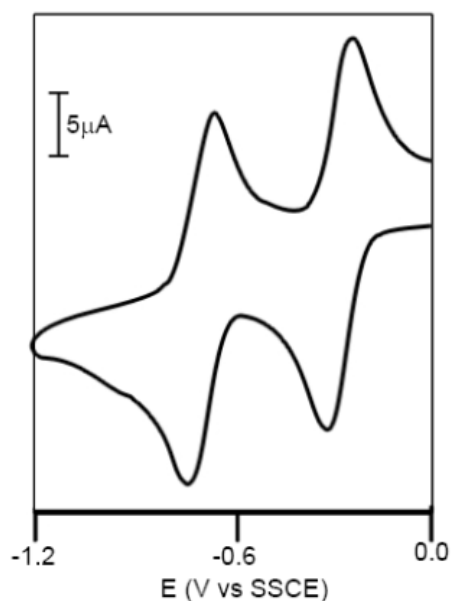


Figure 1.26. CV of CBPQT⁴⁺4PF₆⁻. 0.5mM solution in 0.1M TABPF₆/MeCN at 25°C. Scan rate 50mV/s. ^[18]

The reduced species of CBPQT produces an EPR spectrum that has a broad signal that indicates a fast electron exchange between paraquat subunits. The spectrum produced at room temperature is shown in Figure 1.27. [18]

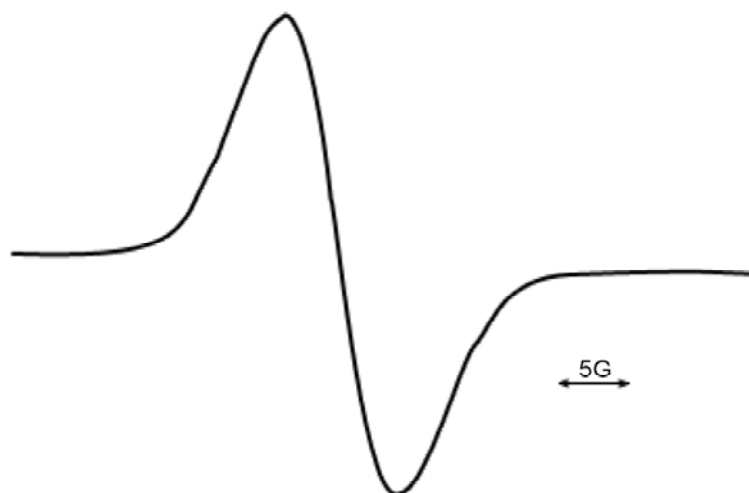


Figure 1.27. EPR spectrum for the CBPQT radical. [18]

1.4.2 Tetrathiafulvalene as redox active guests for CBPQT⁴⁺.

Tetrathiafulvalene (TTF) is a redox active compound that can act as an electron donating or electron accepting substrate depending upon its oxidation state. TTF has been found to have three stable forms; TTF(0), TTF^{•+}, and TTF²⁺. The TTF(0) has electron donating character, while the fully oxidised TTF²⁺ state has electron acceptor character. [19] The structure of each oxidation state is shown in Figure 1.28.

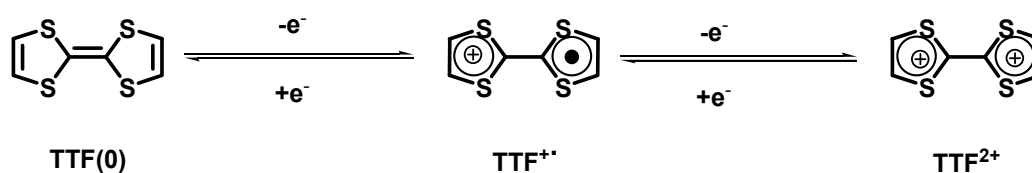


Figure 1.28. The three forms of TTF. TTF(0), TTF^{•+}, and TTF²⁺.

TTF(0) can form inclusion complexes with the electron accepting cyclophane CBPQT⁴⁺, where a strong absorbance band is observed in the UV-Vis absorbance spectrum with $\lambda_{\text{max}} = 855 \text{ nm}$.^{[19] [15] [17]} Upon oxidation to the radical cation, the complex dissociates, but will re-associate upon reduction back to the neutral species. The TTF²⁺ form is fully aromatic and fluorescent with an emission band at 488 nm. In this oxidation state the TTF can form inclusion complexes with an electron donating crown ether 1,5-dinaphtho-[38]-crown-10. Upon complexation, there is a quenching of the fluorescence and a charge transfer band is observed in the UV-Vis absorbance spectrum at $\lambda_{\text{max}} = 840 \text{ nm}$.

Cyclic voltammetry has shown that TTF(0) undergoes two reversible one electron oxidation processes to form the TTF²⁺ species. The complex with CBPQT⁴⁺ displaces the first oxidation process by up to +70mV.^[19] This process is the transformation from TTF(0) to TTF^{•+}. The subsequent oxidation process from TTF^{•+} to TTF²⁺ is unaffected by the presence of the cyclophane.^[19] Additionally the presence of 1,5-dinaphtho-[38]-crown-10 affects the first reduction, where the position is shifted by -14 mV.^[19] This process is associated with the reduction from TTF²⁺ to TTF^{•+}. By mixing the three components in the CV experiment the TTF-CBPQT⁴⁺ is initially formed, and the oxidation process is shifted by +70 mV. Upon oxidation to the TTF^{•+}, the complex dissociates and all components are separate. Further oxidation to the TTF²⁺ leads to the formation of the complex between 1,5-dinaphtho-[38]-crown-10 and TTF²⁺. The reverse process exhibits a shift by -14 mV for the transformation from TTF²⁺ to TTF^{•+}.^[19] Again, the components are non-complexed until further reduction to the neutral species formed at which point the CBPQT⁴⁺ re-complexes with the TTF. From this it can be observed that the radical cation form does not interact with either the CBPQT⁴⁺ or the crown ether. The CV for the free TTF and the mix of CBPQT⁴⁺, 1,5-dinaphtho-[38]-crown-10, and the TTF is shown in Figure 1.29. The complexation-decomplexation switching process by the oxidation / reduction of TTF with the two host molecules is shown in Scheme 1.2.

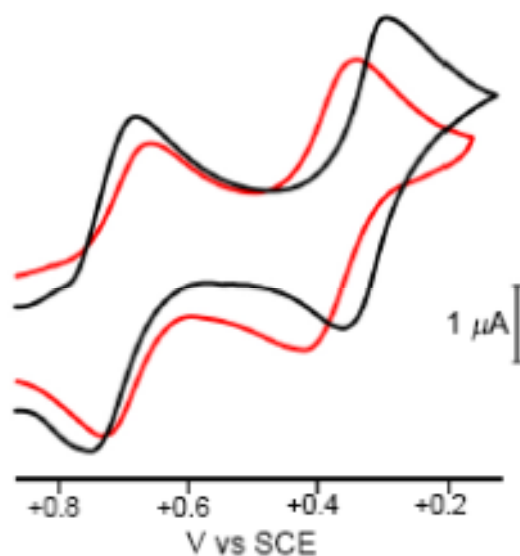
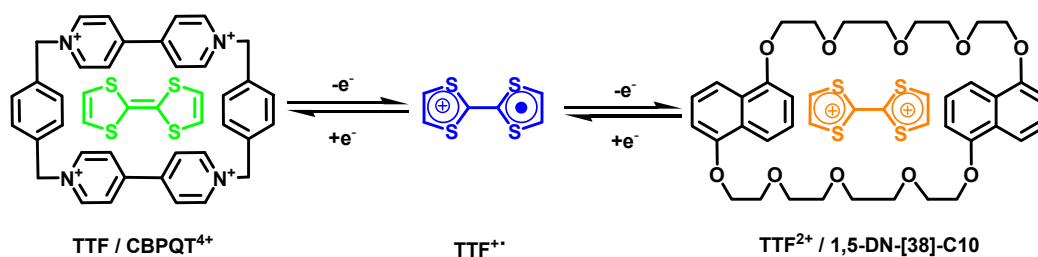


Figure 1.29. Cyclic voltammogram for TTF (black) in the presence of CBPQT⁴⁺ and 1,5-DN-[38]-C10 (red).^[19]



Scheme 1.2. Complexation switching by redox oxidation reduction processes for TTF.^[19]

1.4.3 Cyclodextrins.

Cyclodextrins are water soluble, hollow, truncated cone shaped structures that contain 6-8 glucose units linked by α -1,4-glucoside bonds. These structures have hollow hydrophobic cavities that can vary in size from 0.45 to 0.95 nm.^{[20] [21] [22]} The structure of these molecules is shown in Figure 1.30. Inclusion complexes are formed readily with these compounds and many other low molecular weight guest molecules that can vary in their physicochemical properties, where the molecules can contain polar groups such as amines or acids or can be completely non-

polar. Metallocenes can form inclusion complexes with cyclodextrins in their reduced state. Upon oxidation of the metallocene, complete decomplexation occurs.^[23]

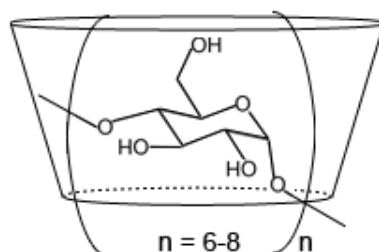
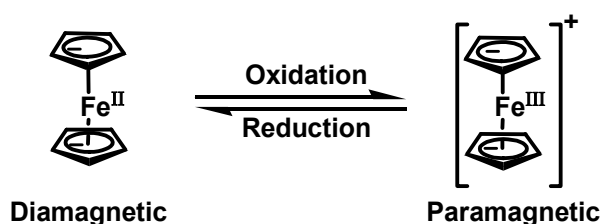


Figure 1.30. Structure of a cyclodextrin. n = number of glucose units that make up the structure.

The interactions of cyclodextrins can be tuned by the modification of the pendant hydroxyl groups. By methylating, the solubility in organic solvents can be improved and the binding of metallocenes has been observed to be enhanced by this modification. Cyclodextrin has a great many applications from use within sensing devices,^{[11] [24]} to use as insulation for 'molecular wires'.^[25] The sensing applications utilise the competitive binding of substrates within the cavity of the cyclodextrin. The attachment of fluorophores, such that partial incorporation into the cavity leads to a quenching in fluorescence, can be used in sensing devices. As substrates that can competitively form inclusion complexes with the cyclodextrin displace the fluorophore, quenching ceases and the fluorescence is activated. An example of this is the formation of dimer complexes with a series of bile acid steroids.^[24] The formation of pseudorotaxanes and rotaxanes with semiconducting polymer chains with either α - or β -cyclodextrin have been shown to reduce self-quenching of photoluminescence within the polymer chains and there is a retention of the semi-conducting and optical properties.^[25]

1.4.4 Ferrocene as a redox active guest.



Scheme 1.3. Conversion of Ferrocene to Ferrocenium.

Ferrocene is comprised of iron in an oxidation state of 2+ sandwiched between two ($\eta\text{-C}_5\text{H}_5$) cyclopentadienyl rings (Cp) in a structure that is overall neutral in charge and diamagnetic. It can undergo reversible oxidation to the ferrocenium species which has an overall positive charge and is paramagnetic, as shown in Scheme 1.3. The redox activity of ferrocene can be modulated by the functional groups pendant to the Cp rings. The potential shift is dependent upon the ability of the substituent attached to either donate or accept electrons.^[26] The electrophilicity of the substituent is measured by the Hammett constant σ_p . σ_p is calculated by the following equation, where ρ stands for the reaction constant, K and K_o are the rate constants for the substituted and unsubstituted compounds.

$$\log \frac{K}{K_o} = \rho \sigma_p \qquad \text{Equation 1.1. The Hammett Equation}^{[27]}$$

Functionalised ferrocenes have found a wide scope of applications within catalysis, materials and coordination chemistry. The electronic properties of ferrocene are key for the range of applications available for its use.^[28] The incorporation of these structures into signalling / reporter molecules is of use as the spectroscopic and redox activity of ferrocene is altered with the binding of guest molecules. By undergoing redox

processes prior to guest binding, the affinity for the guest to the receptor can be altered. The two processes of redox activity and host-guest interactions are interrelated and each affects the other. The relationship between electron transfer and guest binding can be expressed by Equation 1.2.^[28-29] The equation is derived from the Nernst equation the Gibbs free energy equation. The derivation is given in Equation 1.3. From the equation it can be seen that ΔE° ($E^\circ - E^\circ_+$) is proportional to the affinity of the receptor to guest molecules ($\ln(K_+/K)$). An example where this effect is observed is with the complexation of Sodium with N-ferrocenylmethylaza-18-crown-6,^[28] where a shift in the oxidation potential is induced upon the complexation of sodium ions into the cavity of the crown ether. The transformation is shown in Figure 1.31.

$$nF(E^\circ - E^\circ_+) = RT\ln(K_+/K)$$

Equation 1.2.
Derived equation from Gibbs Free Energy
and the Nernst Equation.^{[28] [29]}

$$\Delta G^\circ = -nFE^\circ = -RT\ln K$$

For closed systems there is no change in ΔG

$$\sum \Delta G = 0 = nF(E - E^\circ_+) - RT\ln(K_+) + nF(E^\circ - E) + RT\ln(K)$$

$$nF(E^\circ - E^\circ_+) = RT\ln(K_+/K)$$

Equation 1.3. Derivation of Gibbs Free Energy and the Nernst Equation to yield
Equation 12.^[29]

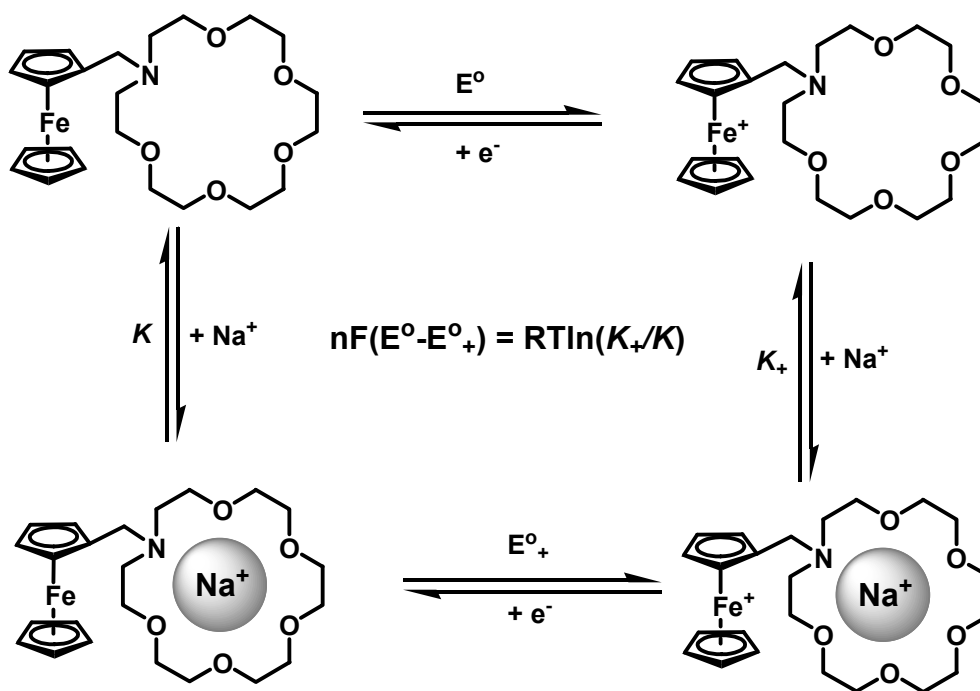


Figure 1.31. The complexation of Sodium with N-ferrocenylmethylaza-18-crown-6.

Ferrocene and its derivatives can form inclusion complexes with cyclodextrins and cucurbiturils. The optimal interaction between ferrocene and cyclodextrin is formed with β -cyclodextrin, where a 1:1 complex is formed. Studies have shown that ferrocene and α -cyclodextrin form inclusion complexes where the ratio of cyclodextrin to ferrocene is 2:1. γ -cyclodextrin, the largest of these compounds can accommodate up to two ferrocene groups within its cavity and has a ratio of ferrocene : cyclodextrin greater than 1:1^[20]. The structures of the inclusion complexes formed are illustrated in Figure 1.32.

The complexes have been shown to be stable, such that there are examples where the complexes have been crystallised from water and are thermally stable up to the melting point of cyclodextrin $\sim 200^{\circ}\text{C}$.^[30] The binding constant K_a has been reported to be in the range of 10^3 - 10^4 M^{-1} .^[31] The driving force for the inclusion complex is through hydrophobic interactions, and the interaction and formation of the complex occurs irrespective of the charge on the ferrocene derivative and is unaffected by the presence of buffer or salt in the solution.

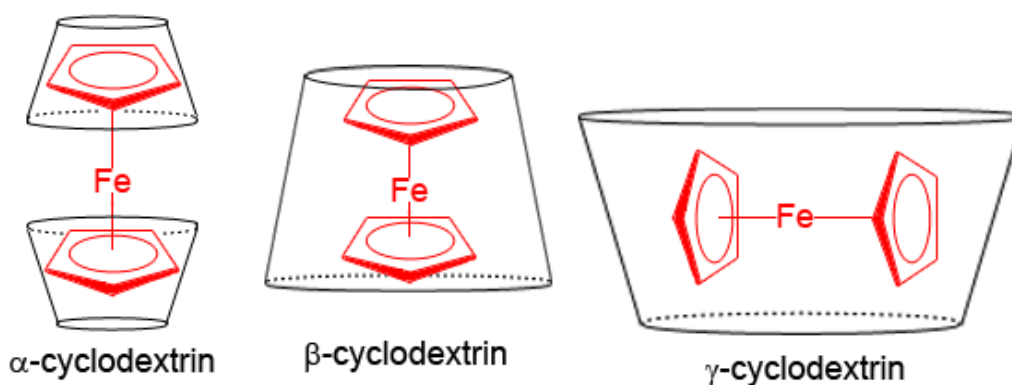


Figure 1.32. Illustration of the inclusion complexes of ferrocene and α , β and γ -Cyclodextrins.

It has been found that for ferrocene-cyclodextrin complexes to undergo redox processes, partial or full decomplexation from the cavity must occur prior to the oxidation process to form the ferrocenium species.^[20] The complexation/ decomplexation processes required for the oxidation of ferrocene with each cyclodextrin is shown in Figure 1.33.^[20] With α -cyclodextrin, only partial decomplexation from the $\text{Fc}(\alpha\text{-CD})_2$ is required for oxidation to occur. However it has been shown that full decomplexation may occur prior to oxidation. For both β , and γ -cyclodextrin, full decomplexation is required before oxidation of the iron can occur.

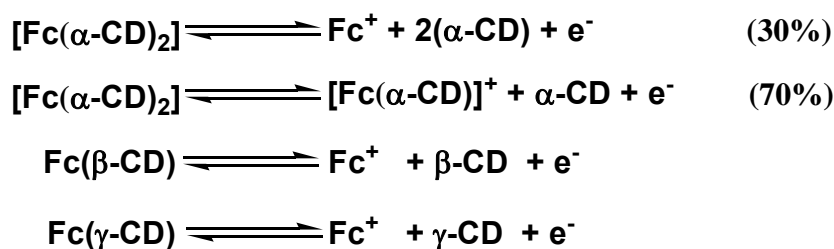
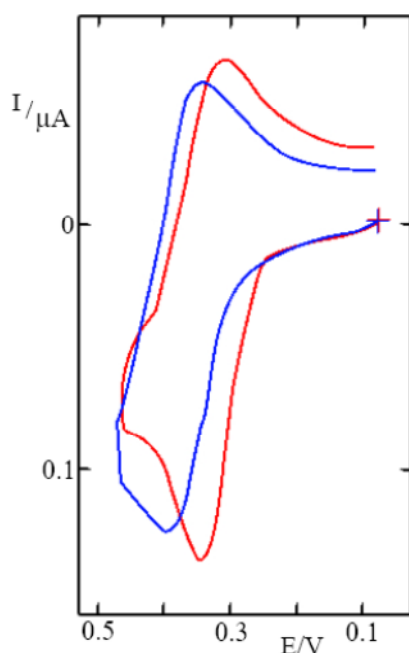


Figure 1.33. Complexation/Decomplexation process required for the oxidation of ferrocene cyclodextrin inclusion complexes.

The cyclic voltammogram of ferrocene changes upon complexation with cyclodextrin such that the half wave potential $E_{1/2}$ becomes more positive and the intensity of the signal diminishes slightly.

This change is illustrated in Figure 1.34.^[20] Cyclic voltammetry will be discussed in greater detail in § 1.8.2.



Cyclic voltammogram 0.1 mM ferrocene + 0.1 M LiClO₄ in H₂O in the absence (—) and presence (—) of 1.3 mM β-cyclodextrin. Scan rate : 50 mV/s

Figure 1.34. Cyclic voltammogram of ferrocene with the complex of ferrocene with β-cyclodextrin overlaid.^[20]

¹H NMR spectroscopy can be used to show that the inclusion complex has formed. Typically, addition of a large excess of β-cyclodextrin to a ferrocene derivative causes a broadening of shifts as the complex forms. This broadening is due to shielding and de-shielding effects on the ferrocene compound. These changes are exemplified by the shifts observed for the ferrocene derivative as shown in Figure 1.35.^[32]

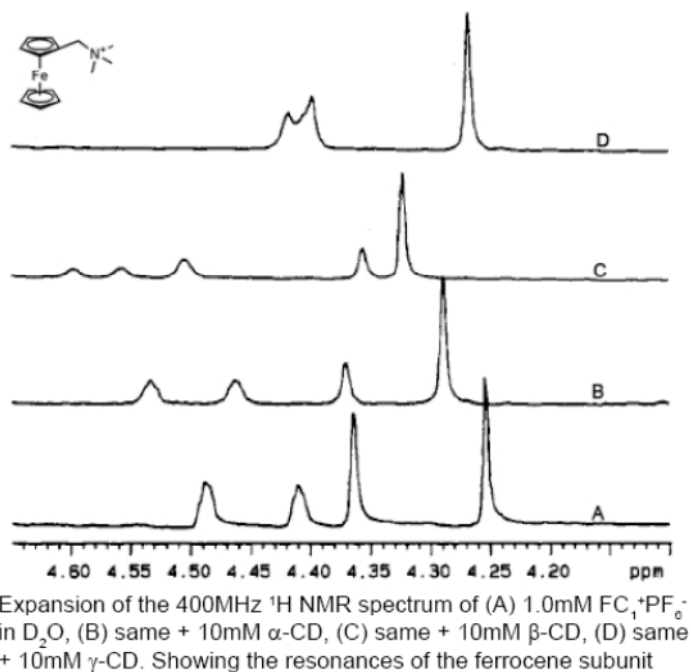


Figure 1.35. ^1H NMR shifts observed for the ferrocene derivative with cyclodextrins.^[32]

Where cyclodextrins are structurally like truncated cones, cucurbiturils are barrel shaped compounds that are made of 6-8 glycoluril units. The cavities are fully symmetrical and as a result molecules can enter the cavity from either end of the structure. The structure of these compounds are shown in Figure 1.36.

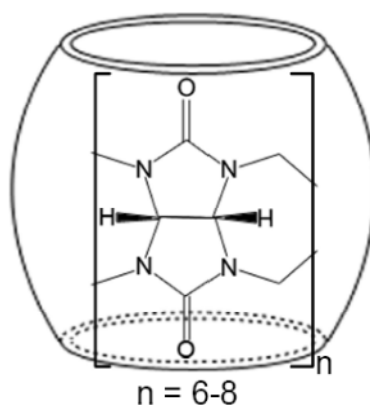


Figure 1.36. Structure of a cucurbituril. n = number of glycoluril units that make up the structure.

These molecules are similar to cyclodextrins in relation to their cavity diameters, where the cucurbit-[7]-uril (CB7) is equivalent to β -cyclodextrin. The inclusion complex formed between ferrocene and, in particular, CB7 has a higher binding constant in the range of 10^9 - 10^{13} than that of the complex between ferrocene and β -cyclodextrin.^[31] There are also examples where the binding constant reaches levels comparable to avidin-biotin binding.^[33] The driving forces for the formation of inclusion complexes with ferrocene are hydrophobic and ion-dipole interactions. The binding is affected by the charge on the ferrocene where cationic derivatives exhibit stronger binding interactions, and anionic derivatives tend not to form complexes due to charge repulsion interactions.^[31] ^[34] The effect of buffer or salts in solution also diminishes the interactions with ferrocene and its derivatives where ion-dipole interactions will occur with the salts over the ferrocene derivative used. The effect of complexation on the ^1H NMR spectrum differs from the shifts exhibited by cyclodextrin with ferrocene, whereby the cyclopentadiene protons move upfield towards 3.5 ppm from 4.25 ppm. The spectra recorded for the ferrocene derivative with CB7 is shown Figure 1.37.^[31]

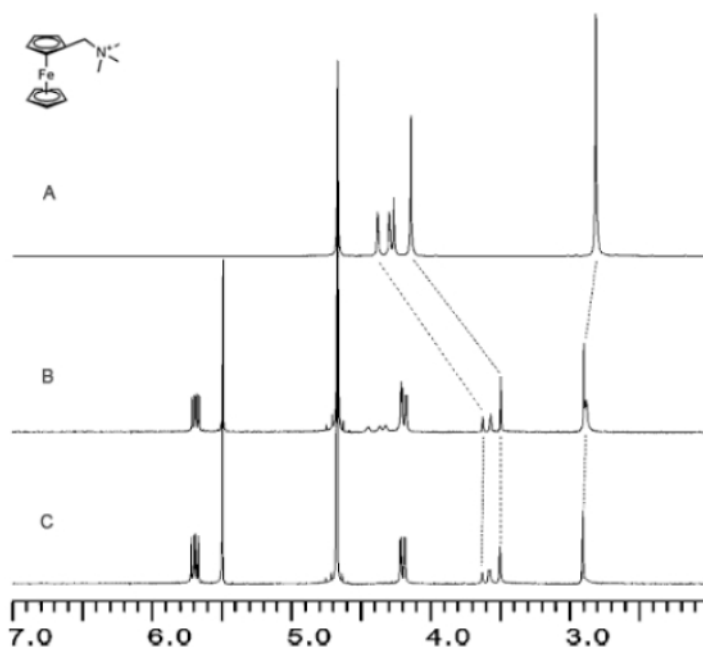


Figure 1.37. ^1H NMR spectra of ferrocene derivative (A) in the absence, and in the presence of (B) 0.5 equiv and (C) 1.1 equiv of CB7. ^[31]

Investigation of the effects of the inclusion complex between CB7 and ferrocene on the redox activity of ferrocene derivatives has shown that the complex behaves in a similar way to cyclodextrin complexes, where there is a positive shift in the half potential and the current flow is reduced. However, the degree of change exhibited upon the $E_{1/2}$ varies with the substitution on the ferrocene derivative. As with cyclodextrin, the ferrocene form of the redox couple is stabilised by the inclusion complex over the ferrocenium species.

1.5 Molecular Machines.

Molecular devices are molecular assemblies that can carry out a function of some sort using non-covalent interactions in host-guest complexes. Molecular machines are molecular assemblies that with the addition of a stimulus cause a net nuclear displacement of one molecule relative to another in the complex. This displacement can, in turn, affect the external environment in a way that can be utilised. An example of this is the ON/OFF of fluorescence by a molecular switch in the presence of a quenching agent. Molecular machines can be made from singular- or multi-component structures interacting using intermolecular interactions. Singular component structures can contain multiple moieties that can interact with each other joined together covalently, whereas multi-component structures have at least two distinct complexes joined either by a physical barrier to avoid separation, or simply by intermolecular interactions allowing the separate components to move freely relative to one another.

1.6 Sensors and Biosensors.

Sensors are devices that can detect changes in the environment from the presence of a material or chemical, to changes in temperature. Upon recognition of this stimulus, the sensor undergoes feedback where the change is translated into a readable output.

Stoddart and co-workers have created a chromophoric receptor for TTF.^[12] By taking advantage of the molecular recognition properties found in the complex between the electron rich aromatic group of 1,5-dioxynaphthalene groups with the electron deficient aryl rings in the cyclophane, CBPQT⁴⁺. The tetracationic macrobicyclic structure shown in Figure 1.38 was proven to change its conformation upon addition of TTF.^[12] The tethered bicyclic compound in its native conformation has the naphthalene moiety sandwiched between the two bipyridyl groups. The conformation is stabilised by π - π stacking, hydrogen bonding between polyether linkage and the α - and β -bipyridinium hydrogen atoms. CH— π interactions between the C_{4/8} hydrogen atoms on the naphthalene with the *p*-xylyl aromatic ring also aids in the stabilisation of this complex.^[12]

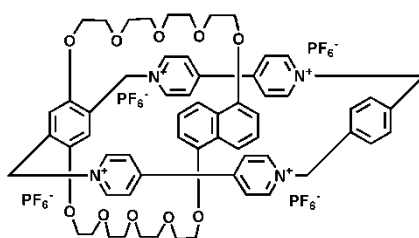


Figure 1.38. Structure of tetracationic macrobicyclic molecule in its native conformation.^[12]

The ¹H NMR spectrum for this complex shows the protons on the naphthalene at the H_{4/8} position resonate at 2.14 and 2.67 ppm, indicating the inclusion complex is formed. Heating above 36°C causes a rotation about the CH₂C₆H₂R₂CH₂ axis and the naphthalene group exits the cavity of the CBPQT⁴⁺.^[12] This decomplexation event can also be induced by the

addition of 1 eq of TTF. The complex undergoes a colour change from purple to green, where the absorption maximum changes from $\lambda = 537$ nm to $\lambda = 846$ nm upon this addition.^[12] It is also noted that the naphthalene protons are now all in the typical aromatic region with shifts at 6.57, 7.25, and 7.53 ppm. The loss of peaks at $\delta = 2.14$ and 2.67 ppm show that the naphthalene is no longer found within the cavity of the CBPQT⁴⁺, while the resonance for TTF is a singlet at $\delta = 5.68$ ppm, suggesting that it is now within the cavity of CBPQT⁴⁺.^[12] The change in conformation of the complex is shown in Figure 1.39.^[12]

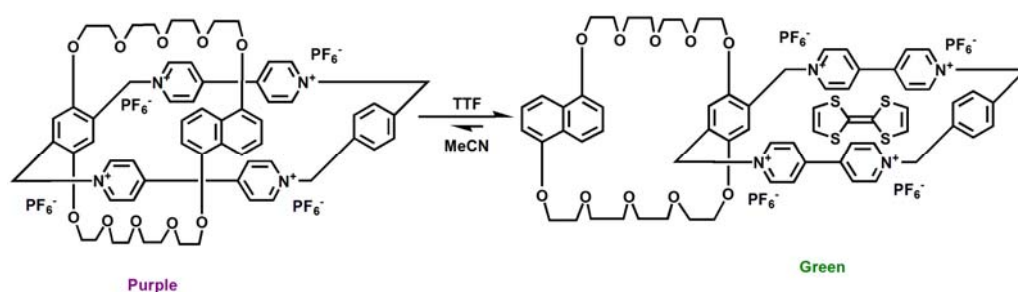


Figure 1.39. Chromophoric switching of the macrobicyclic molecule with the addition of TTF.^[12]

Biosensors are a specific type of sensing device that use living organisms^[35] or biological molecules to detect the presence of chemicals.^[36] Biosensors can be thought as containing two components; a bioreceptor and a transducer.^[36] The bioreceptor binds biomolecules and chemicals and the transducer translates the change resulting from binding into an output signal that is readable.

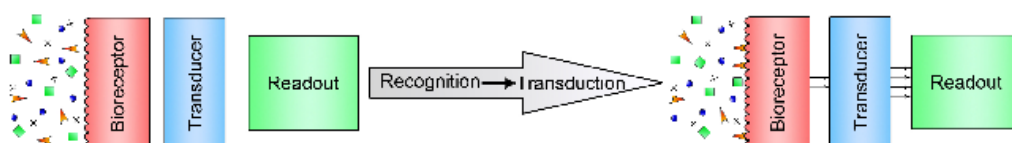


Figure 1.40. Schematic Illustration of a biosensor.

As will be shown throughout later chapters, sensors can take multiple forms and can utilise multiple functionalities for the sensing of particular stimuli. The interaction between the bioreceptor and the analyte can be measured using various analytical techniques^[37] such as UV-Vis spectroscopy for chromaphoric changes,^[38] and fluorescence spectroscopy to measure changes in the fluorescence emission spectrum.^[39] Electrical signals such as a change in electrical current can also be measured easily.^[35] Changes in the redox activity observed by cyclic voltammetry^[40] among other techniques such as square wave voltammetry may be adopted for measuring the changes upon complexation.

1.7 Cells and their adhesion properties.

Cell adhesion to surfaces or the extracellular matrix (ECM) is key to cell growth and development. Cells adhere to the ECM through the formation of integrin mediated adhesion complexes. These complexes can have a large variation in the subcellular distribution, size and form. However, there are two common features found in the adhesion complexes; firstly, cell adhesion is mediated through integrin proteins, and secondly, the integrin links to the actin cytoskeleton at the cell interior^[41]. Integrins are a family of heterodimer membrane spanning proteins that link the extracellular matrix to the inside of the cell. The different types of integrin are denoted by the α - and β - subunits that make up the heterodimer.^{[42] [43]} The integrin proteins connect to the ECM through binding interactions with proteins such as fibronectin or vitronectin. A simplified cartoon of cell adhesion through the formation of focal adhesions is shown in Figure 1.41.

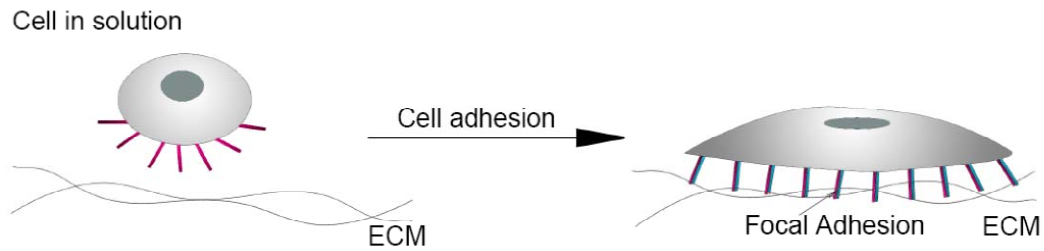


Figure 1.41. Cartoon of cell adhesion to the ECM via focal adhesions.

The ECM contains a large variety of proteins that interact with cells either by physical or chemical signalling. These interactions can control a great many processes with relation to cell development. In particular, the ECM can control gene expression, differentiation, protein expression and proliferation. The ECM can also direct cell adhesion, migration, orientation and cell guidance through these physical and chemical signalling processes. Within the cell, the cytoskeleton controls detection, transduction and regulation of the cellular interactions with the extracellular matrix, and so controls the fundamental functions of the cell.^[44] In cell culture, surfaces that can mimic the ECM either topographically or by the underlying chemical properties are highly sought after. By utilising the interactions between the ECM and cells, researchers can manipulate cells on surfaces by tuning the interactions that are exhibited between the surface and the cells. Nanotopologies have been found to modulate cell adhesion, proliferation, gene expression and cytoskeleton development.^{[45] [46] [47]}

By changing the surface chemistry, cell adhesion and growth can be modulated. Cell adhesion to surfaces can be mediated by the prior adsorption of a layer of proteins to the surface such as fibronectin and a number of immunoglobulins.^[48] The chemistry of the surface affects the adsorption of proteins and so the adhesion of cells. The underlying chemistry of the surface can dictate the protein interactions that can then lead to the changes in the phenotype of cells. For example, changing the physiochemical properties of a surface can induce the differentiation of stem cells into specific cell types from blood, bone, cartilage, and skin.^[49]

Changes in surface chemistry can affect the signalling pathways used by the cells which in turn can lead to changes in gene expression within the cell.^[50]

The surface chemistry of self assembled monolayers (SAMs) can be modulated by the functional groups attached. Thus, by incorporating different functionality the properties of the SAMs can be modulated. Non-polar groups produce hydrophobic surfaces that are not wettable. The water droplet contact angle on these surfaces typically measures $\theta > 80^\circ$. These surfaces will adsorb protein readily onto their surface, which leads to cell adhesion. Groups that are charged at physiological pH such as carboxylic acids and amino groups have moderate wettability and their water contact angles measure in the range of $\theta = 48 - 62^\circ$. Polar substituents such as hydroxyl and polyethylene glycol chains are very hydrophilic and the water contact angles measure $\theta < 35^\circ$. These surfaces tend to repel non-specific protein adsorption and are deemed to be biologically inert.^{[51] [52]}

Protein adsorption to a surface generally correlates to the hydrophobicity of the surface, whereby the degree protein adsorption increases with increasing hydrophobicity. Surfaces can be made where the deposition protein is repelled. These surfaces also repel cell adhesion and are described as 'biologically inert'. Typically surfaces presenting oligomer chains of ethylene glycol are biologically inert. Pre-adsorption of proteins such as BSA can have a similar effect, where additional adsorption cannot occur. However, gradual denaturation of the adsorbed protein over time occurs and the protein may undergo exchange with other proteins present in solution. Another limiting factor to pre-adsorption of protein to surfaces is that additional functionality cannot be presented on the surface.^[52]

SAMs have been used extensively for the modification of surfaces for a number of applications ranging from the use in sensing technologies to tunable surfaces for cell culture work.^{[53] [54] [55] [56]} Surfaces for modification with SAMs cover a wide range of materials, from metallic

coated glass (typically gold films) for the immobilisation of functionalised thiols and disulfides, functionalised carboxylic acids on alumina, to oxides and silicates for adhesion of derivatised silane SAMs. The examples described herein will focus in particular on work carried out for cell culture experiments and their applications.

The gold surfaces that thiolate SAMs can adsorb onto can be of varying thicknesses, from the transparent 5-20 nm range to greater than 100 nm opaque, reflective surfaces.^[52] All thicknesses have been found to be electrically conductive and are stable for several months to air and solvent.^{[52] [57]} They have been found to be stable up to temperatures of 145° C before desorption of the monolayer will occur. Desorption may be induced by the application of UV light in the presence of oxygen.^[57]

Further modulation of surface chemistry can be controlled by the formation of mixed solutions of two or more thiols. Microcontact printing (μ CP) is a method for the formation of patterned SAMs where a specific thiol can be placed onto a gold surface with high precision. By using these different methods for deposition of the thiols onto the surface it is possible to produce multifunctional surfaces with a high degree of precision. Furthermore, it has been shown that the surface chemistry of gold-thiol SAMs can be tuned to respond to stimuli such that the activity towards non-specific protein adsorption and cell adhesion can be switched on and off.^{[53] [54] [55] [56]} The attachment of the tripeptide with sequence RGD can be used to mimic the integrin binding proteins found in the ECM. This sequence is found in several integrin binding proteins such as fibronectin. The peptide has been shown to be sufficient to induce focal adhesions to the surface by the cells.^{[54] [55]}

This form of dynamic surfaces is exemplified by the formation of mixed surface where a C₁₈ thiol [HS(CH₂)₁₇CH₃] was microcontact printed onto gold/titanium coated glass slides. The SAMs produced areas for non-specific protein adsorption. A second thiol containing a chain of three ethylene glycols [HS(CH₂)₁₁(EG)₃] was used to coat the remaining gold, in order to create areas that were resistant to protein adsorption.^[53] Bovine

capillary endothelial (BCE) cells were grown on this surface where they were confined to areas that were purely C_{18} thiol monolayers. After an application of -1.2 V electrical potential for 30 s through the underlying gold surface, the $C_{11}EG_3$ thiols desorbed from the surface of the gold, allowing the BCE cells to spread and grow across the entire surface. Monitoring by surface plasmon resonance (SPR) showed that after the electrical treatment, the layer of proteins adsorbed onto the surface increased, indicating that the $C_{11}EG_3$ thiols were no longer present.^[53] Cyclic voltammetry studies showed that the $C_{11}EG_3$ thiol monolayers had desorbed off the gold with the application of the electrical potential. Quantitative fluorescence experiments with rhodamine labelled fibronectin showed that the proteins that had adsorbed to the surface prior to application of the -1.2 V potential were retained and were unaffected by this electrical potential.^[53] Close inspection showed that the BCE cells appeared to be unaffected by the electrical pulse such that they underwent normal growth and cytokinesis.^[53]

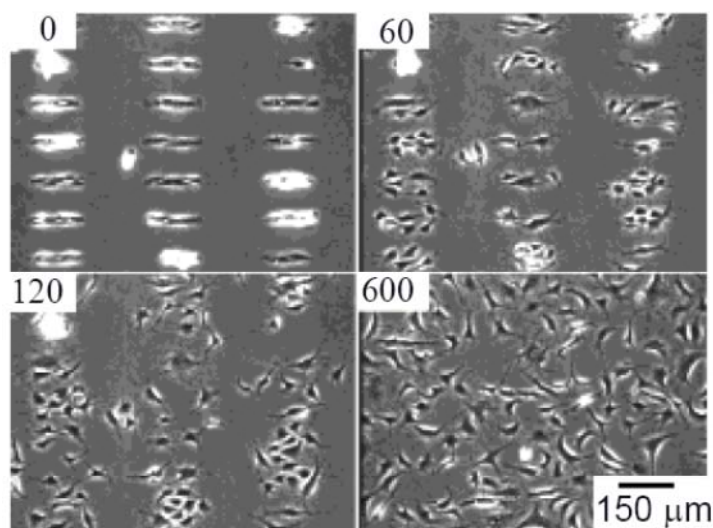


Figure 1.42. The growth and migration of BCE cells on a surface after the application of an electrical potential where the time in minutes after the voltage pulse is indicated.^[53]

The efficacies of a number of drugs affecting motility of cells were tested using the migration of the cells after the pulse of voltage had been applied. The drugs used were fumagillin, an inhibitor of motility in

capillary cells; cycloheximide, a general protein synthesis inhibitor; and nocodazole, which depolymerises microtubules. The motility of the BCE cells was inhibited by these drugs, where the rate of spreading over the surface was reduced by the both the fumagillin and the cycloheximide, and completely halted with the nocodazole. The results are shown in Figure 1.43.^[53]

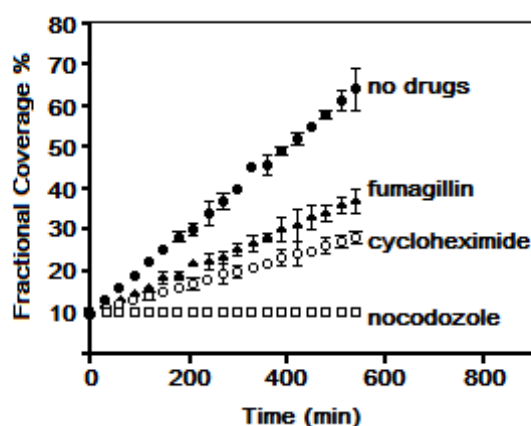


Figure 1.43. Summary of the influence of drugs on the motility of BCE cells after the application of a voltage pulse of -1.2V for 30s.

Additional complexity has been incorporated into gold surfaces patterned with hexadecane thiol, presenting CH₃, using microcontact printing to form islands on the gold where non-specific protein absorption and so cell adhesion could occur. The bare gold was then treated with a mixed thiol solution of 1% hydroquinone thiol (HQ) and penta(ethylene glycol) thiol (EG₅OH) to give a protein-inert SAM on the remaining gold.^[54] Swiss 3T3 fibroblast cells were grown onto the surface where the growth and adhesion of these cells were confined to the areas coated with the hexadecane thiol SAMs. Application of a 500 mV electrical potential for 10 seconds in the presence of serum-free growth media containing a peptide functionalised cyclopentadiene-RGD-Cp, converted the inert hydroquinone to a selectively labile surface for integrin binding, thus allowing the fibroblast cells to be released from the areas of the hexadecane thiol.^[54] The hydroquinone was electrically oxidised to the

quinone moiety that was then reacted by Diels-Alder cycloaddition with the RGD-cyclopentadiene to give the labelled thiol SAMs.

The Swiss 3T3 fibroblasts then quickly migrated across the surface such that after 22 hours of incubation with fresh media the cells had evenly distributed across the surface. After a period of two days the cells had reached confluence across the entire surface, indicating that normal growth and motility had occurred on this surface.^[54] Blank experiments showed that both the electrical potential and the addition of the RGD-Cp were required for the activation of the surfaces for cell growth and motility. The conversion of the SAMs from the hydroquinone moiety to the RGD functionalisation is shown in Figure 1.44. The results of the cell growth and migration after electrical activation and the Diels-Alder reaction is shown in Figure 1.45.

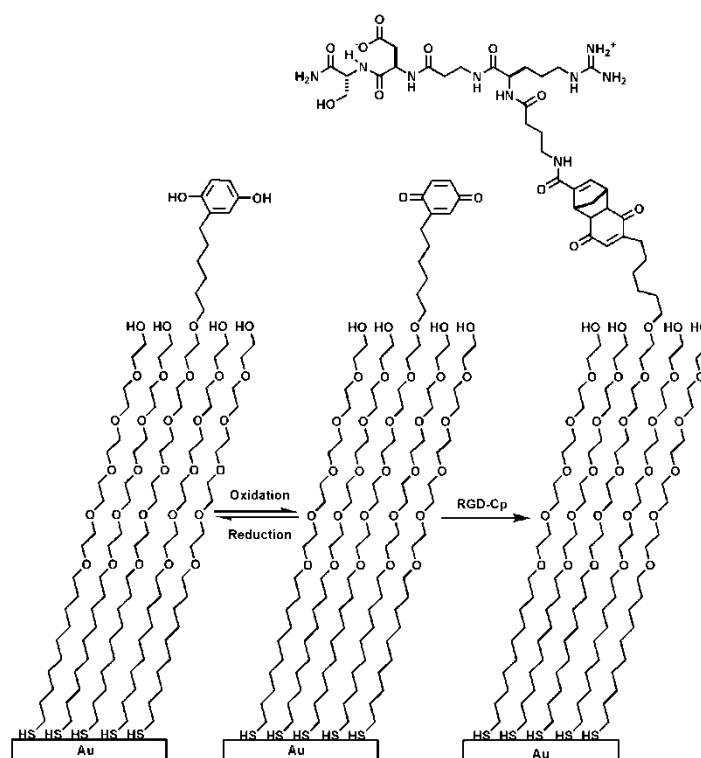


Figure 1.44. Redox process to form the benzoquinone from the hydroquinone followed by Diels alder reaction to create biologically active SAMs for Swiss 3T3 fibroblast cell migration.^[54]

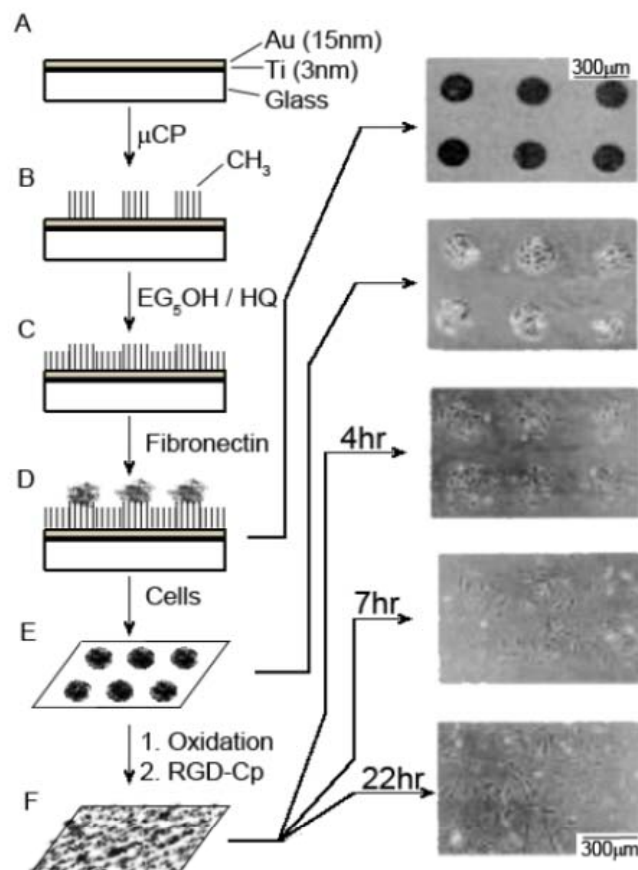


Figure 1.45. Production and activation of surfaces for the migration and growth of cells with an electroactive substrate.^[54]

Further experiments to show the use of this system as an assay for testing the effectiveness of drugs that affect mobility of cells were carried out. By treating the culture with either 15 μM cytochalasin D or 5 μM nocodazole, drugs that disrupt the remodelling of the cytoskeleton and so inhibit cell migration. After the application of the electrical potential with the RGD-Cp and either drug present in the media, it was found that even after 7 hours both drugs had retarded the movement of the cells almost completely. It was found that after refreshing the media, the cells were then able to spread across the surface again, showing that the drugs were not cytotoxic at the level used.^[54] The results are shown in Figure 1.46.

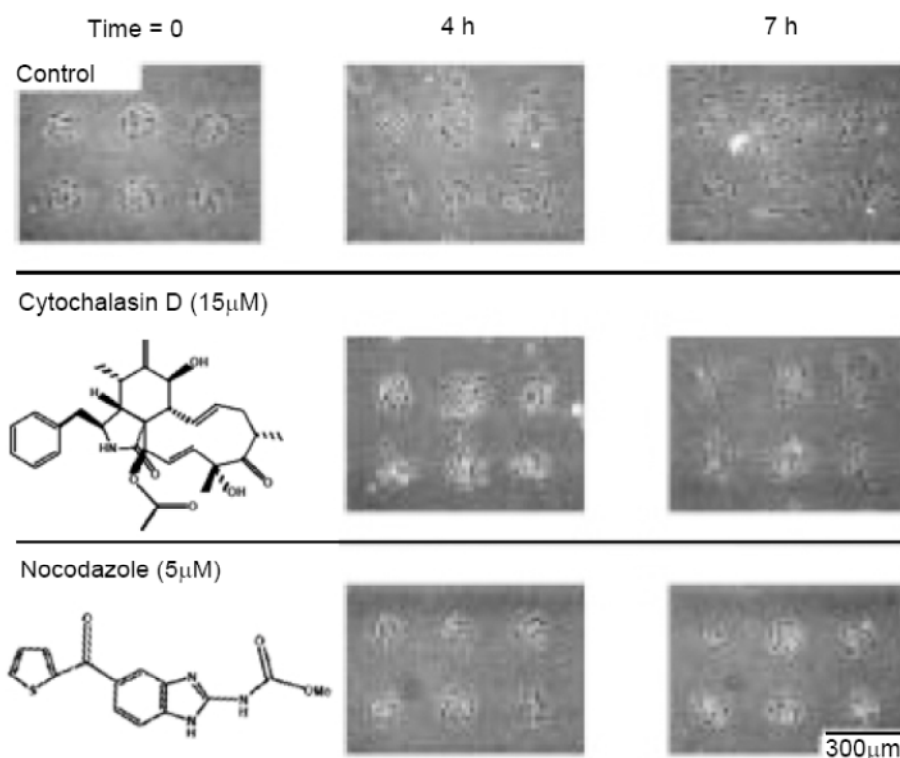


Figure 1.46. The effects of anti-motility drugs on the migration of Swiss 3T3 fibroblasts after the application of an electrical potential.^[54]

Following on from this work, functionalised surfaces were prepared by microcontact printing of hexadecane thiol onto gold/ titanium glass slides. The remaining gold surface was then treated with a mixed solution of 0.02% diethylisopropylsilyl hydroquinone-terminated alkanethiol (E*-RGD) with tri(ethylene glycol) terminated alkane thiol. The structure of E*-RGD is shown in Figure 1.47.^[55]

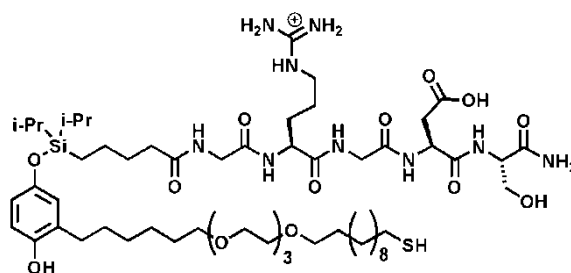


Figure 1.47. Structure of E*-RGD.^[55]

The patterned surface was then treated with fibronectin.^[55] The fibronectin adsorbed only on the regions of the hexadecanethiolate SAMs. The triethylene glycol terminated SAMs repel all non-specific adsorption of protein to the surface and the RGD peptide also repelled further deposition of the protein. Swiss 3T3 fibroblast cells were incubated onto the surface for two hours, where the cells adhered uniformly across the entire surface with no preference for the areas of fibronectin or the RGD peptide.^[55] Application of 550 mV electrical potential for 5 minutes across the gold surface led to the oxidation of the O-silyl hydroquinone in the E*-RGD thiol to the benzoquinone, releasing the RGD peptide and the peptide-bound cells. The fibronectin bound cells were retained on the surface.^[55] The SAMs around these areas had become non-adsorbant and so the cells could not freely migrate across the surface. The cell culture was then treated with serum-free medium that contained RGD-Cp. The structure of RGD-Cp is shown in Figure 1.48.^[55]

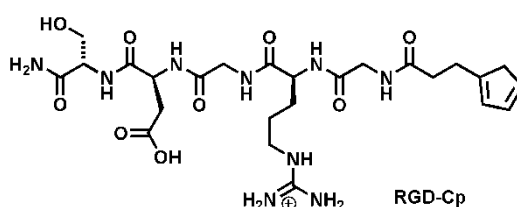


Figure 1.48. Structure of RGD-Cp.^[55]

The RGD-Cp reacted with the benzoquinone moiety in a Diels-Alder reaction. After 1 hour of incubation, the medium was replaced with serum containing medium. The cells were incubated for 14 hours, after which time the cells had spread across the surface uniformly such that by 24 hours the patterning was no longer evident.^[55] The release and remigration across the patterned substrate is shown in Figure 1.49. It was observed that the fibroblast cells were unaffected by the conditions applied where the cells on the hexadecanethiol SAMs were not only

retained by the surface, but they were also able to grow and spread across the surface in a normal fashion after the reaction with RGD-Cp.^[55]

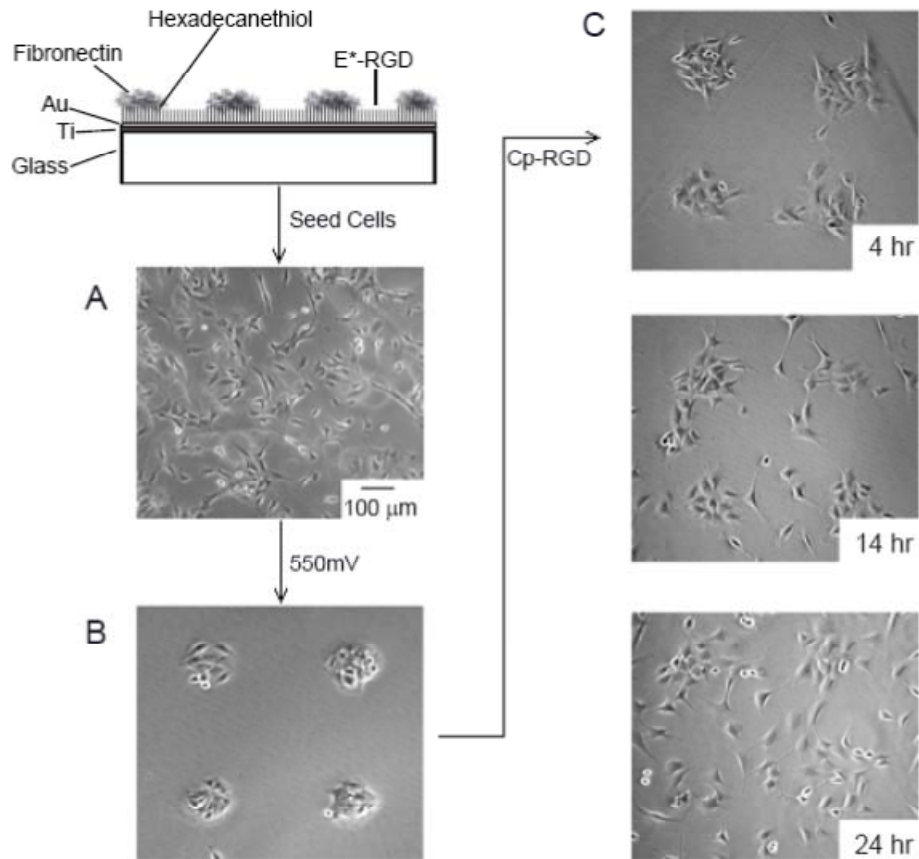


Figure 1.49. Release of cells then remigration across surface after addition of RGD-Cp.^[55]

Additional experiments where the RGD-Cp was either left out completely or substituted with RGE-Cp showed no migration of the fibroblast cells across the surface, showing that the cells were bound to the surface via the specific interactions with fibronectin and the fibronectin mimic RGD only.^[55]

1.8 Analytical Techniques used in this research programme.

1.8.1. Isothermal titration calorimetry.

ITC is a direct accurate method of measuring individual thermodynamic parameters.^[58] It allows for a greater understanding of the favourable and un-favourable processes that occur during binding interactions. ITC is used primarily for the direct measurement of enthalpy upon binding of biomolecules and their ligands in aqueous media.^{[58] [59] [60] [61]} The binding of molecules will cause a change in heat, where the system will either release or absorb heat from the surroundings depending upon the nature of the association.^{[60] [61]} The degree of change is directly proportional to the amount of binding. By quantifying this change in heat, calculation of additional thermodynamic parameters for the interaction such as: association constant K_a , binding stoichiometry N , and change in enthalpy ΔH can be performed. Additional information can be calculated by investigating the dependence of ΔH with temperature and by applying thermodynamic functions such as those shown in Equation 1.4 and Equation 1.5.^{[62] [61]}

$$\Delta G = -RT \ln K_a = \Delta H - T\Delta S \quad \text{Equation 1.4. Free Energy Equation.}$$

$$\Delta C_p = \frac{\Delta H_2 - \Delta H_1}{T_2 - T_1} \quad \text{Equation 1.5 Calculation for heat capacity}$$

The experimental set-up of the Microcal VT isothermal calorimeter used in this research programme consists of two cells encased within a thermally insulating shield.^[60] The cells are the reference and sample cells and both are equipped with heating elements and thermocouples. The thermally insulating shield guards against temperature fluctuations that are unrelated to the interactions. A diagram of the set-up of a calorimeter is shown in Figure 1.50.

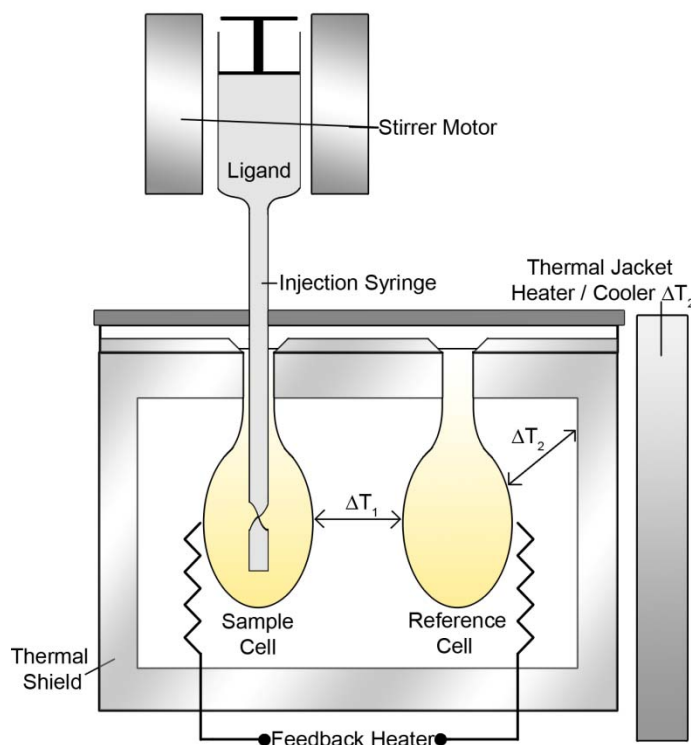


Figure 1.50. Schematic of ITC instrument showing the layout the sample and reference cells, insulating shield and injection syringe.^[60]

The reference cell is maintained at a required temperature throughout the experiment, where it is subjected to a fixed amount of power.^{[60] [61]} The injection syringe is incorporated into the sample cell for the experiment, where the cell contains the macromolecule and the ligand is within the syringe.^{[62] [61]} Using the calorimeter's software, the ligand is titrated into the cell in set volumes over the course of a period of time. As the ligand binds to the macromolecule, the temperature of the sample is corrected where the power variance to either heat or cool the cell back to the starting temperature is measured.^{[58, 62] [61]} As the macromolecule is saturated with the ligand the change in heat diminishes until dilution effects are all that is observed.^{[62] [61]} The change in power applied is referred to as the cell feedback signal. For exothermic binding interactions, the feedback signal is negative as power is removed from the thermocouple in order to cool the sample.^{[58] [62] [61]} Correspondingly, endothermic interactions produce positive a spectrum, where additional

heating of the thermocouple is required to regain the initial temperature.^{[62] [61]}

The cell feedback signal is plotted against time and the area under each peak is integrated to generate the value of heat associated with each injection.^{[58] [62] [60] [61]} The final binding curve is then obtained from a plot of the association heats from each injection against the molar ratio of the ligand and macromolecule in the cell.^{[62] [61]} Using the required set-of-sites binding model, the curve can be analysed to gain the K_a , N and ΔH of binding.^[58] The set-of-sites binding model uses a set complex equations to best fit a line through the curve from which the thermodynamic data is then calculated the single set of sites uses the assumption that there are n identical degenerate binding sites on the macromolecule.^[61] The standard graph produced is shown in Figure 1.51.^[61]

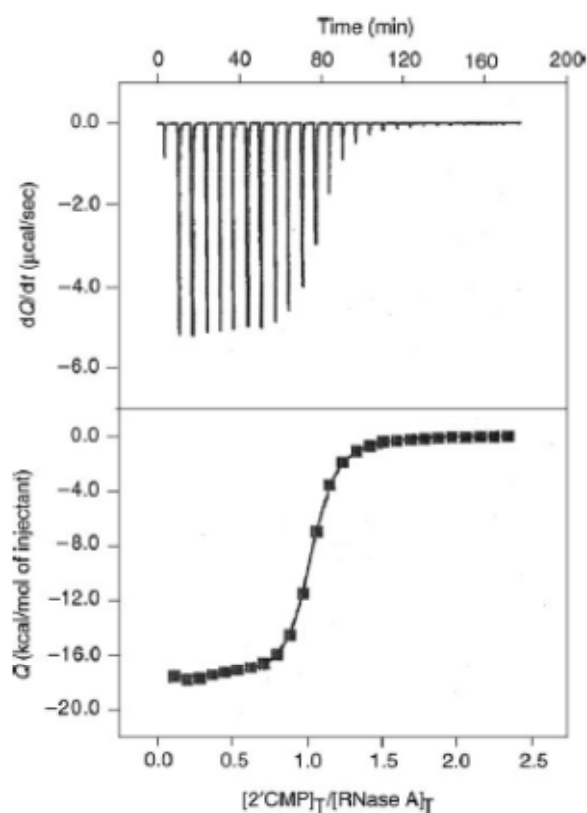


Figure 1.51. Typical binding curve produced by an ITC experiment.^[61]

1.8.2 Cyclic Voltammetry.

For a reversible electrochemical reaction the ratio between the concentrations of the oxidised (C°_{ox}) and reduced species (C°_{red}) can be related to the standard electrical potential E° , required for the electrochemical process.^{[63] [64]} When the electrical potential E , is changed the ratio between oxidised and reduced species also changes to satisfy the Nernst equation shown in Equation 1.6.

Equation 1.6. Nernst Equation.

$$E = E^{\circ} - \frac{RT}{nF} \ln \frac{C^{\circ}_{red}}{C^{\circ}_{ox}}$$

E° = Standard reduction potential for the redox couple, R = molar gas constant

T = absolute temperature, n = number of electrons transferred, F = Faraday constant

C°_{red} = concentration of reduced species, C°_{ox} = concentration of oxidised species.

As E becomes more positive there is a reduction in the ratio between C°_{red} and C°_{ox} , where the reduced species is oxidised. Correspondingly, as E becomes more negative the oxidised species is reduced and the ratio is enlarged.^{[63] [64]} The change in electrical current I is an important variable when measuring a cyclic voltammogram. The Butler-Volmer equation links the variables for electrical potential, current and species concentration together and from it the effects of a parameter on the system can be observed.^{[63] [64]} Equation 1.7 shows the Butler-Volmer equation.

$$\frac{i}{nFA} = k^{\circ} \{ C^{\circ}_{ox} \exp[-\alpha\theta] - C^{\circ}_{red} \exp[(1 - \alpha)\theta] \}$$

Equation 1.7.

Butler-Volmer Equation

$$\theta = \frac{nF(E - E^{\circ})}{RT}$$

E° = Standard reduction potential for the redox couple, R = molar gas constant

T = absolute temperature, n = number of electrons transferred, F = Faraday constant

C°_{red} = concentration of reduced species, C°_{ox} = concentration of oxidised species

k° = heterogeneous rate constant, α = transfer coefficient i = current

Additionally the current I , is also dependent upon the flux of the material to the electrode.^[65] When there is an increase in the concentration of either oxidised or reduced species diffusion away from electrode into the bulk solution E° occurs. As the other species is diminished in concentration, the diffusion of more of that species towards the electrode from the bulk solution also occurs.^[65] It has been found that the flux of the material is proportional to the concentration gradient and is described by Fick's law as shown in Equation 1.8.

$$\Phi = -AD_o \left(\frac{\partial C_{ox}}{\partial x} \right)$$

Equation 1.8. Fick's Law.

Φ = flux of material, A = area of electrode, D_o = diffusion coefficient of Ox,

x = distance from electrode

Cyclic voltammetry is a solution based electroanalytical technique for use in mechanistic studies of redox systems.^{[63] [64] [65] [66]} The oxidation reduction potential can cycle through a range of electronic potentials to find the redox couple of the compound to be studied. Repetition through a triangular excitation signal for the cyclic voltammogram triggers the potential at the working electrode to sweep back and forth between the two switching potentials.^{[64] [66]} The current at the working electrode is monitored during the sweeping process. A diagram of the triangular excitation signal is shown in Figure 1.52.

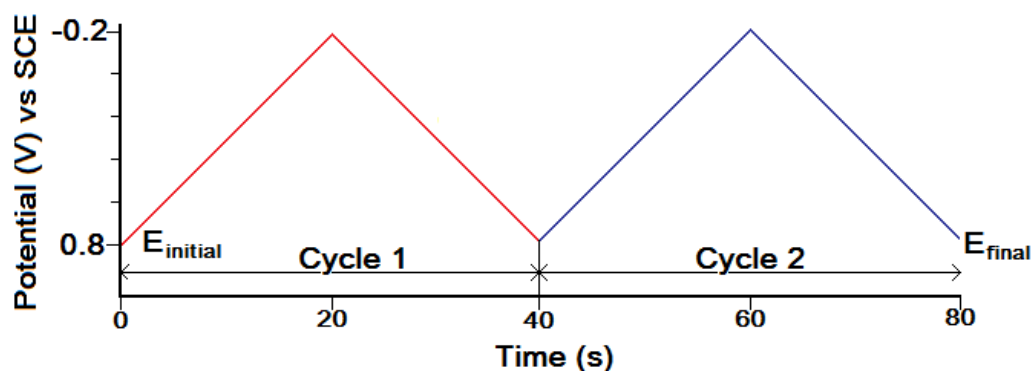


Figure 1.52. Triangular sweeping of the electrical potential.

As the sweep proceeds, the potential becomes positive.^{[64] [66]} Once the potential is sufficiently positive, oxidation of the redox couple is performed.^{[64] [66]} The anodic current rapidly increases as the reduced form is oxidised until the concentration of oxidisable material is diminished and the current reaches a peak and then slowly is itself diminished.^{[64] [66]} Once the potential is switched there is a gradual increase in cathodic current until the potential reaches a level at which the oxidised species is electrochemically reduced back to its initial form.^[63] The reverse peak in current occurs as the concentration of the oxidised species diminishes in the same mechanism as observed for the oxidation wave. The CV wave for the reversible redox wave for Fe^{2+} to Fe^{3+} is shown in Figure 1.53.^[64] From the peaks E_{ox} and E_{red} the halfwave potential $E_{1/2}$, can be calculated. In the ideal case $E_{\text{ox}} = E_{\text{red}} = E_{1/2}$.^[63] However this typically does not occur, and peaks are slightly shifted. As result $E_{1/2}$ is taken as the point halfway between the two peaks and can be described by Equation 1.9.^[64] This can be simplified down to Equation 1.10, by virtue that the diffusion coefficients $D_{\text{red}} \sim D_{\text{ox}}$ leading to the potential being very close to the value of the standard reduction potential E° .

$$E_{1/2} = E^\circ + \left(\frac{RT}{nF}\right) \ln \left(\frac{D_{red}}{D_{ox}}\right)^{1/2} \quad \text{Equation 1.9.}$$

$$E_{1/2} = \left(\frac{E_{red} + E_{ox}}{2}\right) \quad \text{Equation 1.10}$$

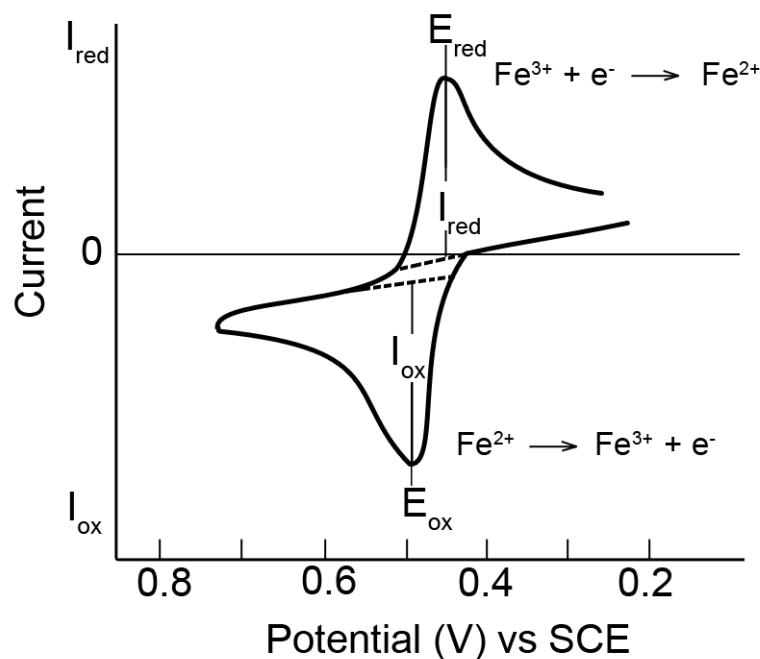


Figure 1.53. CV wave for the reversible redox process for Fe²⁺ to Fe³⁺.^[66]

A cyclic voltammetry experiment can be performed in a variety of solvents from water to acetonitrile.^[64] The solvent used is required to not be electrochemically active in the range of electrical potential used. The range of electrical potential used is dictated by the solvent, electrolyte and electrodes used.^[64] An electrolyte is required to ensure conductivity through the solution. CV utilises a three electrode set-up.^[64] These electrodes are the working electrode, the counter electrode and a reference electrode.^[64] The working electrode and counter electrode are typically made from glassy carbon, platinum, or gold. The counter electrode is separated from the working electrode using a glass frit.^[64] It conducts the electrical potential without affecting the bulk solution.

The reference electrode can be a large variety of materials in aqueous solutions, where typically saturated calomel electrodes (SCE) or silver / silver chloride electrodes are used. The reference electrode has well defined redox activity and is highly stable.^[64] For non-aqueous conditions a quasi-reference electrode is used such as ferrocene or cobaltocene.^[64] This is due to the incompatibility of the aqueous electrodes with the solvent used. The solutions require degassing to remove dissolved oxygen, to avoid the redox processes of oxygen impeding the experiment. The setup of an aqueous cyclic voltammetry experiment is shown in Figure 1.54.

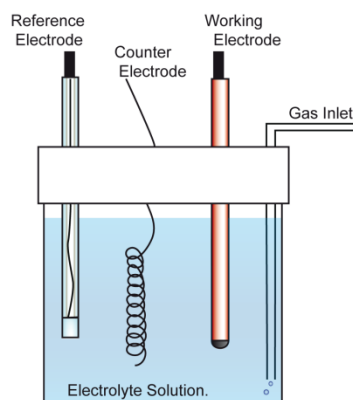


Figure 1.54. Schematic diagram of a cyclic voltammetry experimental setup.

1.8.3 Dynamic Light Scattering.

DLS measures the Brownian motion exhibited by particles in solution.^[67] The Brownian motion exhibited by a particle is directly correlated to the size of the particle and the viscosity of the solution it is suspended in.^[67] The hydrodynamic diameter of a particle is calculated using the Stokes-Einstein equation which is presented as Equation 1.11 overleaf. d (H) signifies the hydrodynamic diameter, k is the Boltzmann constant ($1.38 \times 10^{-23} \text{ JK}^{-1}$). D is the translational diffusion coefficient, T is the absolute temperature, and η signifies the viscosity of the solution.^[67]

$$d(H) = \frac{kT}{3\pi\eta D}$$

Equation 1.11. Stokes-Einstein equation.

Particles in dispersion move in the constant and random manner of Brownian motion.^[67] By directing a beam of light with a known wavelength into a sample, the light is scattered upon impact with the particles in the solution. The degree of scattering observed relates to the size of the particle hit with the light. By measuring the rate at which scattered light fluctuates as a function of time the size distribution of the particle can be measured. The detector can be positioned at various angles from the direction of the incident light path.^[67] Typically the position of the detector lies either at 90° or 173° to the laser beam. A schematic diagram of the DLS set up is shown in Figure 1.55. For monodisperse samples, the function $G(\tau)$, a correlation function of scattered light intensity, has an exponential decay pattern that follows the formula shown in Equation 1.12.^[67]

$$G(\tau) = A [1 + B \exp(-2\Gamma\tau)] \quad \text{Equation 1.12}$$

A = baseline of correlation function. B = intercept of correlation function

$$\Gamma = Dq^2 \quad \text{Equation 1.13}$$

D = The translational diffusion coefficient

$$q = \left(\frac{4\pi n}{\lambda_0}\right) \sin(\theta/2) \quad \text{Equation 1.14}$$

n = refractive index of dispersant. λ_0 = wavelength of laser. θ = scattering angle

For polydisperse samples, the function $G(\tau)$ is modified slightly as shown in Equation 1.15. Where the $g_1(\tau)$ relates to the sum of all exponential decays in the correlation function.^[67]

$$G(\tau) = A [1 + B g_1(\tau)^2] \quad \text{Equation 1.15}$$

The correlation data using a number of complex algorithms produces the mean size of the particles (Z_{AV}) and an estimate of the distribution width referred to as the polydispersity index (PDI).^[67]

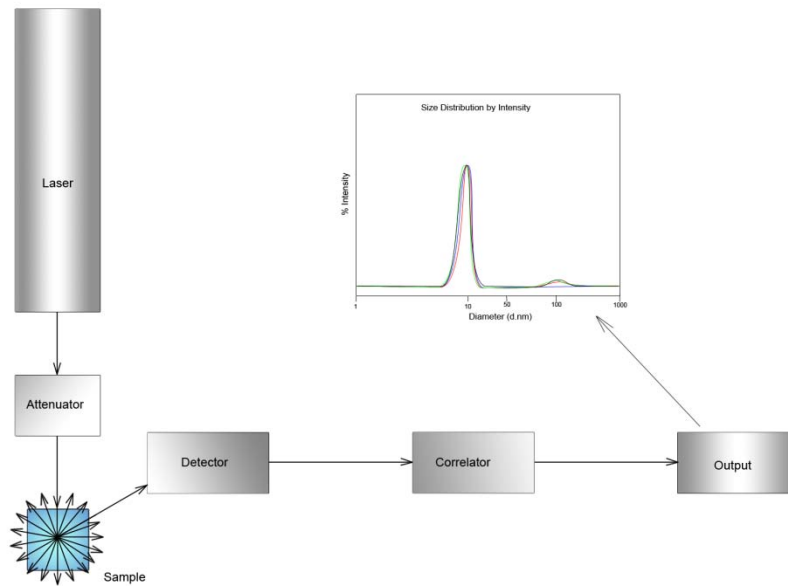


Figure 1.55. Schematic diagram of a typical DLS experimental setup.^[67]

1.8.4. UV-Vis and Fluorescence spectroscopy.

UV-Vis and fluorescence spectroscopy are two complementary spectroscopic techniques.

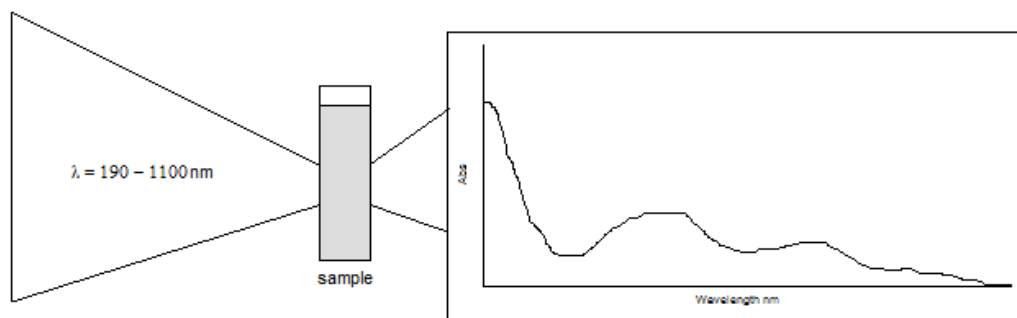


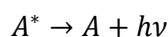
Figure 1.56. Schematic diagram of a UV-Vis experiment.

UV-Vis measures the absorbance of light by a solution. Electrons from the ground state are elevated to an excited state upon absorption of the light.^{[68] [69]} Absorbance of light follows the Beer-Lambert Law, where $[c]$ corresponds to the concentration of the solution, ϵ is the molar extinction coefficient, l is the pathlength and A is the absorbance at λ_x as shown below in Equation 1.16. From the absorbance spectrum the λ_{\max} can be observed which in turn be used to measure the fluorescence emission spectrum.^{[70] [69]} The concentration of a sample can vary from typically 10^{-3} - 10^{-4} M depending upon the chromophore intensity of the sample. The measurement occurs by reading the wavelengths of light that pass directly through the sample. The light that does not pass through the sample is absorbed.^{[69] [68]} Figure 1.56 shows a schematic of a UV-Vis experiment.

$$A = [c]\epsilon l$$

Equation 1.16. Beer-Lambert Law.

Fluorescence spectroscopy utilises the irradiation of a compound in solution at λ_{max} where electrons from the ground state are elevated to an excitation state.^[71] The compound then loses energy as the electron returns to the ground state.^[72] The release of the energy through fluorescence can be measured. The emission spectrum is measured by irradiating the sample with the λ_{max} for the absorbance in the UV-Vis spectrum^[68] ^[70] where the emission over the course of a range of wavelengths is measured. The concentration of samples used for fluorescence tend to not exceed 10^{-5} M as Raleigh scattering becomes a prominent effect at higher concentrations.^[72] The set-up for a fluorescence experiment is shown in Figure 1.57. The light emitted from the sample after irradiation is measured at 90° to the beam of light. The light emitted follows the equation below, where $h\nu$ signifies the amount of light emitted at a specific wavelength.^[72]



Equation 1.17

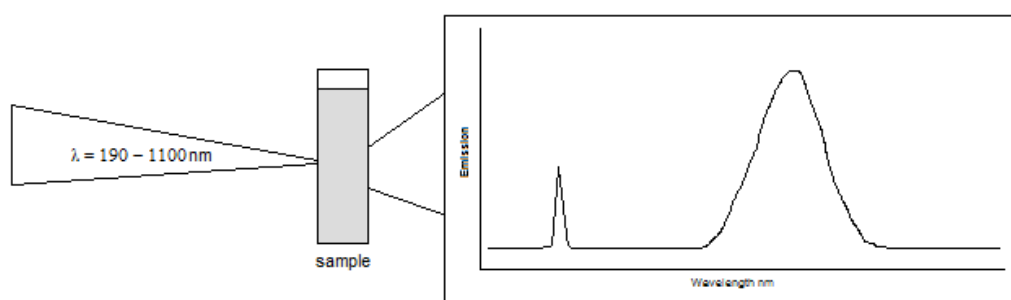


Figure 1.57. Schematic of a fluorescence experiment

2. Functionalised Dihydro-imidazo-phenanthridine Intercalating Agents.

2.1. Dihydro-imidazo-phenanthridines and Imidazo-phenanthridines.

2.1.1. Synthesis of Dihydro-imidazo-phenanthridines and Imidazo-phenanthridines.

Modifications of phenanthridine and its derivatives have been carried out in an attempt to tune the cytotoxic and intercalative properties. It is hoped that by tuning the properties, these compounds can be used as molecular probes, and potential chemotherapeutic drugs. Key modifications include the addition of hydroimidazole and imidazole functionality to the phenanthridine core to form dihydro-imidazo-phenanthridines, DIP^[73] and imidazo-phenanthridines, IP.^[74] The general structures are for these compounds are shown below in Figure 2.1.

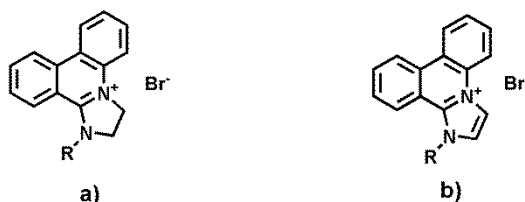
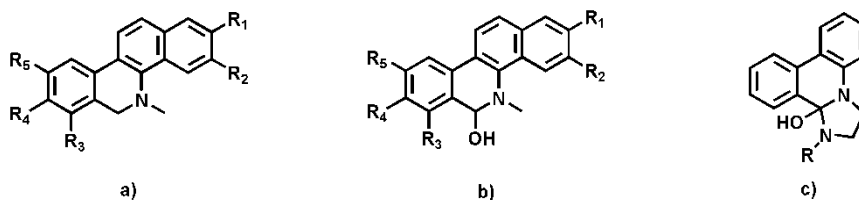


Figure 2.1. General structures of derivatised phenanthridine derivatives.
a) Dihydro-imidazo-phenanthridine. b) Imidazo-phenanthridine.

The addition of the imidazole functionality to the phenanthridine core blocks the metabolic pathway which rapidly deactivates these compounds by forming a neutral dihydrogenated species.^[73] ^[75] Benzo[c]phenanthridine alkaloids (BCPA) are naturally occurring biologically highly active intercalators with a phenanthridine core that undergo rapid reduction by NADH *in vivo* to give these inactive forms.^[76] The general structure of the reduced benzo[c]phenanthridine alkaloids are shown in Figure 2.2 (a).^[75] This addition also gives a degree of resistance to the formation of a pseudobase by the α -addition of

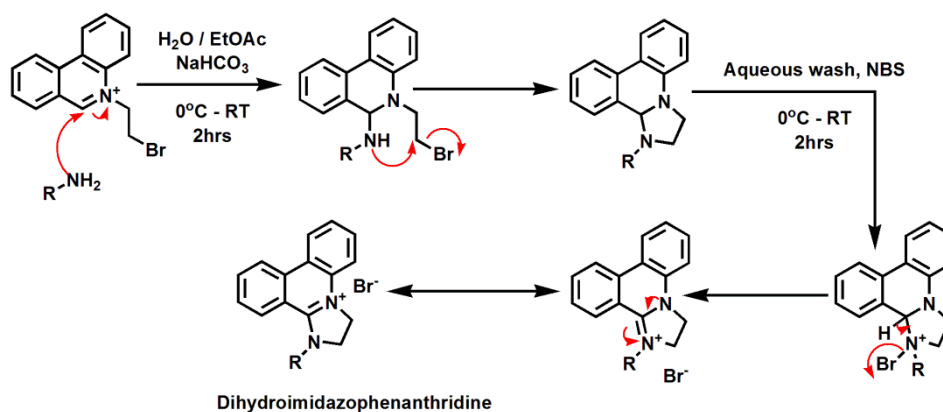
hydroxide to the structure as shown in Figure 2.2 (b) and (c), and so increases the stability of these structures *in vivo*.^[73]



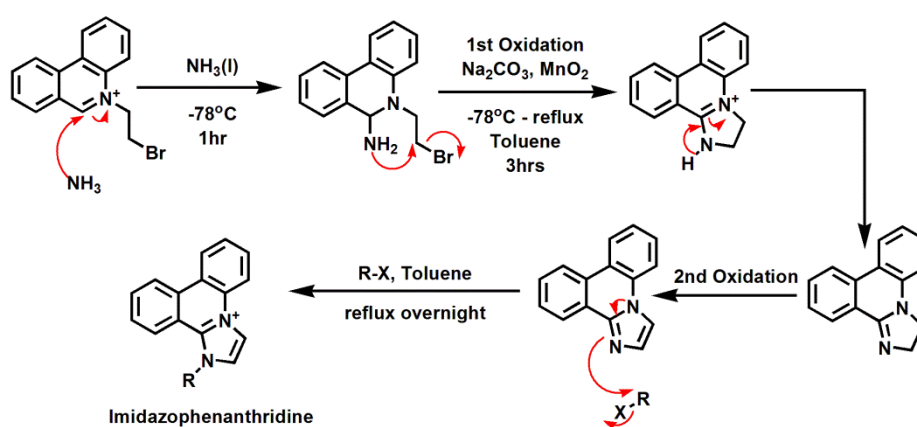
**Figure 2.2. a) Generalised structure of a reduced BCPA b) Pseudobase of a BCPA
c) Pseudobase of a DIP.**

The DIP and IP moieties are made from a common starting material of 5-(2-bromoethyl) phenanthridinium salt. The dihydroimidazo phenanthridines are formed in a one-pot-three-step reaction. The 5-(2-bromoethyl) phenanthridinium salt is reacted with a primary amine in the presence of base in a biphasic solvent mixture of ethyl acetate and water for two hours. After an aqueous wash, NBS is added to the reaction mixture and allowed to react for two hours in the dark, to give the required DIP as a precipitate in high yield.

The imidazo phenanthridines (IP) are produced by the reaction of 5-(2-bromoethyl) phenanthridinium salt with liquid ammonia at -78°C for 1 hour. Base and MnO_2 are added and the reaction is then refluxed in toluene for three hours, at which point an alkylating agent R-X is added and the reaction mixture is refluxed overnight. The product is then recovered by filtration in high yield. The oxidation steps are thought to occur prior to the re-aromatisation of the central ring in the IPs as attempts to convert the DIP structures into their equivalent IPs with a number of agents failed to give the required transformation. It is thought that the high stability of the compounds after the re-aromatisation of the core stops the further oxidation to the IP functionality to form. The reaction mechanism for the formation of DIP and IP are shown in Scheme 2.1 and Scheme 2.2.



Scheme 2.1. Formation DIP from 5-(2-bromoethyl) phenanthridinium salt.^[74]



Scheme 2.2. Formation IP from 5-(2-bromoethyl) phenanthridinium salt.^[74]

Both DIP and IP can support a large degree of functionality at the N1 position.^[77] The numbering of the general DIP structure with N1 and N2 labelled is shown below in Figure 2.3. Examples of the range of amines that have successfully been added to the DIP core are shown in Table 2.1.^{[73] [74] [77] [78] [79]}

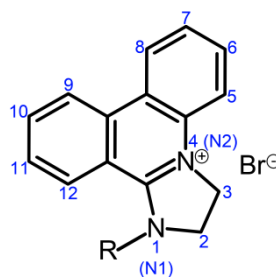
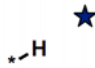

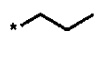
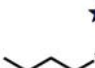
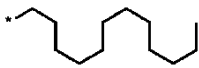
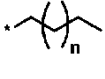
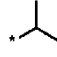

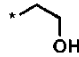
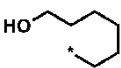
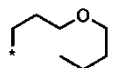
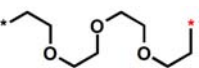
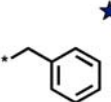
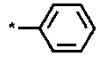
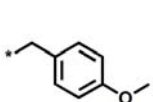
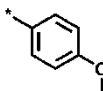
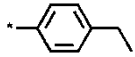
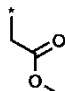
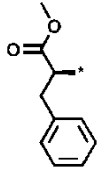
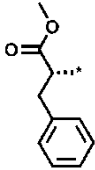
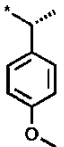
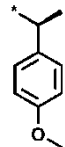
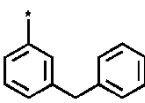
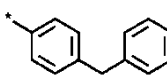
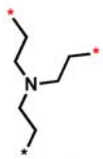
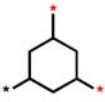
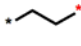
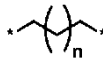


Figure 2.3 Numbered general DIP structure with the N1 and N2 positions labelled in blue.

R-* (* = NH ₂)			
 1	 2	 3	 4
 5	 n = 1-14 6	 7	 8
 9	 10	 11	 12
 13	 14	 15	 16
 17	 18	 19	 20
 21	 22	 23	 24
 25	 26	 27	 n = 7 - 10 28

* Indicates additional NH₂ to which a DIP can form.

★ Indicates groups also tethered to the IP core^[74]

Table 2.1 Functionalised amines used to synthesise DIP compounds.

2.1.2 Intercalative and Cytotoxic Properties of DIP and IP compounds.

As phenanthridine and the benzo[*c*]phenanthridine alkaloids have been previously shown to be cytotoxic to certain cancer cell lines, a variety of the compounds shown in Table 2.1 were tested against human ovarian tumour cell line A2780, whereby the cell line was treated with the required DIP at varying concentrations for 24 hours then allowed to recover for three days, prior to treatment with MTT stain.^[79] From data collected the IC₅₀ – the concentration at which 50% of the A2780 cells died upon culture with that particular DIP over 24 hours.^[79]

The cytotoxicity of these compounds is thought to be due to DNA binding, namely, intercalation of DNA. To investigate the relationship between binding and cytotoxicity, isothermal titration calorimetry (ITC) was carried out with the DIP compounds that had sufficient solubility. As the size of the functionality at the nitrogen increased, the hydrophobicity increased, whereas the aqueous solubility of the DIP compounds decreased to a point that calorimetry could not be carried out on all samples.^[79] For the samples that ITC was carried out on, the majority gave the expected results where the thermodynamic and binding data could be measured. The IC₅₀ data and *K_a* values for key ligands are shown in Table 2.2. A typical ITC spectrum recorded for these compounds is shown in Figure 2.4.

Ligand	<i>K_a</i> (10 ⁴ M ⁻¹)	IC ₅₀ (μM)
EtBr	12.9	0.30
DIP-H	2.6	1.56
DIP-Me	4.6	2.60
DIP-Bn	4.3	2.32
DIP-Bn- <i>p</i> -OMe	2.9	1.53

Table 2.2. IC₅₀ and *K_a* values for key phenanthridine based ligands. Salmon Testes in PBS.^[79]

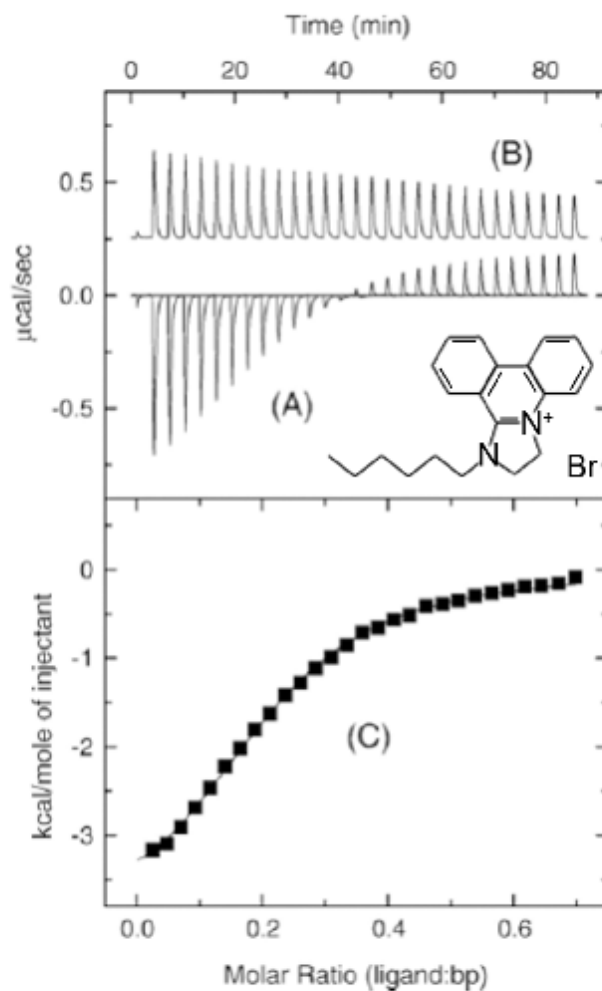


Figure 2.4. An example of ITC data for binding of a DIP ligand to salmon testes DNA. ^[78]

Segment A of Figure 2.4 shows the raw data collected for both ligand–DNA binding. Segment B shows the ligand dilution control. Part C shows the integrated data fit to a single set of sites binding model. ^[78] Table 2.3 shows the ITC data parameters recorded for key functionalised DIP and IP ligands in a) PBS^[78] and b) PIPES buffer^[74].

Ligand	<i>N</i>	<i>K_a</i> (10 ⁴ M ⁻¹)	ΔH (kcal/mol)
Ethidium Bromide ^a	0.32	11.7	-7.3
DIP-H ^a	0.3	2.6	-3.6
DIP-Me ^a	0.19	1.7	-5.9
DIP-Bn ^a	0.15	1.1	-4.7
IP-Bn ^b	Not Reported	6.1	Not Reported
DIP-Bn- <i>p</i> -OMe ^a	0.26	1.1	-4.4
IP-Bn- <i>p</i> -OMe ^b	0.09	11.8	-9.9
DIP-CH(CO ₂ Me)(C ₇ H ₇) ^{a*}	Not Defined	Not Defined	Exothermic

Table 2.3. ITC data parameters recorded for key ligands with Salmon Testes DNA. ^aPBS ^bPIPES buffer^{[78] [74]}. *The data recorded did not fit a one-set-of-sites binding model, with a more complex mode of binding.

The binding constant K_a for IP ligands was greater than that of the corresponding DIP ligands. This is thought to be due to increased planarity and the fully aromatic nature of the IP core where π -stacking between base pairs is stronger than the interaction between the less aromatic DIP and the base pairs. From the ITC data it can be shown that the binding properties can be modulated by the changing R groups. Nevertheless it can also be noted that the R group used does not block the binding to DNA by intercalation.

2.1.3. Microtubule Formation with Polyoxometallate (POM) Crystals.

It has been found that the solutions of DIP compounds can interact with polyoxometallate Keggin net crystals such that, the crystals partially dissolve in the aqueous media.^{[80] [81] [82]} Upon solvation of the outer edges of the crystal the dissolved POMs come in contact with the DIP molecules in solution and salt exchange occurs, whereby the resulting complex comes out of solution forming a semi-permeable membrane-like

structure around the inner crystal structure.^{[80] [81] [82]} The semi-permeable complex allows water to enter but not leave. As the osmotic pressure reaches its maximum, the membrane-like structure bursts and the contents flow out at the site of rupture.^{[80] [81] [82]} As this occurs the POM interacts with the positively charged DIP / IP molecules and precipitation of the complex occurs forming a tube.^{[80] [81] [82]} The flow of liquid continues along the hollow tube and exits the end precipitating out as it comes in contact with more substrate, until all the POM or DIP / IP has been used up. The images shown in Figure 2.5 show an example of the growth of a microtubule with time.

The diameter of the microtubes formed are typically in the range of 1-100 μm and it has been found that the diameter can be modulated by a number of factors including: the concentration of DIP used;^{[80] [81] [82]} the functionality on the DIP derivative,^{[80] [81] [82]} and the particular POM crystals used.^[80] By increasing the concentration of DIP used the tubes become narrower, and dilution causes a widening of the tube diameter.^[80]^{[81] [82]} This control of size is exemplified in Figure 2.6.

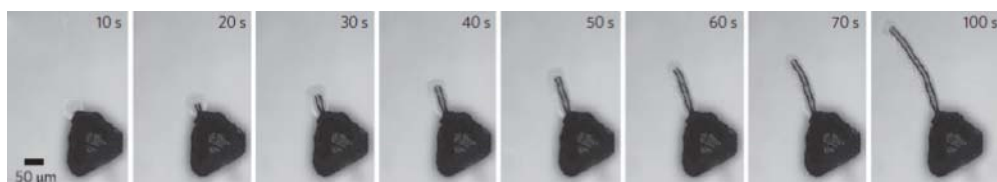


Figure 2.5. Time-lapse images of a single tube emerging from a crystal.^[81]

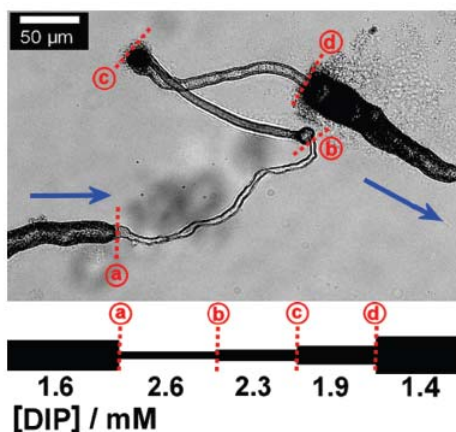


Figure 2.6. Size control of a growing tube by altering the available concentration of cations at points (a), (b), (c), and (d). The estimated concentrations at each point are shown in the lower section.^[82]

The direction of the microtube growth can also be modulated by the application of an electrical potential over the sample, where the application of a minimum 9 V potential across the sample causes localised heating and the flow of bulk solvent through convection and the tubes flow towards the cathode electrode. This has led to a number of motifs being formed by the microtubes with careful manipulation of electrical potentials across the sample. Figure 2.7 shows the different motifs that have been made by this method of manipulation.^[82]

Puncturing the growing tube will cause a halt in the direction the tube was flowing in and a new tube will sprout from the site of rupture allowing control of movement manually. Figure 2.8 shows an example of this manipulation of tube growth. When tubes from different crystals collide the two tubes will merge and form one wider tube. Figure 2.9 shows an example of this where the two tubes run parallel and then merge to form a larger tube.^[82]

It has been found that these tubes are hollow and it has been shown that the tubes can retain any liquids that are very carefully injected into them. An example of liquids that have been injected into the tubes successfully include the fluorescein isothiocyanate dye. It was found that it was possible to inject 10 mM solutions into the POM microtubule with

no damage to the microtubule. The flow of the flourescein dye could be monitored by fluorescence. Figure 2.10 shows the images taken of the flourescein stained POM microtubes.^[81]

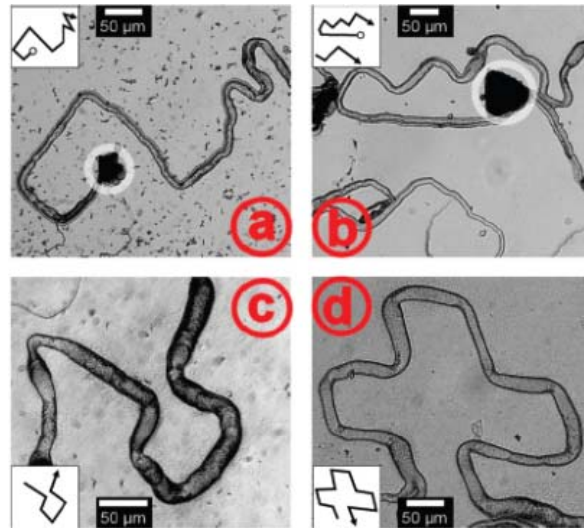


Figure 2.7. Motifs formed by controlling the tube growth direction.^[82]

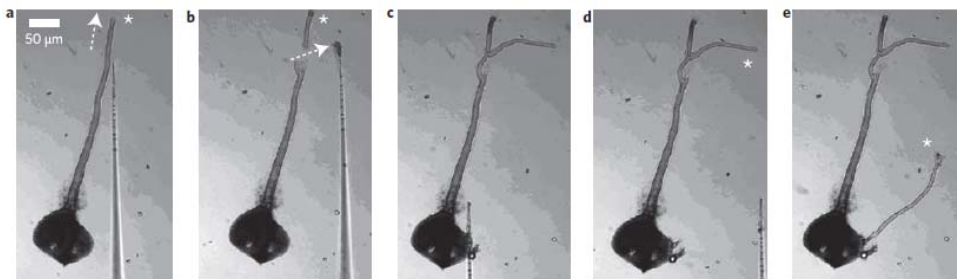


Figure 2.8. Manual breakage of tube to causes branching then manipulation growth.^[81]

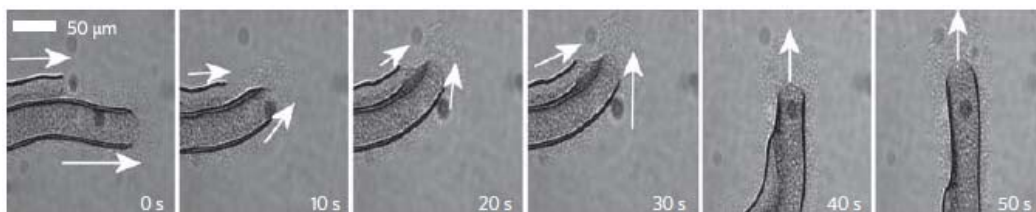


Figure 2.9. Two microtubes merging to form a larger tube.^[81]

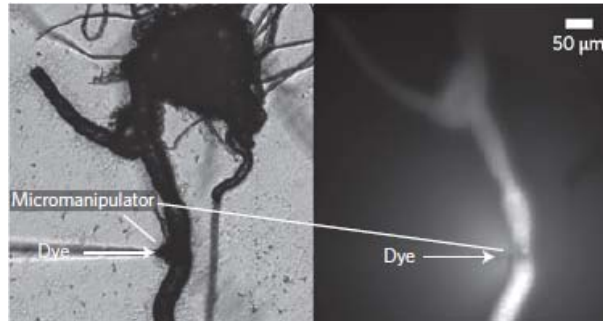


Figure 2.10. POM microtubule injected with fluorescein isothiocyanate dye.^[81]

2.2. Aims and Objectives.

The aims of this project were to synthesise two DNA intercalating agents that could undergo additional host-guest interactions. The addition to the functionalised intercalator could then give an indirect modulation of the DNA, with the ability to introduce groups to the structure that would normally not associate.

Prof L Cronin's group had recently formed dihydro-imidazo-phenanthridines in a three-step-one-pot reaction with potent intercalative properties that could tolerate a great deal of functionalisation at the N1 position.^[77] In collaboration with the Cronin group we then had a basis for the synthesis of the intercalating agents.

The 1,5-dioxynaphthalene subunit's ability to form stable and reversible deep pink complexes with CBPQT^{4+} , was seen as the preferred substrate for attachment to the DIP compound. The motivation for this was the pseudorotaxane formed when the naphthalene is threaded into the CBPQT^{4+} host cavity can be reversed by the treatment with a number of stimuli that can be thermal, electrochemical and chemical, with the change in complexation state easily observed by a simple colour change. Ferrocene was chosen as the alternative to naphthalene, where pseudorotaxane formation with cyclodextrins would give us a neutral additional host-guest interaction that could also be reversible by electrochemical means. The target DIP compounds for synthesis are shown in Figure 2.11.

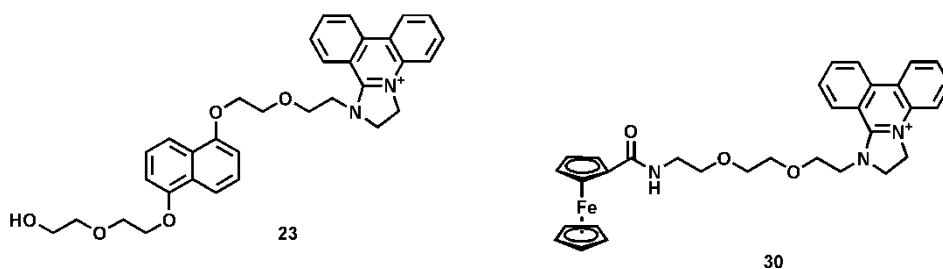
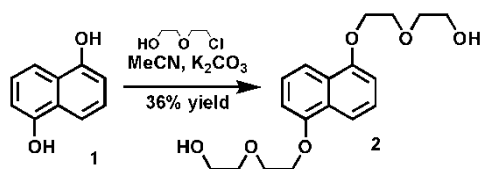


Figure 2.11. Final DIP products.

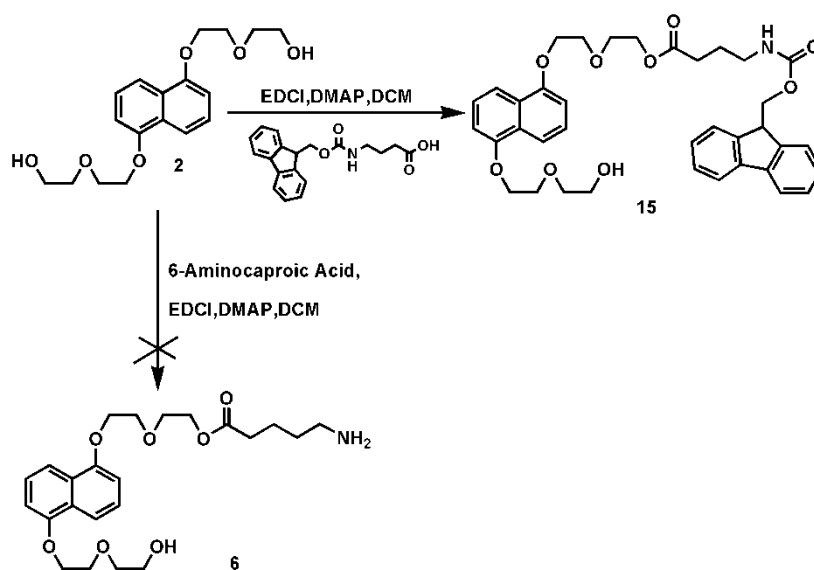
2.3 Results and Discussion.

2.3.1 Synthesis of the naphthalene amine 5a.



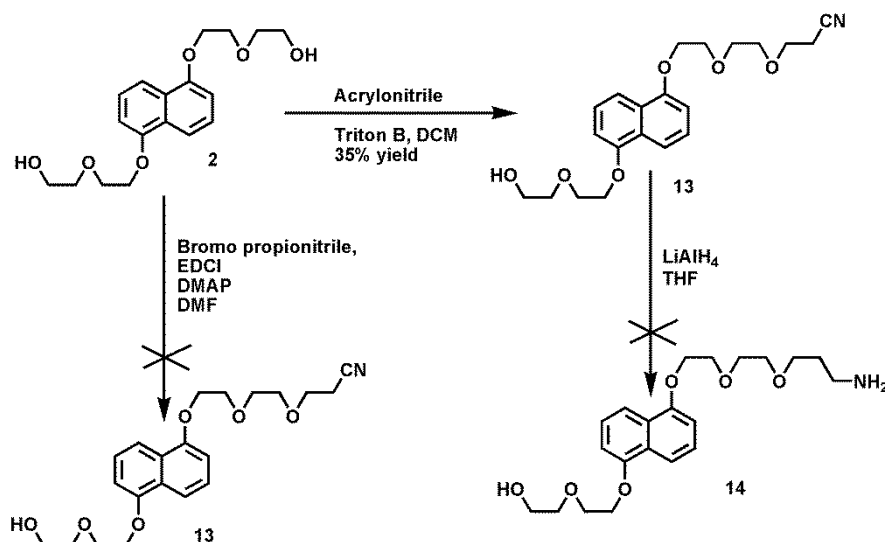
Scheme 2.3. Alkylation of 1,5-Dihydroxynaphthalene.

The first reaction in the synthesis of the possible naphthalene amines, involved the reaction between 1,5-naphthalene diol with 2, 2-(chloroethoxy)ethanol in acetonitrile with potassium carbonate, as shown in Scheme 2.3. The reaction took one week under reflux to complete and gave the dialkylated product in moderate yield. The yield of this reaction varied and was dependent on concentration, where the higher the concentration typically the better the yield. The reaction could be performed on quite a large scale and optimal results were gained on a 20 g scale. This diol (**2**) was the starting material for all the naphthalene based systems described in later chapters.



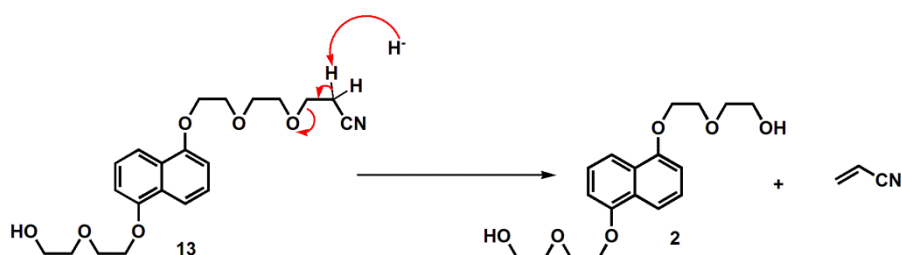
Scheme 2.4. EDCI couplings to the alkylated naphthalene.

EDCI coupling reactions with Fmoc-GABA and 6-amino caproic acid were carried out with diol 2 as shown in Scheme 2.4. The EDCI coupling of 6-amino caproic acid with the alkylated naphthalene in DMF failed to react, even at high temperatures. The EDCI coupling reaction with Fmoc protected 4-aminobutyric acid succeeded in producing the required product; however, we could not remove the EDCI reaction by-product impurities from the required protected amine even after repeated column chromatography. Changing the coupling agent from EDCI to EEDQ had very little effect, such that the quinoline impurities from the reaction continued to contaminate the Fmoc amine, even after repeated column chromatography. The Fmoc protection was chosen as the DIP formation conditions would also deprotect the amine *in situ*.

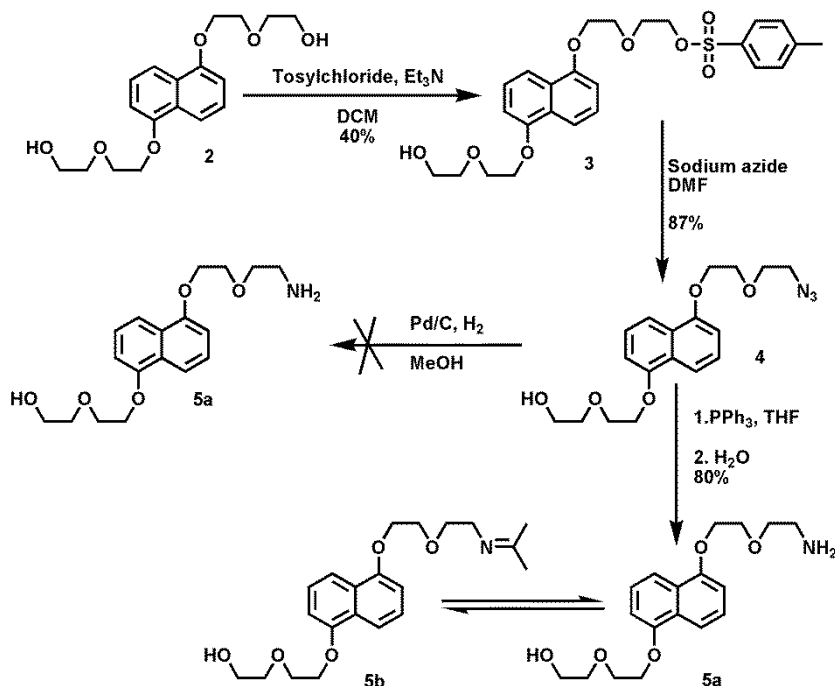


Scheme 2.5. Methods for amine synthesis via nitrile formation.

Attempts to form the naphthalene functionalised amine **14** via nitrile formation were carried out as shown in Scheme 2.5. The reaction with bromopropionitrile in dry DMF to gain the nitrile product, **13** that would then be reduced to the amine in a subsequent step failed react, and the starting material was recovered by column chromatography. The successful addition of propionitrile was achieved by the reaction with acrylonitrile in the presence of base Triton B in DCM.^[83] The addition gave both the mono and di-propionitrile products, where separation by column chromatography to recover the required compound in a 36% yield. Subsequent lithium aluminium hydride reduction failed to yield the required amine and instead gave the retro-Michael reaction product of the starting material **2** quantitatively. It may have been possible to reduce the nitrile with Raney nickel, but due to the pyrophoric nature of the reaction this was viewed purely as a last resort if all other attempts to synthesise an amino-PEG-naphthalene compound failed. The proposed mechanism for the Retro-Michael reaction is shown in Scheme 2.6.



Scheme 2.6. Retro-Michael reaction for the cleavage of the acrylonitrile.



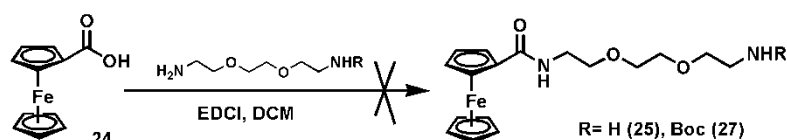
Scheme 2.7. Tosylation reaction scheme.

The treatment of the alkylated diol **2** with tosyl chloride gave a mixture of the monotosylate, (**3a**), ditosylate (**3b**) products, and the starting material in equal proportions. The products were easily separated by column chromatography and the unreacted starting material could also be recovered by this manner. Conversion to the azide (**4**) was successful, where the product was separated from any impurities present by column chromatography, which also removed the last traces of DMF from compound. The full reaction scheme is presented in Scheme 2.7.

Initial reduction of the naphthalene azide **4** with palladium on carbon failed to give either starting material or product. However,

reduction using triphenylphosphine in the Staudinger reaction succeeded in forming the desired product **5a**. However, the column chromatography failed to yield the pure product as observed by proton NMR. Thin layer chromatography showed only one spot, which indicated the presence of an impurity at the same R_f value. The impure product still gained the required DIP functionalisation in high yield which indicated that the impurities did not impede the formation of the DIP reaction, or its purification by precipitation. Closer investigation of the crude mixture from the column chromatography was that the elution solvent of acetone – dichloromethane mixtures with 2% triethylamine was producing the acetone imine form of the amine, and the impurities in the ^1H NMR spectra were as a result of a mixture of the amine and imine forms. The imine produced was fully reversible in the presence of weak acidic conditions, such that chloroform was able to convert it to the amine cleanly with the only bi-product being acetone. Thus, subsequently to avoid the formation of the imine, the solvent used in the chromatography step was changed from acetone-DCM mixtures to methanol-DCM mixtures with good success.

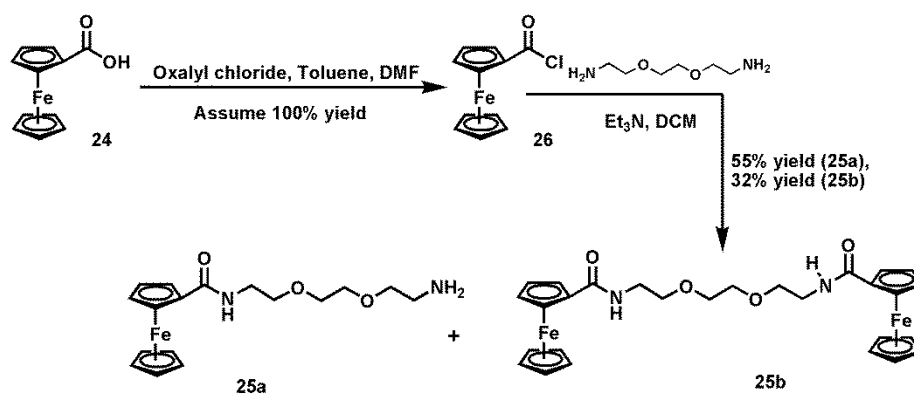
2.3.2 Synthesis of the ferrocene amino derivative **25a**.



Scheme 2.8. EDCI couplings to ferrocene carboxylic acid.

EDCI coupling reactions of amines and carboxylic acids generally afford the required amide in good yields. It was for this reason that we decided upon forming the ferrocene modified amine **25a** from the ferrocene carboxylic acid and 2,2'-(ethylenedioxy)diethylamine.

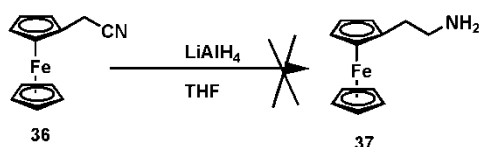
Unfortunately, the standard conditions with DMAP in DCM failed to react in any way. Changing solvent and heating to reflux still had no effect on the reaction. When the non-protected amine failed to react, the aim was then to produce the protected monoamine that would then be deprotected prior to DIP formation. Use of the equivalent Boc-protected amine in the presence of pentafluorophenol in the EDCI couplings also failed to react and the unreacted starting material was recovered by column chromatography. The reaction Scheme 2.8 shows the route attempted for this synthesis.



Scheme 2.9. Amine formation via acid chloride formation.

The formation of the reactive acid chloride (**26**) by treatment of the ferrocene carboxylic acid with oxalyl chloride followed by the subsequent addition to 2, 2'-(ethylenedioxy)diethylamine in DCM gave us the required amine (**25a**) plus the unwanted diferrocenyl compound (**25b**) to varying degrees. The slow addition of the acid chloride to a mixture of the diamine and triethylamine, where the diamine was in excess and at a higher concentration compared to the slowly added acid chloride pushed the ratio of the products made towards the required amine, as shown in Scheme 2.9. By learning the lessons from the naphthalene amine we decided to avoid the acetone when dealing with the amine in order to prevent any chance of imine formation. It was also observed that this compound also oxidised in the air over a period of time as the orange oil became black with time as the amine degraded.

The product was also passed onto Dr C Richmond from Prof L Cronin's group for the subsequent formation of the ferrocene DIP **30** as a dark red / brown solid.



Scheme 2.10 Ferrocene acetonitrile reduction.

As an alternative, where the ferrocene would be attached almost directly to the DIP, we investigated the synthesis of the amine from the ferrocene acetonitrile by lithium aluminium hydride reduction. The reaction performed gave only degradation products, where all the starting material was consumed, but no amine product formed. This attempted conversion is shown in Scheme 2.10.

As the ferrocene DIP (**30**) was not sufficiently soluble in aqueous media, it was expected that the equivalent DIP from the ferrocene amino derivative (**37**) would be even less soluble and so this compound synthesis was not pursued further.

2.3.3 Analysis of the functionalised Dihydro-Imidazo-Phenanthridines.

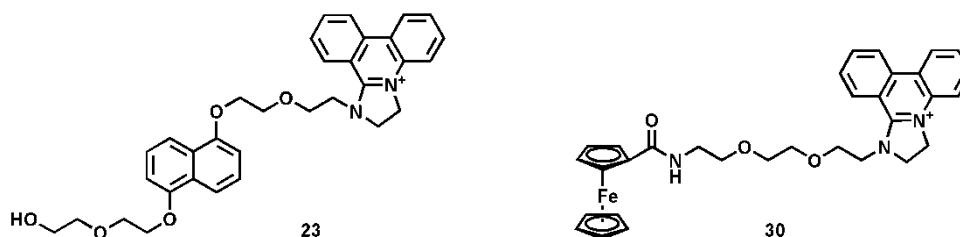
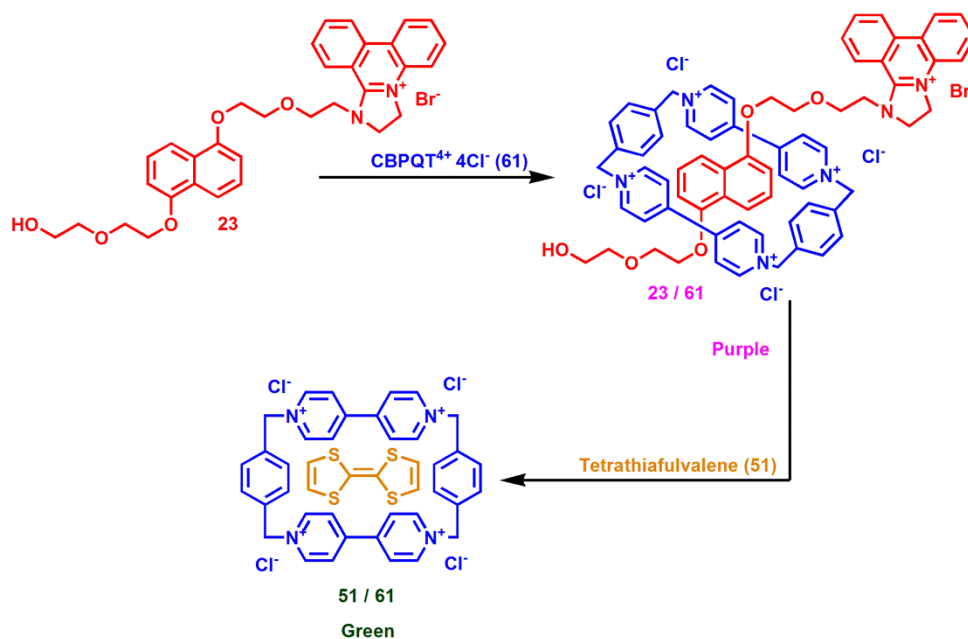


Figure 2.12. Functionalised DIPs **23** and **30**.

The dihydro-imidazo-phenanthridines (DIPs) were synthesised by Dr C. Richmond of Prof L Cronins' group from their respective amines. Appendix 1 contains the experimental conditions used to synthesise these compounds from their amines. These compounds were produced as bromide salts form and were poorly soluble in aqueous media, in particular the ferrocene DIP compound **30**. Salt exchange reactions were attempted on the **23** with a view to increase the solubility in water. The exchange reactions that were carried out had no beneficial effect on the solubility, to the point that the DIP compound became more insoluble in water after salt exchange had been performed. All analysis from then on was carried out with the original bromide salts.

2.3.3.1 UV-Vis Spectroscopy of Naphthalene DIP (**23**) and CBPQT⁴⁺ (**61**).



Scheme 2.11. Nap-DIP complex with CBPQT^{4+} then displacement with TTF.

A UV-Vis experiment in aqueous 1 mM solutions with the **23** and $\text{CBPQT}^{4+} 4\text{Cl}^-$ (**61**) was carried out where the complex formed gave the standard pink solution that is found with naphthalene- CBPQT^{4+} systems indicating that complexation had occurred^[13] [12]. 1-5 equivalents of TTF (**51**) were added to displace the naphthalene from the cavity of the CBPQT^{4+} ; this displacement was observed by a colour change from pink to green. Additional equivalents of TTF intensified the green band observed as more TTF dissolved and full complexation with CBPQT^{4+} occurred. The spectroscopic data gained from this experiment are shown in Figure 2.13.

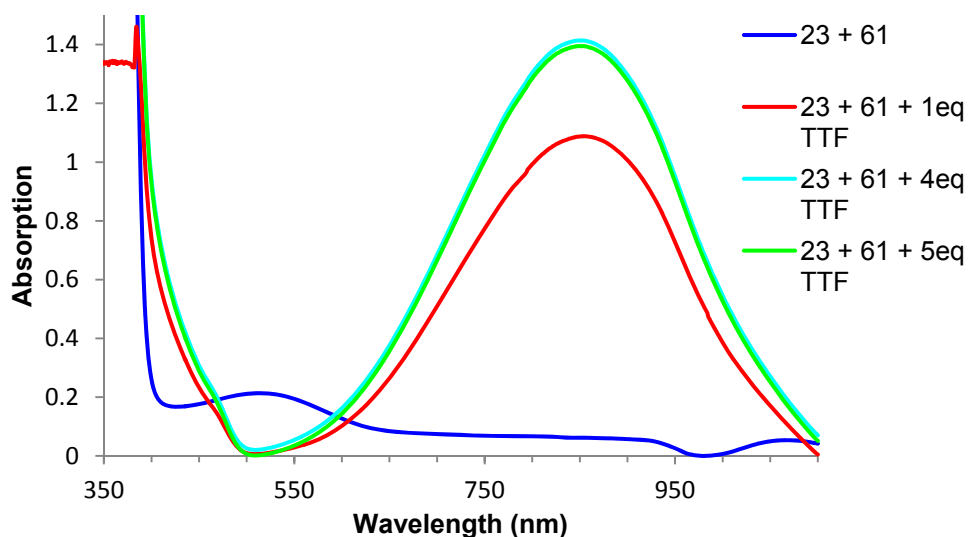


Figure 2.13. UV-Vis data from the complex of 23 and 61 at room temperature with baseline correction. Concentration 10^{-3} M in water.

From Figure 2.13 we can observe that the binding interactions between the CBPQT^{4+} and naphthalene are quite weak when compared to the binding interactions between TTF and CBPQT^{4+} . This is typical of these systems, where the stronger charge transfer interactions between TTF and the cyclophane compared to that of the naphthalene moiety, cause the TTF to competitively displace the naphthalene from the cavity of the cyclophane.^{[12] [84]}

2.3.3.2 ^1H NMR spectroscopic studies.

^1H NMR spectra were recorded in D_2O for the naphthalene functionalised DIP (**23**), and for its complex with CBPQT^{4+} . As the complex formed the typical colour change to dark purple was observed^[13]. The ^1H NMR spectrum recorded for the complex was extremely broad and most of the detail became obscured. In an attempt to regain some of the details that had been obscured, the solution of the complex was diluted by half, but to no avail. The appearance of two broad signals in the region of $\sim 2.45\text{ppm}$ and 2.25ppm are typical of the shift

exhibited by the H_{4/8} protons on the naphthalene group upon inclusion into the core of the CBPQT⁴⁺[14]. The loss of definition and the distinct dark purple colour change upon addition of the CBPQT⁴⁺ also indicates that the pseudo rotaxane had formed. Figure 2.14 shows the spectra recorded at room temperature for the individual compounds **23** and **61** plus the pseudorotaxane complex.

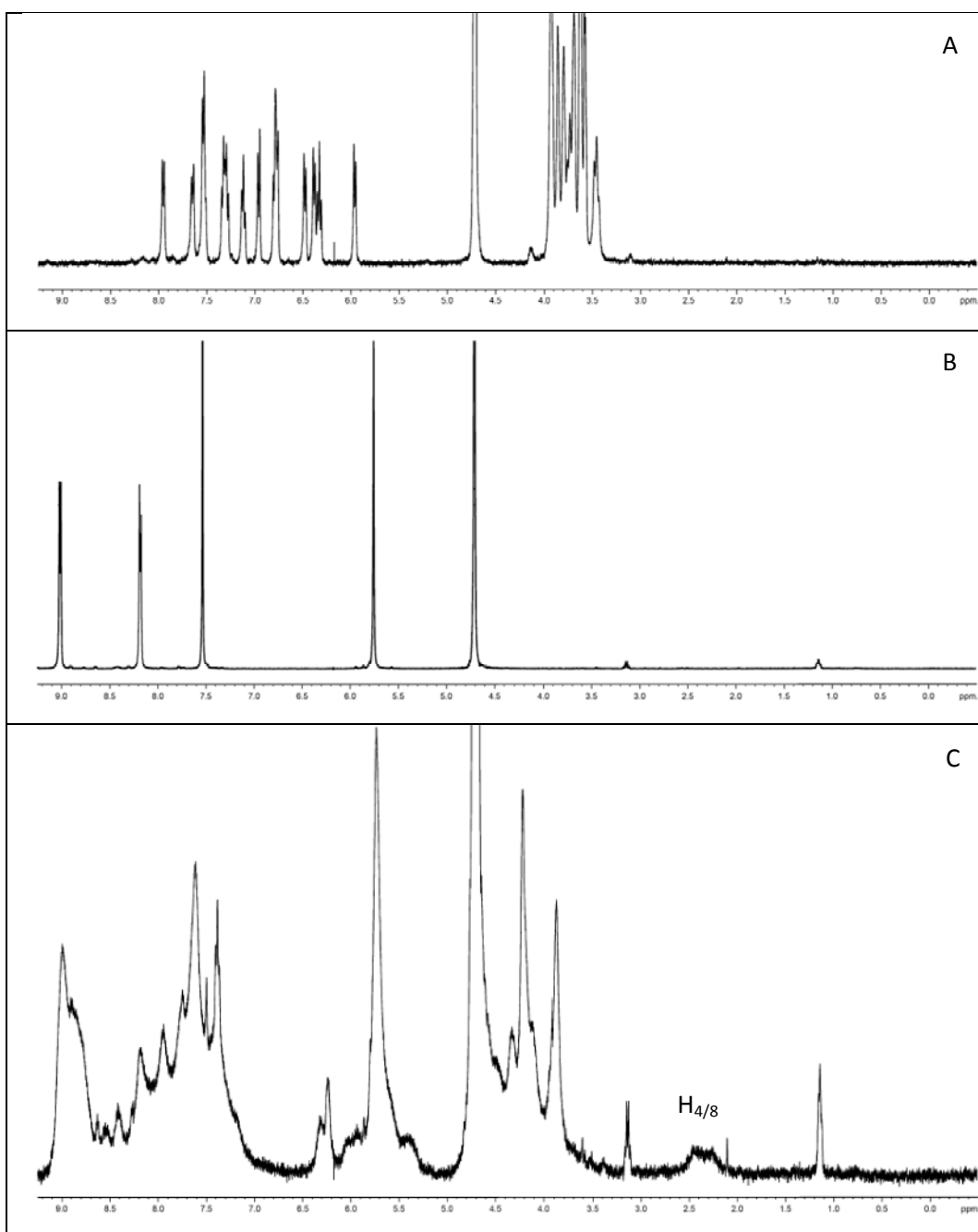


Figure 2.14. ¹H NMR spectra recorded for A) **23** B) **61** C) 1:1 Complex of **23/61** in D₂O.

2.3.4 DNA Interactions with the DIP compounds.

2.3.4.1 ITC experiments with calf thymus DNA.

In order to measure the binding constants for the interaction of the **23** with DNA a number of ITC experiments were carried out using calf thymus DNA (CT-DNA). Later the interactions with **23** and a synthetic duplex D-DNA were carried out. The aqueous solubility of the ferrocene DIP was not sufficient to allow calorimetric experiments to be carried out.

Initially the isothermal titration calorimetry (ITC) experiments were carried out in water. The data collected showed good binding interactions between the **23** compound and CT-DNA. However, the data recorded indicated that **23** did not interact with the CBPQT⁴⁺, which was contradicted by the fact that the solution for these compounds when mixed turned pink, indicating interaction. An added complication was that it appeared that the CBPQT⁴⁺ interacted with the CT-DNA, which contradicted previous experiments that showed no binding. Figure 2.15 shows the data recorded for the experiments for water. The thermodynamic data recorded for this experiment are shown below in Table 2.4.

	<i>N</i>	<i>K_a</i> (M ⁻¹)	ΔH (cal mol ⁻¹)	ΔS (cal mol ⁻¹ K ⁻¹)
23 into CT	1.47 ± 0.02	3.76 x10 ⁵ ± 6.75 x10 ⁴	-6259 ± 140.5	4.52
CBPQT into 23 /CT	0.31 ± 0.01	7.34 x10 ⁶ ± 3.58 x10 ⁶	5026 ± 185.8	48.27
CBPQT into CT	0.36 ± 0.01	3.49 x10 ⁸ ± 6.58 x10 ⁸	-5088 ± 174.2	22.02

Table 2.4. Thermodynamic data recorded for ITC titrations in water.

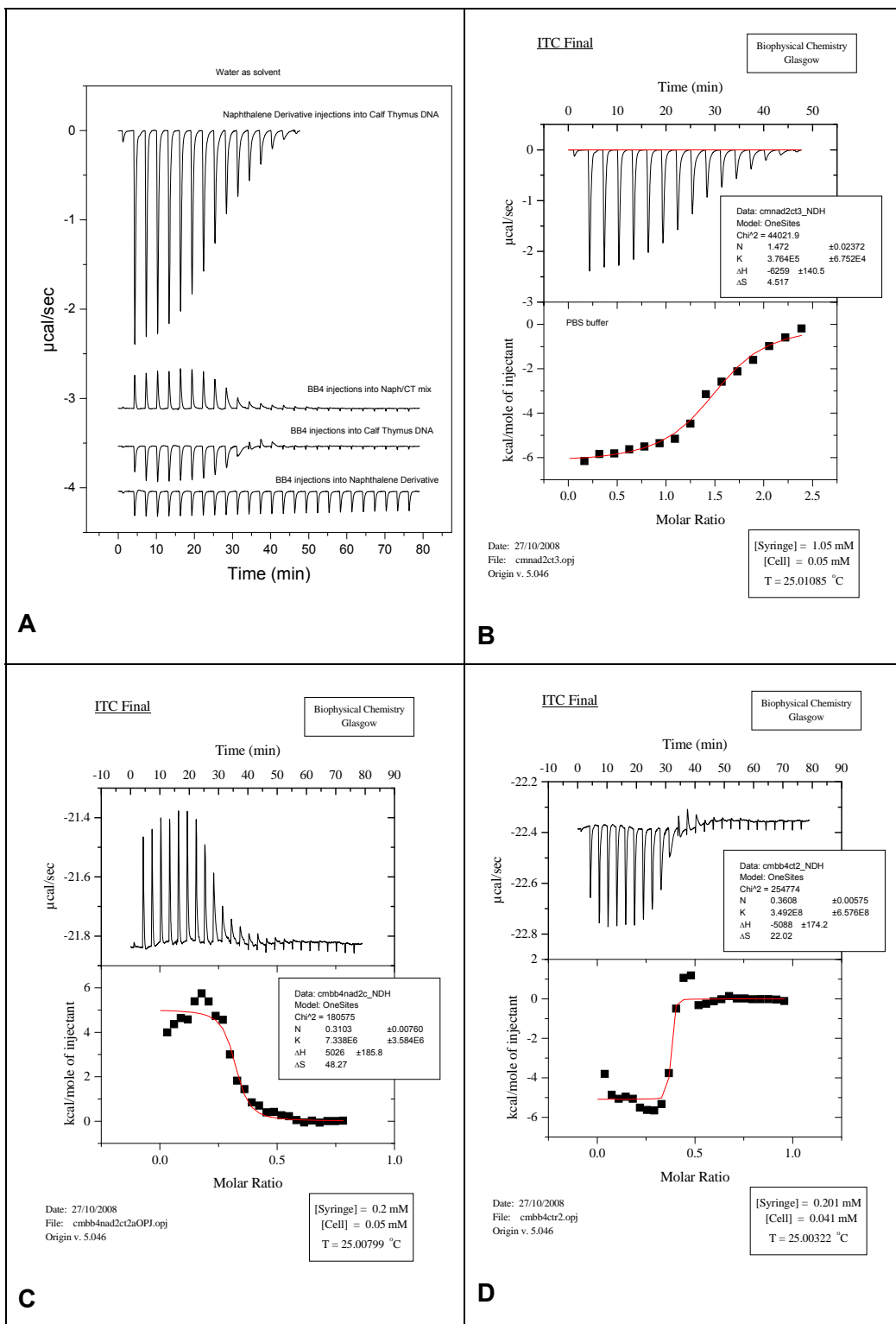


Figure 2.15. ITC data for experiment with water as the solvent. A) is the raw data recorded. B) is analysed DIP injected into CT-DNA. C) is CBPQT injected into DIP/CT-DNA. D) is CBPQT injected into CT-DNA.

It was then proposed that the exotherms were not binding interactions and were heats of neutralisation, where the different pH of

the solutions mixed and gave the temperatures that appeared to binding interactions rather than the thermal neutralisation artefacts that they potentially were. The pH of each solution was measured in order to confirm or negate the probability that the thermal signals observed were purely neutralisations. As can be seen from Table 2.5, the pH differences were such that the results could not be explained purely by acid base neutralisation.

Component	pH of solution
CT-DNA	5.70-6.20
Naphthalene DIP 23	6.20
CBPQT ⁴⁺ 4Cl ⁻ 61	5.10

Table 2.5. pH of the aqueous solutions used.

In order to avoid the neutralisation interactions, experiments were then carried out in phosphate buffered saline (PBS) at pH 7.0. The changing of solvent to PBS added its own set of complications, namely that compound **23** was poorly soluble in this media, so that suspensions of the DIP had to be used and actual concentrations used for the experiments could not be accurately measured. This set of experiments showed the standard binding interactions for naphthalene and CBPQT⁴⁺. The solubility of the compound **23** in PBS was very low and there appeared to be very little binding interaction with CT-DNA. This lack of binding may have been due to the lack of solubility of the DIP in the PBS. The titration of CBPQT⁴⁺ into CT-DNA showed only dilution effects, indicating that there was no binding to CT-DNA occurring. Addition of CBPQT⁴⁺ to the **23** / CT-DNA mixture showed a diminished binding interaction which would indicate a partial blocking of the naphthalene group to threading into the CBPQT⁴⁺ cavity when compared to the titration data recorded for the experiment without the CT-DNA present. The data recorded are shown in Figure 2.16 with the thermodynamic data recorded shown in Table 2.6.

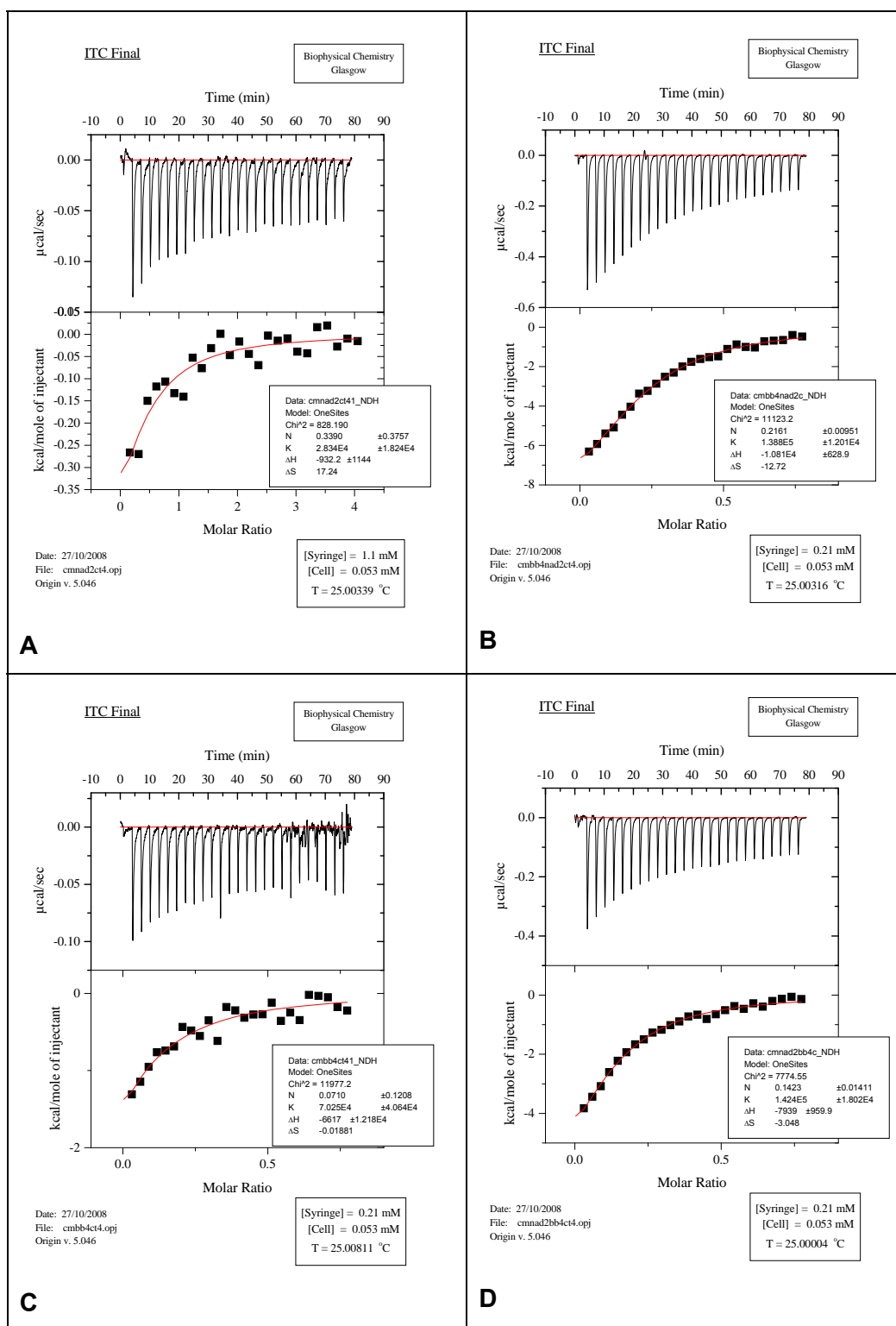


Figure 2.16. The ITC data for 23 with CT-DNA in PBS. A 23 into CT-DNA. B CBPQT into 23/CT-DNA. C CBPQT into CT-DNA. D 23 into CBPQT/CT-DNA.

	23 into CT	61 into CT
<i>N</i>	0.34 ± 0.37	0.07 ± 0.12
K_a (M ⁻¹)	2.83 x10 ⁴ ± 1.82 x10 ⁴	7.03 x10 ⁴ ± 4.06 x10 ⁴
ΔH (cal mol ⁻¹)	-932.2 ± 1144	-6617 ± 1.22 x10 ⁴
ΔS (cal mol ⁻¹ K ⁻¹)	17.24	-0.02
	61 into 23/CT	23 into 61/CT
<i>N</i>	0.22 ± 0.01	0.14 ± 0.01
K_a (M ⁻¹)	1.39 x10 ⁵ ± 1.20 x10 ⁴	1.42 x10 ⁵ ± 1.80 x10 ⁴
ΔH (cal mol ⁻¹)	-1.08 x10 ⁴ ± 628.9	-7939 ± 959.9
ΔS (cal mol ⁻¹ K ⁻¹)	-12.72	-3.05

Table 2.6. Thermodynamic data recorded for ITC titration experiments in PBS

An added complication of the **23** was that the solutions tended to precipitate over a period of a few hours such that the solutions could not be prepared in advance and had to be made fresh directly before use. This issue was especially prevalent in the PBS solutions. In an attempt to improve the solubility of compound **23** in solution the ITC experiments were run in phosphate buffer at pH = 7.0 with no salt added. The observed results from these experiments were extremely complicated and no interaction with CT-DNA occurred for the first 17 injections and then interaction for the remaining 12. Subsequent addition of CBPQT⁴⁺ to this mixture also gave a complicated response where there appeared to be up to three different interactions occurring. The data collected could not be fitted to any data sets.

The effect of the buffer used was then probed further by the use 3-(*N*-morpholino) propanesulfonic acid (MOPS) at pH = 7.3. The data recorded for this were highly complicated to the point that graphs could not be fitted to any data set. The interactions observed between Nap-DIP and CT-DNA was extended and suggested multiple interactions occurring stepwise that could not be fully elucidated. The interaction of CBPQT⁴⁺ with the mixtures followed a similar path to the interactions seen in the experiments in phosphate, which would indicate that the naphthalene was

in more than one environment. At this point the experiments with unbuffered water were repeated with no change in the results for the aqueous experiments. This indicated that the results for the MOPS and phosphate were not due to the experimental method and were due to complications with the substrates used. The concentrations used for the three sets of experiments are shown below in Table 2.7. The raw data results for phosphate, MOPS, and water are shown in Figure 2.17.

Solvent	Concentration of:		
	23	Calf Thymus	61
Phosphate	1.15mM	50 μ M	1.09mM
MOPs	1.08mM	50 μ M	1.00mM
Water	0.91mM	50 μ M	1.09mM

Table 2.7. Solvent vs concentration of component.

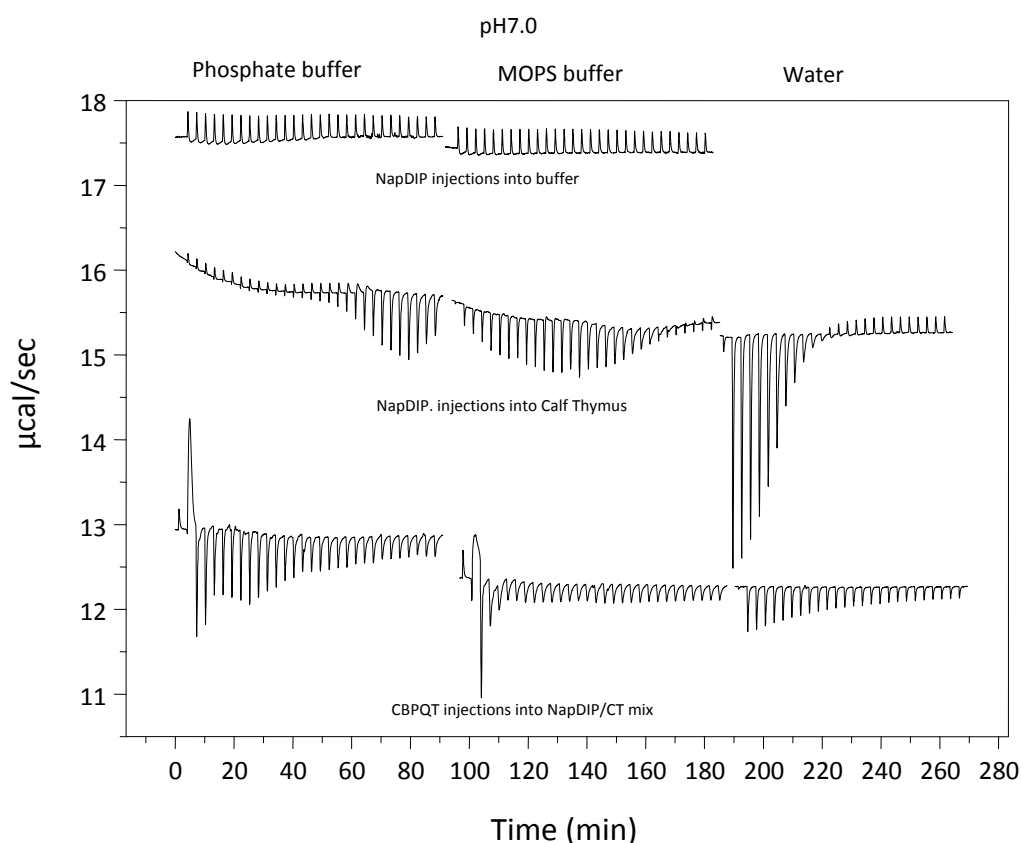


Figure 2.17. The raw ITC data recorded for Phosphate, MOPS, and Water.

A final set of experiments with CT-DNA in 20 mM piperazine-1,4-bis(2-ethanesulfonic acid) (PIPES) buffer were carried out in an attempt to elucidate the binding interactions. The results showed very little interaction between the **23** and the CT-DNA. By titrating the pseudorotaxane of the CBPQT and **23** into CT-DNA, a binding curve was observed that incorporated the dissociation of the pseudorotaxane and binding to the CT-DNA. Titration of the complex into the PIPES buffer gave a good dissociation curve that was almost a perfect reflection of the titration of CBPQT into **23** /CT-DNA mix. The raw data can be seen in Figure 2.18.

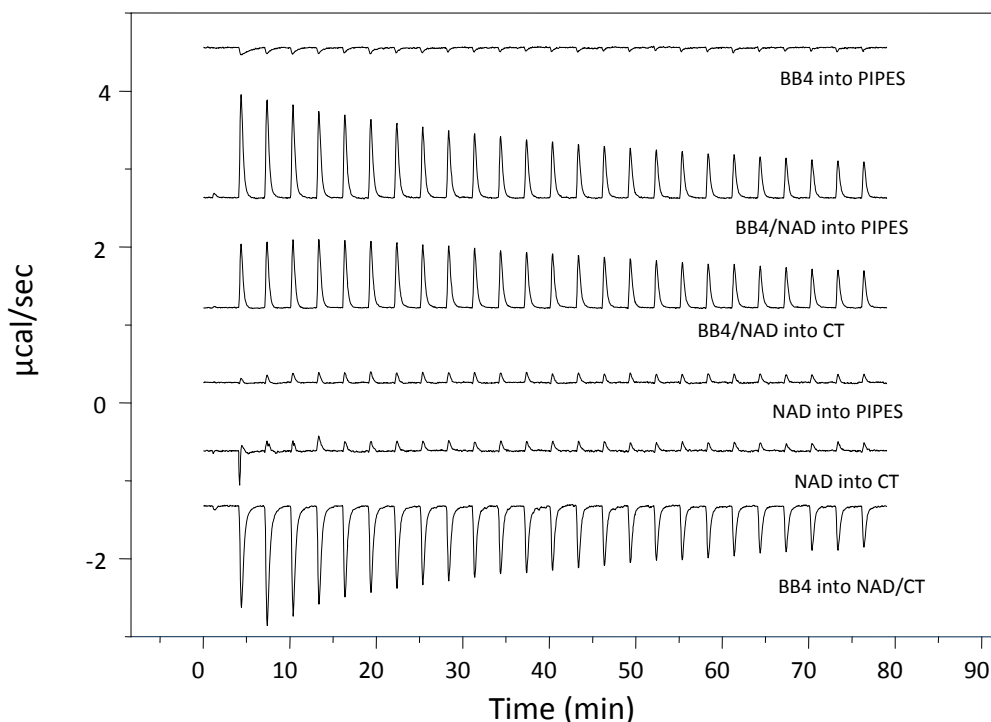


Figure 2.18. Raw ITC data for experiments ran in PIPES buffer.

2.3.4.2 ITC experiments with a synthetic dodecamer DNA.

Experiments with the synthetic ‘Dickerson’ dodecamer DNA in 20 mM phosphate buffer were carried out. This DNA sequence is known to form hairpin conformations and so perform the same interactions with the DIP as natural DNA.^[85] The synthetic dodecamer DNA (D-DNA) was annealed repeatedly prior to use by rapid heating to 80°C, allowing the material then to cool slowly. Once cool the DNA was reheated to 85 °C then allowed to cool. The process was repeated three times per sample of the D-DNA. From the absorption at $\lambda = 260$ nm, where the extinction coefficient ϵ_c was taken as 12828 per base pair,^[77] the concentration of the D-DNA of the solutions could be measured, where the number of base pairs per molecule was 12. Equation 2.1 shows the formula used to calculate the concentration of D-DNA in a solution.

$$Conc = \frac{A_{260}}{12 * 12828}$$

Equation 2.18. Formula for calculating the concentration of the D-DNA from the absorption at 260nm.

Table 2.8 shows the details of each ITC experiment carried out. Figure 2.19 shows the raw results of the experiments. Figure 2.20 contains the analysed data from the ITC. The interaction between **23** and the D-DNA was weak, however the curve could be fitted to a single set of sites binding model. The result of CBPQT into the D-DNA gave a very weak binding curve that would indicate that there is a very slight interaction. The pre-formed complex gave a complex strong binding interaction that could not be fitted to a single set of sites, but a sequential set of sites binding model. It may be that the pseudorotaxane was aiding in the solvation of the **23** leading to a greater interaction with the D-DNA. There may have also been an additional interaction with any uncomplexed naphthalene DIP **23** with the D-DNA, leading to the additional binding site. Other possibilities include the unwinding of the DNA allowing additional binding to occur after initial insertion. The thermodynamic data gathered from the analysed ITC data is given in Table 2.9.

Experiment No.	Contents of Cell	Contents of Syringe
1	Phosphate buffer	CBPQT ⁴⁺ 0.93 mM
2	D-DNA 30 µM	CBPQT ⁴⁺ 0.93 mM
3	D-DNA 30 µM	Nap DIP 1.01 mM
4	D-DNA / Nap DIP	CBPQT ⁴⁺ 0.93 mM
5	Phosphate buffer	Nap DIP/CBPQT ⁴⁺ 1 mM
6	D-DNA 30 µM	Nap DIP/CBPQT ⁴⁺ 1 mM

Table 2.8. Experimental details of the 23 and CBPQT⁴⁺ with D-DNA.

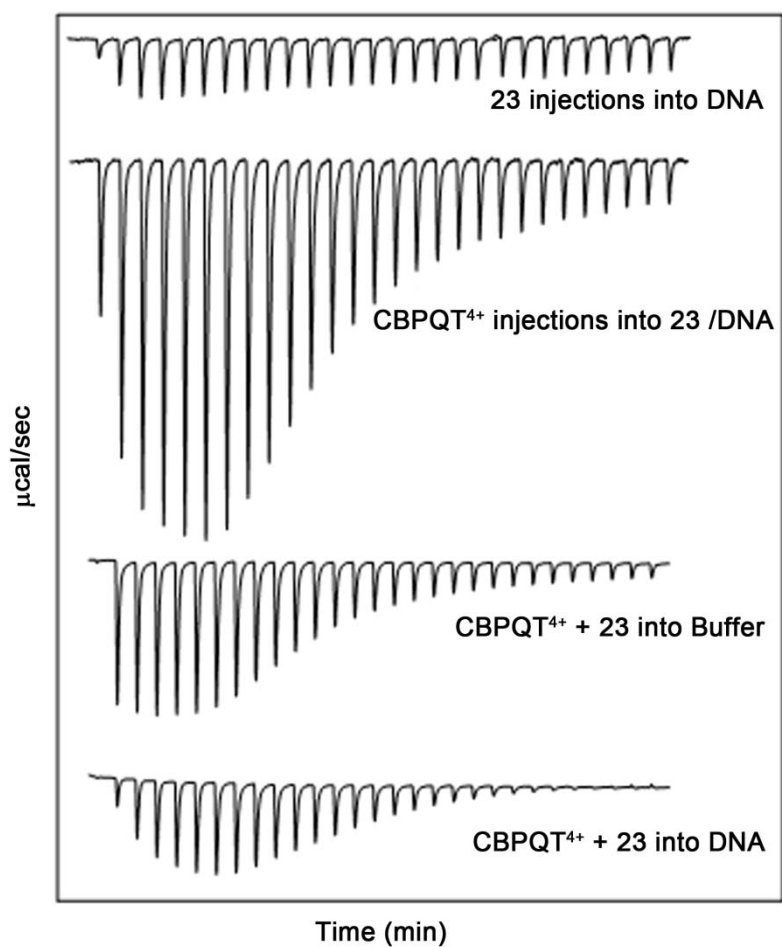


Figure 2.19. Raw ITC data of 23 and CBPQT⁴⁺ with D-DNA.

Ligand	<i>N</i>	<i>K_a</i> (M ⁻¹)	Δ <i>H</i> (cal/ mol)	Δ <i>S</i> (cal K ⁻¹ mol ⁻¹)
23	2.02 ± 0.323	1.88 × 10 ⁴ ± 4125	-1948 ± 416.1	13.03
CBPQT	1.76 ± 0.1018	9.51 × 10 ⁵ ± 7.50 × 10 ⁵	863.7 ± 77.53	30.25
23 / CBPQT	N/A	1.0 × 10 ⁵ ± 1.42 × 10 ⁴	-1015 ± 271.3	19.48
	N/A	4.40 × 10 ⁴ ± 2503	-3.52 × 10 ⁴ ± 467	-96.90

Table 2.9. Thermodynamic data recorded for the interaction between 23, CBPQT⁴⁺ and D-DNA.

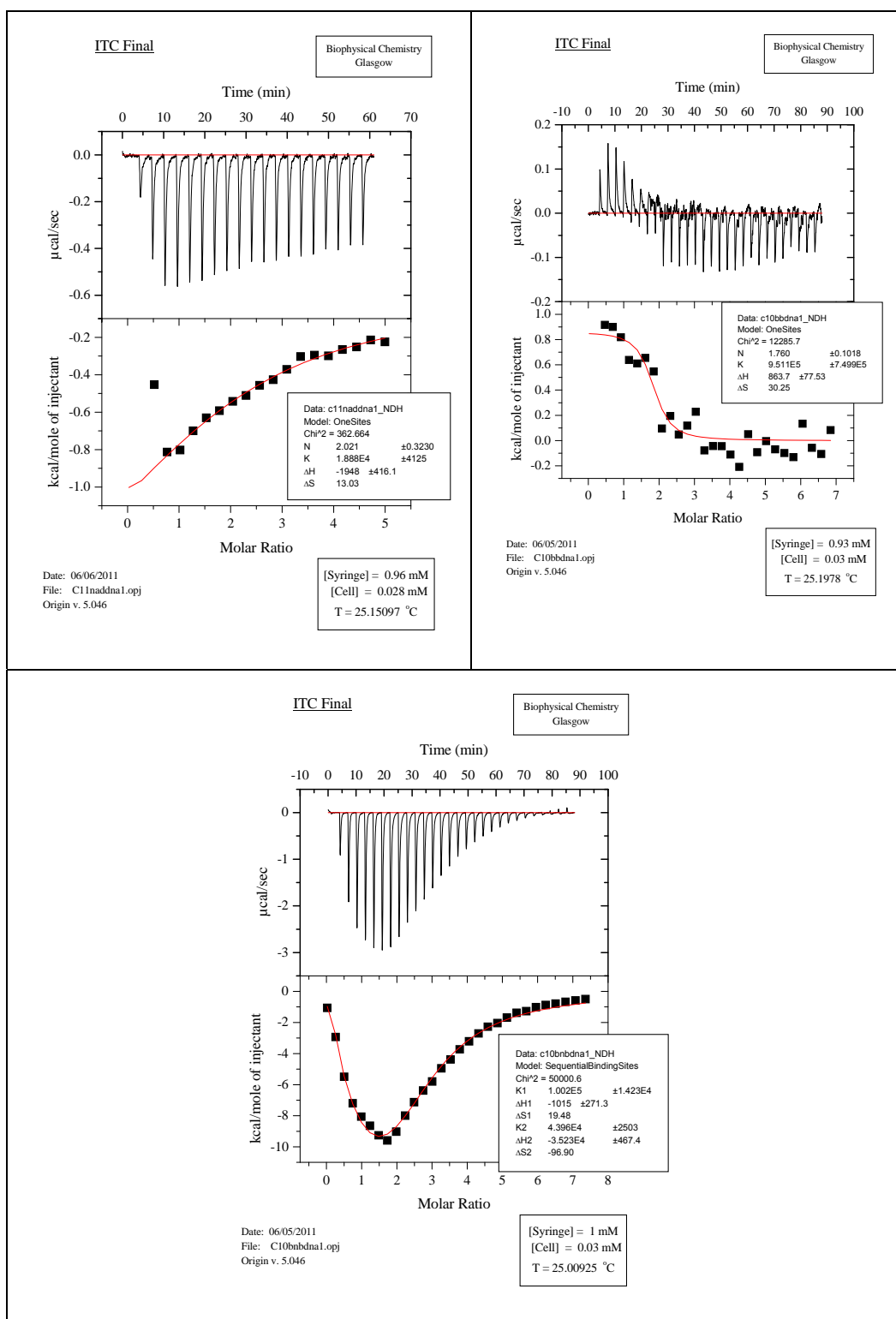


Figure 2.20. Analysed ITC experiments with D-DNA. A) 23 into D-DNA. B) CBPQT⁴⁺ into D-DNA. C) 23 /CBPQT⁴⁺ into D-DNA.

2.3.5 Cell Culture Studies.

2.3.5.1 Cell Injection studies.

The principle for the cell injection studies was that we wished to form complexes with our substrates within living cells, where the two components were injected separately and the complexation would be monitored by both fluorescence and by observing a visible colour change.^[86] The cells used for these experiments were Madin-Darby canine kidney epithelial cells (MDCK).

The primary substrate that we wished to investigate was the naphthalene trimethylammonium bromide compound **9** shown in Figure 2.21. The reasoning for using this substrate was that this molecule has a strong fluorescence excitation at $\lambda = 295 \text{ nm}$ ^{[87] [88] [14]} that can be quenched by CBPQT⁴⁺.^{[87] [88] [14]} In addition to the changes in fluorescence, the complex is also strongly coloured. A further aspect was that it was hoped to be fairly non-toxic to the cells.^{[89] [90]} The fluorescence spectra of the naphthalene trimethylammonium bromide and its complex with CBPQT⁴⁺·4Cl⁻ are shown in Figure 2.22. This compound will be described in greater detail in §5.3.1

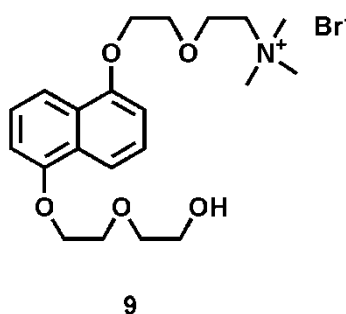


Figure 2.21 Naphthalene trimethylammonium bromide (9).

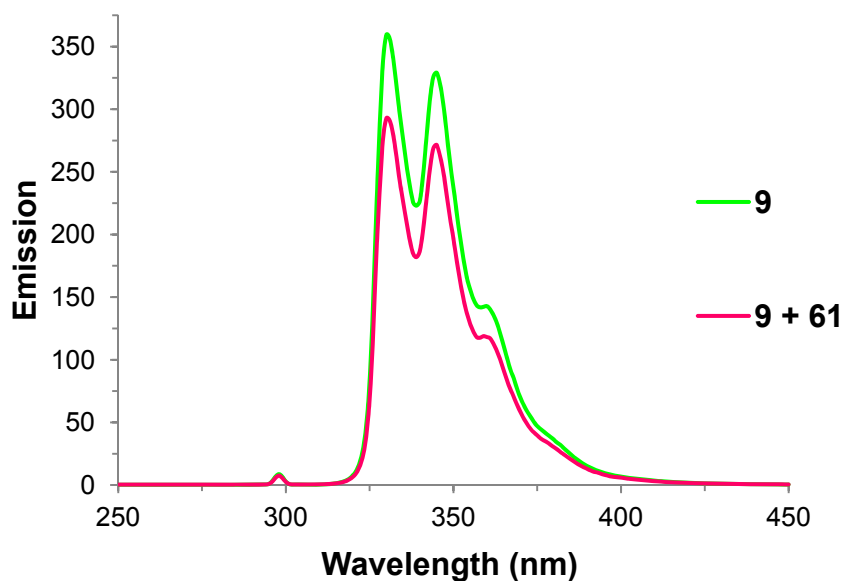


Figure 2.22 Fluorescence of Naphthalene trimethylammonium bromide with CBPQT⁴⁺ (61)
Ex = 295nm at room temperature. 10⁻⁵ M in water

It was at this point that it was noted that the naphthalene trimethylammonium bromide did not fluoresce at the required wavelength for the microscope. It was found that the operational wavelengths of the microscope were excitation $\lambda = 365$ nm and emission from 420 nm. At this point we then looked at the DIP compounds as these substrates contain the phenanthridine moiety that is highly fluorescent and its derivatives fluoresce under the conditions used with the microscope. The fluorescence measurements for **23** with CBPQT⁴⁺.4Cl⁻ are shown in Figure 2.23.

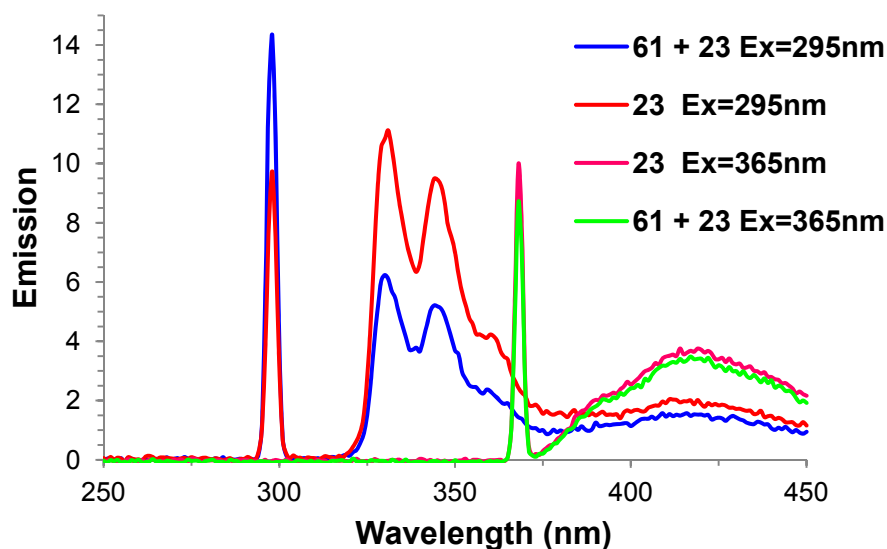


Figure 2.23. Fluorescence of **23** with and without CBPQT⁴⁺ at room temperature. Excitation wavelengths of 295 nm and 365 nm. Concentration 10^{-5} M in water.

The fluorescence of the ferrocene DIP **30** with cyclodextrin was also measured to compare intensities with the spectra of **23**. As can be observed in Figure 2.24 compound **30** had a stronger signal intensity relative to that of the naphthalene compound at excitation λ of 365 nm. The complex with β -cyclodextrin (**63**) also gave a more significant drop in intensity compared to the changes given with **23** and CBPQT⁴⁺ (**61**).

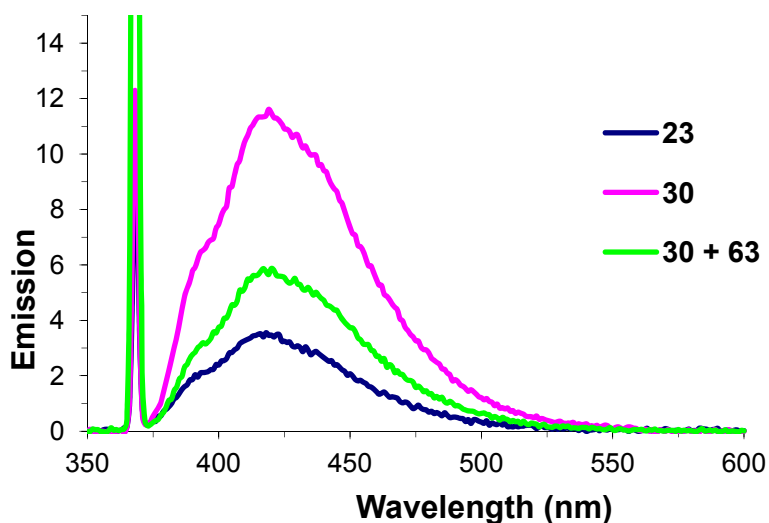


Figure 2.24. Fluorescence of **30** with **63** compared to **23**. Ex 365 nm. 10^{-5} M in water at 25°C.

Although the compound **30** had improved fluorescence characteristics; the improved solubility of the naphthalene substrate, with its ability to form coloured complexes with CBPQT⁴⁺ was chosen for use in the initial cell injection work. It was thought that time permitting, once the procedure and monitoring of the fluorescence was optimised, we would then move onto work with substrate **30** and its complex with β -cyclodextrin.

The MDCK cells were seeded onto glass coverslips with a diameter of 3 cm at a cell density of ~5000 cells/ml. The cells were grown for three days to reach the required level of confluence. Solutions of **23** were made up at a concentration of 10^{-3} M, 10^{-4} M, and 10^{-5} M in 100 mM PIPES buffer with 0.1 mM MgCl₂ at pH 6.5. Microlitre volumes of the solutions were added to a capillary sealed at one end and centrifuged in order to remove any particulates that may have been in solution. Up to 5.0 μ l of the spun solutions were then transferred into the micro-syringe for injection into the cells. An illustration of the syringe is shown in Figure 2.25.

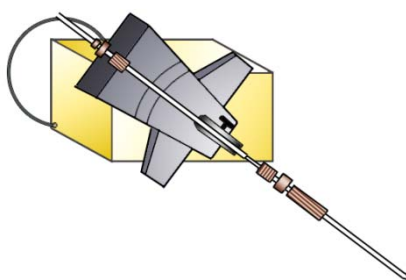


Figure 2.25 Illustration of the micro-syringe within its holder.

The syringe was positioned at a set level above the cells called the search plane. Once the required cell is in the correct position underneath the needle, the needle is inserted into the cell and a small amount of the solution is injected into the cell. After injection the syringe moves back to its position on the search plane. Injection of the solution is controlled by an application of air pressure to the needle capillary which causes the

fluid to leave the needle. The amount of pressure applied can be modulated and the injection time can be varied in which the length of time the pressure is applied for. This in turn will allow control over the volumes of liquid released per injection. This is illustrated in Figure 2.26 and Figure 2.27.

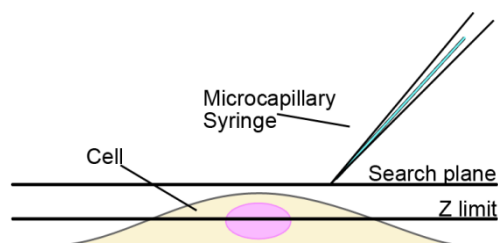


Figure 2.26. Illustration of Syringe at search plane over a cell.

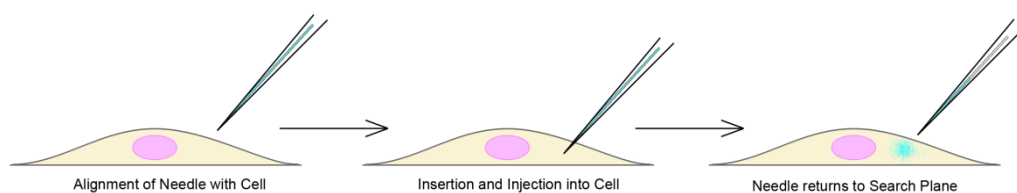


Figure 2.27. Illustration of the movement of the needle from the search plane to cell injection then return to search plane.

Upon injection of the 10^{-3} M solution of **23** into the MDCK cells it was found that the DIP was, as expected cytotoxic and cells rapidly died when the DIP was injected directly into the nucleus. This would indicate that the DIP's cytotoxicity is by the interaction with DNA, most likely by the same intercalation pathway exhibited by other phenanthridine based compounds.^[76]

Further optimisation in order to investigate the minimum concentration required to kill and to observe the changes by the addition of CBPQT⁴⁺ to the **23** to the cells was planned. However, the microscope developed a fault that meant that it could not be used and so this work could not be carried out.

From the initial work we observed that the DIP, when it entered the cell, killed the cell fairly rapidly. From this work we decided to investigate how cytotoxic these compounds were when present in the growth medium, and whether the DIPs could pass the cell membrane, and so kill the cells.

2.3.2.5.2 Cell toxicity studies.

As there is precedent for these compounds to be cytotoxic to cell culture, as exemplified with the cell injection studies, several live/dead and cell viability experiments were carried out using the MDCK cell line and the DIP compounds. Varying volumes of 0.5mM solutions of the **23** (Nap DIP) and **30** (Fc DIP) in 1:1 ratios of water: DMEM were added to cells seeded into a 24 well plate (~5000 cells/ml) and allowed to grow for one week ahead of treatment with the DIP compounds. The cells were incubated with the DIPs for 24 hours. The volumes and resulting concentrations of DIP in each set of wells is shown in Table 2.10 Each concentration was run in a minimum of triplicate per experiment.

DIP Volume Added	Effective Concentration of DIP
0 ml	0 M
2 μ l	0.99 μ M
20 μ l	9.8 μ M
200 μ l	83 μ M
1 ml	0.5 mM

Table 2.10. Concentrations of DIP treatment from volumes of 0.5 mM DIP to 1 ml wells.

The medium containing the DIPs was removed and the cells were carefully washed with PBS (2x1 mL). Live / Dead stain was added to the wells with incubation for 30 minutes. The cells were then fixed and stored

in PBS, prior to investigation under the microscope. The Live/ Dead stain contained propidium iodide and Hoechst 33342. The propidium iodide, is an intercalating agent that fluoresces red when bound to DNA and cannot penetrate the cell membrane of living cells, but will freely enter the cells where the membrane is damaged and the cell is dead. Hoechst 33342 is a groove binding fluorescent agent that can penetrate the cell membrane and will stain the nucleus of these cells blue. The structures of these molecules are shown in Figure 2.28.

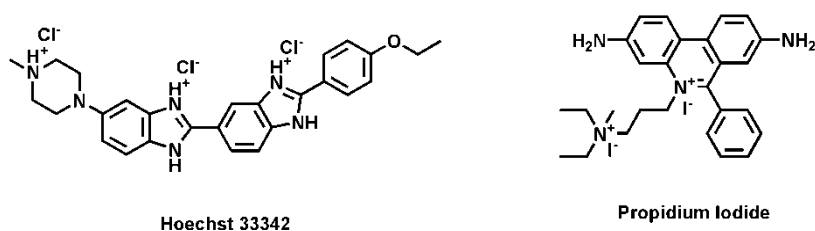


Figure 2.28. Live/Dead Stain Components: Hoechst 33342 and propidium iodide.

From these experiments we found that there had been no significant cell death and indeed there did not appear to be any insertion of the DIP compounds by the lack of fluorescence before the application of the Live/ Dead stain. Later experiments were carried out after 2 days of incubation from seeding. The concentrations used for this set of experiments were 0 M, 9.8 μ M, and 83 μ M, with each set of concentrations applied to 4 wells each. Again there appeared to be no cell death after 24 hours as there showed no red staining observed until a sample was treated with methanol for 5 minutes and re-stained with Live / Dead, whereby the red stain was observed predominately, showing that there was no issue with the staining and the cells were still alive after 24 hours of exposure to the DIPs. Representative images of each set of samples are shown in Figure 2.29.

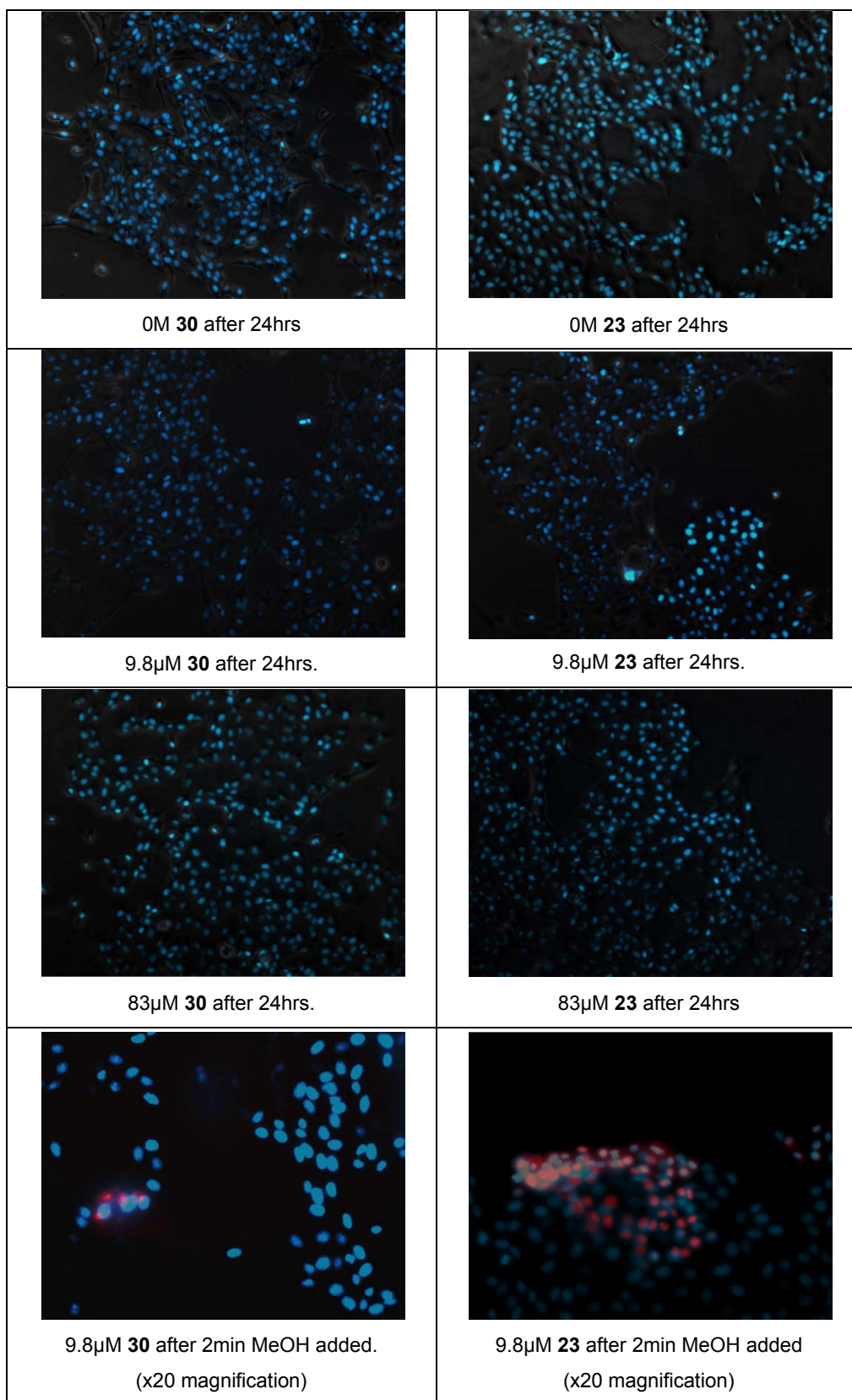


Figure 2.29. Live Dead stained cells after treatment with **23** and **30**. Blue the nuclei of stained Live cells stained with Hoechst 33342 and red are the nuclei of dead cells stained with propidium iodide. 10x optical zoom magnification.

Although the DIPs were clearly not cytotoxic by the Live/Dead staining, the effects on growth of the cells were investigated using MTT staining experiments. Alongside the MTT experiments, further Live/Dead experiments were carried out in parallel. Results of the Live Dead stain for each set of substrates are shown below in Figure 2.30.

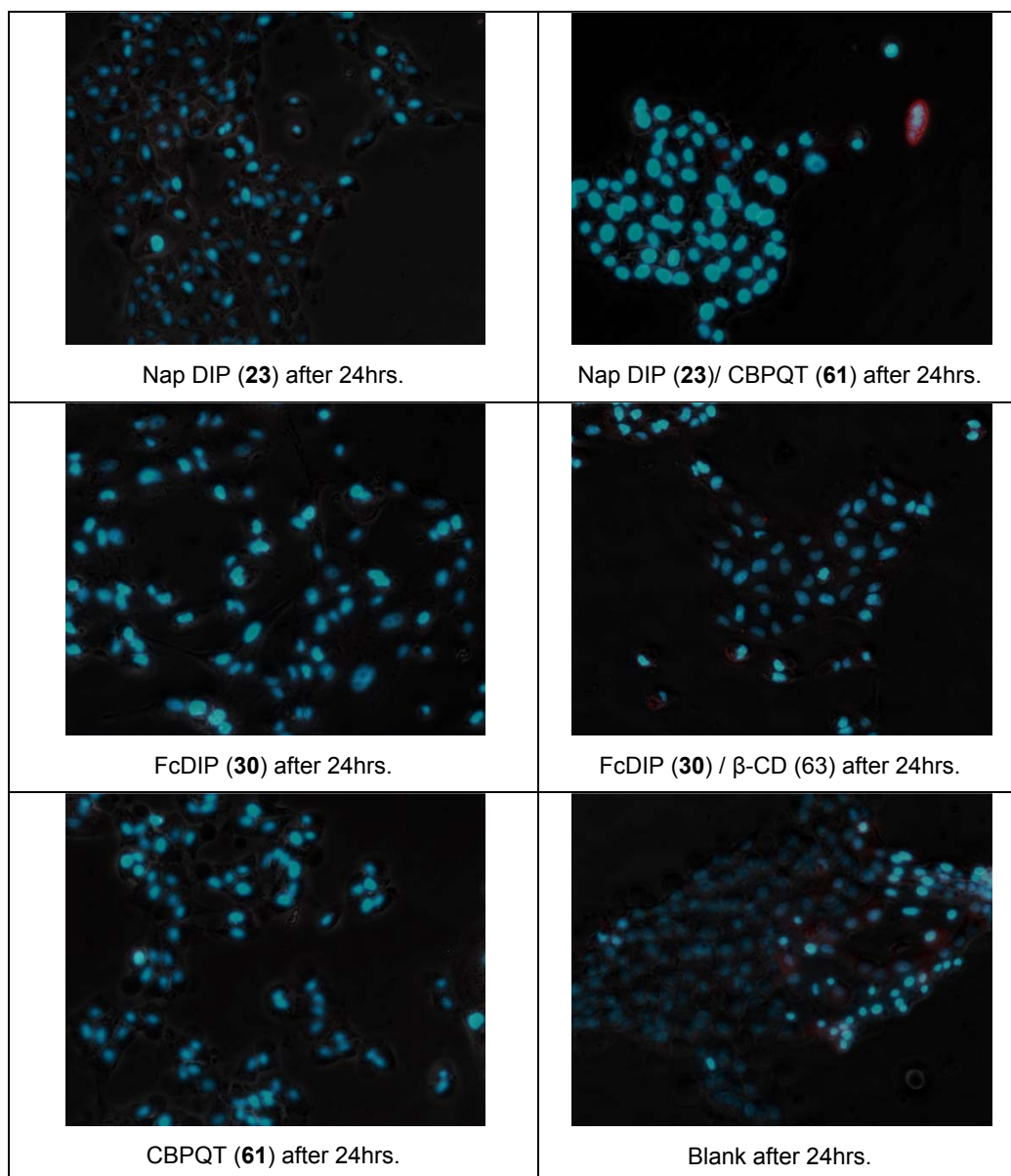


Figure 2.30. Live Dead stained cells after treatment with DIP substrates. Blue the nuclei of stained Live cells stained with Hoechst 33342 and red are the nuclei of dead cells stained with Propidium Iodide. 10x magnification.

The MTT agent used was thiazoyl blue tetrazolium bromide. This compound is metabolised by the mitochondria of living viable cells. Upon metabolism, the purple formazan salt is formed, and the culture goes from yellow to blue / purple, where the intensity of the colour can be correlated to the viability of the cell culture. Structures of the thiazoyl blue tetrazolium bromide and its metabolite are shown below in Figure 2.31.

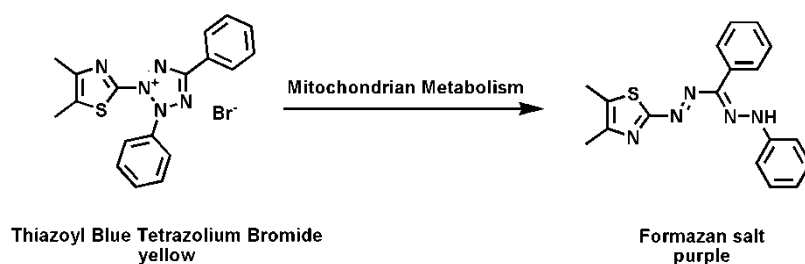


Figure 2.31. MTT staining agent and its metabolite.

The cells were cultured for 3 days to grow to a suitable level of confluence after seeding at a general cell density of 5000 cells/ml. After this time, 200 μl of a 0.5 mM solution (0.083 mM overall) of the required treatment material was added. Table 2.11 shows the treatment material and the label used to denote it.

Treatment Material	Treatment Label
Naphthalene DIP 23	N
23 / CBPQT ⁴⁺ .4Cl ⁻ (200 μl of 1:1 complex)	NB
CBPQT ⁴⁺ .4Cl ⁻	B
Ferrocene DIP 30	F
30 / β -Cyclodextrin (200 μl of 1:1 complex)	FC
Blank (Reverse Osmosis distilled water 200 μl)	X

Table 2.11. MTT treatment materials with the letters denoting treatment label.

The solutions were added to the 1 ml fresh growth media present in the well. The cells were then incubated with the solutions for 24 hours. The media was then removed and the cells washed with PBS (2x 1 ml). The MTT (300 μ l/ well) solution was then added and the cells were incubated for 1.5 hours in the dark. After this time the MTT was removed and warmed DMSO (150 μ l) was added to the cells and left to react for ten minutes. The cell–DMSO mixtures were then transferred into a 96 well plate. The plate was then read by a DYNATECH MR700 $\lambda = 550$ nm to yield the results. X_{AV} denotes the average reading for a particular treatment material.

$$\text{Viability is calculated using } \frac{X_{Av}}{Blank_{Av}} \times 100$$

Each set of solutions per experiment was carried out 4 times in a 24 well plate. The array positions for the 24 well plate is shown below in Figure 2.32 Experiments with the 96 well plate were carried out where the location of each treatment solution was placed in an array as shown in Figure 2.33.



Figure 2.32. Layout of the DIP treatments for MTT in 24 well plate.

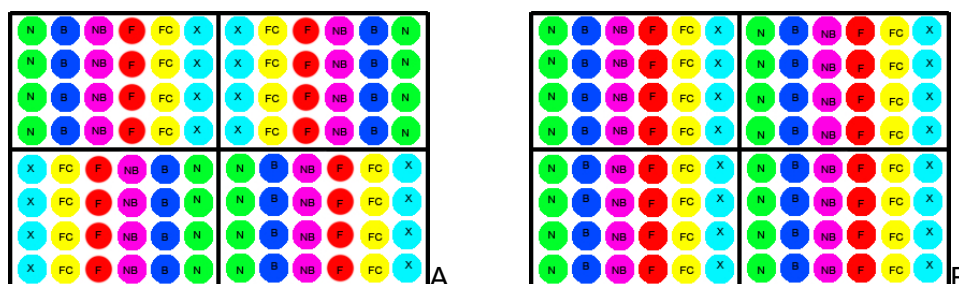


Figure 2.33. Layout of the DIP treatments for MTT in 96 well plates A and B.

Average %age viabilities for Treatments C=83μM after 24 hours					
#	N	B	NB	F	FC
1	71	73	67	75.5	75
2	78	81	68	76	75
3	98.7	102	67.5	90.2	92
4*	56.6	59.2	44.0	62.4	56.7
5**	97.0	97.5	93.5	97.4	96.9
6*	56.2	56.4	51.4	87.5	84.6
7A [§]	119	105	67	87	81
7B [§]	133	116	110	115	73
*Loss of cells during staining procedure. **High seeding experiment. §96 well plate experiment					

Table 2.12. Average Percentage viabilities for several runs.

The MTT experiments were exceedingly difficult to gain reproducible results. The cells were easily removed from the surface of the culture wells such that removal of any liquids during the staining process could result in loss of cells. This is exemplified with run 6, where the viabilities appear particularly low. Upon removal of the MTT staining agent fragments of purple/blue came out with the stain and so resulted in lower readings from the plate reader. During run 4 it was observed that there had been a significant loss of cells after the PBS rinse. The homogeneity of the cell suspension at cell seeding was fairly difficult to control and measure, but by thorough mixing prior to addition to each well, this issue was reduced. By allowing several days worth of growth and then inspection of each well prior to staining this potential for variation was reduced.

By inspection of the results generally, slight trends can be observed. It appears that **23** and CBPQT⁴⁺ separately have comparable effect, whereas the complex of the two shows consistently a drop in viability when compared to the two individual compounds alone. Compound **30** and its complex with β-cyclodextrin shows very little

variation as results for these substrates are almost identical with the viabilities always within 10% of each other with the exception of experiment 7B. Further experimental repeats would be needed for precise statistical analysis of the results.

Whether the DIP compounds have any effect on the growth of the MDCK cell line is inconclusive due to the great variation in results found per run. By looking at the results along with the Live/Dead studies, it can be concluded that these molecules are not causing cell death. This in turn, when compared to the initial cell injection work, would indicate that the DIP compounds do not penetrate the cell membrane.

2.3.6 Microtubule Formation from Anionic Polyoxometallate crystals and Cationic DIPs.

As previously described in §2.1.3 it has been found that microtubule growth can be initiated by mixing solutions of DIP compounds with anionic polyoxometallate (POM) clusters, where the DIP exchanges with the cation counter ions in the POMs that then causes a precipitation out of the aqueous medium that the DIP was initially dissolved in. Microtubule formation is dependent of the concentration of the DIP and correspondingly the solubility of the POM crystal used.

Courtesy of Mr A G Boulay of the Cronin group, several experiments with polyoxometallate Keggin net crystals (POM) with a general molecular formula of $(C_4H_{10}NO)_{40}[W_{72}Mn_{12}O_{268}Si_7].48H_2O$ and the DIP compounds with their respective guest molecules were undertaken to investigate the possibility of microtube formation that could undergo additional host-guest interaction, where the effects of forming the host-guest complex would be measured. The general structure of the

POM and the structures of the components used in these experiments are shown below in Table 2.13.

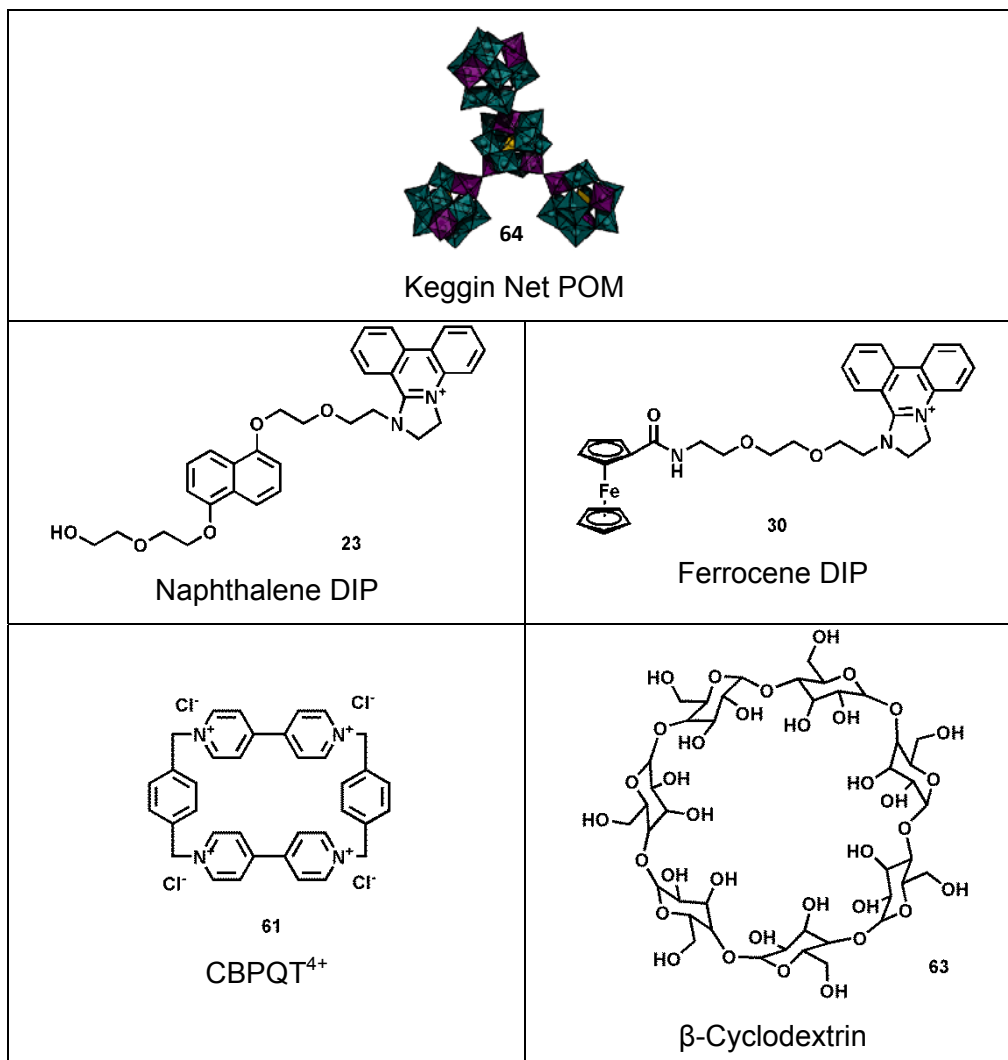


Table 2.13. Structure of POM crystal, DIPs and guest molecules used in experiments.

The concentration of components used was 5 mM in distilled water. A POM crystal was placed on a microscope slide and drops of the 5 mM solution were added to the slide. Table 2.14 shows the experiments carried out with the POM crystals.

Compound / Complex	Tube Formation	Comments
23	No	DIP precipitated POM dissolved
CBPQT ⁴⁺ 4Cl ⁻	Yes	Tubes successfully formed
23 / CBPQT ⁴⁺ 4Cl ⁻	Yes	Pink solution
CBPQT ⁴⁺ 4Cl ⁻ then 23	Yes then No	DIP precipitated POM dissolved
30	No	DIP precipitated POM dissolved
β -Cyclodextrin	No	POM dissolved
30 / β -Cyclodextrin	No	DIP precipitated POM dissolved

Table 2.14. Experiments with POM and substrates for microtube formation.

It was necessary that both the ferrocene and naphthalene DIPs were heated and vigorously stirred in order to gain a solution of the required concentration prior to addition to the slide. Compound **30**, upon addition to the microscope slide with the crystal present, instantly precipitated out of solution, whereby the remaining DIP did not have either the concentration or ionic strength required for tube formation and the POM dissolved into the aqueous media. Similarly, solutions of β -cyclodextrin also had no effect on the POM and no tubes formed with this mixture. The ferrocene DIP (**30**)/ β -cyclodextrin complex was marginally more soluble than that of compound **30** by itself; however, the gain in solubility was not enough to keep the mixture in solution upon addition to the microscope slide and again no microtubes formed with this mixture.

The complex between compound **23** and CBPQT⁴⁺4Cl⁻ had an improved solubility in comparison to **23** by itself to the point that microtubule formation occurred with this mixture upon addition to the POM crystals. It was found that the CBPQT⁴⁺ 4Cl⁻ could also form microtubes with the POM crystals by itself as it freely exchanged with the

morpholinium counter ion of the POM crystal. Images showing microtubule formation by the POM and the complex **23** /CBPQT⁴⁺ are shown in Figure 2.34.

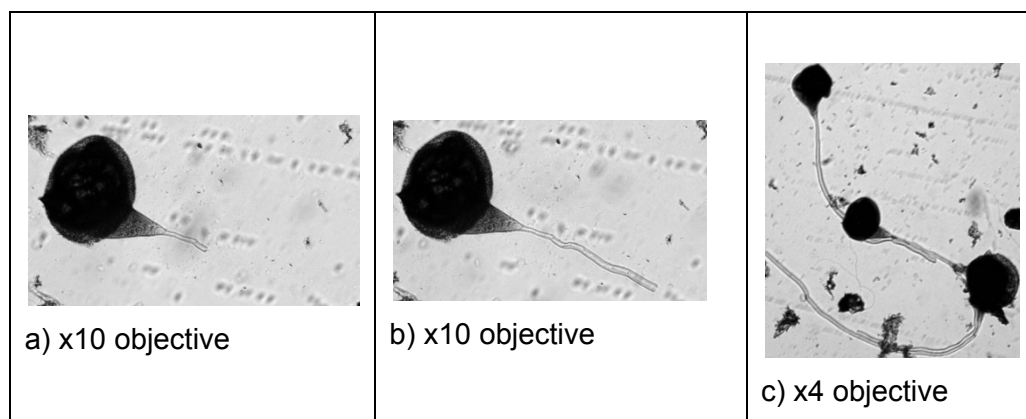


Figure 2.34. Microtubule growth of Naphthalene DIP/ CBPQT⁴⁺ 4Cl⁻ with POM Keggin net crystal over time.

In an attempt to form the complex between **23** and CBPQT⁴⁺ and microtubule growth *in situ*, the tube growth was initiated with the addition of CBPQT⁴⁺ 4Cl⁻ to a POM crystal. Compound **23** was then added to the mixture in an effort to form the complex whilst growing the microtubule. However, precipitation of the DIP occurred at a faster rate than the complexation with CBPQT⁴⁺ causing a significant dilution of the local concentration of CBPQT⁴⁺, halting the growth of the microtubule. The POM then gradually dissolved into the aqueous media. Figure 2.35 shows the initial growth of the microtube and then the subsequent halting and the destruction of the POM crystal as it was dissolved by the distilled water.

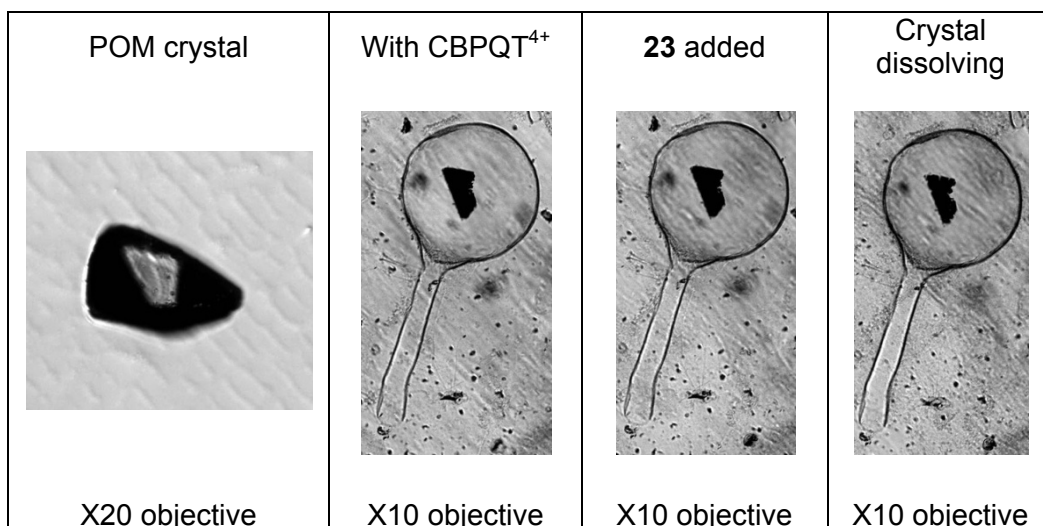


Figure 2.35. Growth of CBPQT⁴⁺ POM microtube which is halted by addition of **23**.

From these experiments we can see that microtubule formation by our DIP substrates cannot occur due to the lack of solubility in aqueous solutions. Compound **30** failed to achieve the level of solubility required for the growth of microtubes either by itself or upon formation of an inclusion complex with β -cyclodextrin. Compound **23** also failed to stay in solution for a sustained amount of time such that, precipitation from the solution occurred rapidly and microtubule growth failed to occur. By forming the pseudorotaxane with CBPQT⁴⁺ the solubility of the complex was far greater than the uncomplexed DIP such that microtubes formed with the POM Keggin net crystals. However, the complex had to be formed prior to addition to the POM crystal. Through the investigation of the microtubule formation it was found that CBPQT⁴⁺ could form microtubes with the POM crystals without the DIP present.

2.4 Conclusions and Future Work.

2.4.1 Conclusions.

To summarise we have successfully synthesised two derivatised dihydro-imidazo-phenanthridine compounds that can undergo host-guest interactions with either the cyclophane CBPQT⁴⁺ or β -cyclodextrin respectively. The ferrocene functionalised DIP was fairly insoluble in aqueous media, to the degree many of the analysis techniques employed for these compounds could not be carried out.

The **23** has been shown to interact with CBPQT⁴⁺ to form coloured solutions that can be monitored by UV-Vis and fluorescence measurements. The ITC studies have shown that **23** undergoes a highly complicated interaction with DNA that is buffer dependent, such that the binding model and binding constant K_a cannot be determined consistently.

We have shown that these compounds although they are cytotoxic if they can enter the nucleus of the cell, cannot penetrate the cell membrane, and so do not kill the cell culture when present in the growth medium for up to 24 hours. From the Live Dead staining we can see that the DIPs and their complexes appear to have little effect on the cells. The MTT studies are inconclusive as to whether there is any significant effect on cell viability and further investigation is required.

It has been shown that although both DIP compounds failed to form microtubes with POM Keggin net crystals, by forming the pseudorotaxane complex with **23** and CBPQT, microtubes can be successfully formed in aqueous media.

2.4.2 Future Work.

If there had been more time available, further investigations would have been carried out on the cell culture experiments, such that the cell injection would have been further optimised so as to investigate the effect of low concentrations of both DIP molecules on the cells.

The MTT experiments would have been subject to further repeats in order to identify outliers from the experiments and gain an improved statistical value for each substrate. By increasing the number of results we can then observe any trends that are actually there rather than potential artefacts of the experiments.

The effects of changing from aqueous loading of the DIP substrates to DMSO loading into the cell experiments would have been carried out in order to observe the changes in toxicity of these compounds. If time had permitted changing the cell type from the MDCK cells may have been an interesting pathway to investigate the changes in toxicity with changing cell type.

3

**Functionalised Self Assembled Monolayers for Cell
Adhesion Studies**

3.1 Introduction.

As previously described in § 1.7 self assembled monolayers (SAMs) have been used widely in cell culture experiments due their ability to model the extra-cellular matrix interactions. The chemical properties presented by the SAMs can be tuned by a number of stimuli, ranging from electrochemical conversions of functional groups, to the covalent modification of the pendant functionality as described in § 1.7. Host-guest interactions can also utilised in the control of cell adhesion and growth properties.

Mrksich and co workers^[91] have produced a system where cell adhesion is tuned by the presence of a connector protein^[91]. SAMs made of a mix of a 1% amine functionalised thiol and a triethylene glycol thiol were reacted with 1 mM benzenesulfonamide-*N*-hydroxysuccinimide solution to form the required functionalised substrate. The benzenesulfonamide moiety could bind selectively carbonic anhydrase proteins with micromolar affinity. Human carbonic anhydrase IV (hCAIV) was functionalised with a peptide presenting the peptide chain RGD (CA-RGD) in order to facilitate the binding of integrin proteins found on the surface of cells.^[91] This is illustrated in Figure 3.1.

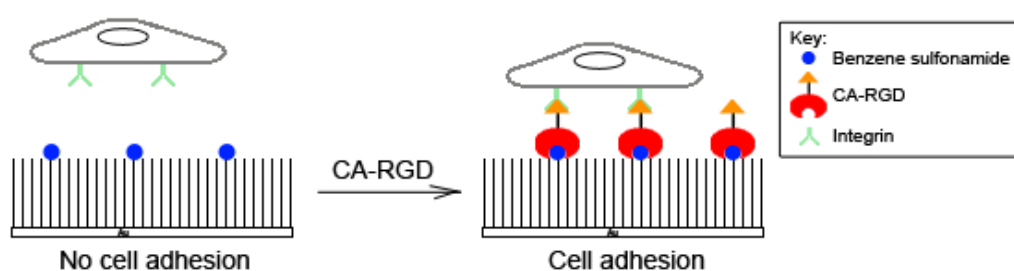


Figure 3.1. Illustration of the selective adhesion to the surface with CA-RGD present.

The CA-RGD adaptor protein produced from hCAIV at the gene expression level where the peptide sequence GGSGGGGSGGRGDS was coded for at the end of the reverse complementary sequence of

hCAIV. The vector formed was inserted into *Escherichia coli* (strain Origami B DE3) cells for the production of CA-RGD.^[91]

SPR experiments showed that the CA-RGD connector protein bound to the surface *via* interactions with the benzenesulfonamide moiety only and was repelled by the triethylene glycol groups. The SPR results for the 1% benzenesulfonamide and 100% triethylene glycol SAMs are shown in Figure 3.2.

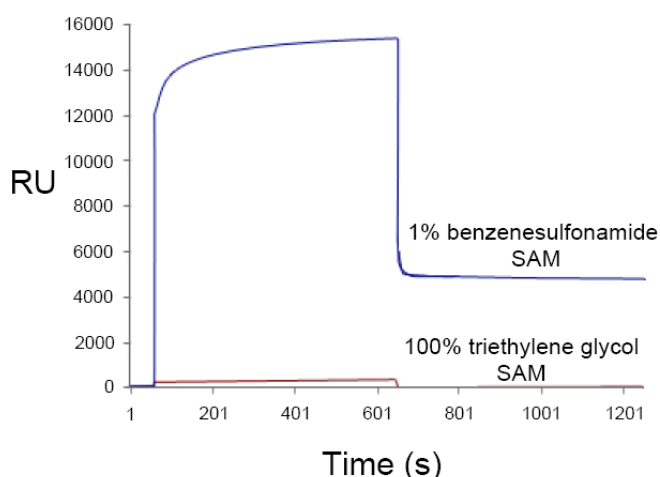


Figure 3.2. SPR sensorgrams that show that CA-RGD binds to 1% benzene sulfonamide, but fails to bind to 100% triethylene glycol SAMs.^[91]

When Chinese hamster ovary (CHO) cells were introduced to the SAMs without the CA-RGD present in the growth medium, no cell adhesion occurred. After the addition of the CA-RGD to the growth medium in concentration up to 10 μM , adhesion of the cells to the surface proceeded successfully such that when compared to cells on surfaces with RGD covalently bound there was no discernible difference. Addition of CA-RGD in concentrations above 10 μM led to an inhibition of the cell adhesion due to the division of the binding interactions into binary complexes where the CA-RGD bound either to the SAMs or the cells only. The formation of SAMs with the GRGDSC peptide attached covalently showed that the CHO cells adhered normally through integrin binding to the peptide and the appearance of the cells were identical to those grown on the benzenesulfonamide functionalised surface when the connector protein was present. An illustration of the effect CA-RGD

concentration on cell adhesion is shown in Figure 3.3. The cell adhesion mediated by CA-RGD with the benzenesulfonamide SAMs and onto SAMs presenting the peptide GRGDSC is shown in Figure 3.4.

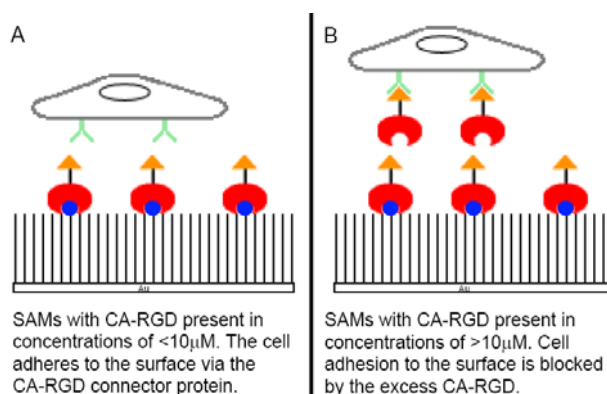


Figure 3.3. Illustration of the effect of CA-RGD concentration on cell adhesion to the surface.

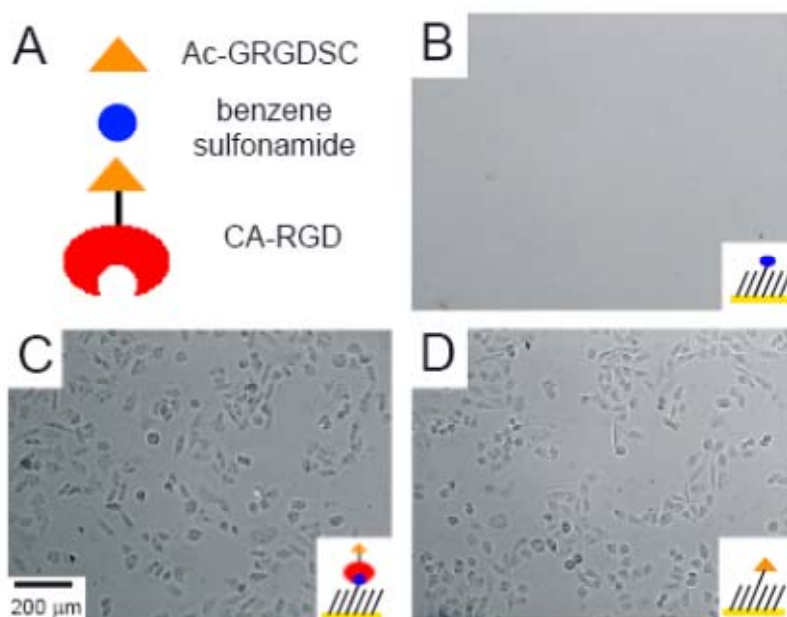


Figure 3.4. CHO cell adhesion mediated by CA-RGD on 1% benzenesulfonamide (C) and 1% Ac-GRGDSC (D). Cells failed to adhere to benzenesulfonamide monolayers (B).^[91]

Although thiol SAMs on gold have been studied extensively due to their useful properties and ease of synthesis, silane SAMs on glass have also been studied. Silanes on glass behave in a similar manner as thiols on gold however, it has been found that the silane SAMs when compared

to the equivalent thiols on gold have a significantly higher thermal stability. For example 1H,1H,2H,2H-perfluorodecanethiol has been found to desorb from gold at temperatures exceeding 145-165°C, whereas the silane equivalent on silicon or glass is thermally stable up to 350°C.^[57] SAMs on glass have the added benefit that they are completely transparent, while gold surfaces are semi-transparent to opaque. The applications of silanes on glass and silicon wafers has been predominately found within the field of electrical engineering. However, there are examples where silanes have been used to form thin films on glass for the modulation of cell adhesion properties and the creation of anti-bacterial surfaces for potential implant coatings. This is exemplified by work carried out by Mohorcic and co-workers.^[92]

Slides of indium tin oxide (ITO) glass functionalised with polymyxin B (PMB), a known anti-microbial agent were created in order to investigate the effectiveness of immobilised PMB on the viability of gram negative *E coli*. PMB is an anti-microbial polycationic lipopeptide that permeabilises the inner membrane of bacteria. This permeabilisation induces an uptake of water which then leads to cell apoptosis.^[93]

The silane, 3-glycidyloxypropyl trimethoxysilane (GPTMS), as a 50% solution in isopropyl alcohol (IPA) was partially hydrolysed using 0.1 M hydrochloric acid, where the ratio of silane to water was 1:3, for 15 minutes. The mixture was diluted with IPA to gain a concentration of GPTMS of 0.3 M. The slides were dip coated and then fixed for 30 minutes at 120 °C.^[92] The structure of the silane GPTMS is shown in Figure 3.5.^[92] An illustration of the functionalised surface is shown in Figure 3.6.^[92]

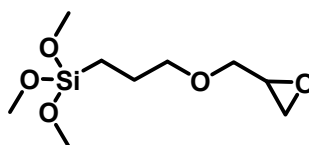


Figure 3.5. Structure of GPTMS.

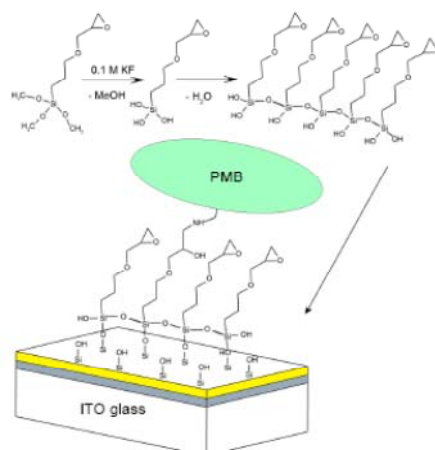


Figure 3.6. Illustration of the functionalised ITO glass surface.

The silanised glass was then treated with the PMB in the presence of an epoxide opening catalyst, either WCl_6 or $\text{H}_3\text{P}(\text{W}_3\text{O}_{10})_4 \cdot \text{H}_2\text{O}$ (PWA) to form the functionalised surface. The silanisation and modification of the surface was monitored by FTIR.^[92] Once functionalised the slides were immersed in distilled water for 20 hours, and then cleaned by ultrasonication in fresh distilled water in order to remove the excess PMB and catalyst from the surface. Optimal conditions were found to be 2.5 mg / mL concentration of PMB in the presence 0.6 mg / mL of the WCl_6 catalyst for a period of 1-3 hours. The effectiveness of the functionalised surfaces against *E coli* as a function of reaction time with either catalyst with PMB is shown in Figure 3.7.^[92] By varying the pH, and the concentration the anti-bacterial properties could be tuned. The surfaces formed by the optimal conditions reduced the *E coli* cell count by up to 5 orders of magnitude per millilitre of cell suspension.^[92]

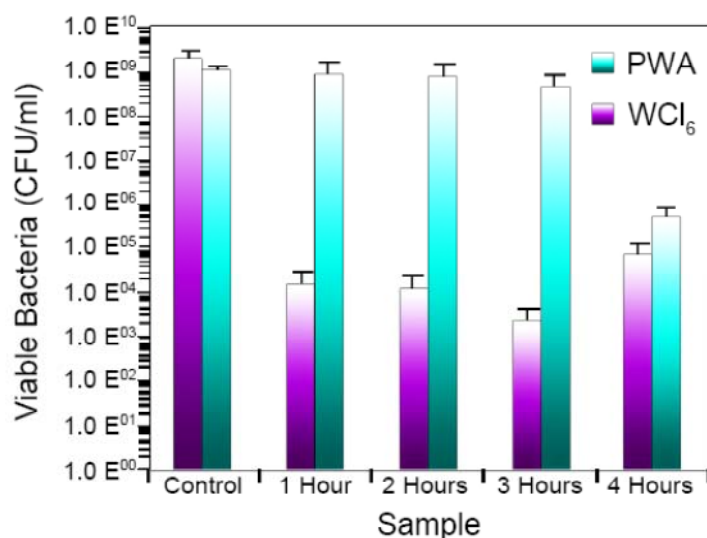


Figure 3.7. E coli viability on the functionalised surfaces vs the time treated with WCl₆/PWA with PMB.

To ascertain that the activity came from the PMB tethered to the surface and not as a result of cleavage from the surface, experiments where the functionalised slides were placed within dialysis tubing in the presence of *E coli*. The sealed tubing was then immersed into media containing *E coli*. The premise was that if there was significant cell death outside and within the dialysis tubing, then the PMB was no longer attached to the surface. Positive and negative tests were run for comparison results. The bacteria were incubated in the dialysis tubing experiments for 18 hours, after which time the viability of the cells was measured. The results of these experiments are shown in Figure 3.8.^[92] It was found that cell death only occurred within the dialysis tubing for the functionalised surfaces showing that the PMB was retained on the surface.^[92]

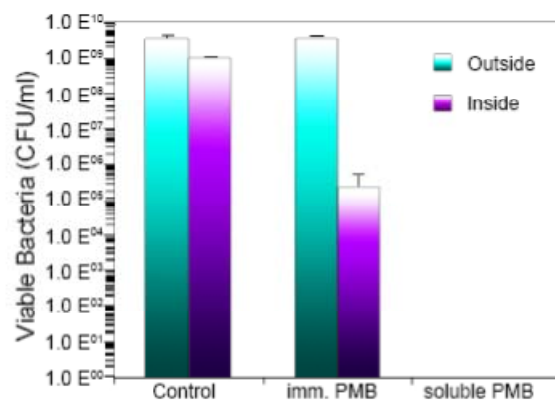


Figure 3.8. Bactericidal activity of the surface vs Controls of PMB and PMB-free experiments.

As these examples show the multitude of applications and types of modification available for surfaces modified by SAMs is wide ranging, allowing for further development of the area.

3.2 Aims and Objectives.

The aims were to produce functionalised surfaces for investigation of the effects of host-guest interactions on cell adhesion and growth. The functional groups that were chosen to investigate were naphthalene, tetrathiafulvalene (TTF), and ferrocene. As these groups can undergo host-guest interactions it was hoped that the formation of their complexes with either CBPQT⁴⁺ or β -cyclodextrin could modulate the adhesive properties of the surface and so control cell culture adhesion and growth. By incorporating each functional group the investigation into the effects of charged and neutral host-guest complexes on cell growth and adhesion could be performed.

For the formation of tunable SAMs, there was a variety of choices for the substrates that could be used to form these SAMs onto. Of the options available two substrates were chosen to investigate; glass with the immobilisation of silanes, and gold surfaces for the attachment of disulfides and thiols.

3.2.1 Modified Silanes.

The synthesis of self-assembled monolayers onto glass surfaces was thought to be a straightforward method of controlling the adhesion and growth of cell tissue culture, whereby the formation of a SAM onto transparent surfaces that could utilise intermolecular interactions to modulate cell adhesion and growth. One aim of this project was therefore to produce derivatised silanes that could form pseudorotaxanes with a guest substrate on the surface of a glass coverslip, such that a switching of adhesive properties of the surface could be controlled to either become non-adhesive or very adhesive to cells. The silanes could be modified by two methods, either prior or post formation of the monolayer. The silane target molecules for cell culture experiments are shown Figure 3.9.

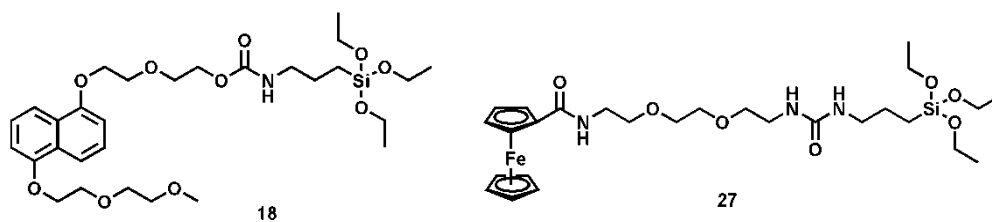


Figure 3.9. Silane Target Molecules.

3.2.2 Modified Disulfides.

The synthesis of self-assembled monolayers onto gold surfaces via disulfide bonds was thought to be a good alternative to the surfaces formed onto glass as a method of controlling the adhesion and growth of cell tissue culture. A second aim of this project was therefore, to produce derivatised disulfides that could form pseudo-rotaxanes with a guest substrate on the surface of a gold slide, such that a switching of adhesive properties of the surface could be controlled to either become non-adhesive or very adhesive to cells. The target molecules to be used in the formation of SAMs on gold surfaces are shown below in Figure 3.10.

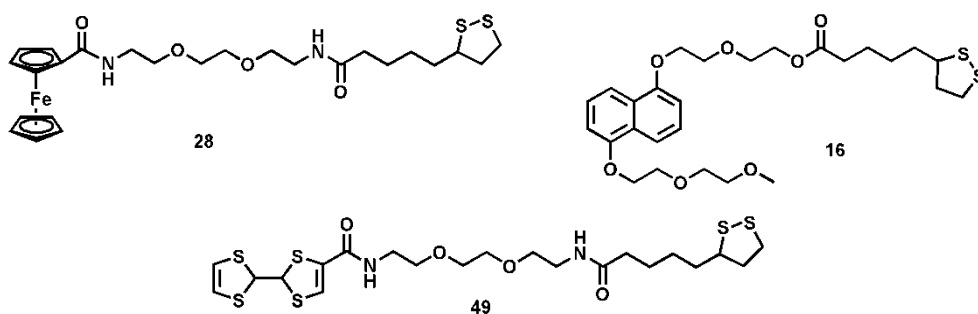
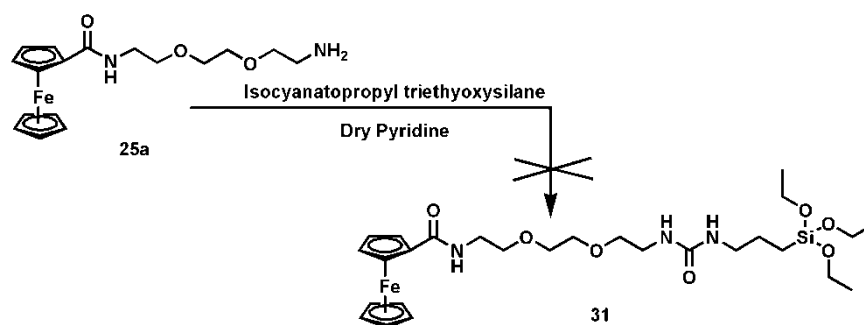


Figure 3.10. Target Molecules for Functionalised Disulfide Synthesis.

3.3 Results and Discussion.

3.3.1 Synthesis of functionalised silanes.

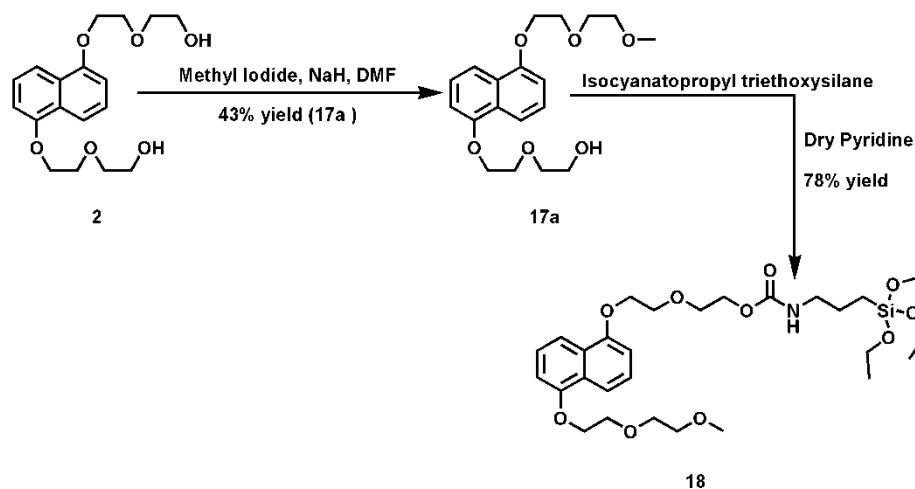
3.3.1.1 Ferrocene silane synthesis.



Scheme 3.1. Attempted formation of Ferrocene based silane.

From the ferrocene amino compound **25a** which was synthesised under the same conditions as described in § 2.3.2, a direct coupling of the amine with isocyanatopropyl triethoxy silane in dry pyridine was attempted. However, the reaction failed to yield the required product and the starting materials were consumed. As we could not form the required ferrocene disulfide as described in § 3.3.2, further investigation into the possible identity of the compound produced from this reaction was not carried out.

3.3.1.2 Naphthalene silane synthesis.



Scheme 3.2. Synthesis of the naphthalene silane **18** from the diol **2**.

The naphthalene silane **18** was synthesised in a two step synthesis from the starting naphthalene diol **2**. The synthesis of this material as described in § 2.2.1. The naphthalene diol **2**, was methylated with methyl iodide. This reaction gave the mono-methylated **17a** and dimethylated naphthalene **17b** compounds with in varying ratio that was not controllable to any real degree. The dimethylated compound was, although not useful for this project, a key material for other syntheses within Prof G Cooke's group. The two products were easily separated by column chromatography and any unreacted starting material could be recovered. The monomethylated naphthalene alcohol (**17a**) was then reacted with isocyanatopropyl triethoxy silane in dry pyridine. The pyridine was dried over calcium hydride overnight under an atmosphere of nitrogen and collected by vacuum distillation directly before use. The silane product (**18**) was produced in 78% yield.

3.3.2 Monolayer formation of **18** on glass surfaces.

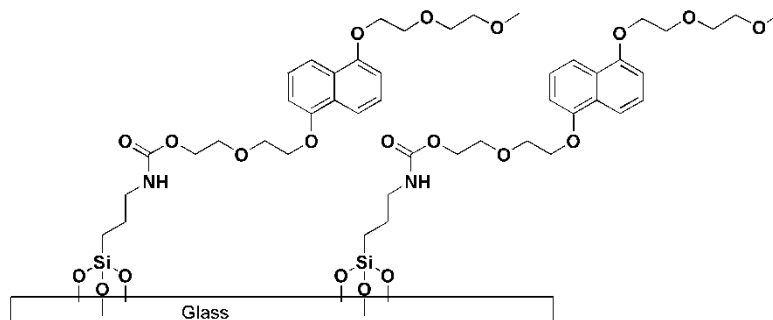


Figure 3.11. Naphthalene Silane SAM on glass.

Prior to treatment with compound **18** the glass slide coverslips were first cleaned in a fresh solution of Caro's acid solution. After the acid clean, treatment of the coverslips with 5M sodium hydroxide was performed to increase the number of hydroxyl groups on the surface of the now clean glass. Once complete, the coverslips were rinsed with copious amounts of water to remove any excess base residues, and then stored at 80°C until use in the formation of SAMs with compound **18**. The protocol used can be found in **Appendix 4**.

The glass coverslips were treated with a solution of 1% silane in 1% acetic acid in ethanol for 30 minutes. The treated coverslips were then rinsed with ethanol followed by water to remove any excess silane. Water contact angle measurements were recorded for both the treated and untreated clean glass coverslips. The results indicated that the SAMs had successfully formed on the glass with a drop in contact angle observed as shown in Figure 3.12. The decrease in contact angle indicated a small increase in hydrophilicity and wettability of the surface. This would indicate an influence of the diethylene glycol on the chemical properties of the surface.^[51]

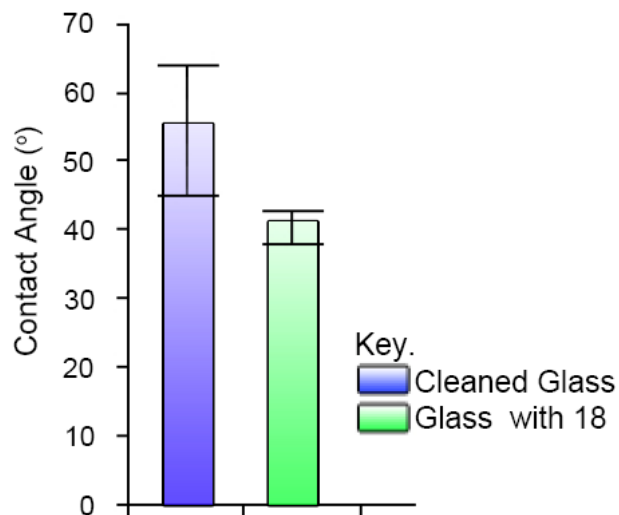


Figure 3.12. The Average Contact Angles measured in triplicate for cleaned glass coverslips and cleaned coverslips treated with the naphthalene silane 18.

Cells from Madin Darby Canine Kidney (MDCK) cell culture were then seeded onto the treated coverslips and incubated for 1 week to allow for adhesion and growth onto the surfaces. After this time the cells were fixed with 4% formaldehyde in PBS and stained with Coomassie Blue. Protocols for these procedures can be found in **Appendix 3**.

Repetition where the glass was left in the solution overnight and then treated with CBPQT⁴⁺ solution for one hour prior to seeding, gave inconclusive results due to the seeding density used. The cells successfully reached confluency and were found to be extremely densely packed on the surface of the glass. It should be noted that upon treatment of CBPQT⁴⁺ the concentration of naphthalene was too low to observe the change in colour. This may have been due to the lack of space between the naphthalene groups and so the pseudorotaxane may not have formed. Images of the cells for both with and without CBPQT⁴⁺ added are shown in Figure 3.13.

From the images it can be observed that the cells adhered to both surfaces, and grew to confluency rapidly, showing that the surfaces did not impede this process in any way.

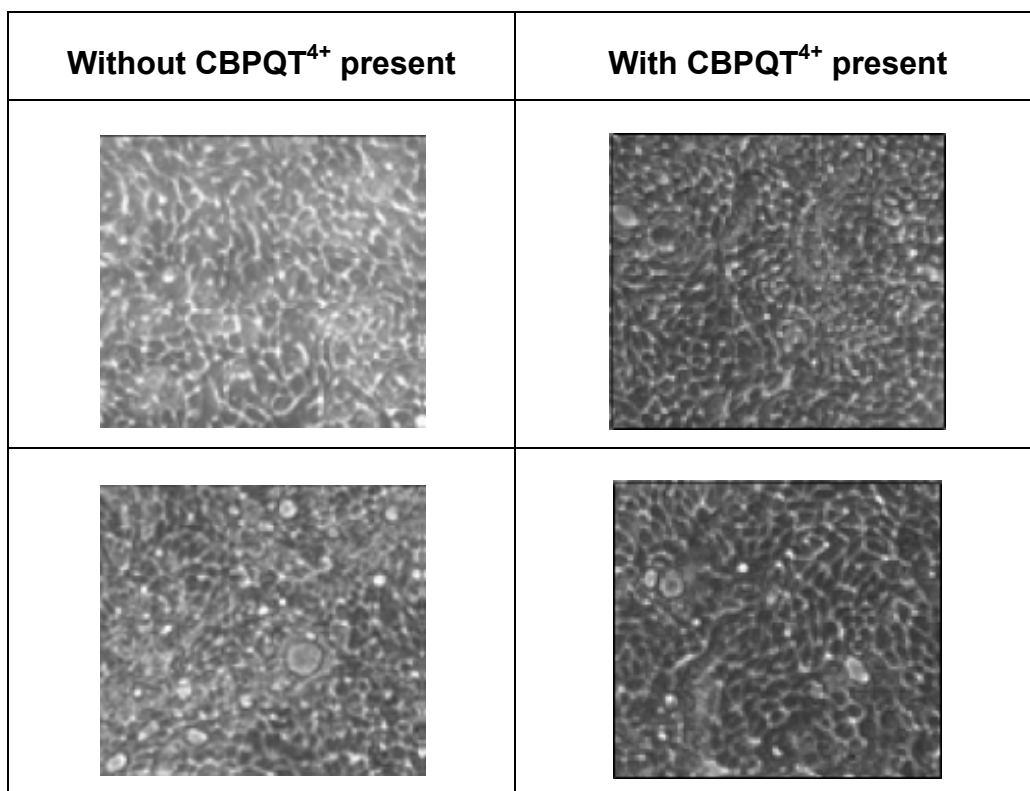
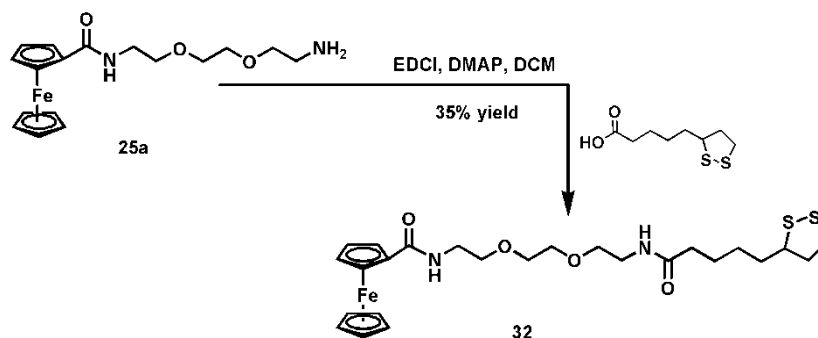


Figure 3.13. Phase contrast images of MDCK cells grown on Naphthalene silane functionalised glass slides with and without CBPQT⁴⁺ present. X10 optical zoom.

3.3.3 Synthesis and analysis of thiotic acid functionalised electron rich moieties.

3.3.3.1 Synthesis of ferrocene disulfide.



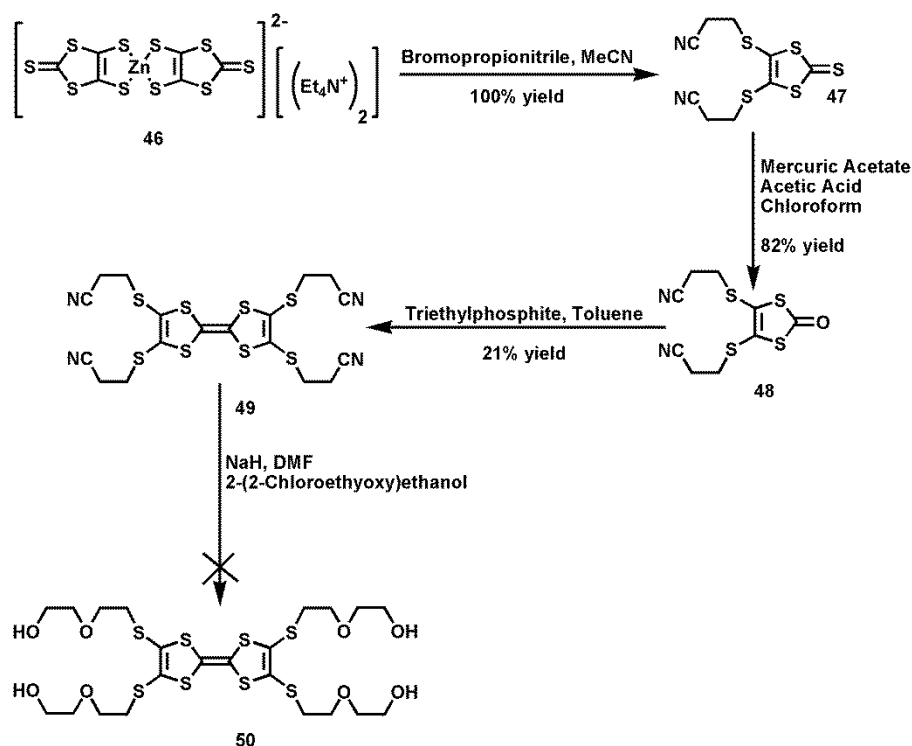
Scheme 3.3. EDCl coupling of ferrocene amine **25a** with thiotic acid.

The ferrocene disulfide compound (**32**) was synthesised by reacting the ferrocene amino compound (**25a**),^[94] with thiotic acid in the presence of EDCI. The reaction gave a good yield and column chromatography gave the clean product as a sticky orange oil. The reaction conditions tolerated large scale reactions so the material could be made in bulk and then stored at 0°C until use.

3.3.3.2 Synthesis of tetrathiafulvalene disulfide.

Two synthetic pathways were attempted to create the TTF functionalised disulfides. The TTF derivative was chosen for its inherent redox activity and its strong association with CBPQT⁴⁺. The first pathway utilised a zincate intermediate, as shown in Scheme 3.4, whereas the second pathway used the formation of a lithiated form of TTF to synthesise the required disulfide as shown in Scheme 3.5.

Synthesis 1 – Via Zincate intermediate.



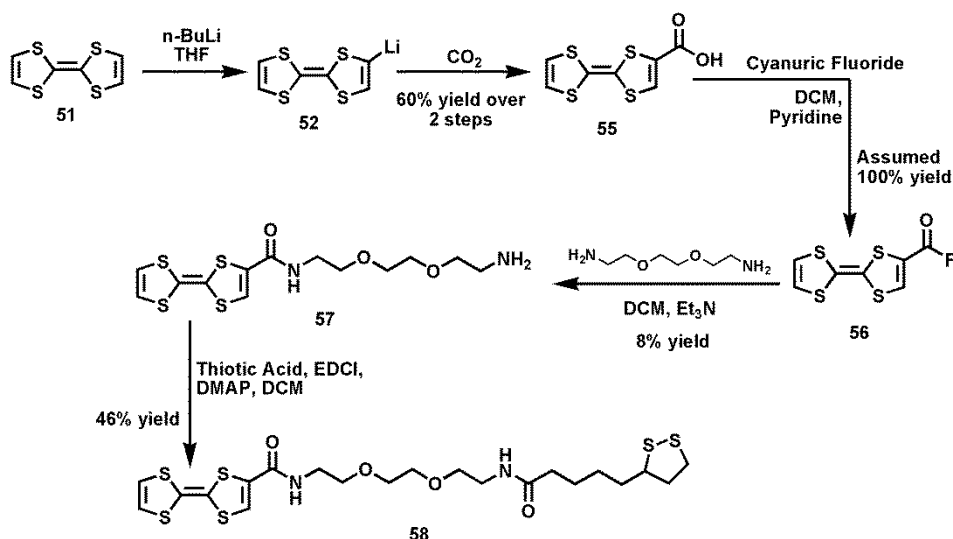
Scheme 3.4. TTF alcohol synthesis from the starting zincate compound.

The zincate salt **46**,^[95] was reacted with bromopropionitrile to gain the 4,5-bis(2-cyanoethylthio)-1,3-dithiole-2-thione **47**.^[95] The product of this reaction was recovered by precipitation from toluene with diethyl ether. Any product that failed to precipitate out was then recovered by column chromatography followed by precipitation from toluene with diethyl ether. Compound **47** was then reacted with mercuric acetate to form the 4,5-bis(2-cyanoethylthio)-1,3-dithiol-2-one **48** in an 82% yield. The impurities were removed by filtration followed by a base extraction to remove any acetic acid present. Compound **48** was then taken on without any further purification required.

The formation of the tetra(2-cyanoethanethio)tetrathiafulvalene **49** by the reaction of compound **48** with triethyl phosphite in methanol gave the product in a 21% yield, where the product was recovered by precipitation and column chromatography of the liquor to remove the

phosphite by-product.^[95] The *in situ* deprotection of the thiol groups and subsequent reaction with 2-(2-chloroethoxy)ethanol failed to yield either starting material, product **50** or deprotection product, where complete decomposition of the TTF compound **49** occurred. Due to lack of starting materials and the problematic synthesis to create the zincate salt that had been the initial starting material, it was decided that this pathway would be abandoned.

Synthesis 2 – Via Lithiation route.



Scheme 3.5. Reaction scheme for the synthesis of TTF disulfide **49** starting from TTF.

The TTF disulfide **49** was made in a four step synthesis, starting from TTF as shown in Scheme 3.5. Tetrathiafulvalene (TTF) was first lithiated and then reacted with CO₂^[96] in a one pot synthesis to gain the TTF carboxylic acid **55**. The TTF acid was reacted with cyanuric fluoride^[97] in DCM. The reaction gave a dark red solid that was water stable. The acid fluoride **56** was then reacted with 2,2'-(ethylenedioxy)diethylamine, where there was an assumed 100% yield from the acid fluoride formation step. The resulting TTF amine **57** was contaminated with the 2,2'-(ethylenedioxy)diethylamine that had been used in excess in

order to drive the reaction to form the TTF mono amine rather than the TTF dimerised product, as was observed in the synthesis of the equivalent ferrocene amine **25a** and **25b**. The TTF-amine **57** was found to co-elute off the silica column with its contaminant such that repeated chromatographies led to loss of product with no gain in purity.

The impure TTF amine **57** was reacted with thiotic acid via an EDCI coupling that gained the required disulfide compound **58** as an orange oil. Column chromatography successfully removed all impurities from the compound. It was found, however, that the TTF readily oxidised in solution. Ascorbic acid addition to the oxidised compound returned the TTF disulfide **49**, indicating that the oxidation was partially reversible. Over the four steps the yield overall was 2%; this poor yield may be due to the fairly harsh conditions used and that the TTF oxidised readily at the last stage of the synthesis. The repeated column chromatography in the penultimate step, where the amine co-eluted with the product also had a detrimental effect on the yield as the product was lost with each chromatograph without any decrease in the amounts of impurity present. Due to the lack of stability of the final product, and poor overall yield it was decided that it was impractical to repeat the synthesis in order to gain more material.

3.3.4 Immobilisation of naphthalene disulfide **16** onto gold.

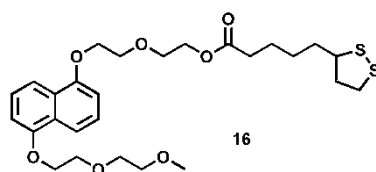


Figure 3.14. Structure of the Naphthalene disulfide **16**.

The naphthalene disulfide **16** had been made previously within Prof G Cooke's group^[98] shown in Figure 3.14. Studies of this compound in chloroform with gold surfaces showed that successful immobilisation

was possible. In collaboration with Dr M Kadodwala's group, studies were carried out on silicon wafers coated with 5 nm Ti overlaid with 20 nm gold were connected to a circuit, where the resistance over the gold surface was measured with time as the slide was brought into contact with a 10 mL solution of disulfides at a total concentration of 1 mM in chloroform. As the SAMs formed on the gold, the resistance increased until the saturation of the surface reached a maximum and the resistance measurements reached a plateau. 100% butyl disulfide; 1:1 butyl disulfide: naphthalene disulfide; and 100% naphthalene disulfide solutions were typically used for these experiments. The butyl disulfide was used as a reference and a spacer group for the naphthalene disulfide, where interaction with CBPQT⁴⁺ was not expected to occur. An experiment with CBPQT⁴⁺4PF₆⁻ on a clean wafer was also carried out as a reference for subsequent experiments and showed the non-specific adsorption of material onto gold. The changes in resistance for each substrate are shown in Figure 3.15, Figure 3.16, Figure 3.17, and Figure 3.18.

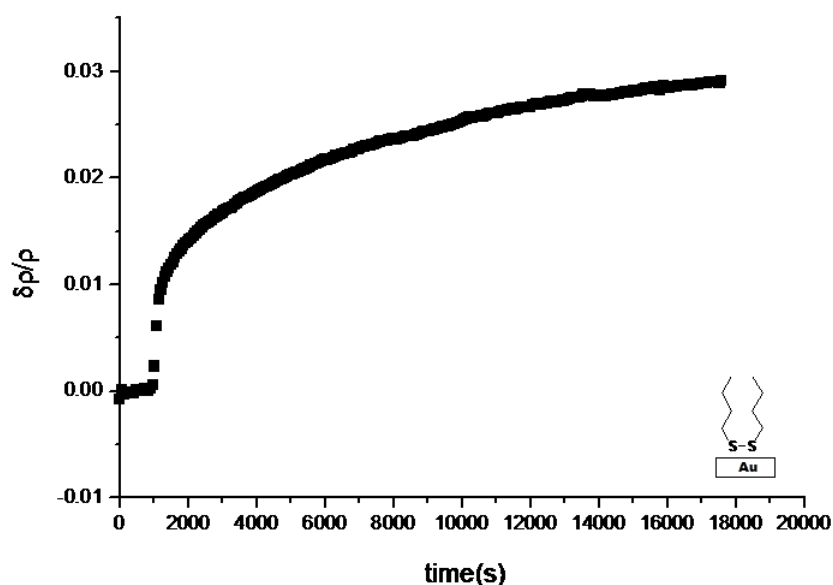


Figure 3.15. Resistivity measured for the formation of the butyl disulfide SAM onto the gold surface at room temperature.

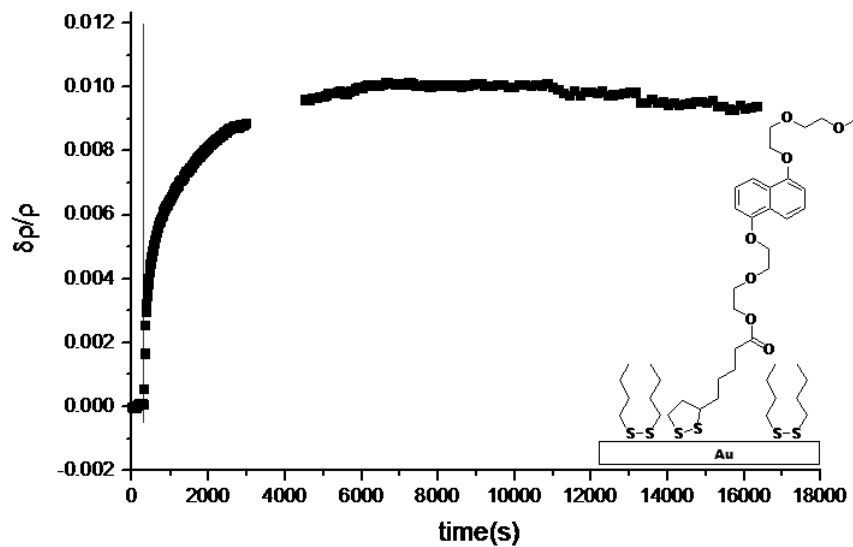


Figure 3.16. Resistivity measured for the 1:1 butyl - naphthalene disulfide SAM onto the gold surface at room temperature.

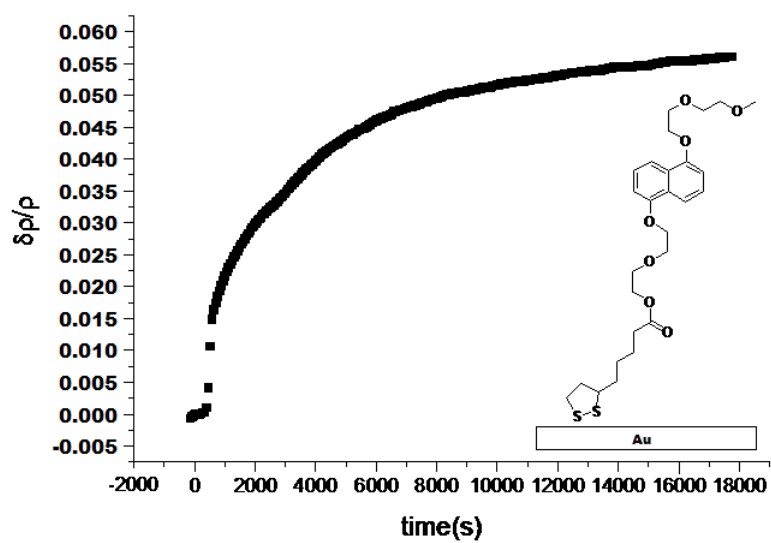


Figure 3.17. Resistivity measured for the formation of the naphthalene disulfide SAM onto the gold surface at room temperature.

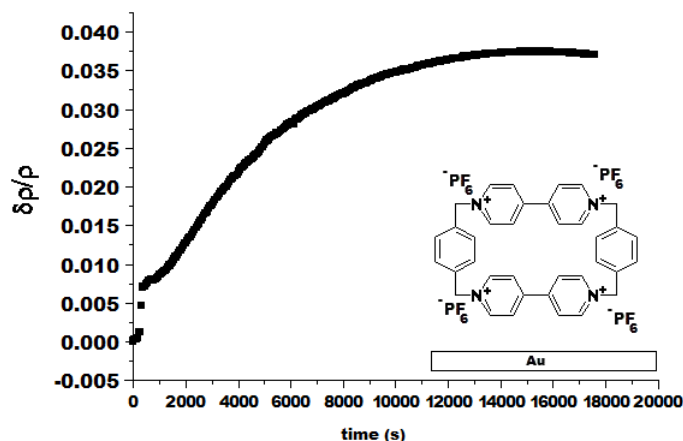


Figure 3.18. Resistivity measured at room temperature for the addition of CBPQT onto the gold surface.

After removal from the disulfide solutions, the wafer was rinsed with chloroform, and then immersed in a solution of 1 mM $\text{CBPQT}^{4+} 4\text{PF}_6^-$ in acetonitrile and measurements were carried out. Initial experiments showed a dramatic decrease in resistance and the formation of a blue solution indicating the formation of the $\text{CBPQT}^{2+\cdot}$ di-radical species. The formation of the di-radical species was attributed to the reduction of CBPQT^{4+} by the copper wire and / or the zinc solder used to connect the wafer to the circuit coming in contact with the solution. It was thought that the di-radical species then caused the disulfide to be removed from the surface of the gold leading to a drop in resistance.

EPR spectroscopy experiments were carried out using solutions of CBPQT^{4+} treated with either zinc powder or copper wire. The results are shown in Figure 3.19. The EPR spectroscopy confirmed the formation of a radical species, which from literature precedent indicated the formation of the diradical species.^[18] From the EPR spectra shown in Figure 3.19 it can be observed that the addition of copper produced a strong signal, and so reduced the CBPQT^{4+} more readily when compared to the equivalent conditions with zinc. This would indicate that the formation of the diradical was due to reaction of the CBPQT^{4+} with the copper rather than the zinc.

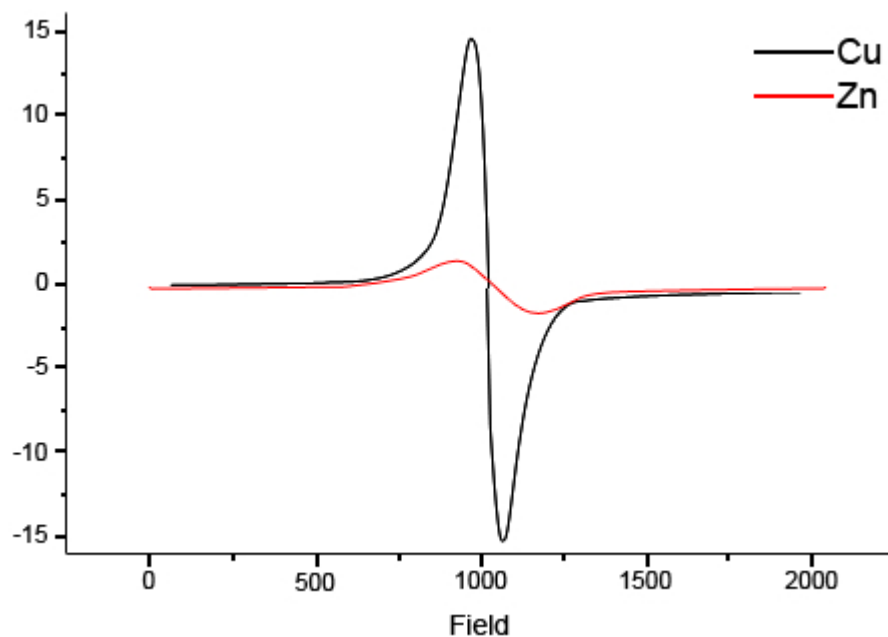


Figure 3.19. EPR of $\text{CBPQT}^{2(+)}$ diradical formed by the addition of either zinc or copper.

To confirm that the diradical species was the cause of the removal of the SAMs from the gold, experiments were carried out where the immobilised SAMs were immersed in acetonitrile, and then $\text{CBPQT}^{4+} 4 \text{PF}_6^-$ solutions were very carefully added to the slide ensuring that the solution did not come in contact with either the zinc solder or the copper wire and the resistance measurements were recorded. Figure 3.20 shows the data recorded for the addition of $\text{CBPQT}^{4+} 4\text{PF}_6^-$ to butyl disulfide SAMs and naphthalene disulfide SAMs.

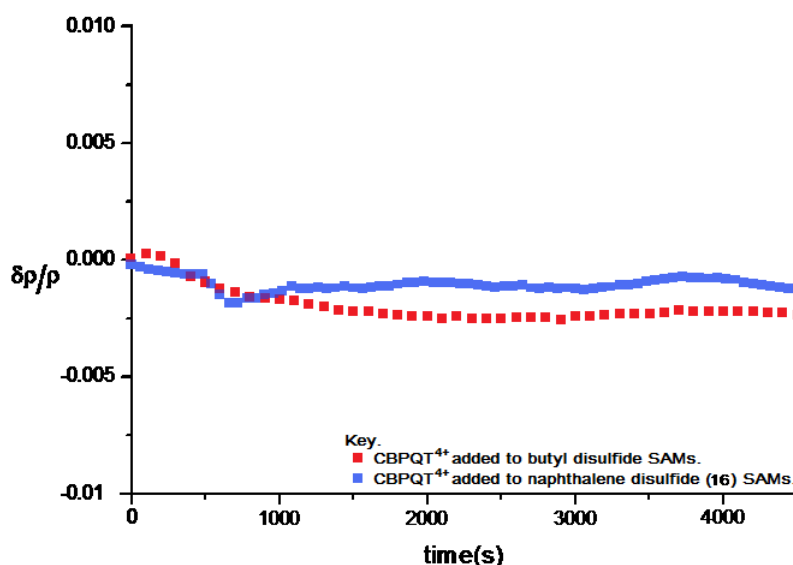


Figure 3.20. The addition of CBPQT⁴⁺ to the butyl and naphthalene SAMs in acetonitrile at room temperature.

After addition of the CBPQT⁴⁺ 4PF₆⁻ a slight rise followed by a small drop in resistance was observed for the butyl SAMs whereby the resistance then levelled out. For the naphthalene SAMs after addition of the CBPQT⁴⁺ 4PF₆⁻ there was a drop in the resistance observed. The resistance then was partially regained, where it equilibrated over time. Addition of copper to a solution of CBPQT⁴⁺ 4PF₆⁻, formed the di-radical, and subsequent treatment of a SAM immobilised surface gave the expected drop in resistance as the disulfide was removed from the surface. By the corresponding addition of zinc to the CBPQT⁴⁺ 4PF₆⁻ solution followed by a filtration and application to a SAM immobilised gold surface, it was observed that the removal of the disulfide from the surface of the gold. Figure 3.21 shows the data recorded for both the butyl and the naphthalene disulfide SAMs upon exposure to the pre-formed CBPQT²⁺ species. Reduction was via the addition of copper to the solution of CBPQT⁴⁺ in acetonitrile.

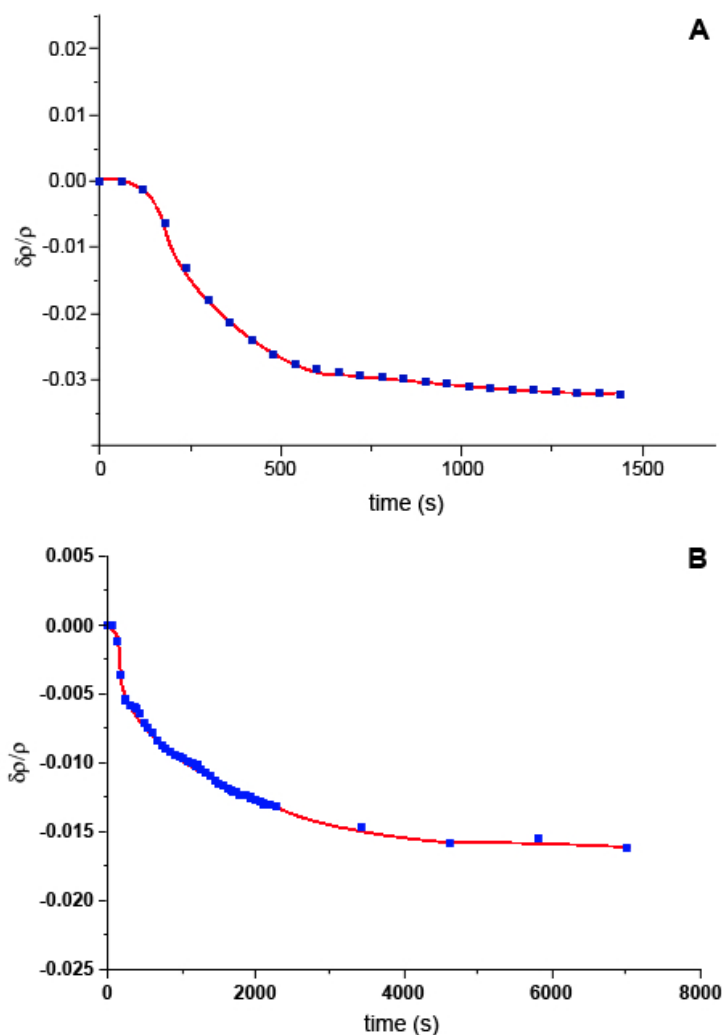


Figure 3.21. Resistivity for SAMs treated with CBPQT²⁺ at room temperature A) butyl disulfide SAM. B) naphthalene disulfide SAM.

Due to the overall reduction in resistance for the addition of CBPQT⁴⁺ 4PF₆⁻ to the SAMs on the wafer there was a degree of uncertainty as to if there had been successful formation of the pseudorotaxane or if there had been a small degree of dissociation of the disulfides from the gold as a result of the addition of the CBPQT⁴⁺. As part of the cell culture experiments was to selectively separate the pseudo rotaxane formed by the reduction of CBPQT⁴⁺, this set of experiments showed that by adding a reducing agent in this case copper or zinc, the CBPQT²⁺ was formed and removal of the disulfides occurred non-selectively, where both the naphthalene and the butyl disulfides desorbed from the gold surface. Due to the successful synthetic route

applied that could tolerate gram scale synthesis, the ferrocene disulfide gold SAMs were chosen as the preferred vehicle to further investigate this methodology.

3.3.5 Cell Engineering experiments.

Glass microscope slides were spatter coated with Ti/Au with a layer thickness of 2 μ m Ti and 26 μ m Au. The slides were cut to fit a 24 well plate with the approximate dimensions of 1cm². These cut slides were cleaned by rinsing with acetone x2, methanol x2, IPA x2, and ethanol x2 prior to treatment with the disulfide. A number of solutions were made where the amount of ferrocene disulfide (**32**) was varied relative to the amount of butyl disulfide spacer. The solutions were kept at 1mM total disulfide concentration. All solutions were in ethanol and in order increase the probability of SAM formation these solutions were made directly before immobilisation onto the gold surface. The slides treated with the disulfide mixtures for 1.5 hours and then rinsed thoroughly with ethanol and water. These slides were then stored below 0°C until use in cell culture experiments. Table 3.1 shows the amounts of ferrocene disulfide and butyl disulfide used in each solution mixture.

Concⁿ Butyl disulfide	Concⁿ Ferrocene Disulfide	Ratio / Percentage
1 mM	0 mM	100% Butyl disulfide
0.91 mM	0.01 mM	10:1 butyl : ferrocene
0.83 mM	0.17 mM	5:1 butyl :ferrocene
0.75 mM	0.25 mM	3:1 butyl :ferrocene
0.5 mM	0.5 mM	1:1 butyl :ferrocene
0.25 mM	0.75 mM	1:3 butyl :ferrocene
0 mM	1 mM	100% Ferrocene disulfide

Table 3.1. Concentrations of ferrocene and butyl disulfide.

The treated slides were washed with ethanol and then HEPES prior to cell seeding. MDCK Cells were seeded onto the slides at a typical density of around 5000 cells per mL. The culture was then incubated in DMEM supplemented media for one week, where the media was changed every 2-3 days. The cells were grown for one week, after which time they were treated with either Live/Dead stain or fixed and stained with Coomassie Blue. Figure 3.22 shows the images gained from the Coomassie Blue staining of the cell culture experiment.

As can be seen from the images, the MDCK cells became densely spread across all slides. What can be noted is that the cells grew more densely on the 100% ferrocene SAMs with β -cyclodextrin added compared to the density of cells on just 100% ferrocene SAM. There did not appear to be much change observed with the differing percentages of disulfide. From then on it was decided that for ease of solution formation and comparison that the ratios to investigate were 100% butyl disulfide, 1:1 butyl disulfide: ferrocene disulfide, and 100% ferrocene disulfide.

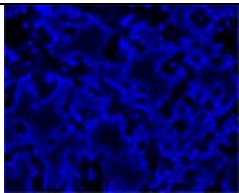
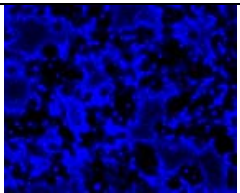
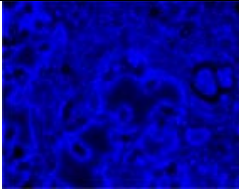
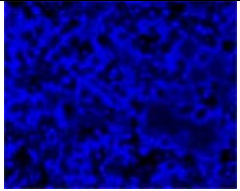
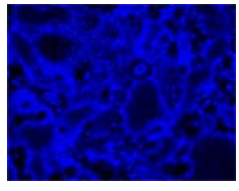
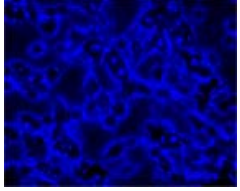
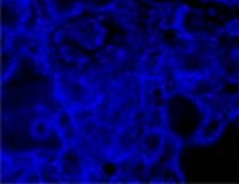
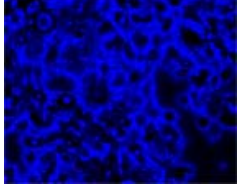
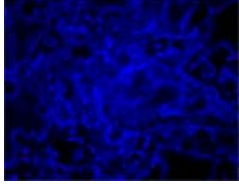
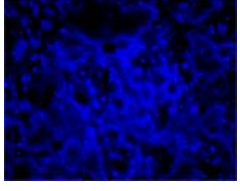
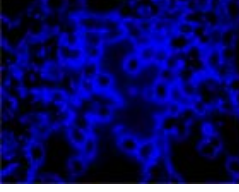
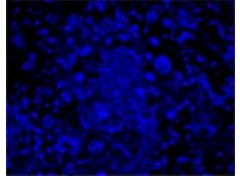
Disulfide Mixture	Disulfide SAM only	With β -cyclodextrin
A 100% Butyl Disulfide		
B 90% Butyl Disulfide 10% Ferrocene Disulfide		
C 75% Butyl Disulfide 25% Ferrocene Disulfide		
D 50% Butyl Disulfide 50% Ferrocene Disulfide		
E 25% Butyl Disulfide 75% Ferrocene Disulfide		
F 100% Ferrocene Disulfide		

Figure 3.22. Coomassie Blue staining of MDCK cells on the disulfide SAMs with and without β -cyclodextrin added. X10 optical zoom.

To investigate the effects of oxidation of the ferrocene to ferricenium on cell growth we treated a set of SAMs of each mixture with iron trichloride. At the same time another set of SAMs on gold were treated with β -cyclodextrin in order to probe the changes in growth and adhesion with the addition of a guest species to the ferrocene group on the SAM. The iron trichloride and β -cyclodextrin were dissolved in distilled water to form 1 mM solutions. Treatment of the iron trichloride was left for

no more than 5 minutes before removal of the solution. The slides were washed with water x2 and ethanol to remove any iron trichloride residue. The β -cyclodextrin solutions were left for 15 minutes before rinsing with water x2 and ethanol x1.

Prior to the cell culture experiments it was found that the culture media that had been used previously contained ascorbic acid, a known anti-oxidant that would reduce the ferricenium species back to the ferrocene before the cells could settle and so voiding an investigation of the role oxidation of the ferrocene on controlling adhesion. After a detailed search it was found that F10 HAM media did not contain ascorbic acid and could be used to suit our purposes. The slides were then rinsed with ethanol and HEPES prior to seeding. The cell culture was split by normal means, whereby the trypsin activity was quenched with DMEM media for centrifugation. The media was removed and the cells were taken up in the F10 HAM, and spun down. This procedure was performed in order to remove any traces of the DMEM. The cells were seeded onto the slides in the ascorbic acid free media at a cell density of ~5000 cells per mL.

Alongside the gold slide experiment, a 24 well plate (containing cleaned glass coverslips) was also seeded and the cells grown in F10 HAM, in order to discount any changes observed that were due to the change in media. The cell cultures were allowed to grow over the course of 1 week; at which point they were fixed with 4% formaldehyde solution, permeabilised, and stained for actin and tubulin. The cells were also stained with DAPI to highlight the nucleus of the cells. For all the surfaces the MDCK cells successfully grew and spread across the surfaces. It can be seen that there is very little change in the appearance of the MDCK cells showing that there is very little perturbation of the culture from the SAMs on the gold surface. The images presented in Figure 3.23 show that there is very little difference in growth and adhesion between the SAMs indicating that there is no preference for each surface and that the cells will readily grow on all surfaces.

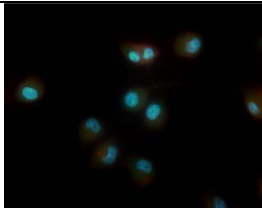
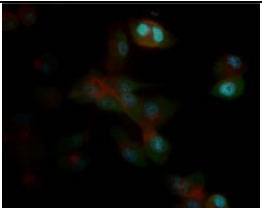
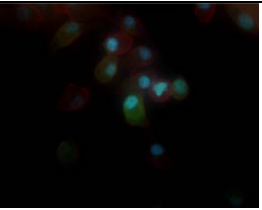
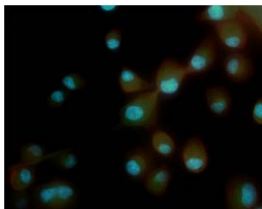
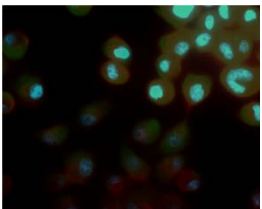
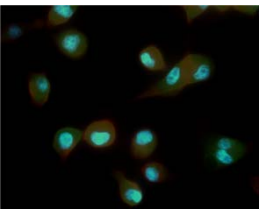
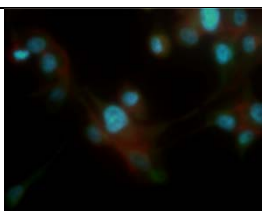
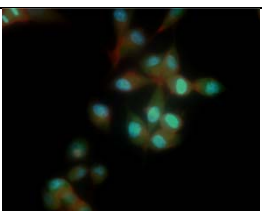
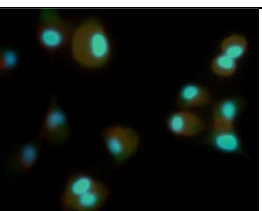
Disulfide Mixture	SAMs Only	SAMs after FeCl ₃ treatment	SAMs with β-cyclodextrin
100% Butyl disulfide			
50% Butyl disulfide 50% Ferrocene disulfide			
100% Ferrocene disulfide			

Figure 3.23. MDCK images stained for Actin (red), Tubulin (green) and with DAPI (blue).
40x optical zoom.

Appendix 5 shows the individual black and white images of each stain for the images in Figure 3.23 above.

3.4 Conclusions and Future Work.

3.4.1 Conclusions.

Several monomers have been successfully synthesised for applications to form SAMs onto either glass or gold surfaces.

Experiments with the naphthalene silane derivative with and without the presence of CBPQT⁴⁺ have shown that MDCK cell growth and adhesion are unaffected by these moieties, where the cells successfully grew to confluence rapidly.

Experiments with the ferrocene disulfide on gold and its interaction with β -cyclodextrin also showed to have very little effect on the growth and adhesion of these cells in culture where the cells grew and spread across the surfaces with no specific preference for one surface over another. The formation of the ferrocenium species also had very little effect on the cells.

Work with the naphthalene disulfide onto gold wafers with the addition of CBPQT⁴⁺ showed that the disulfides will quickly adsorb onto the surface of the gold. Addition of the CBPQT²⁺ radical was shown to remove the disulfide and thiol functionalities of the surface of the gold.

The TTF disulfide was synthesised, however, it was found to be sensitive to solvent and rapidly oxidised, which may account for the very low overall yield.

3.4.2 Future Work.

Had there been greater quantities of the TTF disulfide available, and with further time, investigation into the effects of this moiety on cell adhesion could be performed. The addition of ascorbic acid to solutions of the TTF would potentially reduce the degree of oxidation and so allow the SAMs to form.

Investigation of the adsorptions onto gold by SPR would be a key extension to this work, where the adsorption of protein onto surfaces could be measured.

Investigations into the SAMs on gold with other cell types may be an interesting extension to this work, where the sensitivity to the surfaces may vary.

4.
**Pseudorotaxane modification of diacetylene
liposomes.**

4.1. Introduction.

The name liposome is derived from the Greek 'lipo' meaning fat and 'soma' meaning body. Liposomes can be singular or multilaminar vesicles that may be formed using either artificial lipid molecules or biological phospholipids. Liposomes have multiple applications including drug transport molecules and sensing devices. The general structure of a liposome is shown in Figure 4.1.

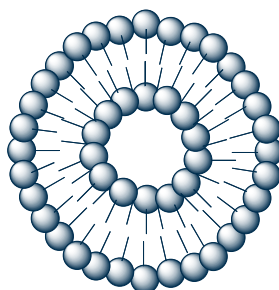


Figure 4.1. Illustration of a liposome.

Diacetylenes are an important class of artificial lipids that can form liposomes upon polymerisation in solutions. Structurally ordered diacetylene monomers in either vesicle forms, or thin films can be polymerised by the application of 254nm UV light in solution.^{[99] [100]} γ -radiation can also be used to polymerise solid powders of diacetylenes.^[39] Upon irradiation the diacetylenes undergo a 1,4-addition to form ene-yne polymer chains.^{[99] [100] [39] [101]} The polymerisation will only proceed when the diacetylenes are in a structured lattice with the required geometry to undergo the 1,4-addition. Propagation of the polymerisation is thought to be from a dicarbene species.^[101] This polymerisation mechanism can be seen in Figure 4.2.

The resulting blue materials can undergo a colour change to red upon addition of a stimulus. The colour change is caused by the perturbation of the conformation of the polymer such that there is an

increase in rotational freedom leading to the decrease in coplanarity and so the length of effective conjugation is reduced and the backbone is de-symmetrised.

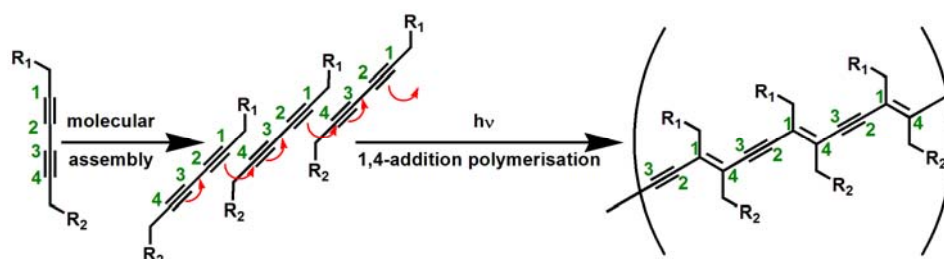


Figure 4.2. 1,4-addition ene-yne polymerisation of diacetylene chains.

In addition to a distinct colour change from blue to red, it has been observed that there is an activation of fluorescence upon the change from blue to red. The mechanism for fluorescence switching is not fully understood, however, it is thought to occur by the radiative decay of the lowest excited state B_u . In the blue phase this excited state has an A_g symmetry that has the dipole forbidden transition for the decay from the singlet excited state and so no fluorescence is possible. In the red phase this excited state is no longer symmetrical and the decay is an allowed transition, thus producing a fluorescent emission spectrum.^[39]

This transformation makes this type of substrate valuable in the synthesis of chemo and biosensors. Functionalisation of the diacetylene prior to polymerisation allows for the incorporation moieties that can interact with a great deal of substrates leading to a large scope for the potential application of sensing materials.^[39] The polydiacetylene structures can be sensitised to a great number of types of stimuli that can range from thermal,^[102] chemical,^[103] electrochemical,^[104] and biological.^[39] ^[99] However, the observed colour change is typically irreversible, where once the colour change has occurred the polydiacetylene materials will not revert back even once the initial

stimulus has been removed. Figure 4.3 shows a schematic of the possible interactions available for use in PDA sensing applications.

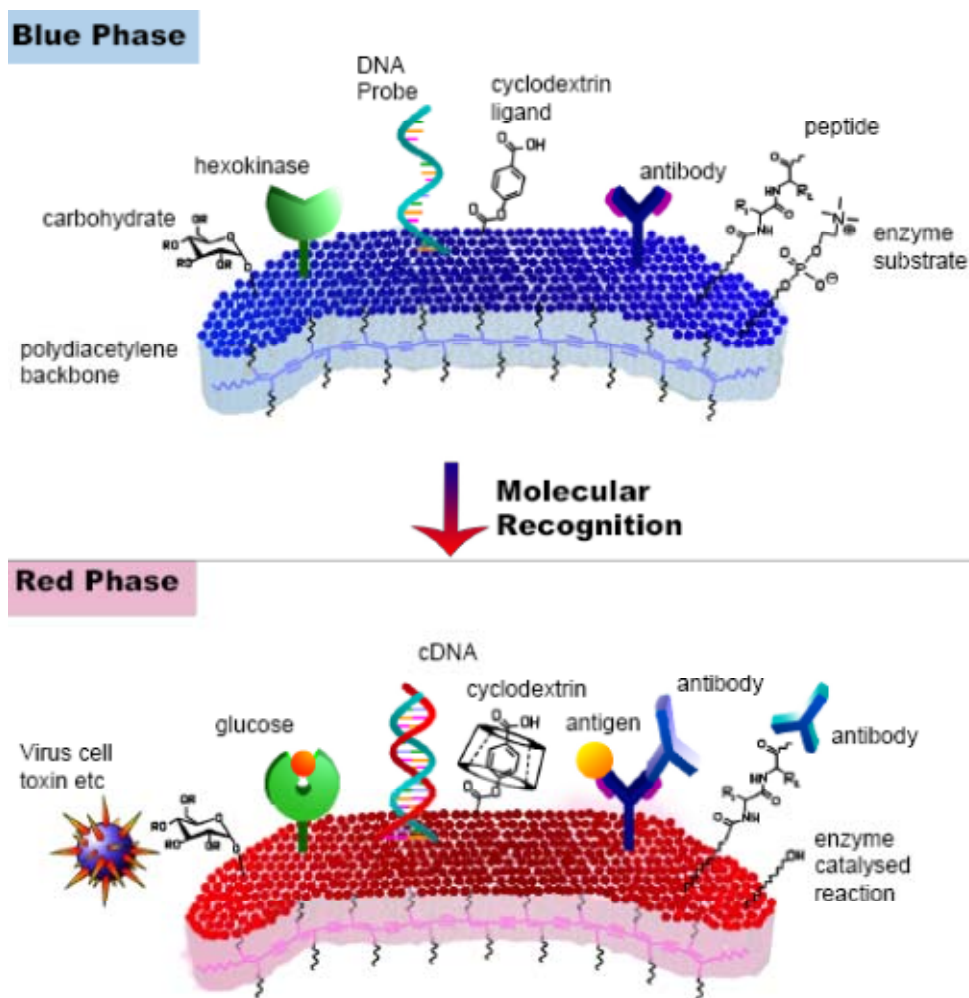


Figure 4.3. A schematic representation of the possible interactions that can be incorporated into colorimetric polydiacetylene sensors.^[39]

Polydiacetylene liposomes and thin films make good sensing substrates due to the signal amplification and easy readout of a positive signal. Work carried out by Charych and co-workers have shown that it is possible to create thin films or liposomes that are selectively sensitive down concentrations of 10^{-10} M.^[105]

Several polydiacetylene systems have been synthesised. The incorporation of a sialic acid functionalised diacetylenes in a mole ratio of

5% sialic acid diacetylene to 95% pentacosadiynoic acid produced a liposomal suspension that was sensitive to the influenza virus. The influenza virus binds to the α -glycolipid of the sialic acid. Upon viral binding to the sialic acid, the colour of the sensor changes from blue to red. The transformation can be measured by observing UV-Vis absorption, where the λ_{max} of the blue phase = ~ 630 nm; binding converts the liposome or film to the red phase and a change in λ_{max} to ~ 550 nm occurs.^[105] The structure of the sialic acid diacetylene is shown in Figure 4.4.

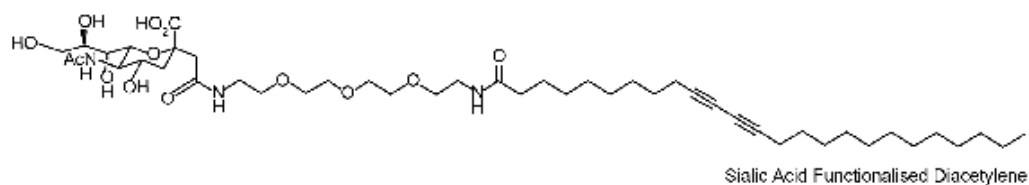


Figure 4.4. Structure of sialic acid diacetylene

Correspondingly, it was found that the non-covalent incorporation of gangliosides in the presence of a promoter diacetylene with pentacosadiynoic acid could produce sensors that were selective for specific neurotoxins.^[105] Two gangliosides were incorporated into the PDA matrix, G_{T1b} and G_{M1} . G_{T1b} which is a ganglioside found in the neuromuscular junction, which is the target for the botulinum toxin responsible for botulism. G_{M1} ganglioside is found on the nerve cells in the intestines and is affected by the cholera toxin.^[105] The gangliosides G_{T1b} and G_{M1} are shown in Figure 4.5.

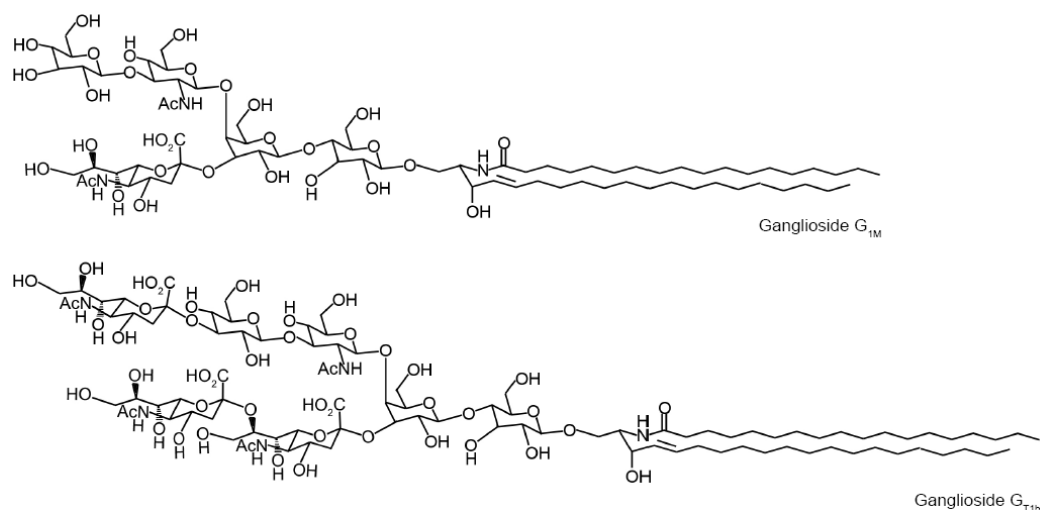


Figure 4.5. Structure of gangliosides G_{T1b}, and G_{M1}.

It was found that the matrices formed with the gangliosides inserted required a promoter diacetylene present in order to induce a colour change upon binding of the required toxin.^[105] The promoter molecules could be either the sialic acid diacetylene or a lactose derived diacetylene.^[105] Optimal ratios of ganglioside, promoter and pentacosadiynoic acid were defined as 5% ganglioside : 2-5% promoter diacetylene to 90-93% pentacosadiynoic acid. Above these ratios the resulting matrix became unstable.^[105] In particular the lactose diacetylene was found to form unstable polymer arrays when in concentration above 2%, whereas the sialic acid formed stable arrays at up to 5% concentration.^[105] The promoter compounds were found to not participate in the binding event with the toxins, but were required for a colour change upon binding to occur. It was thought their function was to lower the activation energy for the transformation from blue to red.^[105] It was also suggested that the interaction between the ganglioside and the toxin interfered with the promoter diacetylenes headgroup *via* steric interactions inducing the colour change observed.^[105]

The introduction of other toxins and agents, including the pertussis toxin, diphtheria toxin and BSA in addition to changing the pH and salt conditions gave a baseline colorimetric response of 5% and showed that the films were selective for their required toxins.^[105] It was found that the

sensing materials underwent chromaphoric changes rapidly, such that within one second of the addition of the substrate, 75% of the colorimetric response (CR) had occurred.^[105] This is exemplified by the addition of the cholera toxin to the films functionalised with G_{M1}, as shown in Figure 4.6. The formula to calculate the CR is given by Equation 4.1.

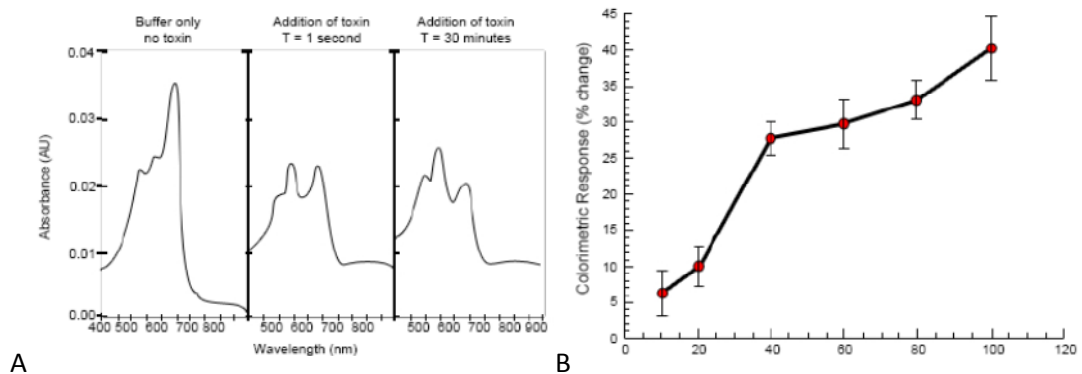


Figure 4.6. A) UV-Vis spectra for cholera toxin addition over time. B) Graph of the colorimetric response plotted % vs time.^[105]*

$$B_0 = \left(\frac{A_{B_0}}{(A_{B_0} + A_{R_0})} \right)$$

1
**A_{B0}/A_{R0} signifies the intensity at
 $\lambda = 550 / 630$ nm prior to addition of
stimuli**

$$B_1 = \left(\frac{A_{B_1}}{(A_{B_1} + A_{R_1})} \right)$$

2
**A_{B1}/A_{R1} signifies the intensity at
 $\lambda = 550 / 630$ nm after the addition of
stimuli**

$$CR = \left[\frac{(B_0 - B_1)}{B_0} \right] \times 100\%$$

3
**Colorimetric Response calculation
as a percentage change relative to B₀**

Equation 4.1. Formulae for calculating the colorimetric response of polydiacetylene sensor.

Although most polydiacetylenes have irreversible colorimetric switching, there have been examples where the colour change can be made to be reversible. Zou and co-workers have successfully produced

reversible thermochromatic PDA films.^[106] They incorporated functionalised azobenzene dyes into the diacetylene moiety. Nitro, cyano and methyl groups at the 4 position of the azobenzene group have been used.^[106] The structures of the functionalised diacetylenes are shown in Figure 4.7.

Thin films of the 1% solutions of azobenzene diacetylenes were cast onto silicon wafers prior to irradiation with UV-light. It is thought that the dye molecules increase the π - π stacking interactions between the side chains of the polydiacetylene in such a way that stabilises the liposome conformation to increased temperature.

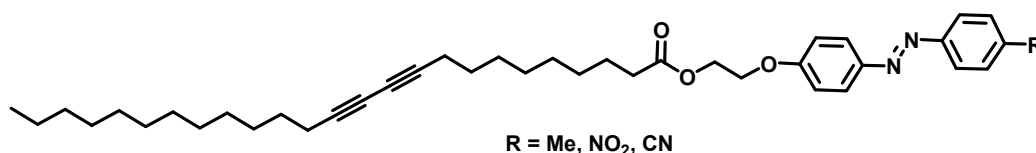


Figure 4.7. Structure of the derivatised Azobenzene diacetylenes.

It was found that the films underwent three transitions upon heating.^[106] Generally, from room temperature to above 50 °C the films changed colour from blue to purple.^[106] From > 50 °C up to 75 °C the films changed to red from purple.^[106] This transformation was fully reversible and the films went blue upon cooling back to room temperature. Heating to 150 °C produced films that were partially reversible, where cooling produced a purple colour that did not revert back to blue. Increasing the temperature to up to 170 °C caused the films to become irreversibly red.^[106] By increasing the temperature further to above 170 °C, the films turned yellow; an effect that was attributed to melting effects, that once cool reverted back to red.^[106] This transformation is shown schematically in Figure 4.8. The critical temperatures for each functionalised azobenzene polydiacetylene film were measured. It was found that the films made from the cyano

functionalised azobenzene diacetylene were the most stable of the films produced. The data recorded is shown in Table 4.1.

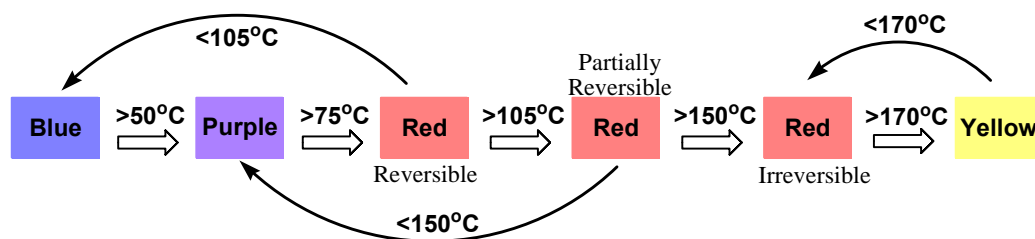


Figure 4.8. Schematic of reversibility of the functionalised polydiacetylene films.

Azobenzene	T_M °C	T_D °C	T_L °C	T_H °C
Nitro	182	291	60	160
Cyano	188	289	57	162
Methyl	173	286	50	154

T_M = Melting Temp. T_D = Decomposition Temperature.
 T_L = Reversibility Temperature. T_H = Irreversibility Temperature

Table 4.1. Critical Temperatures for the azobenzene polydiacetylene films.

4.2. Aims and Objectives.

Naphthalene and ferrocene functionalised diacetylenes were targeted as initial aims for the formation of polydiacetylene liposomes, The ferrocene functionalised diacetylene was formed on the premise of achieving a redox active liposome that could interact with both β -cyclodextrin and β -cyclodextrin polymers. The naphthalene functionalised diacetylene was produced on the basis that addition of CBPQT^{4+} might not only give a colorimetric response, but also the binding might be measured by the change in fluorescence. The target diacetylenes are shown below in Figure 4.9.

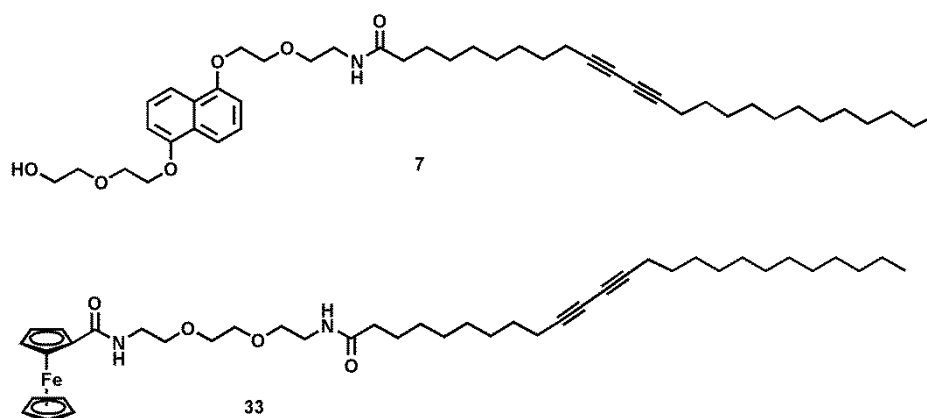
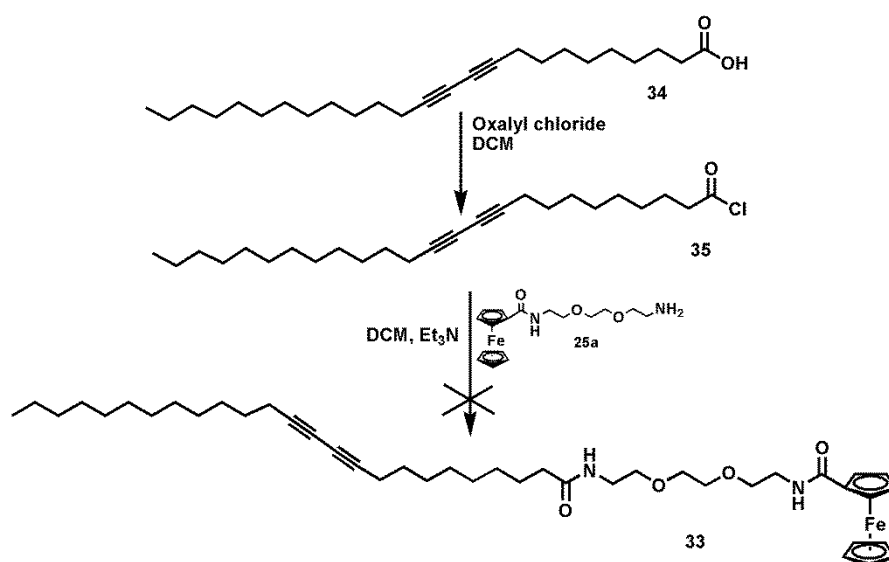


Figure 4.9. Functionalised diacetylene target molecules.

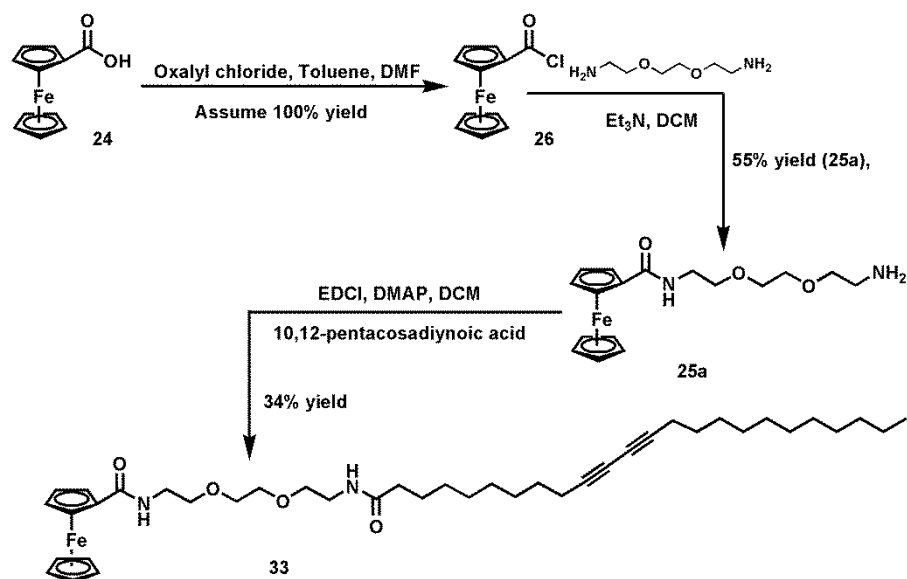
4.3. Results and Discussion.

4.3.1 Synthesis of functional diacetylene monomers.



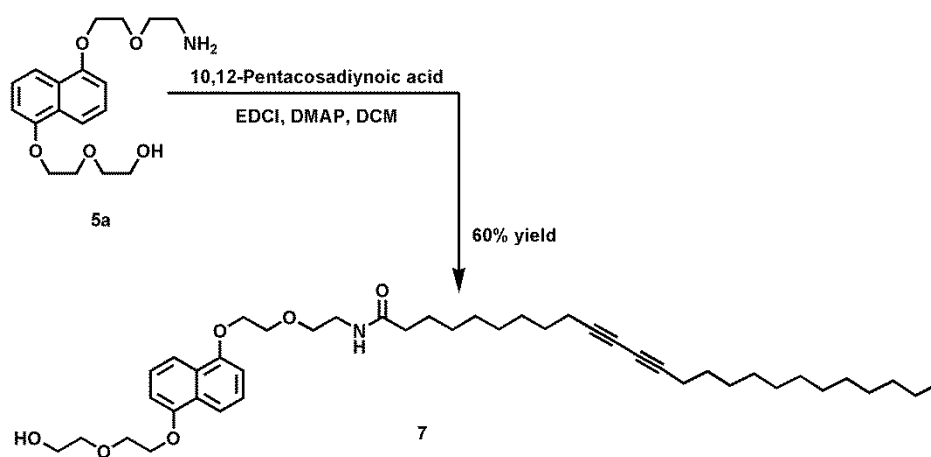
Scheme 4.1. Synthesis of functionalised ferrocene diacetylene via the PDA acid chloride.

The synthesis of the functionalised diacetylenes was initially attempted via the formation of the 10,12-pentacosadiynoic acid chloride followed by the treatment with the required amine, as shown in Scheme 4.1. When it was found that this route failed to yield the required ferrocene functionalised product **33**, coupling reactions using EDCI were carried out successfully. The coupling of the amine **25a** with 10,12-pentacosadiynoic acid (PDA) gave the required functionalised diacetylene **33**. This compound was fairly light sensitive and all work up conditions were carried out in the dark.



Scheme 4.2. Synthetic scheme for the synthesis of the ferrocene diacetylene monomer 33.

The ferrocene amine **25a** was synthesised from the carboxylic acid starting material via the acid chloride intermediate as previously described in §2.3.2. The EDCI coupling between the freshly prepared ferrocene amine **25a** with 10,12-pentacosadiynoic acid gave the required diacetylene as a glassy orange solid in a 34% yield, as shown in Scheme 4.2.



Scheme 4.3. Synthetic scheme for the synthesis of the naphthalene diacetylene 7.

The naphthalene diacetylene **7** was formed by an EDCI coupling reaction from the freshly prepared naphthalene amine **5a** in a 60% yield as a pale blue light sensitive solid as indicated in Scheme 4.3. The synthesis of the naphthalene amine from the 1,5-dihydroxynaphthalene is described in § 2.3.1.

4.3.2 Liposome Formation and Analysis.

The liposomes were formed by following the protocol described by Ahn and co-workers.^[107] First the diacetylenes were dissolved in chloroform and the solvent was evaporated using nitrogen gas. The thin layers of diacetylenes formed was then suspended in water and heated to 70-80°C for 15 minutes. This heating was then followed by sonication at 70-80°C for 15 minutes and the mixture was then immediately filtered through 0.8µm filters. The filtrate was then stored at 4°C for 18 hours prior to irradiating with UV light. All work was carried out in the dark and the samples were wrapped in tinfoil to avoid exposure to the lights from the overhead lighting. The samples were irradiated with 254 nm UV light for 15 minutes. A colour change from clear to blue indicated that liposomes had been created. The reaction set up is illustrated in Figure 4.10.^[107]

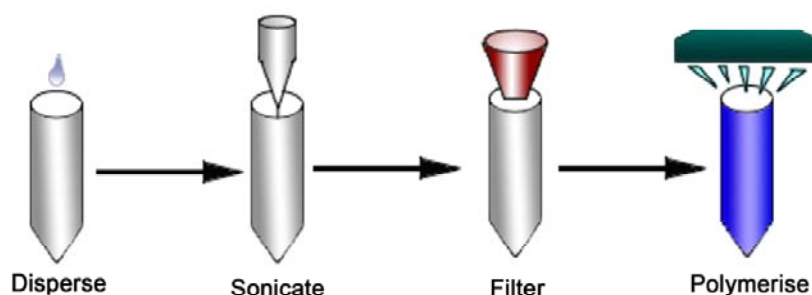


Figure 4.10. Illustration of general liposome formation procedure.^[107]

A number of ferrocene liposomes were attempted, where variable amounts of FcDA were mixed with pentacosadiynoic acid (PCDA). However, the successful formation of the liposomes varied to a large degree. The only consistent formulation was that of the 100% ferrocene diacetylene and the 100% PCDA liposome. The 10% FcDA liposomes failed to form in all but one instance. The 20, 40, 60, and 80% FcDA liposomes formed liposomes to different degrees that were not consistently reproducible. The intensity of the blue solutions produced was fairly low. It should be noted that at the point of filtration there was a large amount of undissolved material left, thus reducing the amount of liposomes that could be polymerised. The UV-Vis of PCDA polydiacetylene and the 100% ferrocene polydiacetylene (FcDA) are shown in Figure 4.11.

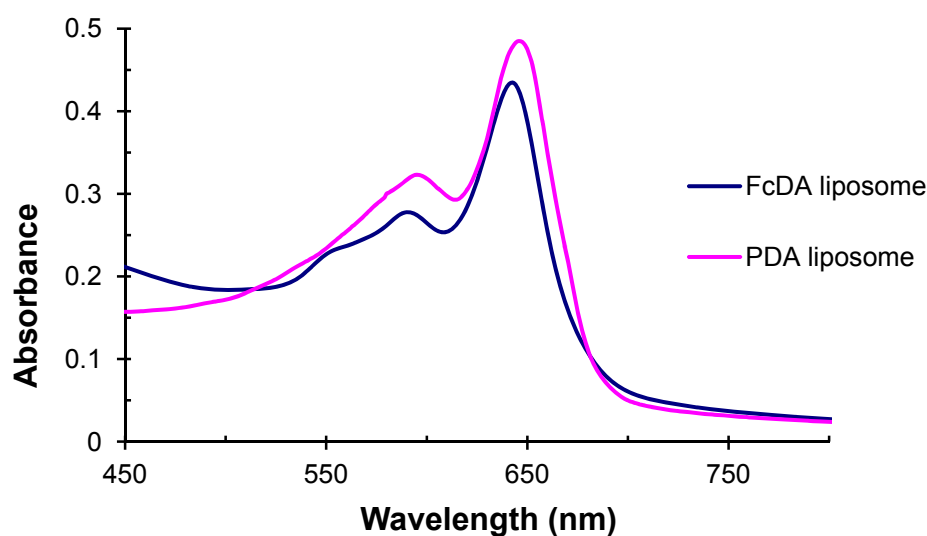


Figure 4.11. UV-Vis of polydiacetylene liposomes.

UV-Vis experiments were carried out on samples of the 100% PCDA and 100% ferrocene polydiacetylene liposomes with poly β -cyclodextrin,^[108] then adamantanol, and with β -cyclodextrin. To 2 mL samples of 100% FcDA liposome varying quantities of β -cyclodextrin

polymer were added; 10^{-2} M, 2×10^{-2} M, and 3×10^{-2} M, where the FW = 3000 g/mol. The structure of the polymer is shown in Figure 4.12.^[108]

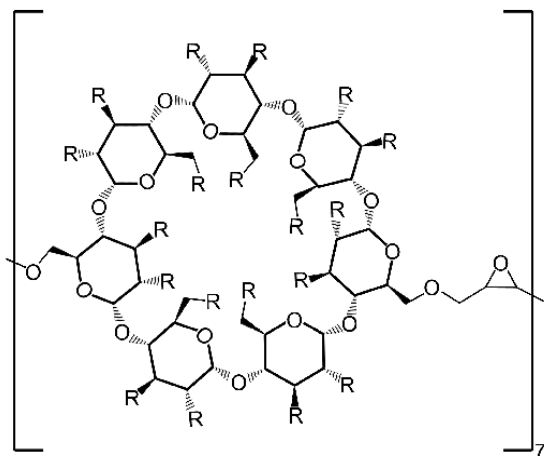


Figure 4.12. Structure of the β -cyclodextrin polymer.^[108]

The colour of each sample changed from blue to shades of purple/pink with increasing amounts of β -cyclodextrin polymer. The spectra are shown in Figure 4.13. The colorimetric response (CR) of the liposomes to the β -cyclodextrin polymer were calculated where the A_{blue} was measured at $\lambda = 646$ nm and A_{red} was measured at $\lambda = 548$ nm. It was found that the CR for these liposomes was 51% after the addition of 3 equivalents of the polymer. The CR was measured using Equation 4.2.

$$CR = \left[\left(\frac{B_0}{B_1} \right) \right] \times 100$$

$$B_x = \left(\frac{A_{\text{blue}_x}}{(A_{\text{blue}_x} + A_{\text{red}_x})} \right)$$

x = before (0) / after stimuli (1)

Equation 4.2. Formulae for calculating the colorimetric response.

To each of these samples varying quantities of adamantanol were added; 10^{-2} M, 2×10^{-2} M, and 3×10^{-2} M. The adamantanol failed to fully

dissolve and had little or no effect on the colour of the samples. The addition of β -cyclodextrin to 2 mL samples of 100% FcDA liposome caused the liposomes to turn pink and partially precipitate out of solution. The cloudy pink suspension that resulted failed to settle and remained cloudy even after filtering to the point that the UV-Vis spectrum could not be recorded.

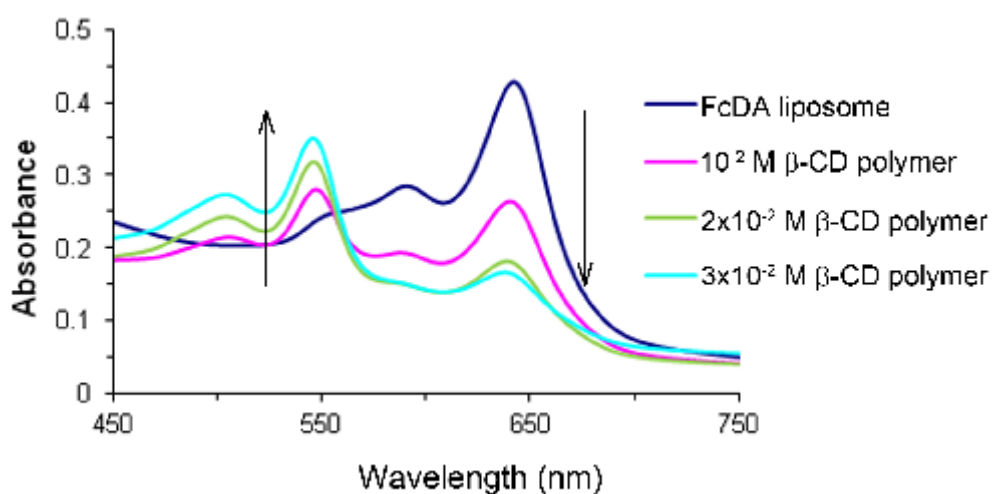


Figure 4.13. UV-Vis of FcDA liposome with β -cyclodextrin polymer.

The corresponding experiments were carried out on 2.5 mL samples of the PCDA liposomes. As the β -CD polymer was added the solutions also turned purple / pink. Figure 4.14 shows the spectra recorded for the addition of β -cyclodextrin polymer to the PCDA liposomes. Similarly, addition of adamantanol also had no effect on the PCDA liposomes. The addition of β -cyclodextrin to 2.5 mL samples of 100% PCDA liposomes had no effect, with the β -cyclodextrin failing to completely dissolve. The intensity of the colour change relative to that of the FcDA liposomes and β -CD polymer is reduced with a slight λ_{\max} blue shift of 10 nm and 7 nm as shown in Figure 4.15. The colorimetric response using $A_{\text{Blue}} \lambda = 641$ nm and $A_{\text{red}} \lambda = 531$ nm was found to be after three equivalents of β -CD polymer to be 54.8%. From the results it

can be seen that there are some subtle differences between the FcDA and the PCDA liposomes.

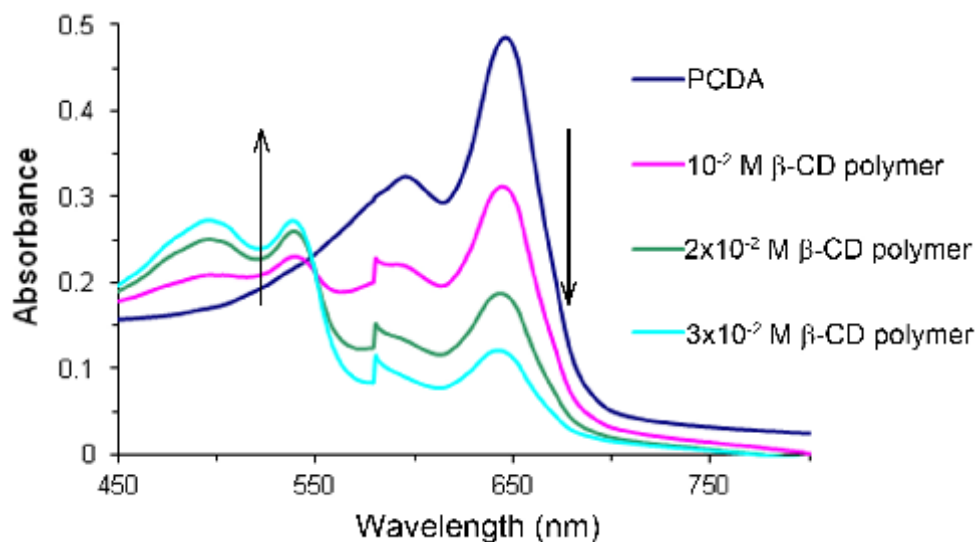


Figure 4.14. UV-Vis of PCDA liposome with β -cyclodextrin polymer.

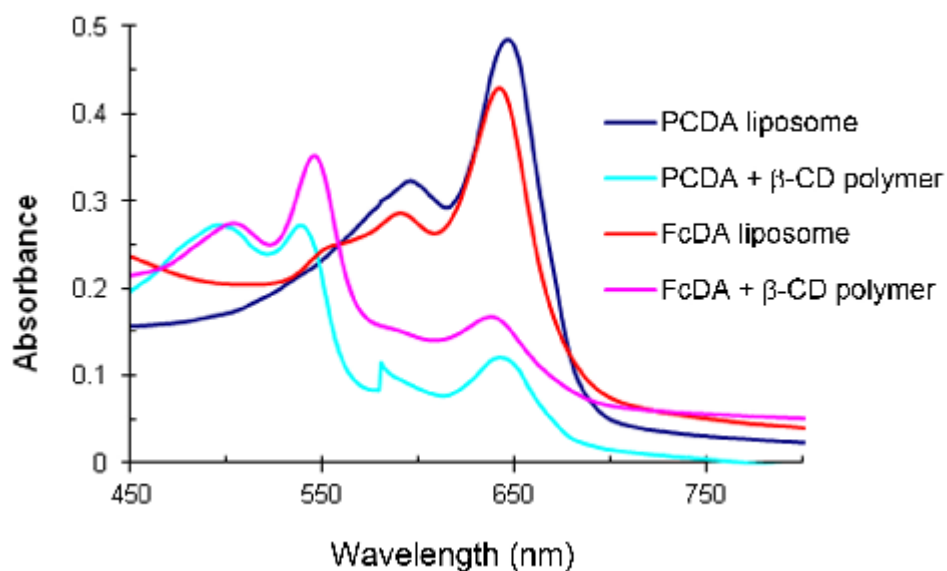


Figure 4.15. UV-Vis of the liposomes with 3×10^{-2} M of β -cyclodextrin polymer added.

Dynamic light scattering (DLS) was used to measure the size of the liposomes formed. Of the liposomes formed the results from the DLS

showed that with increasing amounts of the ferrocene the size of the liposomes increased. In this instance the 20% FcDA liposome precipitated out of the water before DLS could be measured. As can be seen from Table 4.2, the sizes of liposomes formed varied from one batch to another. This may be due to the amounts of ferrocene diacetylene that successfully dissolved into the aqueous media at the formation of the liposomes prior to polymerisation. It was also found that the liposomes started to aggregate under the fluorescent lighting over time.

Liposome	Z_{Av} (nm)	Pdl	Diameter (nm)	%age	Width (nm)
100% FcDA	134.6	0.251	186.9	100	111.4
100% FcDA	132.8	0.223	175.0	100	99.22
10% FcDA	123.8	0.196	155.3	100	75.67
40% FcDA	133.3	0.169	164.6	100	81.05
100% PCDA	146.6	0.361	207.1	98.2	129.6

Table 4.2. DLS measurements for the liposomes formed.

As the 100% Fc DA liposome consistently formed under the conditions described above we decided to concentrate upon the interactions that could be observed compared to those found with the 100% PCDA liposomes. It was also found that the PCDA liposome was generally a larger size with Z_{Av} (d.nm) = 146.6nm while the 100% FcDA liposome had Z_{Av} (d.nm) = 132.8nm liposome. Figure 4.16 shows the graphical data obtained for the 100% ferrocene diacetylene liposome.

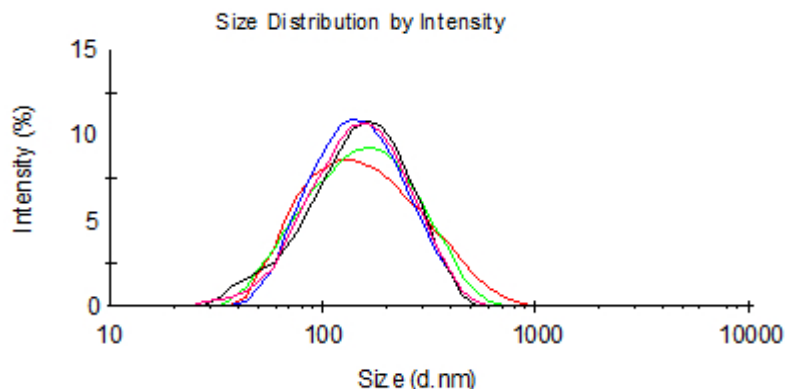


Figure 4.16 DLS data recorded for FcDA liposome.

Cyclic voltammetry experiments were run in 0.1 M sodium chloride solutions against a silver/silver chloride electrode. The redox wave for the FcDA liposome was recorded, where the half wave potential $E_{1/2}$ was recorded as 0.55 V. 10^{-2} M of the β -cyclodextrin polymer was then added to the solution and the redox wave was then recorded for the complex. It was found that the half wave potential had shifted to 0.6 V. The shift in the half wave potential showed that the ferrocene had interacted with the β -cyclodextrin polymer in a manner that hindered the oxidation reduction process. The cyclic voltammogram for the 100% PCDA liposome was also performed to show that the redox activity came purely from the ferrocene moiety. The cyclic voltammograms for the FcDA liposome with the addition of β -cyclodextrin polymer is shown in part A of Figure 4.17. Part B shows the CV spectrum recorded for the PCDA liposome.

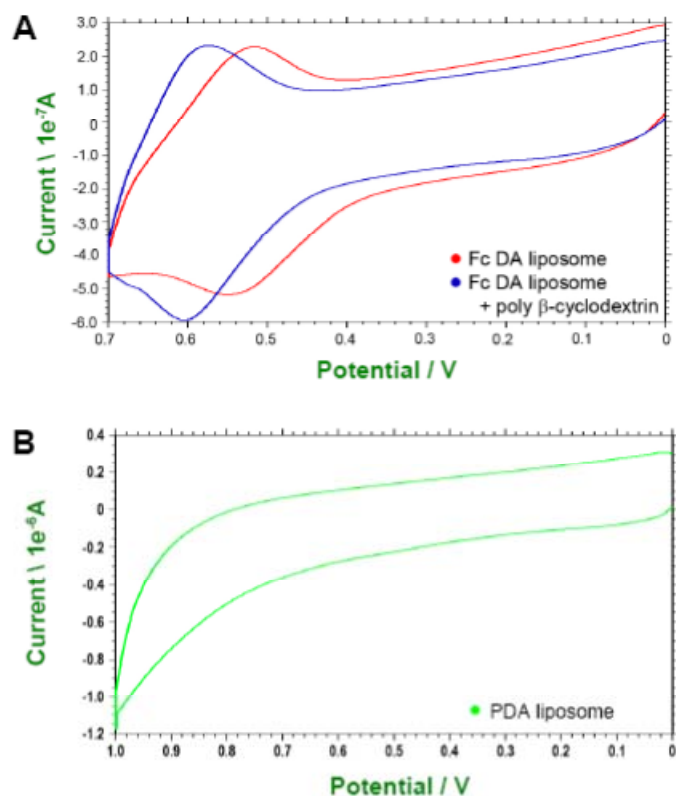


Figure 4.17. CVs of A) FcDA liposome (red) with β -cyclodextrin (blue) B) 100% PCDA liposome.

Formation of liposomes using the naphthalene diacetylene **7** was also attempted. Different ratios of the naphthalene diacetylene with pentacosadiynoic acid were performed, however, on every occasion no liposome formation occurred. Increasing temperature and sonication times appeared to have no effect on the formation of the liposomes. Extended irradiation of the samples also had no effect on this substrate. After filtration there was a significant amount of the diacetylene starting materials remaining, indicating that the solubility of the material may have had a significant effect on the formation of the liposomes.

4.4 Conclusions and Future Work.

4.4.1. Conclusions.

In conclusion two functionalised diacetylenes have been synthesised in good yield from the chosen substrates. Using these functionalised diacetylenes, the formation of functionalised liposomes with pentacosadiynoic acid has been investigated with varying success. The most successful formulation came from the 100% ferrocene diacetylene.

Analysis of the 100% ferrocene diacetylene liposome has shown that the ferrocene can undergo host-guest interactions with both β -cyclodextrin and β -cyclodextrin polymer. UV-Vis experiments showed that the chromaphoric shifts upon addition of β -cyclodextrin polymer for the ferrocene liposome was red shifted by up to 10 nm relative to the shifts observed for the PCDA liposomes with β -cyclodextrin polymer. Additionally, the colorimetric response for the ferrocene based liposomes was reduced in comparison to the measured response for the PCDA liposomes.

DLS measurements have shown that the average size of the ferrocene liposomes is significantly smaller than that of the unfunctionalised PCDA liposome. From the cyclic voltammetry experiments it can be seen that the ferrocene liposomes are redox active, where addition of β -cyclodextrin polymer modulates the half wave potential by up to 0.05V.

Failure to form the naphthalene functionalised liposomes may have been due to the insolubility of this substrate in aqueous media.

4.4.2. Future Work.

As an extension to the work carried out, further investigation into the different percentages of functionalised diacetylene liposomes would have been carried out. The effect of lower percentages of FcDA on the redox activity could be investigated.

Further tuning of the procedure to form the naphthalene functionalised liposomes could be investigated, where variation of the ratios of naphthalene diacetylene : pentacosadiynoic acid could be performed. Once these liposomes had been formed, analysis to investigate host-guest complexation with CBPQT⁴⁺ and the displacement by the addition of TTF could have been carried out using techniques such as UV-Vis, fluorescence, ITC and CV.

5.

Pseudorotaxanes as tunable micelles.

5.1. Introduction.

Surfactant molecules consist of a polar head group and a non-polar tail. The polar head group can be cationic, anionic, amphoteric or non-ionic.^[109] Examples of the different types of surfactant include sodium dodecyl sulfate (SDS), cetyl trimethylammonium bromide (CTAB), cocamidopropyl betaine (CAPB) and palmityl alcohol.^[109] Surfactant molecules lower surface tension and can reduce the interfacial tension between two liquids.^[110] Surfactants can be naturally occurring or synthetic. The general structure is illustrated in Figure 5.1.

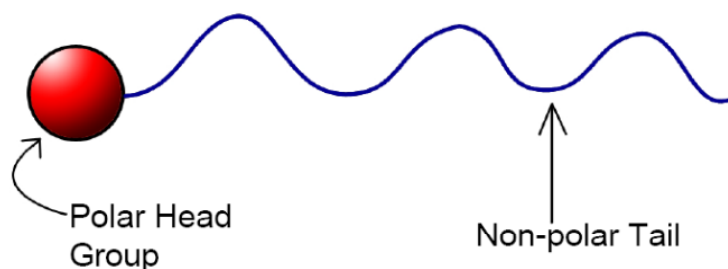


Figure 5.1. Illustration of a typical surfactant molecule.

Surfactant molecules in solution will spontaneously form disordered aggregates called micelles once the concentration of surfactant molecules has reached or surpassed a critical level, referred to as the critical micelle concentration (CMC).^[109] The formation of these 3-D structures is fully reversible where the individual molecules are held together by non-covalent interactions such as the hydrophobic effect.^[111] Micelles tend to be either spherical or cylindrical in shape. It has been shown that spherical micelles will aggregate to form rod-like structures when the concentration of the micelle solution rapidly increases.^[112]

Micelles have two forms in which they can assemble: micellar and reverse micellar structures. Normal micelles present the polar head groups to the aqueous solvent, while the alkyl, non-polar tails are found inside the structure.^[112] Reverse micelles have the non-polar tails on the

outside; presented to the solvent, while the head groups are found inside the micelle.^[112] Reverse micelles mimic cellular environments, where the non-polar tails form an effective barrier between the organic solvent and the water within the cavity of the micelle and can fit proteins within the cavity formed.^{[113] [114]} The two forms are shown in Figure 5.2. The formation of reverse micelles over micelles can be controlled by tuning the proportions of water to non-polar solvent ratios present. It has been found that micelles are fairly stable, where there is evidence of the retained structures in the gas phase.^[112] The applications for micelles and individual surfactant molecules are wide ranging: from detergents,^[111] to use in biomolecule trapping^[112] and protein folding^[113] to the mediation of nanoparticle formation processes.^{[115] [116]}

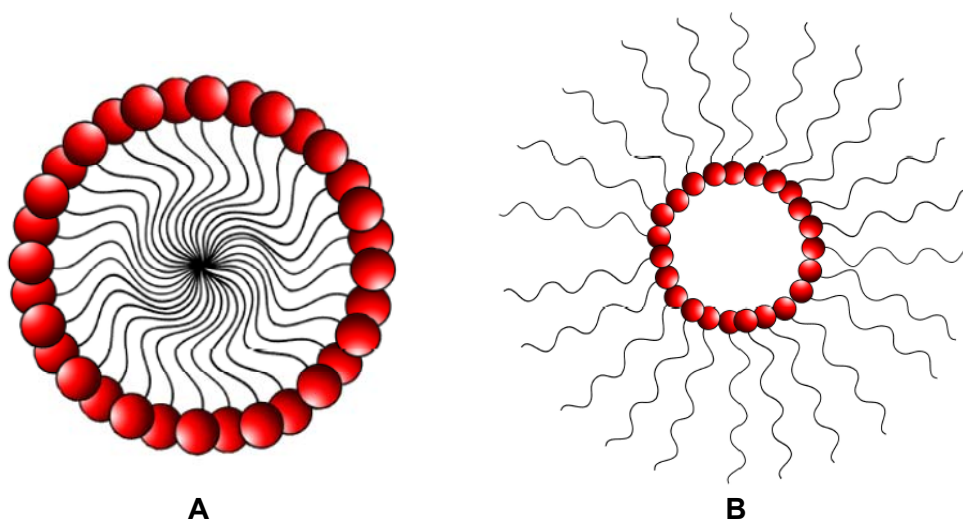


Figure 5.2 Illustration of A) Micelle structure. B) Reversed micelle structure.

Examples of the potential applications include work carried out by Sharon and co-workers.^[112] The properties of CTAB micelles were investigated by electrospray mass spectroscopy. CTAB micelles were prepared by two different methods in order to form normal and reversed micelles. Micelles were first formed by the dissolution of CTAB into aqueous solutions of ammonium acetate at pH 7.0 or 8.0. The concentration of the CTAB used was 8.5 mM to ensure that micelle

formation occurred.^[112] The reverse micelle form was produced by dissolving the CTAB into hexanol under sonication conditions. Aliquots of water, 10 mM ammonium acetate, or 200 mM ammonium acetate were added to enhance the solubility and so the micellisation process. After allowing the solution to equilibrate for 24 hours, horse heart myoglobin in water was added, and the mixture was sonicated until a clear micelle solution was formed.^[112] The structure of CTAB and illustrations of the resulting micelles are shown in Figure 5.3.^[112]

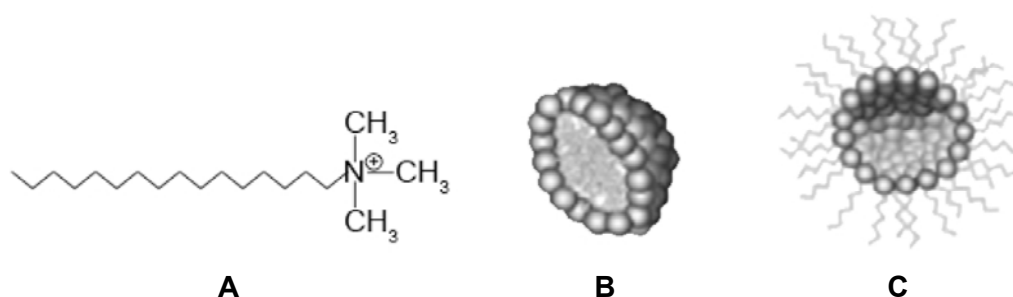


Figure 5.3. A) Structure of CTAB molecule and illustrations of B) micelle and C) reversed micelle.^[112]

Analysis by electrospray mass spectroscopy and tandem mass spectroscopy was carried out on the micelle samples.^[112] The solutions were rapidly evaporated under high pressure to create the mass spectroscopy samples. The results showed that ion exchange had occurred with the micelles created from the aqueous method, where the bromide was exchanged with acetate ions.^[112] Salt exchange did not occur with the reverse micelles where the polar head group was orientated within the core of the micelle structure.^[112]

The results showed that the micellar structures were retained in the gas phase. Additionally, it was found that the micelles were larger than the expected size of ~ 90 CTAB molecules per micelle.^[112] The normal micelles were measured to be > 500 molecules in size. Mass spectroscopy of the reversed micelles showed that the horse heart myoglobin was successfully incorporated into the cavity of the micelle. It

was also found that for every 1 myoglobin there were 230 - 310 CTAB molecules per micelle.^[112] The large micelle sizes were attributed to the aggregation and coalescence of smaller spherical micelles into larger rod-like structures as a result of the evaporation processes used to create the samples for MS analysis.^[112] The MS results are shown in Figure 5.4.^[112]

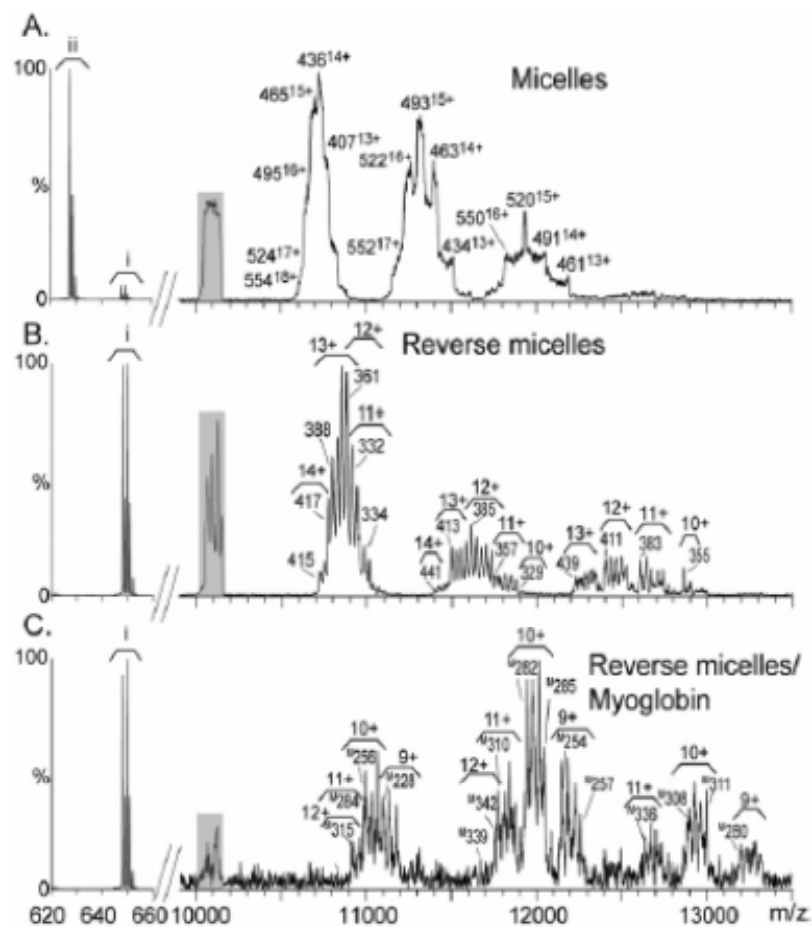


Figure 5.4. Comparison of tandem mass spectra at m/z 10 000 for regular micelles in 200 mM ammonium acetate (A), reverse micelles in H₂O (B), and reverse micelles incorporating myoglobin in 10 mM ammonium acetate (C).^[112]

Furthermore, work carried out by He on the formation polymer based micelles shows the phase transfer applications for micellar constructs.^{[117] [118]} Block co-polymers made of poly((1,2-butadiene)-*block*-ethylene oxide) (PB-PEO) spontaneously form micelles with the poly(butadiene) block segregated within the core of the micelle,

presenting the poly(ethyleneoxide) chains to the solvent of choice. Ionic liquid; 1-butyl-3-methylimidazolium hexafluorophosphate [BMIM] [PF₆] and water will readily form these micelle structures.^[118] The general structures whether spherical, cylindrical or vesicle form was dictated by the length of the PEO block relative to the PB block of the polymer.

The micelles were formed from a 1 wt% solution into [BMIM] [PF₆]. Water was then added to reach from a 1:1 ratio of water to [BMIM] [PF₆]. The mixtures were agitated to allow the micelles to adequately form. After equilibration at room temperature, it was found that the micelles resided within the aqueous layer.^[117] The micelles were a pale blue colour, so the location of the micelles were easily identified by the colour change of the layer from clear to opaque blue.^[117] Upon gradual heating up 75 °C with gentle stirring, the micelles started to migrate from the aqueous layer into the BMIM.^[117] By 90 °C all micelles resided within the ionic liquid layer. Cooling to room temperature led to the transfer back to the aqueous layer.^[117] This process was repeated successfully ten times, showing that the micelles are thermally stable to repeated heating and cooling cycles.^[117]

The hydrodynamic radius (R_h) and size distribution was measured by DLS for micelles at 25 °C, 75, and 90 °C.^[117] It was found that the typical size of the micelles formed was ~80 nm. In aqueous solutions with increasing temperature it was found that the solvent character changed, and the ability of the water to solvate the PEO decreased, leading to a contraction of the R_h from 61 nm down to 57 nm.^[117] Previously it had been shown that the R_h for micelles in [BMIM] [PF₆] did not vary significantly with increasing temperature up to 100 °C.^[117] The cycling from the aqueous to the ionic liquid with increasing temperature is shown in Figure 5.5.

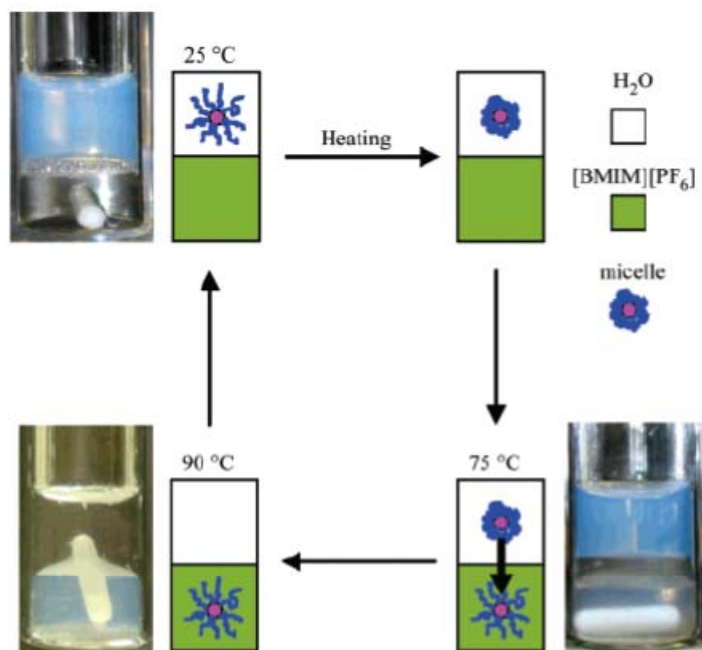


Figure 5.5. Schematic illustration of the round trip of PB-PEO micelles between the [BMIM] [PF₆] and water layers, accompanied by experimental images at each temperature. ^[117]

Formation of the micelles in water under similar conditions to the formation in [BMIM] [PF₆], led to a change in size distribution, the shape of the micelles formed, and the R_h of the micelles^{[117], [118]}. However, from the data recorded, transfer from the [BMIM] [PF₆] layer into the aqueous layer, showed very little variation in size distribution and R_h .^[117] This indicated that the micelles were preserved and crossed the liquid interface intact, rather than dissociating and then reforming from one layer to the other. The R_h data recorded is shown in Figure 5.6. ^[117]

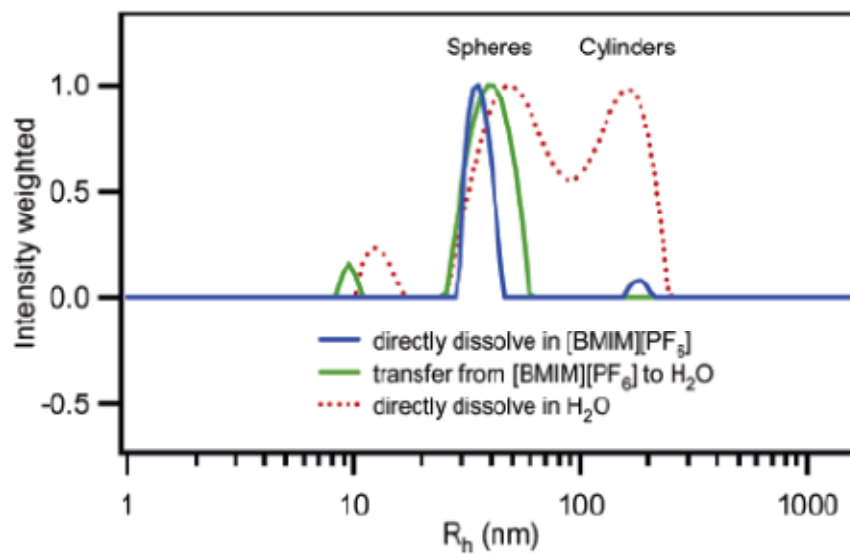


Figure 5.6. Hydrodynamic radius of the PB-PEO micelles in three different solutions (1 wt %) by DLS at ambient temperature.

5.2. Aims and Objectives.

The aims of this project were to produce derivatised trimethylammonium bromide surfactant molecules that could form pseudorotaxanes with the cyclophane CBPQT⁴⁺. Additionally it was hoped that these surfactant molecules could form mixed micelles with the surfactant sodium dodecyl sulfate (SDS), such that further host-guest interactions with CBPQT⁴⁺ could be used to control the assembly and disassembly of the micelle. Initial targets focused upon naphthalene and tetrathiafulvalene systems as shown in Figure 5.7.

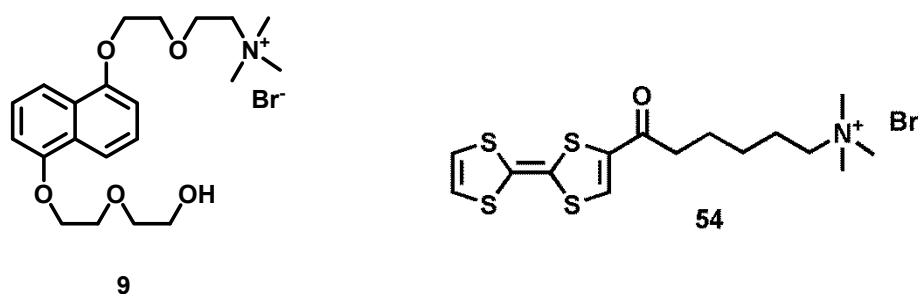
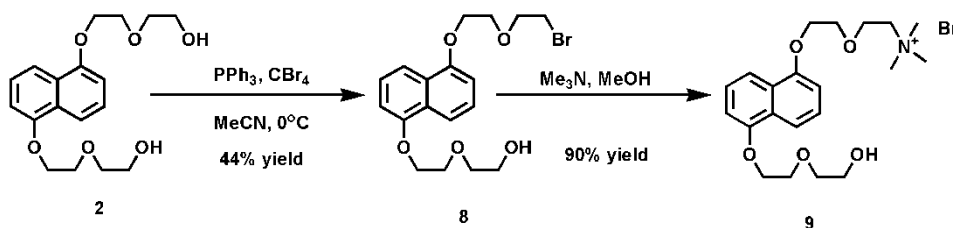


Figure 5.7. Naphthalene trimethylammonium bromide (9) and Tetrathiafulvalene trimethylammonium bromide (45).

5.3. Results and Discussion.

5.3.1. Synthesis of functionalised trimethylammonium bromide surfactants.

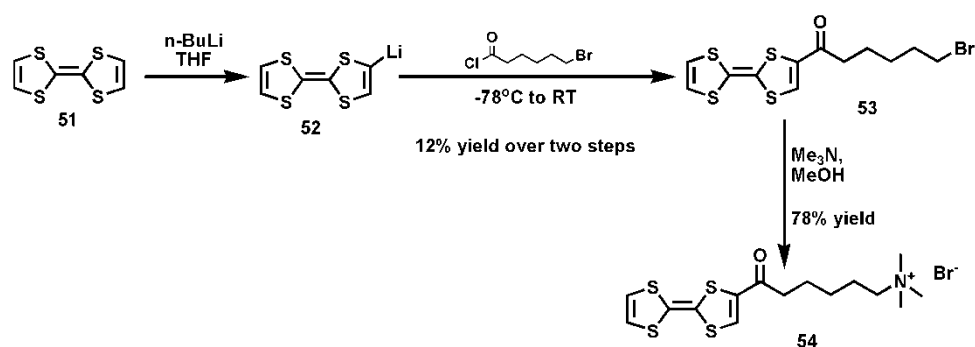
5.3.1.1. Synthesis of naphthalene based surfactant (9).



Scheme 5.1. Synthesis of the naphthalene compound 9.

The synthesis of the naphthalene functionalised trimethyl ammonium bromide compound **9** from the starting naphthalene diol **2** is shown in Scheme 5.1. The reaction of the naphthalene diol **2** to form the naphthalene bromide **8** proceeded with the major product formed being the required monobrominated product **8** in a 44% yield. Any unreacted starting material was recovered in the purification step such that it could be recycled as required. The transformation of the monobrominated naphthalene product **8** into the trimethylammonium bromide **9** was high yielding with very little work up required. The removal of the solvent by reduced pressure also removed the majority of any unreacted trimethylamine from the product. The material was precipitated out of solution and washed thoroughly to remove any traces of the unreacted trimethylamine to afford target **9** in a 90% yield.

5.3.1.2. Synthesis of TTF hexan-1-one-6-Trimethyl ammonium bromide.

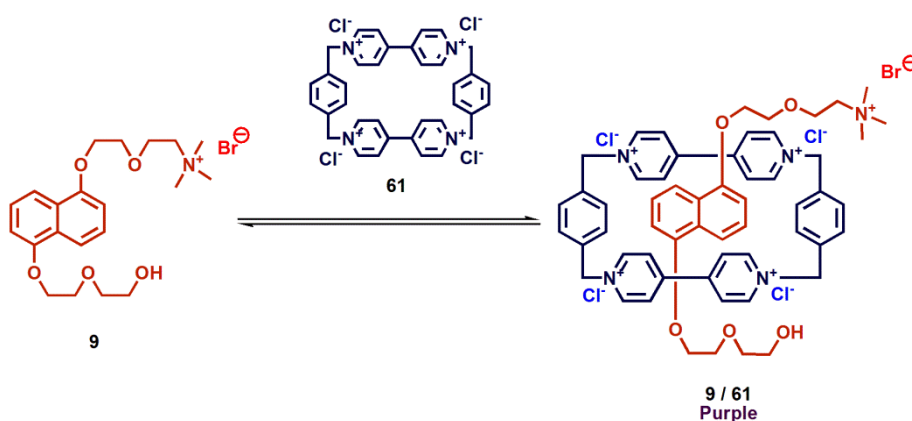


Scheme 5.2. The synthesis of compound 54 from TTF.

Starting from tetrathiafulvalene (**51**), the trimethylammonium bromide functionalised TTF compound (**54**) was prepared in a two-step synthesis, as shown in Scheme 5.2. First the TTF was reacted with *n*-butyl lithium at -78°C to form the lithiated species (**52**).^[119] This compound was then reacted *in situ* with 6-bromohexanoyl chloride to form the 6-bromo-hexanoyl TTF compound (**53**).^[119] Purification of this product was non-trivial requiring three silica column chromatographs to gain pure product in a 12% yield. Displacement of the bromide by heating to reflux in methanol with trimethylamine gave the compound **54** as a dark red/ brown solid. The pure product was recovered by repeated precipitation from methanol by the addition of diethyl ether. Due to the reduced amounts of the TTF derivative that were synthesised only the minimal analysis was carried out, and optimisation of experimental procedures was carried out using the naphthalene derivative.

5.3.2. Complexation of **9** with CBPQT⁴⁺.

The interaction between the monomer **9** with CBPQT⁴⁺ **61** to form the pseudorotaxane as shown in Scheme 5.3, was investigated by a number of techniques including ITC, ¹H NMR, fluorescence and UV-Vis prior to studying the effects of incorporation of compound **9** into SDS micelles.



Scheme 5.3. Pseudorotaxane formation of compound **9** with CBPQT⁴⁺ **61**.

5.3.2.1. Isothermal Titration Calorimetry of compound **9** with CBPQT⁴⁺.

ITC was carried out on the naphthalene trimethylammonium bromide **9** with CBPQT⁴⁺ in water. The experimental details are shown in Table 5.1. Initially the interaction appeared to be incomplete such that the intensity of the peaks produced did not diminish fully to that of dilution effects. However, reduction of the cell concentration had very little effect on the data produced. The data collected for the titration using the lower cell concentration were fitted to a single-set-of-sites binding model. The thermodynamic data calculated from the single set-of-sites binding model are shown in Table 5.2. The recorded data is shown in Figure 5.8.

Experiment	Contents of Cell	Contents of Syringe
1	Water	CBPQT ⁴⁺ 4Cl ⁻ 1.00 mM
2	Nap Me ₃ N ⁺ Br ⁻ 0.051 mM	CBPQT ⁴⁺ 4Cl ⁻ 1.00 mM
3	Nap Me ₃ N ⁺ Br ⁻ 0.021 mM	CBPQT ⁴⁺ 4Cl ⁻ 1.00 mM

Table 5.1. Experimental details of for the ITC of the naphthalene trimethylammonium bromide with CBPQT⁴⁺.

<i>N</i>	3.18 ± 0.22
<i>K_a</i> (M ⁻¹)	8265 ± 553.3
ΔH (cal mol ⁻¹)	-6527 ± 590.7
ΔS (cal mol ⁻¹ K ⁻¹)	-3.97

Table 5.2. Thermodynamic data from the titration of CBPQT⁴⁺ 4Cl⁻ into NapMe₃N⁺Br⁻ **9.**

The binding stoichiometry *N* was found to be greater than 1. This may be associated with salt exchange with the bromide / chloride counter ions, or a change in pH with increasing injections of CBPQT⁴⁺ 4Cl⁻ into naphthalene trimethylammonium bromide, **9**. It may indicate that weak external stacking interactions occur between the CBPQT⁴⁺ and the naphthalene moiety, although this interaction is not evident in other analyses of the complex.

The binding constant *K_a* was found to be diminished in value relative to the *K_a* recorded for the diol **2** with CBPQT⁴⁺, where the *K_a* was measured as 1.48 x10⁶ M⁻¹.^[86] The reduction in *K_a* indicates that the trimethylammonium moiety has a slightly repulsive interaction with CBPQT⁴⁺ which in turn reduces the overall binding stability of the complex.

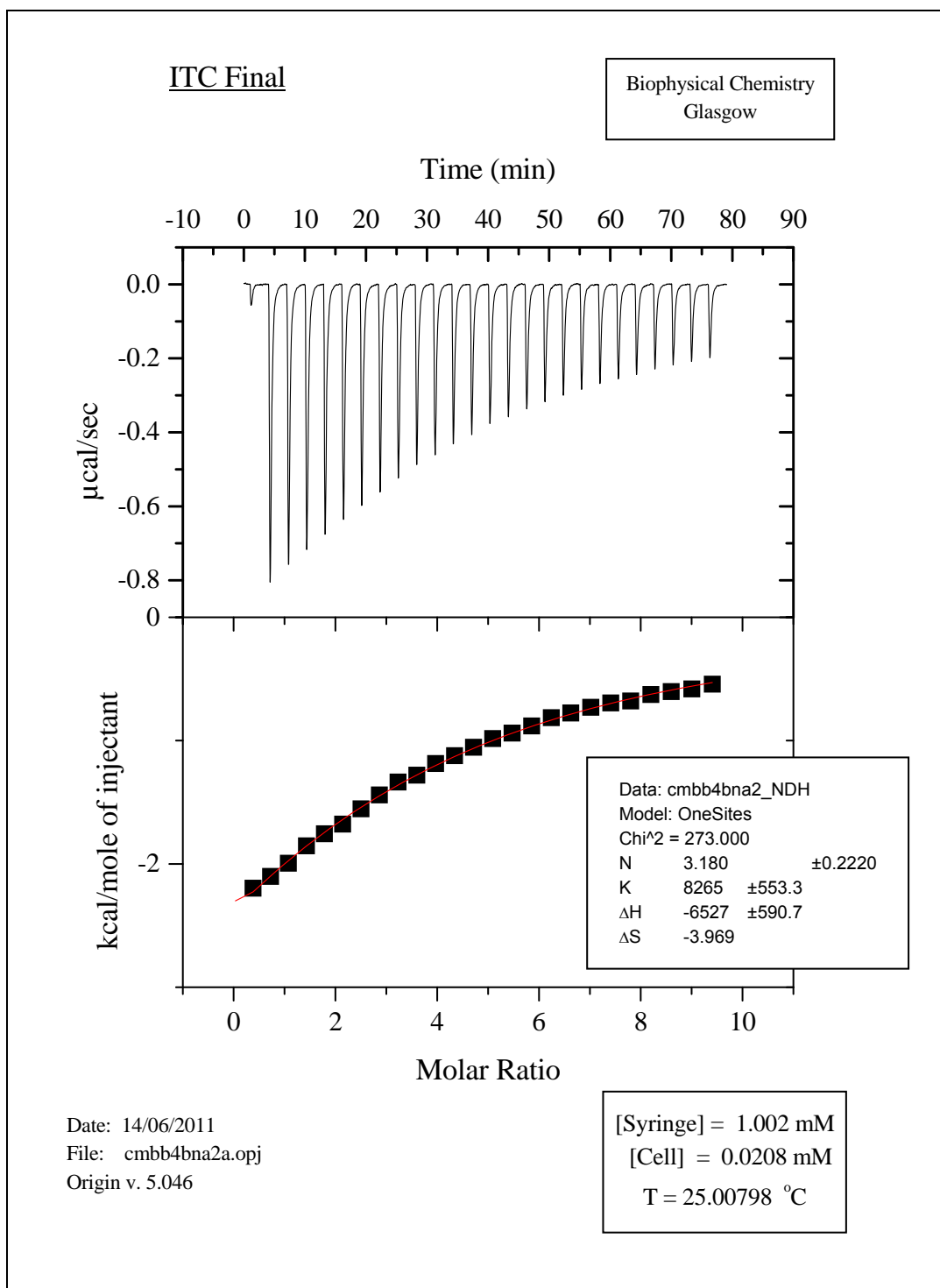


Figure 5.8. ITC data for 9 with CBPQT⁴⁺ in water.

5.3.2.2. ^1H NMR study with CBPQT^{4+} .

The ^1H NMR spectrum of the complex formed by CBPQT^{4+} and **9** was obtained in D_2O . The solution was an intense purple colour upon mixing the two components together, indicating that the pseudorotaxane had formed. The spectrum produced exhibited the typical shifts expected for the formation of the pseudorotaxane, where the $\text{H}_{4/8}$ protons had shifted from their position in the aromatic region at 7.87 ppm and 7.81 ppm down to 2.47 ppm. The proton shifts for the complex relative to each component is shown in Table 5.3. The stacked spectra for these experiments are shown in Figure 5.9.

δ : CBPQT^{4+} (ppm)	δ : Complex (ppm)	δ : $\text{NapMe}_3\text{N}^+\text{Br}^-$ (ppm)	$\Delta\delta$ component (ppm)	
9.03 (H_α)	9.07		+0.04	
	8.89		-0.14	
7.55 (H_{ben})	7.96		+0.41	
8.20 (H_β)	7.53		-0.67	
	7.41		-0.79	
	6.36		7.44 ($\text{H}_{2/6}$)	-1.08
	6.07		7.05 ($\text{H}_{3/5}$)	-0.98
			7.04 ($\text{H}_{3/5}$)	-0.97
5.77 (CH_2)	5.79		+0.02	
	4.33	4.30	+0.03	
	4.27	4.25	+0.02	
	4.19	3.91	+0.04	
	3.95	3.65	+0.30	
	3.80	3.41	+0.40	
	3.28	2.99 (Me_3)	+0.29	
	2.47		7.87 ($\text{H}_{4/8}$)	-5.4
7.81 ($\text{H}_{4/8}$)			-5.34	

Table 5.3. ^1H NMR Shifts of CBPQT^{4+} and NapMe_3N^+ upon complexation.

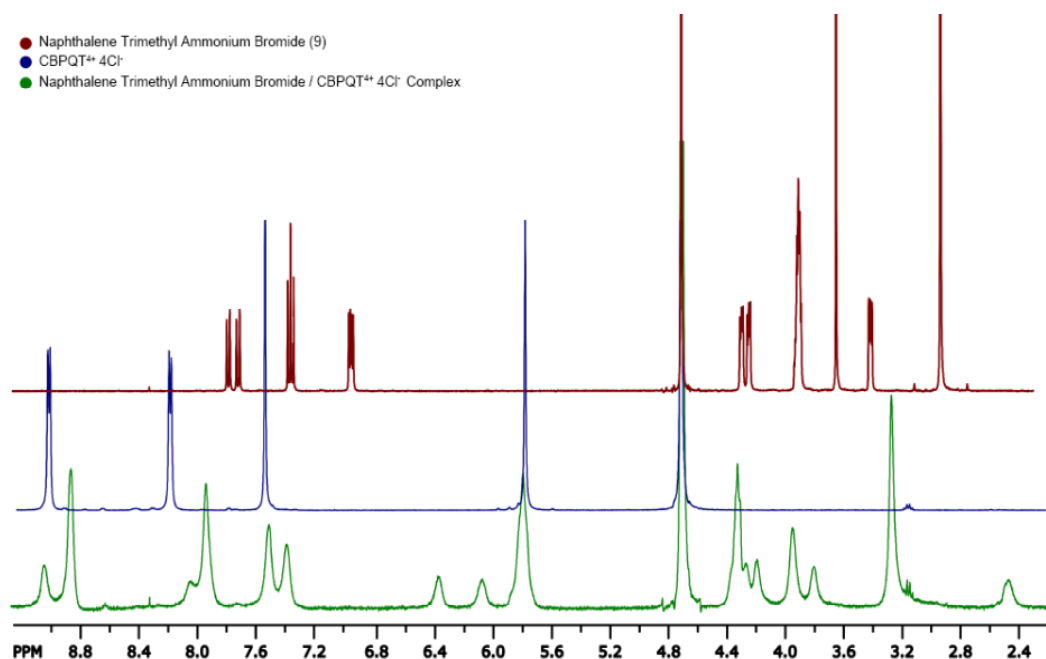


Figure 5.9. Stacked ^1H NMRs of NapMe_3N^+ (red), CBPQT^{4+} (blue) and the 1:1 complex (green).

5.3.2.3. UV-Vis and Fluorescence Spectroscopy.

In addition to the ^1H NMR experiments, UV-Vis and fluorescence spectroscopy experiments were carried out on the complex with CBPQT^{4+} . The UV-Vis spectrum was performed on 1 mM solution of the complex in water. The recorded spectrum showed that band expected for the formation of the pseudorotaxane with $\lambda_{\text{max}} = 518$ nm. Fluorescence measurements were recorded for the naphthalene trimethylammonium bromide in water at a concentration of 1×10^{-5} M. The spectrum produced with the excitation wavelength of $\lambda = 295$ nm was found to be of the form expected for the naphthalene moiety. Addition of one equivalent of CBPQT^{4+} to the aqueous solution formed a pink solution that was typical for the pseudorotaxane formation. The fluorescence spectrum produced by the complex was found to be reduced in intensity, indicating that the CBPQT^{4+} was quenching the fluorescence of the naphthalene moiety.

The graphs for both the UV-Vis and the fluorescence are shown in Figure 5.10.

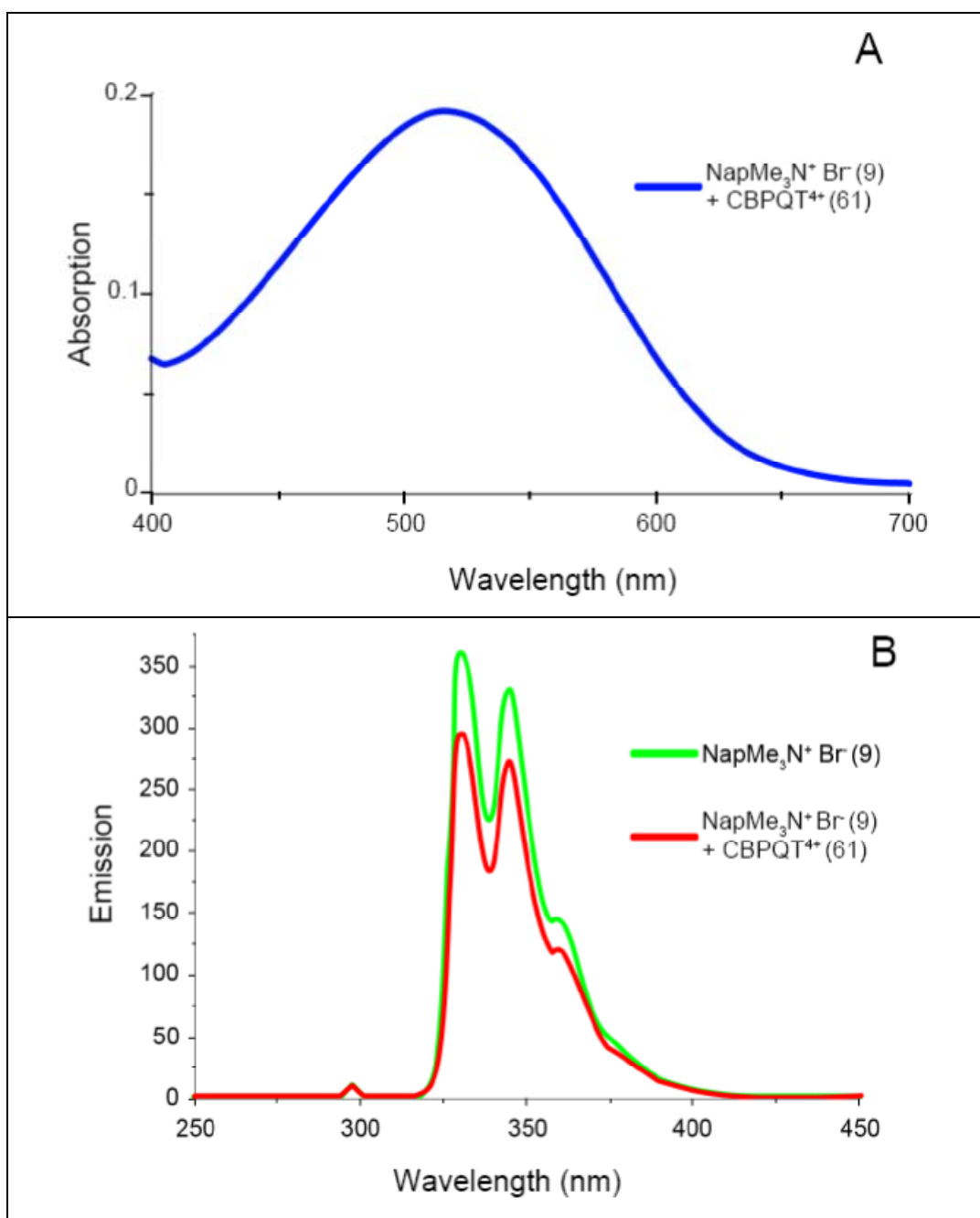


Figure 5.10. A). UV-Vis spectrum of 9+ 61 10^{-3} M B). Fluorescence spectra recorded for 9 + 61 10^{-5} M. All measurements recorded at room temperature in water.

5.3.3. Micelle Formation and Analysis.

5.3.3.1. ¹H NMR titration studies of Naphthalene trimethylammonium bromide **9** with SDS.

The micelle formation with monitoring by ¹H NMR was based upon a procedure published by Nowick and co-workers.^[120] To a sample of the naphthalene trimethylammonium bromide (**9**) in D₂O at a concentration of 1 mM, were added sequentially 1.8 μl aliquots of a 0.8 M solution of SDS in D₂O. After each addition the ¹H NMR spectrum was recorded. The positions of key protons are shown in Table 5.4. The combined spectra recorded for the naphthalene trimethylammonium bromide **9** with SDS added is shown in Figure 5.11, where the key protons noted in Table 5.4 are labelled.

Peak (δ) / ppm	A	B	c1	c2	d1	d2	I
0μl	7.87	7.81	7.44	7.44	7.05	7.04	2.99
1.8μl	7.76	7.73	7.36	7.26	6.87	6.76	2.95
3.6μl	7.79	7.76	7.38	7.28	6.91	6.79	2.99
5.4μl	7.80	7.77	7.40	7.30	6.96	6.85	3.05
7.2μl	7.81	7.78	7.41	7.31	6.98	6.87	3.07
9.0μl	7.81	7.79	7.42	7.32	6.99	6.89	3.08
10.8μl	7.82	7.79	7.42	7.32	6.99	6.89	3.09
12.6μl	7.82	7.79	7.42	7.32	6.99	6.89	3.09
14.4μl	7.82	7.79	7.42	7.32	6.99	6.89	3.09
16.2μl	7.82	7.79	7.42	7.32	6.99	6.89	3.09

Table 5.4. Positions of key protons on the naphthalene trimethylammonium bromide with increasing amounts of SDS.

Naphthalene Trimethyl Ammonium Bromide + SDS added

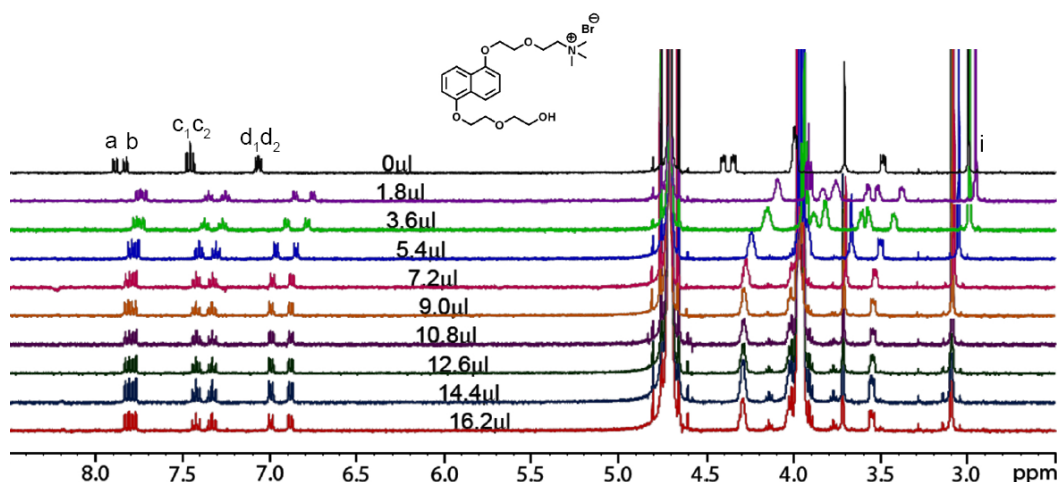


Figure 5.11. ^1H NMR spectra of **9** with increasing aliquots of SDS.

As the SDS was added to the **9** a negative movement of the aromatic naphthalene protons occurred. The two doublets at 7.87 ppm and 7.81 ppm started to draw closer together. Subsequent titrations showed a shift up towards 7.82 ppm and 7.79 ppm, eventual peak movement stopped after 9.0 μl SDS. The triplet at 7.44 ppm split into two smaller triplets with a negative shift of ~ 0.1 and 0.2 ppm towards 7.36 ppm and 7.26 ppm was observed. Again, the signals started to shift up to a maximum position of 7.42 ppm and 7.32 ppm with increasing SDS, where the signals reached their final positions after 9.0 μl had been added. The merged doublets at 7.05 ppm and 7.04 ppm also separated and shifted towards 6.89 ppm and 6.75 ppm. The signals then migrated back to settle at 6.99 ppm and 6.89 ppm after the addition of 9.0 μl of SDS. This splitting of signals indicates that the naphthalene protons are no longer in the same environments.

The alkyl protons on the naphthalene substrate also exhibited shifts with the addition of the SDS. The protons for the trimethyl ammonium group also moved in a manner that could be measured; starting from 2.99 ppm the singlet moved down to 2.89 ppm then moved back to 2.99 ppm after the second aliquot of SDS was added. With further

additions the singlet moved up until it reached 3.09 ppm. The details of shifts are presented in Table 5.5.

δ of 9 (ppm)	δ of 9 after 1eq SDS. (ppm) [$\Delta\delta$]	δ of 9 after 7eq SDS. (ppm) [$\Delta\delta$]
7.87	7.76 [-0.11]	7.82 [-0.05]
7.81	7.73 [-0.08]	7.79 [-0.02]
7.44	7.36 [-0.08]	7.42 [-0.02]
7.44	7.26 [-0.18]	7.32 [-0.12]
7.05	6.87 [-0.18]	6.99 [-0.06]
7.04	6.76 [-0.28]	6.89 [-0.15]
2.99	2.95 [-0.04]	3.09 [+0.10]

Table 5.5. Shifts exhibited for **9** with SDS equivalents. Change in shift relative to 0eq SDS recorded in brackets.

The initial shifts were attributed to aggregation of the SDS and **9**. As the SDS concentration increased to reach its critical micelle concentration (CMC) of 8.3 mM^[109] the protons shifted to a more positive position, downfield. Full incorporation of compound **9** occurred when all signals ceased to move with increasing concentration of SDS. This point was reached 9.0 μ l of SDS had been added. The concentration of SDS corresponded to 14.1 mM.

5.3.3.2. Fluorescence Spectroscopy Titration Studies

In collaboration with Prof Woisel's group, the CMC of naphthalene trimethylammonium bromide functionalised SDS micelles was determined by the titration of SDS into a solution of **9**. To a solution of 3.6 mM **9** were added aliquots of SDS. The intensity of the naphthalene moiety was measured at $\lambda_{\text{Ex}} = 295 \text{ nm}$.^[121] The intensity of the naphthalene emission signal ($\lambda = 329 \text{ nm}$) gradually diminished until the concentration of SDS reached 4 mM where the intensity dropped dramatically. The sudden change in intensity implied that the onset of micelle formation had

occurred. After this point addition of more SDS produced an increase in fluorescence thus indicating that the naphthalene moiety was displaced from the micelle by the additional SDS molecules. The change in fluorescence intensity at $\lambda_{Em} = 329$ nm relative to increasing SDS concentration is shown in Figure 5.12. These results would show that the CMC of these micelles is lower than the measured CMC of SDS by itself, implying that compound **9** promotes the micellisation process when mixed with SDS.^[121]

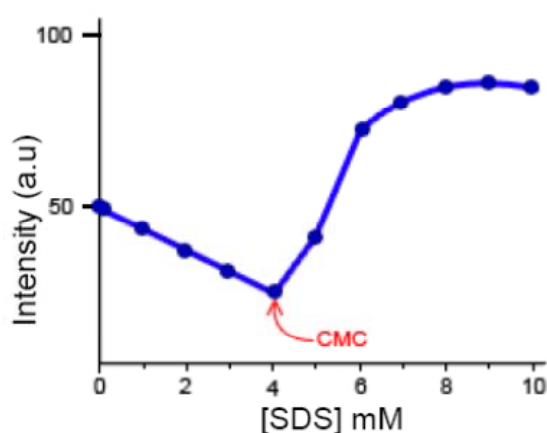


Figure 5.12. Graph showing the change in the fluorescence at $\lambda_{Ex} = 295$ nm. $\lambda_{Em} = 329$ nm of **9** as a function of SDS concentration. Recorded in H₂O at 25 °C.

Addition of CBPQT⁴⁺ to the micellar solutions gave unexpected results, where instead of the distinct colour change upon formation of the pseudorotaxane; a white precipitate formed. Close inspection showed that the solid formed was the product of a salt exchange between the CBPQT⁴⁺ 4Cl⁻ with the Na⁺ DS⁻ to form CBPQT⁴⁺ 4DS⁻ and 4NaCl. Furthermore, the addition of SDS to a solution of the pre-formed pseudorotaxane also formed a white precipitate. Investigation of the supernatant showed that micelles of naphthalene trimethyl ammonium bromide **9** with SDS had formed successfully, while the solid was CBPQT⁴⁺ 4DS⁻. The ¹H NMR spectra recorded for this investigation are shown in Figure 5.13.

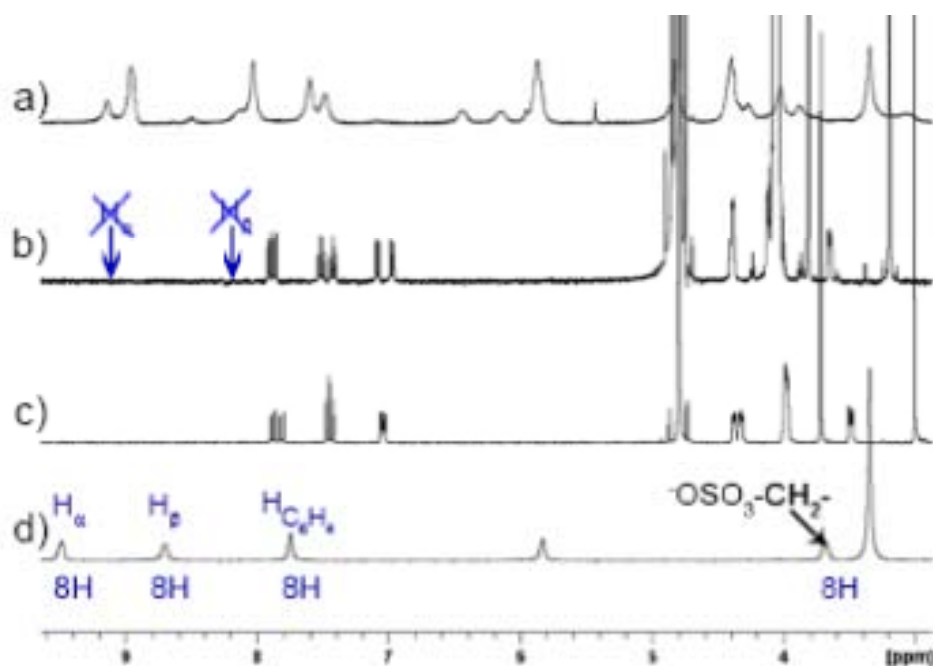
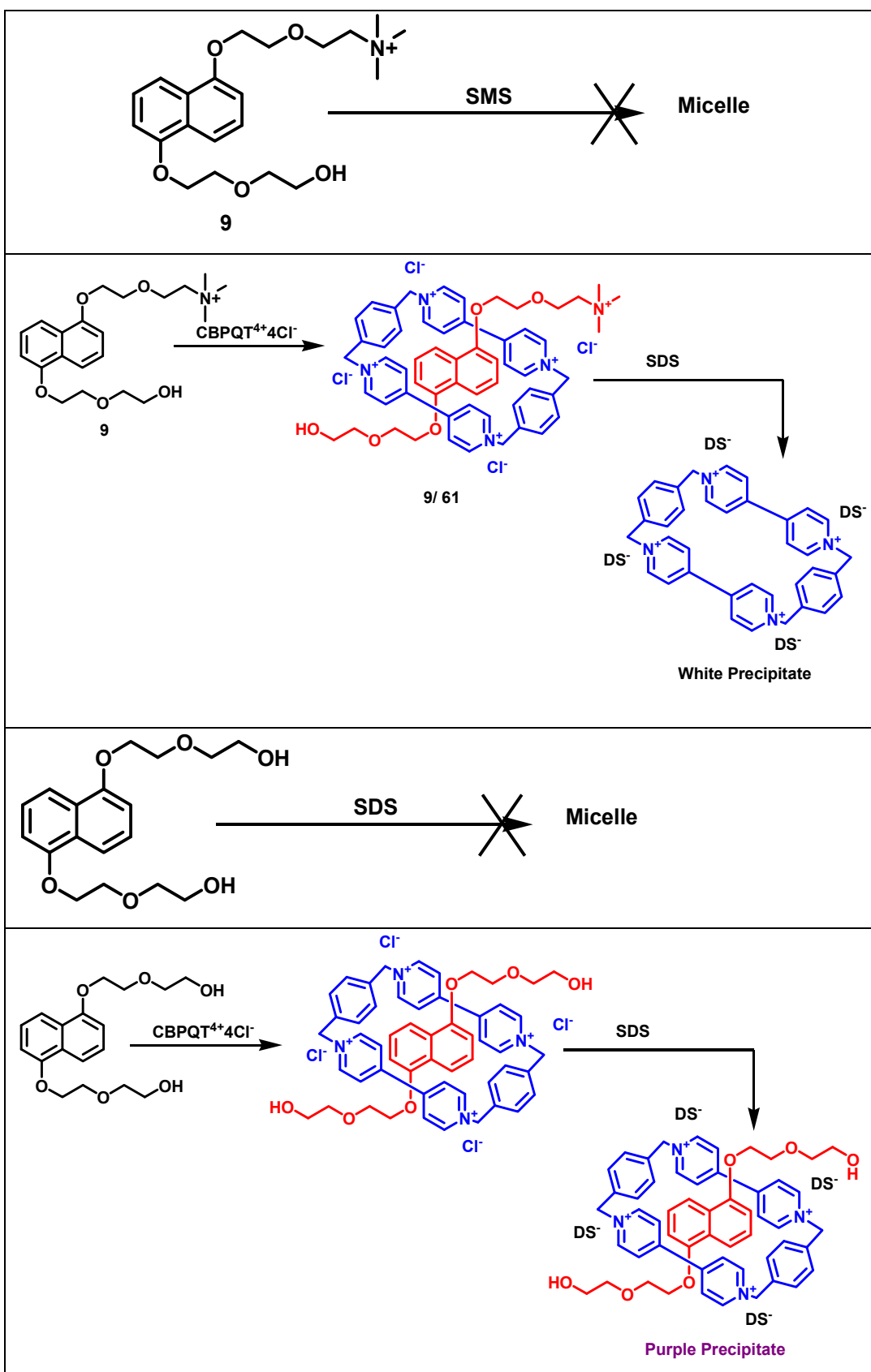


Figure 5.13. Partial ^1H NMR spectra of: (a) **9** + **61** in D_2O . (b) **9** + **61** + SDS (supernatant), (c) **9** recorded in D_2O ; (d) precipitate from **9** + **61** + SDS in d_6 -DMSO $\sim 10^{-4}$ M at 40°C .

Experiments with sodium methylsulfate (SMS) and compound **9** showed that the micellar structures were not formed.^[121] Moreover, the addition of SMS to aqueous solutions of the pseudorotaxane of compound **9** with CBPQT^{4+} (**61**) did not produce a precipitate from potential salt exchange. Similar experiments with the naphthalene diol **2** with SDS showed that the trimethyl ammonium group was required for the formation of functionalised micelles.^[121] Addition of SDS to solutions of the pseudorotaxane of compound **2** with CBPQT^{4+} gave a purple precipitate showing that the pseudorotaxane was intact during and after salt exchange. These results indicate that for the decomplexation and precipitation to occur the trimethylammonium group of **9** and the SDS surfactant is required, where the long chain alkyl precipitates the CBPQT^{4+} out of solution and the charge on the naphthalene species induces dissociation of the complex due to charge repulsion between positive charges present on each compound.^[121]



5.4. Conclusions and Future Work.

5.4.1. Conclusions.

Two functionalised trimethylammonium bromide compounds have been successfully synthesised. It has been found that the naphthalene functionalised surfactant (**9**) can undergo complexation with CBPQT⁴⁺ to form the pseudorotaxane. The complex has been investigated by a number of techniques including ITC, UV-Vis, fluorescence and ¹H NMR. The ¹H NMR studies have shown that the H_{4/8} protons on the naphthalene core shift by up to 5.5 ppm upon complexation, indicating that the pseudorotaxane had formed.

ITC experiments show that the complexation of the monomer and CBPQT⁴⁺ occurs readily although the association constant K_a is reduced in comparison with unfunctionalised 1,5-dihydroxynaphthalene systems indicating that there is some charge-charge repulsion interactions exhibited by the complex.

The formation of micelles with SDS has been investigated for the naphthalene derivatised compound by means of ¹H NMR and fluorescence spectroscopy. It has been shown that the naphthalene promotes micellisation of SDS in aqueous media. Addition of CBPQT⁴⁺ to the formed naphthalene micelles causes a salt exchange of the chloride counter ions with the dodecyl sulfate producing a precipitate of CBPQT⁴⁺.4DS from the solution of naphthalene SDS.

5.4.2. Future Work.

With additional time and material, investigation of the TTF functionalised trimethylammonium bromide (**54**) with SDS would have been carried out.

6.
Modification of BSA via Pseudorotaxane
Formation.

6.1. Introduction.

Proteins can be modified at various stages of formation^[122] from amino acid coding at the genetic level to create chimeric proteins^[123] [91] where specific areas have been re-coded to suit a particular need or application. This is a highly involved biological genetic engineering process that gives precise modifications at required positions. Protein synthesis to form structures at the amino acid level have also been carried out where the growing peptide is immobilised to a surface and selectively coupled with Fmoc protected amino acids.^[124] This method gives a synthetic route to proteins where there is full chemical control over the peptide chains produced.

Examples of proteins modified at the amino acid level include the synthesis of a chimeric integrin-like protein carried out by Mrksich and co-workers to introduce additional specificity for cell binding to the extracellular matrix. The intracellular and transmembrane domains from β_1 integrin were joined to the extracellular stalk domain of the cell signalling protein cytokine, fractalkine, and carbonic anhydrase IV domain was coded for at the terminus of the chimeric receptor.^[123]

The domains from β_1 integrin used permitted the cell adhesion function to be retained, where the intracellular signalling processes that promote actin cytoskeleton reorganisation required for cell spreading and adhesion functions could still occur. The fractalkine domain was incorporated to elongate the CAIV binding domain by ~26 nm from the cell surface. The CAIV domain was utilised for its selective interaction with benzenesulfonamide, the dissociation constant $K_d = 6 \mu\text{M}$ which is similar to the K_d for the interaction between $\alpha_5\beta_1$ integrin with its natural binding partner fibronectin.^[123]

Chinese hamster ovary cells (CHO) were transfected with this chimeric receptor and seeded onto surfaces presenting benzenesulfonamide and triethylene glycol groups. It was shown that these cells selectively adhered to the surface where binding occurred *via*

the chimeric receptor. Cell spreading was observed across these surfaces, showing that the receptor also functioned in the same way as integrin proteins with the actin cytoskeleton. Cell adhesion could also be inhibited by the addition of soluble benzenesulfonamide confirming the adhesion was via benzenesulfonamide binding.^[123]

Alternatively, proteins that are fully formed can be modified by reaction with several different types of reagents to functionalise as required. This method is useful for peptide mapping, labelling and the incorporation of unnatural conjugates such polymers. The main site of modification is cysteine residues, where the free thiol will react to form linkages with the modifier.

Maleimide groups will react selectively with cysteine residues in a Michael type addition.^[125] Maleimide groups can tolerate a great deal of functionality including polymer initiators.^{[126] [127]} An example where maleimide cysteine bonding has been used with good success is with the immobilisation of α -helical peptide cecropin P1 functionalised with a single cysteine residue at the C terminal (CP1c) to polystyrene-maleimide surfaces, for bacterial capture and sensing applications.^[128] Through extensive work it has been shown that biological activity of these surfaces is dependent upon the conformation and orientation of the peptide on the surface. Work was pursued with the aim to control the orientation and conformation of the CP1c in solution in order to reduce the variables in the activity of the surfaces.^[128] An illustration of immobilisation is shown in Figure 6.1.

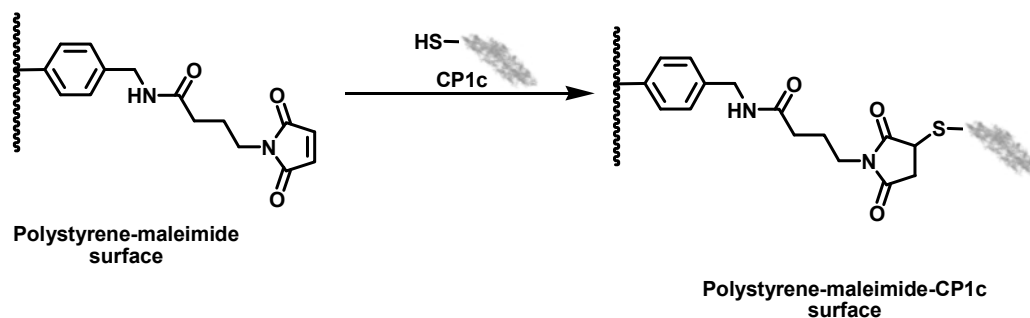


Figure 6.1. Immobilisation of CP1c onto polystyrene-maleimide surface.

Varying the concentration of the peptide in potassium phosphate buffer showed that immobilisation and equilibration times were reduced with increasing concentration. It was shown that the conformation and orientation of these surfaces was the appropriate α -helical form and was associated with reorientation to avoid steric interactions with the close proximity of the substrate onto the surface with increasing molecules immobilised.^[128] The addition of the hydrophobic solvent 2,2,2-trifluoroethanol (TFE) has been shown to induce the conformational change from random coil to the α -helical form in solution of peptides via hydrophobic interactions. The addition of TFE in the phosphate buffer led to changes in the conformation of PC1c to form the α -helix in solution for percentages of 50% and above TFE: phosphate buffer. This then affected the immobilisation of the peptide, by the virtue that there was no longer a need for conformational rearrangement prior to immobilisation.^[128]

Additionally, during the immobilisation process the reducing agent tris(2-carboxyethyl)phosphine, (TCEP) is used to ensure that there are no dimerised products where cysteines from two peptides react to form disulfide bonds. When TCEP is not present immobilisation does not occur, and adsorption with random orientation is observed and biological activity is reduced. By applying high concentrations of peptide with the presence of upto 75% solution of TFE in addition to TCEP, it has been shown that immobilisation of the PC1c onto polystyrene can be completed using maleimide cysteine linkages with no loss of bioactivity against bacteria.^[128]

Methanethiosulfonate reagents will react with the thiol sites with high selectivity to form disulfide bonds with the cysteine.^[129] These molecules tolerate a great deal of functionality. However these reagents are hygroscopic and rapidly hydrolyse in aqueous conditions at room temperature.^[129] The synthesis of polyethyleneglycol (PEG) modified proteins selectively at cysteine residues for potential drug delivery systems have been investigated.^[130] It has been shown that the addition of PEG to drug systems increase the circulation retention times by masking the drug system from the immune system. PEG also increases the hydrodynamic size of the drug, which then leads to lower renal clearance and a greater resistance to proteolysis.

MethoxyPEG (mPEG) was functionalised with either methane thiosulfonate (MTS) or phenylthiosulfonate (PTS) for the modification of two proteins. The reagents were synthesised from the bromo-mPEG derivative with freshly converted thiosulfonates from methanesulfinate and phenylsulfinate respectively in high yields.^[130]

Initially the mPEG-MTS and mPEG-PTS were reacted with papain to verify the reaction conditions and selectivity of the MTS for the cysteine thiol groups. Once this was confirmed by gel electrophoresis, the protein modification was carried out on the pharmaceutically active protein recombinant human granulocyte colony stimulating factor, rhG-CSF. RhG-CSF is used in the treatment of neutropenia, a disorder where there is a reduced number of neutrophils circulating in the blood.^[131] G-CSF stimulates bone marrow to produce granulocytes and stem cells.^[130] Cell viability studies with Murine myeloblastic leukemia NFS-60 cells that are rich in G-CSF receptors were treated with native G-CSF and rhG-CSF-mPEG for 48 hours. After this time MTT experiments were used to measure the bioactivity of the mPEG-protein against the activity of the native protein.^[130] The results are shown in Table 6.1. This value was found to be comparable to other G-CSF modified systems, and showed that the modification may be a viable option for other pharmaceutical proteins.^[130]

Protein	Specific Activity (IU/mg)	% Activity*
Native G-CSF	1.08×10^8	100
mPEG G-CSF	6.25×10^7	59

*% Activity was expressed as the percent residual bioactivity as compared with native G-CSF. Results are the mean values (n = 4)

Table 6.1. Bioactivity of m-PEG-rhG-CSF versus native G-CSF in murine myeloblastic NFS-60 cell line.^[130]

Halogenated acetate and acetamides will also react at cysteine residues to form thioester linkers.^[132] Iodoacetamides have been found to be fairly unselective and will readily react with lysine to form additional adducts in addition to reaction at the cysteine residues.^[133] The less reactive chloro derivatives have been shown to be selective for the cysteine residues only. Iodoacetamide is regularly used during reductive protein digestion,^{[134] [135]} where it is used to react with the free cysteine residues in order to avoid the reformation of random disulfide linkages and further degradation of the cysteine. Mass spectroscopy of protein mapping shows the cysteine residues in the S-acetamide-alkylated form. N-alkylation also occurs at a slower rate and can be generally avoided by reduced reaction times of use of the chloro equivalent reagent.^[133]

The haloacetamides and acetates have also been used to attach functionality to proteins via the cysteine thiol group. One example was the incorporation of redox active *N*-(ferrocenyl)iodoacetamide to a number of thiol-containing compounds with the aim to form redox mediators for glucose oxidase activity.^[40] The structure of *N*-(ferrocenyl)iodoacetamide is shown in Figure 6.2.

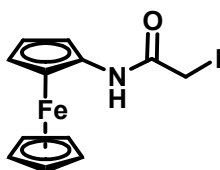


Figure 6.2. The structure of *N*-(ferrocenyl) iodoacetamide.^[40]

The compounds derivatised were: cysteine, glutathione, a sulfhydryl modified BSA, and a sulfhydryl oligonucleotide chain M13-R-Comp-SH. The glutathione and cysteine conjugates are shown in Figure 6.3. The electrochemical properties were measured using cyclic voltammetry (CV). The redox half wave potential, $E_{1/2}$, for the parent compound *N*-(ferrocenyl) iodoacetamide in acetonitrile was measured as $E_{1/2} = +0.342$ V.^[40] The CVs for the conjugates formed were measured in 50 mM potassium phosphate at pH 7.4. $E_{1/2}$ for the oligonucleotide was measured as +0.16 V. The half wave potential with the oxidation / reduction potentials measured for the conjugates reported is shown in Table 6.2.^[40]

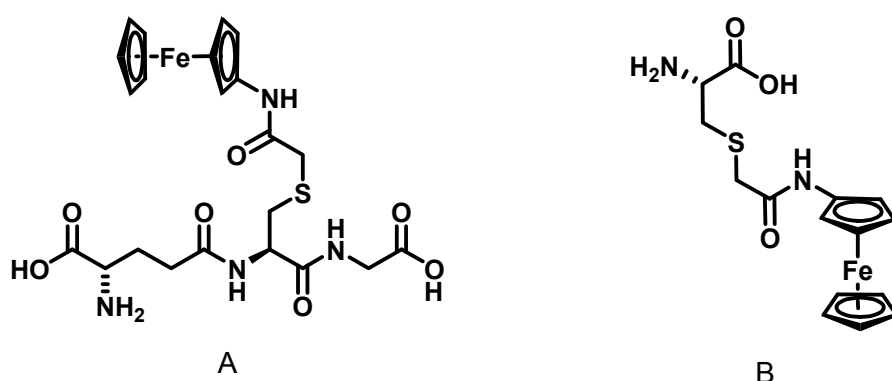


Figure 6.3. Structure of A) Fc-glutathione, B) Fc-cysteine. ^[40]

Conjugate	E_{ox} / V	E_{red} / V	$E_{1/2} / V$
Fc-Cysteine	+0.1	+0.034	0.067
Fc-Glutathione	+0.09	0.021	0.056
Fc-BSA	+0.108	0.023	0.066

Table 6.2. CV data recorded for the ferrocene conjugates. 50mM potassium phosphate pH 7.4 at 298K vs SCE.

Addition of glucose to the conjugates had no effect upon the CV redox wave. Further addition of glucose oxidase in low concentrations, to the cysteine and glutathione conjugates in the presence of glucose gave

rise to a change where the ferrocene conjugate in its oxidised form reacted with the reduced form of the glucose oxidase. The glucose present was then converted into gluconolactone catalytically. Experiments with the larger nucleotide derivative and the BSA gave no response to the glucose oxidase.^[40] This was attributed to the size of the conjugates, where the ferrocene was sterically blocked from reaching the active site of the glucose oxidase. The CV spectra recorded for the Fc-glutathione are shown in Figure 6.4.

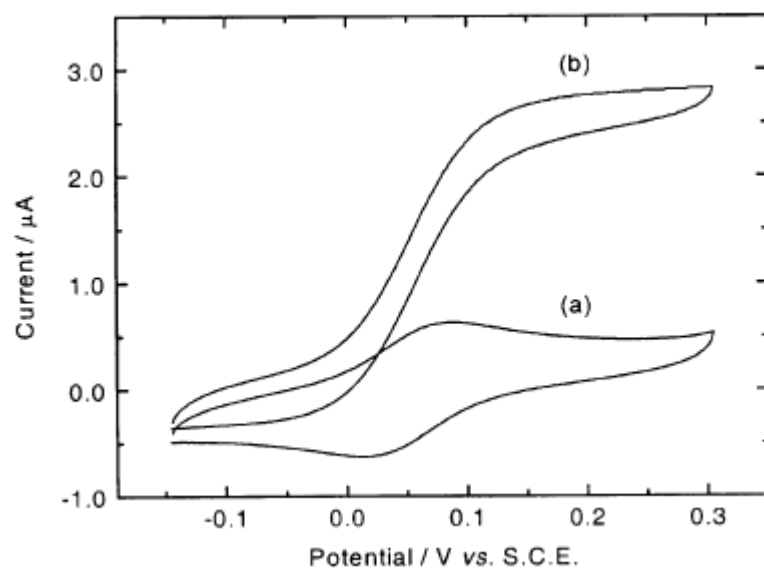
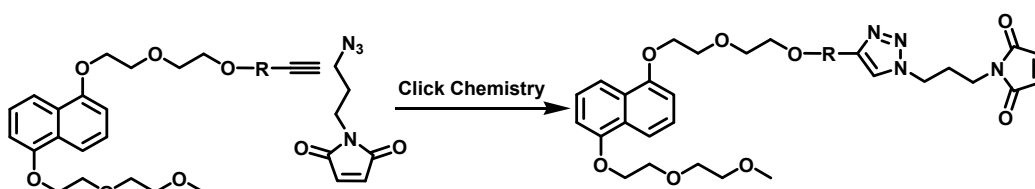


Figure 6.4. CV of Fc-glutathione (0.4 mM) and glucose (32.5 mM) in 50 mM potassium phosphate buffer in the (a) absence, (b) presence of glucose oxidase (40 μM).^[40]

6.2 Pseudorotaxane protein modification aims and objectives.

The aim of this project was to synthesise a naphthalene functionalised conjugate that could be used to modify proteins by covalent interactions that could then lead to the incorporation of unnatural functionality to the protein. By the virtue of the host-guest interactions that naphthalene exhibits with CBPQT⁴⁺ it was thought that by the introduction of the naphthalene moiety to the protein, it would be possible to introduce additional supramolecular interactions to the protein, where interactions could be measured by UV-Vis, fluorescence spectroscopy and electrochemistry.

The protein could be modified by a number of methods. One of the methods used a maleimide functionalised compound that could be coupled to cysteine residues. For the maleimide route the aim was to proceed *via* click chemistry as shown in Scheme 6.1. Another method was by activation and reaction with chloro acetates. The target molecule is shown below in Figure 6.5.



Scheme 6.1 Reaction scheme to produce a naphthalene maleimide for protein modification.

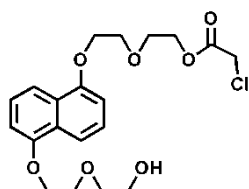
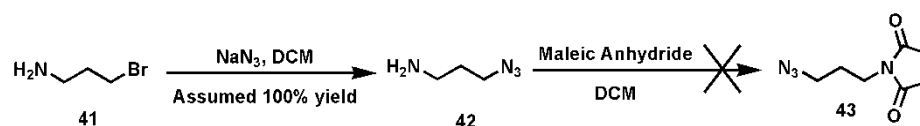


Figure 6.5. Naphthalene chloroacetate target molecule.

6.3. Results and Discussion.

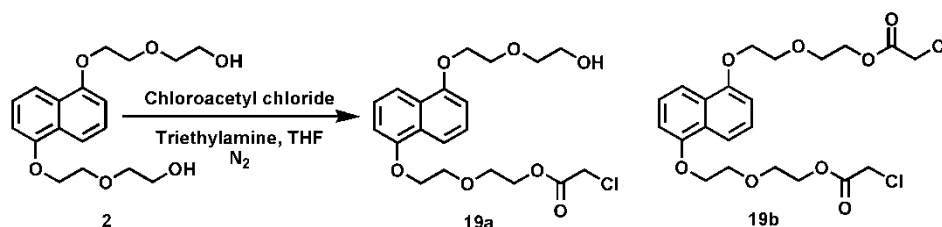
6.3.1. Attempted synthesis for 1-Azido-propyl-3-maleimide (**43**) for click chemistry.



Scheme 6.2. Synthesis of azido propyl maleimide from bromo propylamine.

The synthesis of compound **42**^[136] was fairly straightforward; however, it was found that the product also evaporated under the reduced pressure conditions such that it was found in the rotary evaporator trap essentially impurity free. For later experiments the solvent used in the reaction and workup was changed to DCM with good success, where the crude material was taken on to the next stage without further workup required. The subsequent reaction to form compound **43** produced a bright orange foamy solid rather than the orange oil expected from the literature procedure that had been followed.^[136] The foamy orange solid was not sufficiently soluble in all solvents tried, whereas the product described in the literature had been soluble in chloroform and DCM. After extensive sonication and heating, a small amount of the crude material went into d_6 -DMSO such that a ^1H NMR spectrum could be run. The results of which showed that the majority of the signals were not from the expected product. As this compound was a key intermediate in the synthetic pathway, and that we could not form the product this synthesis was abandoned at this stage.

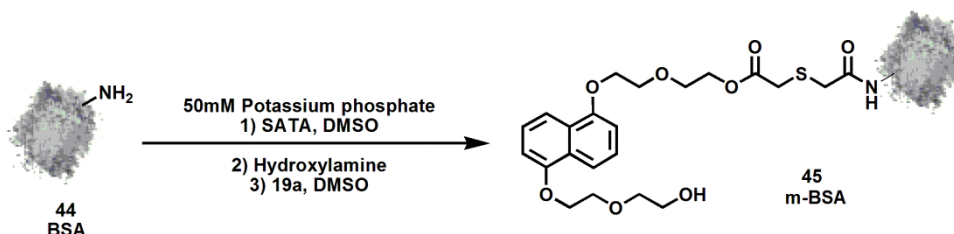
6.3.2 Synthesis of 1-(2-(2-(chloroacetyloxy)ethoxy) ethoxy)-5-(2-(2-hydroxyethoxy)ethoxy) naphthalene (19a).



Scheme 6.3. Synthesis of 19a from diol 2.

Starting from the naphthalene diol **2**, the chloroacetate product **19a** was synthesised in a one step reaction^[137] that produced both the mono and diacylated compounds, where the monoacylated product **19a** predominated with a good yield of 52% while the bisacylated product **19b** was formed in a 5% yield. The remaining unreacted diol was easily recovered and could be recycled as required.

6.3.3 Modification of BSA with 1-(2-(2-(chloroacetyloxy)ethoxy) ethoxy)-5-(2-(2-hydroxyethoxy)ethoxy) naphthalene (19a).

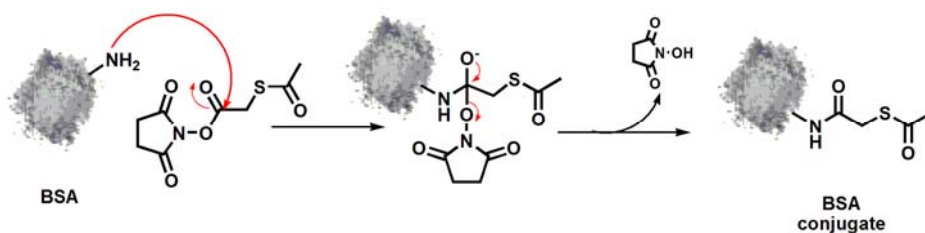


Scheme 6.4. Modification of BSA with compound 19a.

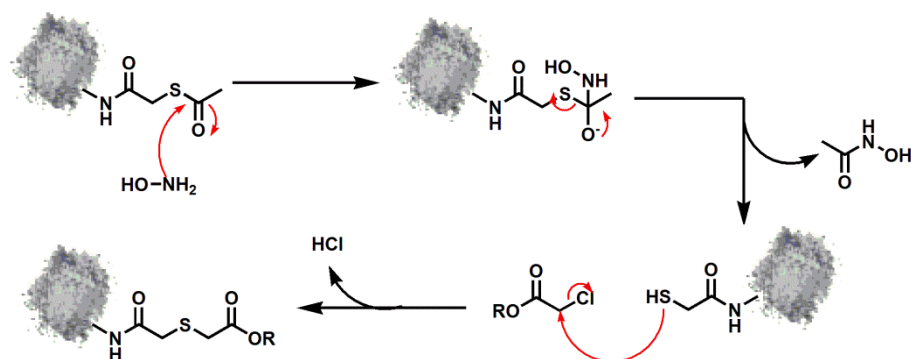
As BSA is readily available it was decided that this protein would be a practical substrate for proof of concept and the optimisation of the

experimental procedure. The procedure for protein functionalisation as reported by Lo *et al*^[40] was followed. Typically the iodoacetamides are used for reaction with cysteine residues in proteins, however, it has been shown within the literature that iodoacetamides can also react with lysine residues to form covalent adducts that are unwanted. It has also been shown that the chloroacetamides can perform this reaction equally well without the additional unwanted reaction with lysine.^[133] By using compound **19a** with the BSA meant that an additional conversion to the iodo acetate was not required.

The BSA in 50mM potassium phosphate was first reacted with N-succinimidyl-S-acetyl-thioacetate (SATA) so as to increase the number of thiol groups available to react with the chloroacetamide. The reaction with the SATA gave a protected thiol. The mechanism for the reaction is shown in Scheme 6.5. After the reaction with SATA, the removal of the by-products and any excess reagent was performed using dialysis tubing with a MWCO of 4000-6000 in 50mM potassium phosphate buffer at pH = 7.2. Following the dialysis, hydroxylamine was used to form the reactive deprotected thiol species. After further dialysis to remove the excess reagent and by-products, the mixture was reacted with **19a**, to complete the modification. Upon addition of **19a**, a white solid precipitated which was removed by centrifugation at the end of the reaction. Extraction of the supernatant with ethyl acetate removed any remaining chloroacetate **19a** from the protein mixture. Further dialysis removed any dissolved ethyl acetate from the aqueous buffered solution. The reaction mechanism for the deprotection followed by treatment with a chloroacetate is shown in Scheme 6.6. The protein buffered solution was then dialysed with the same tubing as before in water to remove the phosphate buffer so that mass spectroscopy using MALDI TOF could be carried out.



Scheme 6.5. Reaction mechanism SATA with BSA.



Scheme 6.6. Deprotection of the thiol followed by addition of a chloroacetate.

6.3.4. Analysis of the modified BSA.

Several techniques were used to analyse the degree of modification that had occurred on the BSA from the treatment described above. MALDI TOF was used to determine the degree of naphthalene modification by the change in the molecular mass compared to unmodified BSA.

6.3.4.1 MALDI TOF analysis.

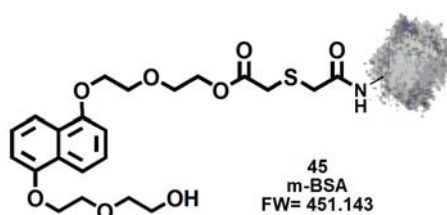


Figure 6.6. Structure of the modification per amino group on the protein BSA.

Samples of the modified BSA (m-BSA) **45** and unmodified BSA were analysed using MALDI TOF analysis. The expected changes to be observed were that the molecular weight (MW) of the m-BSA **45** would be higher by multiples of 451, the total mass of each unit that would be added to each amino group, the structure of which is shown in Figure 6.6. Samples of m-BSA, **45** and BSA were run on an AXIMA-CFR MALDI-TOF Kratos spectrometer using a matrix of sinapinic acid 10 mg /mL in 1:1 acetonitrile/ water 0.1% TFA. Sample mixture with matrix solution ratio of 1:1, with the exception of the BSA sample where a 1 to 5 dilution was used. Due to the nature of the BSA exact values for the MW of the protein could not be produced, where each run gave slightly different results. The typical value for the unmodified BSA starting material was 66839 g/mol or 66849 g/mol. The values for the m-BSA varied from 67493 g/mol to up to 68330 g/mol. The increased masses would indicate a minimum of one naphthalene group was added to a maximum of three naphthalene's added. From these results the degree of functionalisation that occurred onto the BSA appears to be that two naphthalene molecules have been added. The results are shown in Figure 6.7.

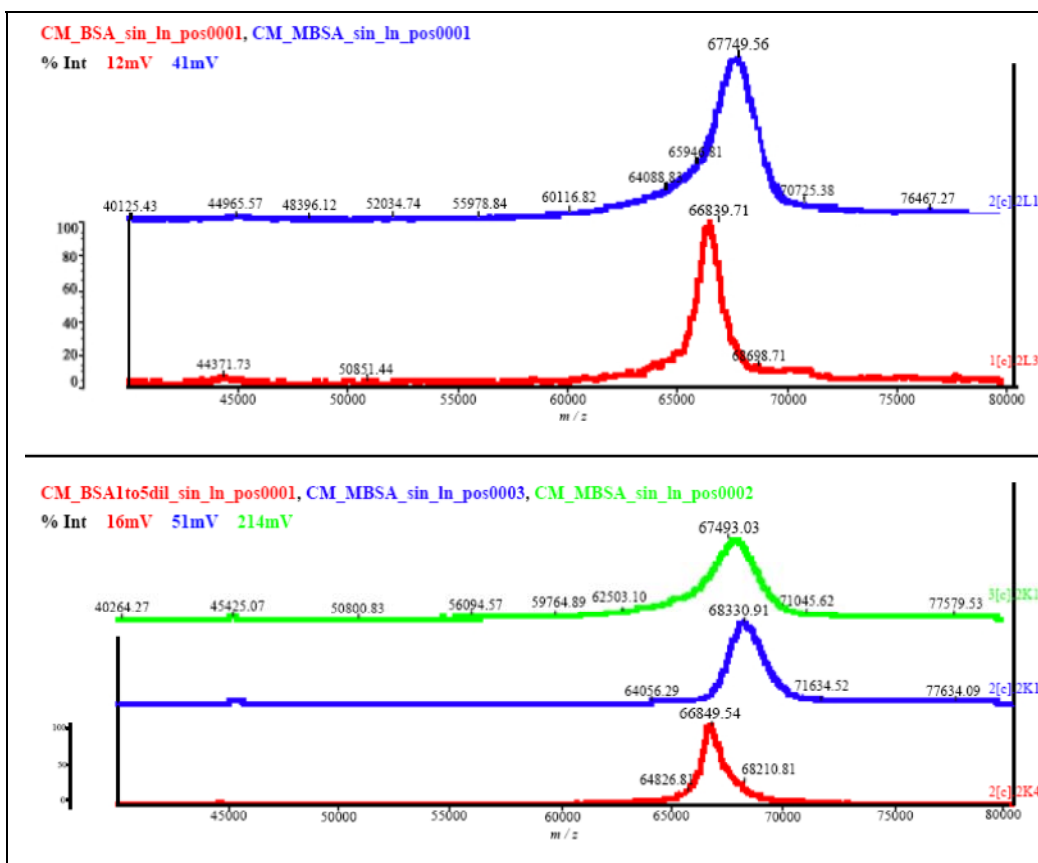


Figure 6.7. MALDI TOF results for m-BSA 45 and BSA.

6.3.4.2 Investigation of binding to CBPQT⁴⁺ by ITC.

To investigate whether the m-BSA could bind CBPQT⁴⁺ in aqueous solutions, ITC experiments were carried out. Solutions of the m-BSA **45**, BSA and CBPQT⁴⁺ were made in 20 mM potassium phosphate at pH = 6.8. The interaction between BSA and CBPQT⁴⁺ gave no binding event, where dilution effects were the only thermal changes present. However, the interaction between CBPQT⁴⁺ and the modified BSA gave a good binding curve with a binding stoichiometry (*N*) of around 1. The raw data for the interaction of CBPQT⁴⁺ with both modified and unmodified BSA is shown in Figure 6.8. Figure 6.9 shows the analysed data for the interaction of CBPQT⁴⁺ with the modified BSA **45** which gave the thermodynamic values shown in Table 6.3 from a single-set-of-sites binding model.

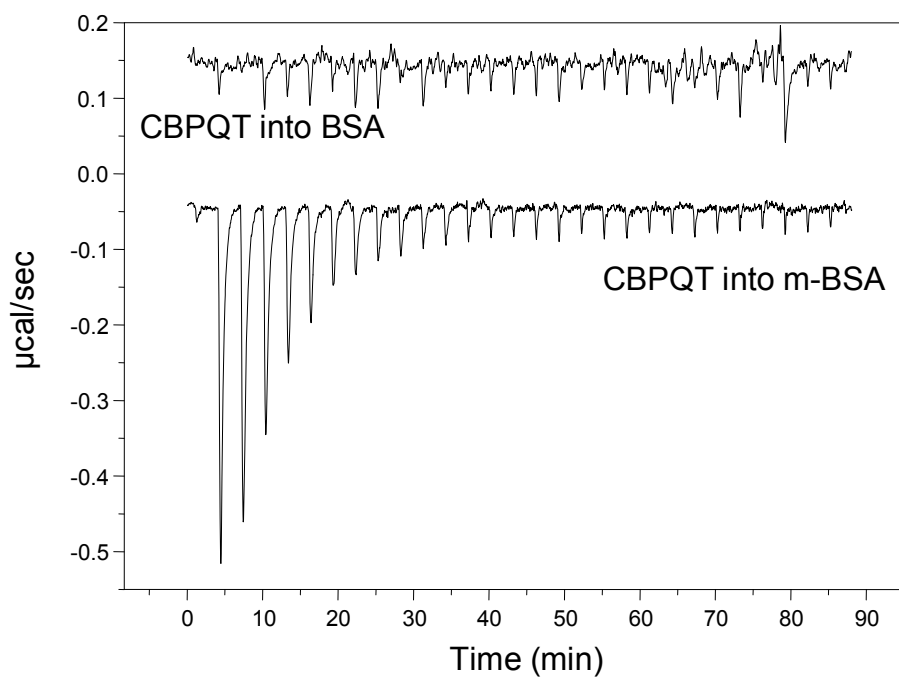
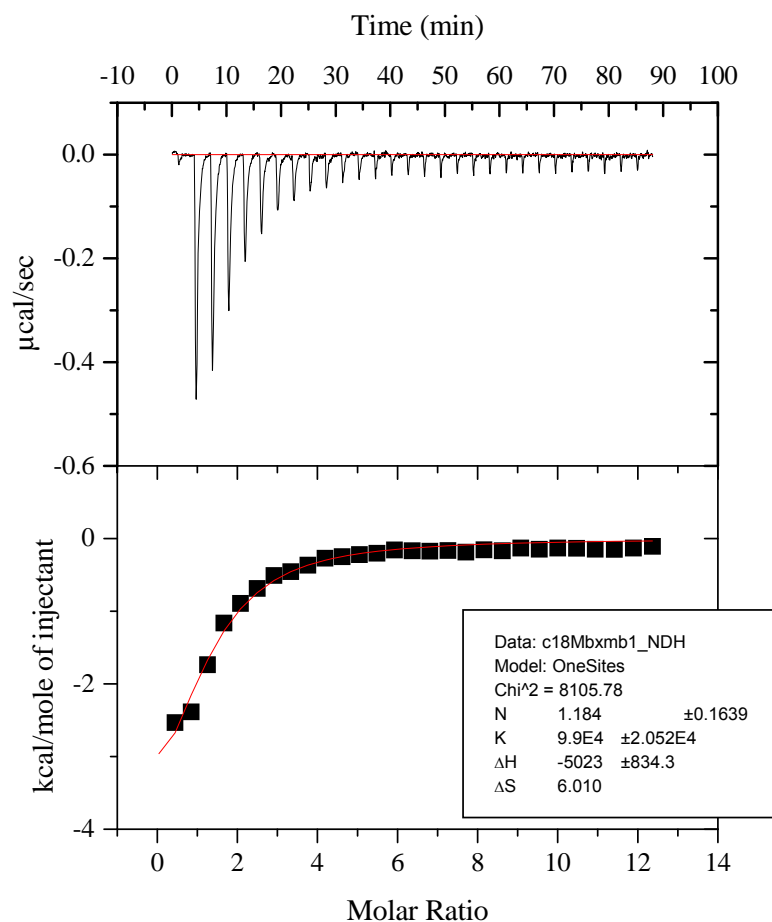


Figure 6.8. Raw ITC data for CBPQT⁴⁺ with BSA and m-BSA.

<i>N</i>	1.184 ± 0.1639
<i>K_a</i> (M⁻¹)	9.9x10 ⁴ ± 2.052x10 ⁴
ΔH (cal mol⁻¹)	-5023 ± 834.3
ΔS (cal mol⁻¹K⁻¹)	6.010

Table 6.3. Thermodynamic data recorded for CBPQT⁴⁺ with the naphthalene modified BSA.



Date: 12/05/2011
 File: c18Mbxmb1b.opj
 Origin v. 5.046

[Syringe] = 0.7 mM
 [Cell] = 0.0125 mM
 T = 25.00903 °C

Figure 6.9. Analysed data for CBPQT⁴⁺ into m-BSA.

6.3.4.3 UV-Vis Spectroscopy.

The UV-Vis spectra of m-BSA **45** upon the addition of CBPQT⁴⁺ were recorded. On addition of increasing aliquots of CBPQT⁴⁺ to the m-BSA **45**, a pale pink colour was observed. By the third equivalent the maximum intensity of the band that was observed in the region of 450 - 650 nm was reached. This band is in the region expected for naphthalene

- CBPQT⁴⁺ pseudorotaxane formation. The presence of this band indicates that the pseudorotaxane had formed with little or no adverse effects from the presence of buffer. The combined spectra recorded for the addition of CBPQT⁴⁺ are shown in Figure 6.10.

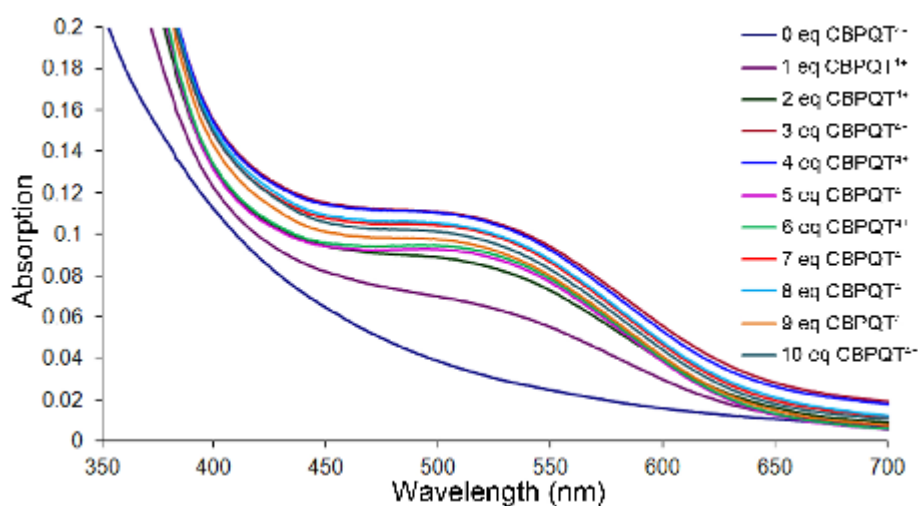


Figure 6.10. UV-Vis spectrum for the addition of CBPQT⁴⁺ to m-BSA at room temperature.

The interaction of the cyclophane with unmodified BSA showed negligible effects whereby a small shoulder appeared with increasing amounts of CBPQT⁴⁺. The lack of a band at 450-650 nm would suggest that the band observed in the modified BSA comes purely from the naphthalene moiety attached to the protein. The spectroscopic data for the unmodified BSA with CBPQT⁴⁺ is shown in Figure 6.11.

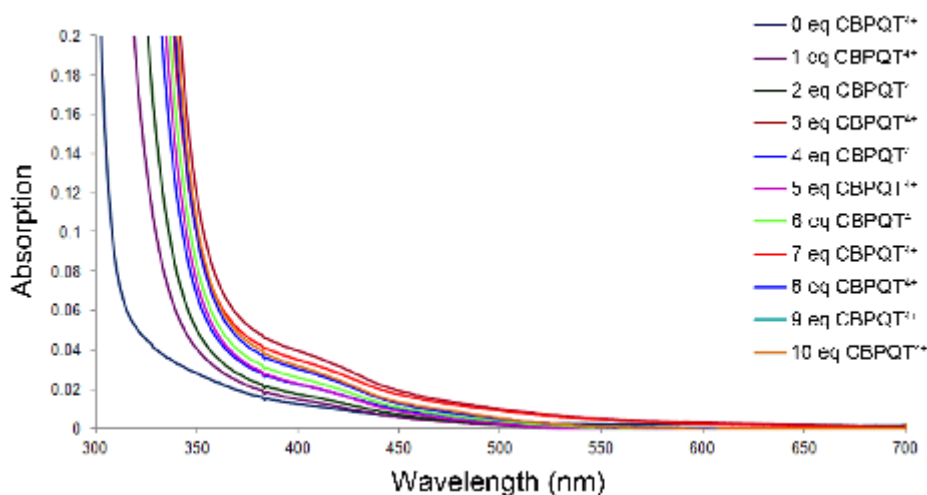


Figure 6.11. UV-Vis spectrum for the addition of CBPQT⁴⁺ to BSA at room temperature.

6.3.4.4 Fluorescence Spectroscopy.

Solutions of BSA and the m-BSA **45** at 8.3×10^{-6} M were prepared in 50 mM phosphate. Equivalents of CBPQT⁴⁺ in water were added, 6.2 μ l of a 4.1 mM solution per equivalent, and the changes in fluorescence at two excitation wavelengths were measured. Blank experiments with 6.2 μ l per aliquot of water added to the proteins were also carried out. For the unmodified BSA, the maximum fluorescence emission peak came from the excitation λ at 282 nm. Excitation at $\lambda = 295$ nm showed the same band as the Ex_{282nm}, but at a lower intensity of around half the height. The addition of aliquots of CBPQT⁴⁺ showed a drop in fluorescence intensity, indicating that the CBPQT⁴⁺ was interacting with the BSA in some way in order to quench the fluorescence. As it is known that CBPQT⁴⁺ non-selectively interacts with π -electron rich substrates including amino acids, the quenching of the fluorescence may be attributed to this form of interaction with the BSA.^[138] Addition of aliquots of water, gave no discernible change in the emission intensity for both excitation wavelengths. The spectra for both Ex_{282nm} and Ex_{295nm} are shown in Figure 6.12.

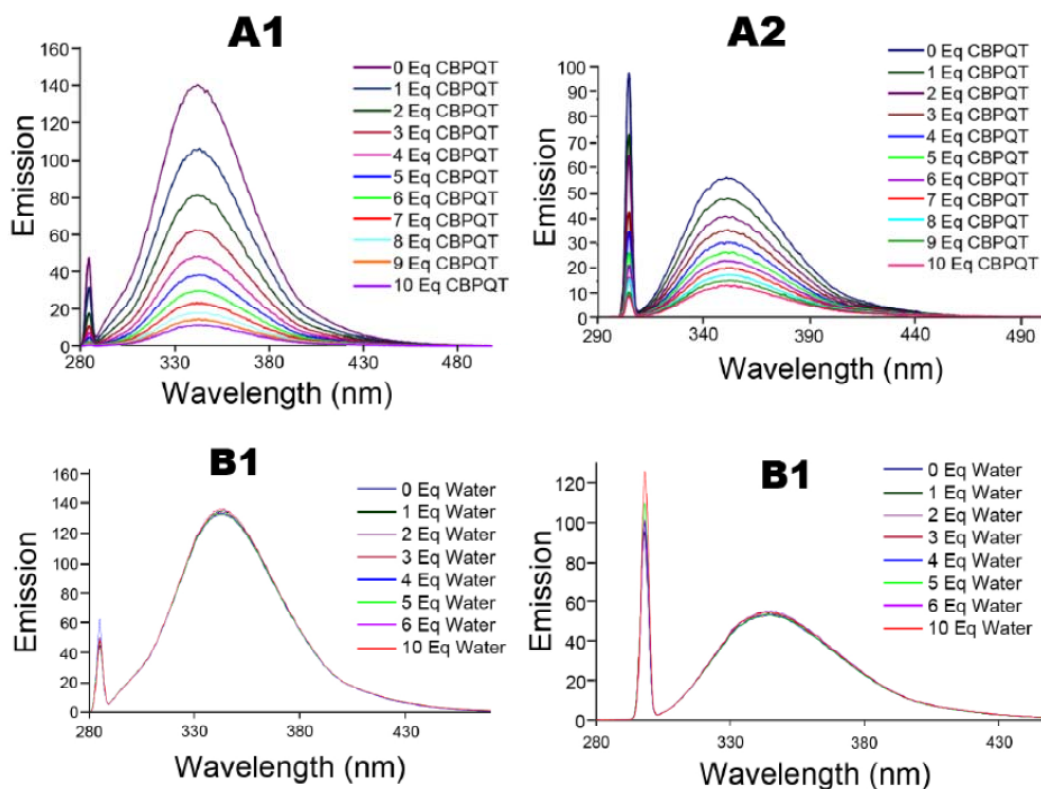


Figure 6.12. Fluorescence emission spectra of BSA upon addition of A) CBPQT⁴⁺ B) H₂O (1- Ex=282nm, 2- Ex=295nm) All measurements were carried out at room temperature.

Fluorescence spectroscopy for the m-BSA **45** gave a maximum emission spectrum at the excitation wavelength of 295 nm. The emission spectrum was of the form typical for naphthalene groups. Excitation at $\lambda = 282$ nm gave the same emission band as observed for $\lambda = 295$ nm, however, the intensity of the signal had dropped by $\sim 17\%$. Addition of CBPQT⁴⁺ aliquots exhibited a drop in fluorescence emission for both excitation wavelengths. With the significant quenching of fluorescence and the colour change observed, it would appear that the pseudo-rotaxane of CBPQT⁴⁺ with the m-BSA had formed. Addition of aliquots of water to the m-BSA **45** had the same lack of effect on the fluorescence emission as observed with the BSA fluorescence emission experiments. These results show that it is only the CBPQT⁴⁺ that is affecting the fluorescence emission, and that the quenching of the fluorescence is not by dilution effects caused by the change in volume of the solutions. The spectra for the experiments carried out with the m-BSA are shown in Figure 6.13.

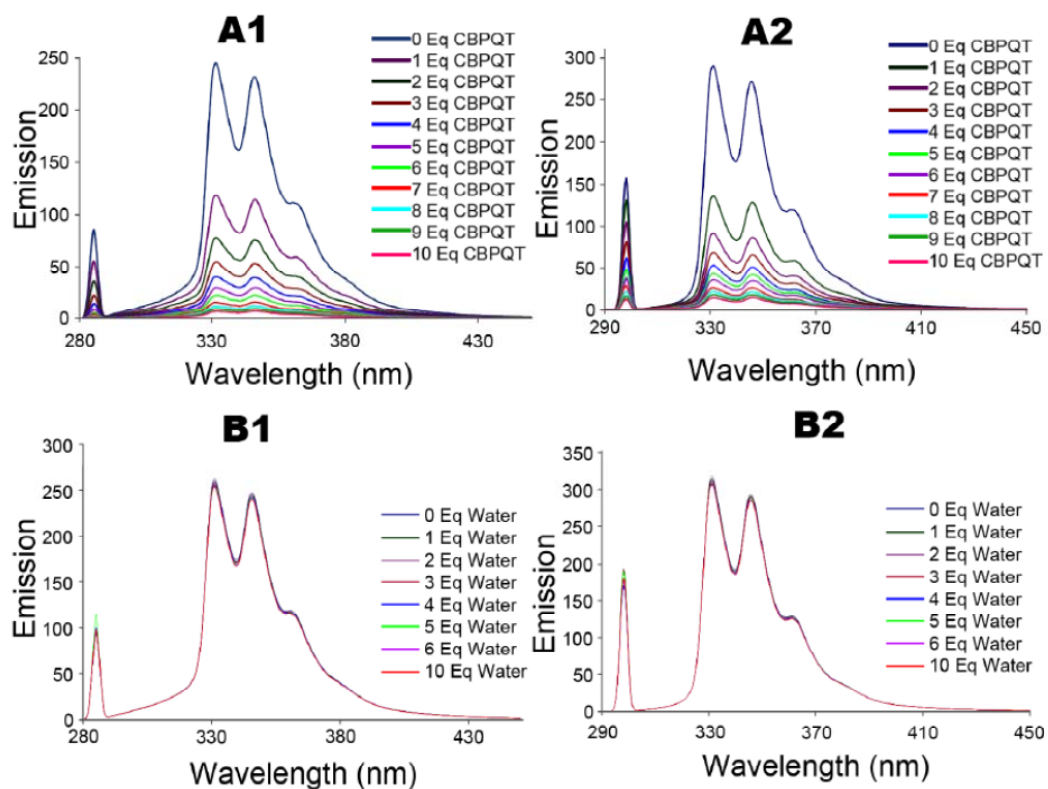


Figure 6.13. Fluorescence emission spectra of M-BSA upon addition of A) CBPQT⁴⁺ B) H₂O (1- Ex=282nm, 2- Ex=295nm) All measurements were carried out at room temperature.

6.4 Conclusions and Future Work.

6.4.1 Conclusions.

To conclude, the naphthalene chloroacetate **19a** has been successfully synthesised in a good yield such that it has been coupled to the protein BSA. Using a number of techniques including MALDI TOF, it has been shown that the chloroacetate derivative **19a** was successfully incorporated into the BSA protein via cysteine thioester linkages. It has been shown that the modified protein can undergo reversible host-guest interactions with CBPQT⁴⁺ in a way that can be observed using a variety of analytical techniques including ITC, fluorescence spectroscopy and UV-Vis spectroscopy.

6.4.2. Future Work.

Additional investigation by electrochemistry to investigate the changes in the redox couple of CBPQT⁴⁺ upon complexation with the protein could be investigated. With further time available, the addition of this substrate to other more complicated proteins, followed by full analysis of the resulting modified protein could be performed.

Further investigation of the reaction to form the azido propylmaleimide in order to gain the product or a similar substrate for click chemistry and/or *in situ* Staudinger/amide reactions with either functionalised primary alkynes or functionalised carboxylic acids would have been carried out had time permitted. This type of modification would have allowed for greater scope of modification possible and the incorporation of other functional groups such as ferrocene, TTF or CBPQT⁴⁺.

7

**Functionalised Biotin Compounds and their
implementation as pseudorotaxane based
bioconjugates.**

7.1 Introduction.

Avidin is a naturally occurring protein that has four degenerate binding sites.^[139] There are several different types of avidin proteins including streptavidin and neutravidin.^[140] Biotin, the vitamin B7, interacts strongly with the avidin family of proteins such that the complex formed has one of the strongest non-covalent interactions found within biochemistry.^[140] The structure of biotin is shown in Figure 7.1. The binding constant, K_a of the complex is $\sim 10^{15} \text{ M}^{-1}$ and is almost completely irreversible.^[140] Upon complexation the protein undergoes conformational changes that lead to the increase in thermal stability and rigidity.^[141] The interaction between avidin and biotin occurs via a complex network of multiple hydrogen bonds which results in a large favourable change in the enthalpy.^[33] The entropy of complexation is close to zero where the unfavourable re-arrangement of the protein is balanced out by the highly favourable desolvation of the binding sites. The interaction overall is remarkably favourable, which in turn leads to the high binding constant.^[33]

The binding of biotin to avidin can be observed by UV-Vis spectroscopy using displacement of 4'-hydroxyazobenzene-2-carboxylic acid (HABA) from the binding sites with biotin.^[142] HABA, a yellow coloured compound will change colour to red upon complexation with avidin. Biotin displaces the HABA from the avidin binding site, resulting in the loss of colour to the solution where the red colour changes to yellow.^[142]

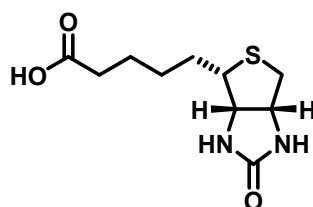


Figure 7.1. Structure of biotin.

The K_a for HABA to avidin has been measured as $\sim 6 \times 10^{-6} \text{ M}$.^[142] The interactions between avidin and HABA can be tuned by the functionalisation of HABA. Changing the position of the carboxylic acid leads to a drop in binding association, where up to one order of magnitude is lost upon movement from the 2-position to the 4-position.^[142] Substitution of the 4'-hydroxybenzene group with a 4-hydroxynaphthalene substituent leads to an increase by an order of magnitude. The addition of substituents around the 3'- and 2'-positions can also modulate the binding affinity to avidin.^[142] Examples of the modifications of HABA and their apparent binding constants K_a are shown in Figure 7.2. K_a was calculated from the DSC measurement for the complexes with avidin. The complex between avidin and HABA can be reversed by the addition of biotin.^[142]

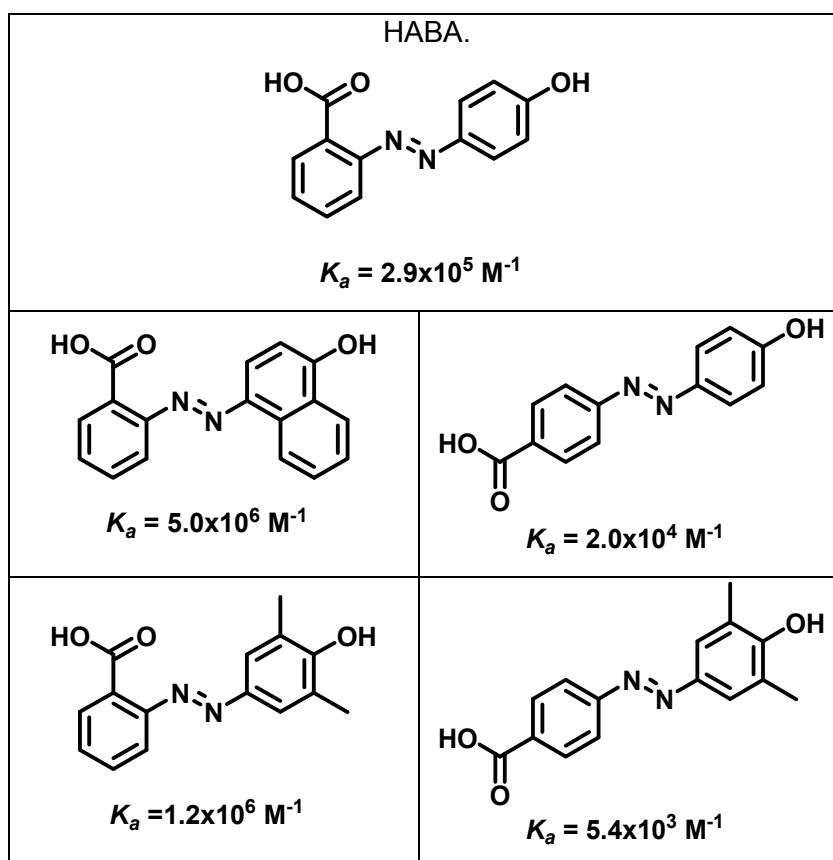


Figure 7.2. Modified HABA derivatives with their binding constants K_a .

The functionalisation of biotin at the carboxylic acid group allows the introduction of groups while retaining strong binding with avidin

proteins.^{[143] [144] [145]} These interactions have been utilised to create functionalised molecules that have known specific protein interactions that may interact with other substrates.^{[143] [144] [145]}

Examples include the formation of SAMs presenting biotin functionality on a quinone propionic ester moiety linker on gold, as shown in Figure 7.3, selectively adsorbed avidin proteins onto the surface while repelling all other proteins from the surface.^[56] Upon the application of an electrical potential of -700 mV to the underlying gold surface, the quinone is converted to the hydroquinone species and a lactonisation occurs where the biotin is cleaved off of the substrate.^[56] Changes in the adhesive properties were measured by SPR where the application of the electrical potential was carried out directly prior to the investigation by SPR.^[56] The removal of the biotin leads to a complete loss of binding of the streptavidin to the surface. After release of the biotin group, the surface was also still inert to other protein adsorption.^[56] It has been shown that the application of the electrical potential of -700 mV had no effect on the behaviour of the SAMs to proteins.^[56] However, it was found that by increasing the voltage potential to -1100 mV caused the monolayer to become damaged such that the complex of streptavidin / biotin started to adsorb onto the surface of the gold, indicating that the monolayer was no longer active in the repulsion of non-specific protein.^[56] The structure of the monolayers and the transformation upon the application of the electrical potential is shown in Figure 7.3. The SPR data recorded are shown in Figure 7.4.

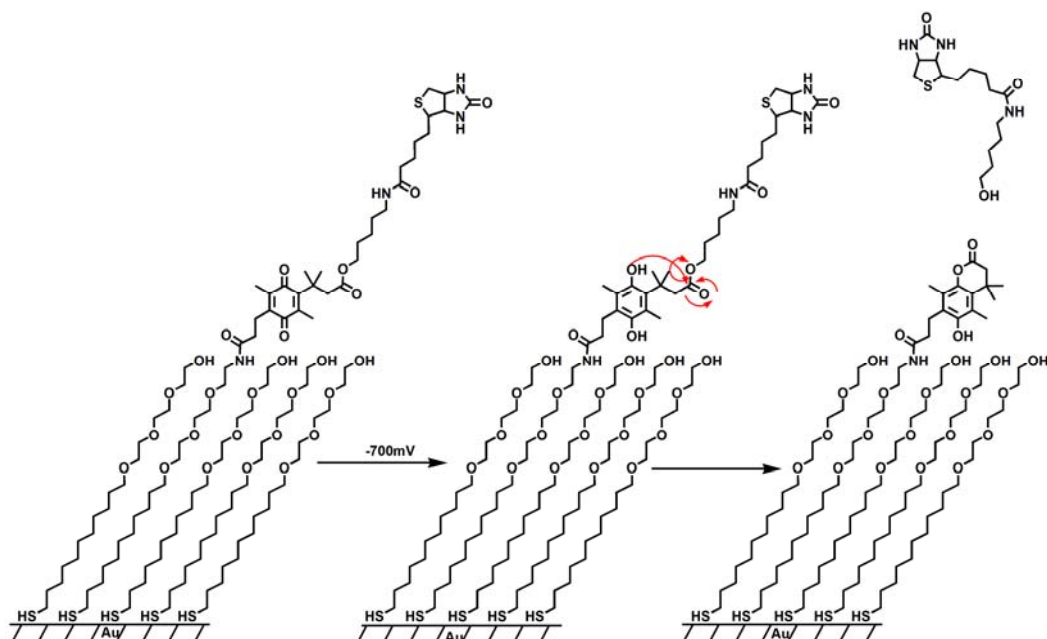


Figure 7.3. SAMs with biotin that is released by the application of an electrical potential. [56]

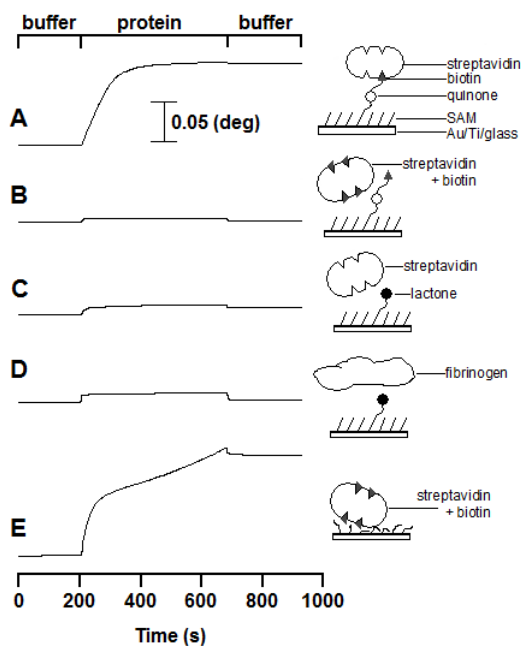


Figure 7.4. SPR data for the SAMs before and after addition of an electrical potential. [56]

Biotin can incorporate functionality that can itself undergo host-guest interactions where either does not inhibit the separate interactions. Work has been carried out by Cooke and co-workers where a

naphthalene group was attached via a diethylene glycol linker to biotin^[146]. It was found that the naphthalene biotin conjugate could perform interactions with both avidin proteins and with the cyclophane CBPQT⁴⁺.^[146] The structure of the naphthalene biotin conjugate is shown in Figure 7.5.

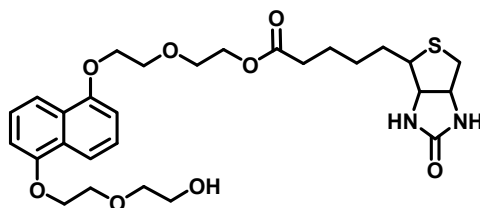


Figure 7.5. Structure of the naphthalene biotin conjugate.^[146]

The interactions with avidin were investigated by UV-Vis experiments with avidin/HABA complex displacement with the naphthalene biotin conjugate.^[146] It was shown that the conjugate displaced the HABA successfully from the binding sites of the avidin. Addition of CBPQT⁴⁺ to the conjugate gave a distinctive purple colour with a λ_{max} of 520 nm, which was typical for the formation of the pseudorotaxane.^[147] UV-Vis experiments showed that the CBPQT⁴⁺ did not interact with avidin itself as mixtures did not exhibit colour changes until the naphthalene conjugate was added.^[146] Subsequent addition of TTF caused the solution to change colour from purple to green showing that the naphthalene group had been displaced from the cavity of the cyclophane.^[146] The spectra recorded are shown in Figure 7.6. ¹H NMR studies also indicated that the pseudorotaxane had formed by the shift of the H_{4/8} protons on the naphthalene by ~5.5 ppm upon complexation with CBPQT⁴⁺.^[146]

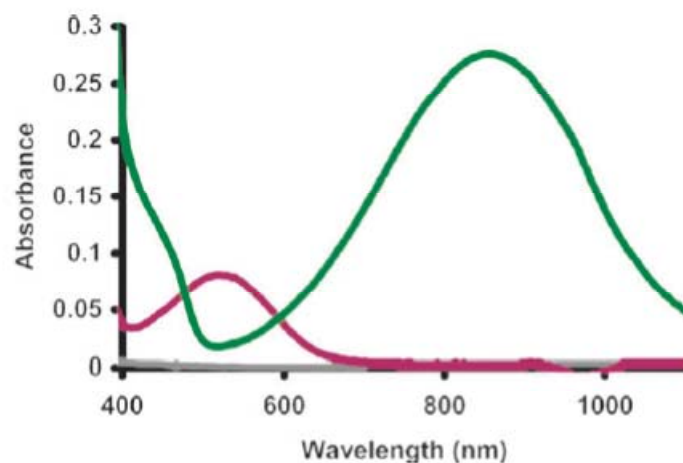


Figure 7.6. UV-Vis recorded in water/ethanol 70:30. avidin + CBPQT (grey); Plus Naphthalene biotin (purple); Plus TTF (green).

ITC was used to measure the binding interactions between the naphthalene biotin conjugate and avidin and CBPQT⁴⁺.^[146] From the experiments the binding constants were measured as $K_a = 7.3 \times 10^6 \text{ M}^{-1}$ for biotin-avidin and $K_a = 4.7 \times 10^4 \text{ M}^{-1}$ for the interaction between naphthalene CBPQT⁴⁺.^[146] The titration of CBPQT⁴⁺ into avidin only, showed purely heats of dilution, confirming that there was no interaction between the cyclophane and the protein.^[146] The ITC data recorded for the interactions plotted heat vs time is shown in Figure 7.7.

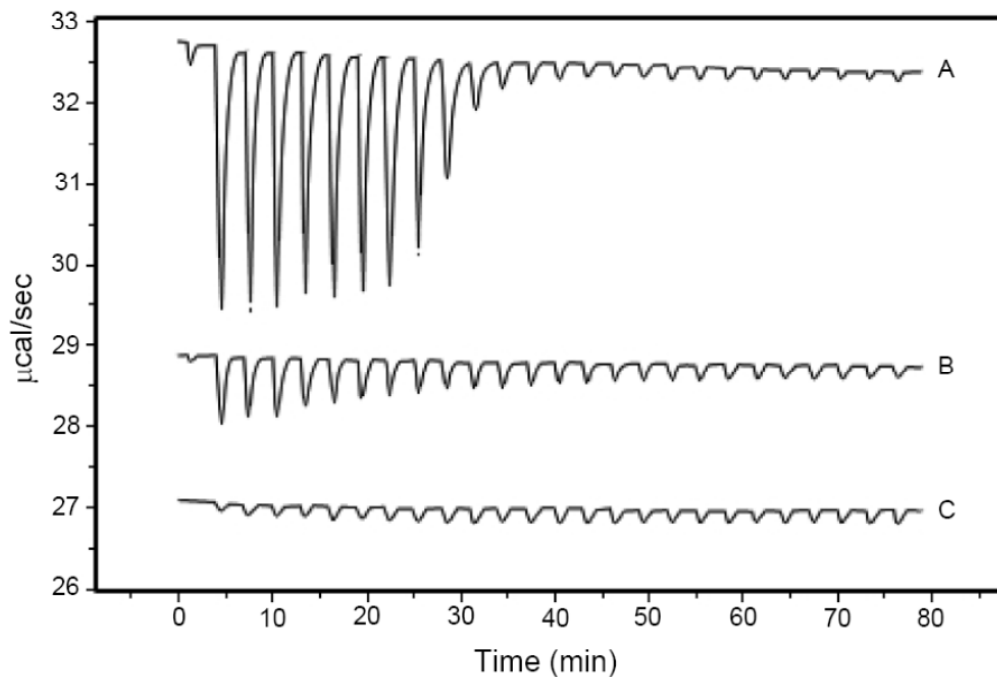


Figure 7.7. Heat vs time plot of A) naphthalene biotin into avidin. B) CBPQT⁴⁺ into naphthalene biotin / avidin complex. C) CBPQT⁴⁺ into avidin.

7.2 Aims and Objectives.

The aim of this project was to synthesise two ferrocene functionalised biotin conjugates for investigating the interactions between avidin proteins and the conjugates. Investigation into the effects of cyclodextrin on the binding interactions with avidin and the redox properties of the ferrocene were also planned. The effects of chain length between the biotin moiety and the ferrocene group would be studied by the comparison of the two compounds.

Moreover, investigation into a long chain naphthalene biotin conjugate and the affect on binding interactions with CBPQT⁴⁺ and avidin was an additional area of interest. The added glycol chain enhances the water solubility of the compound and provides an interesting comparison to the ferrocene functionalised systems.

The target molecules are shown in Figure 7.8, where the solubility in aqueous media should be enhanced by the extended linker chain in compound **21** and **29**. A schematic of the interactions to be investigated is shown in Figure 7.9.

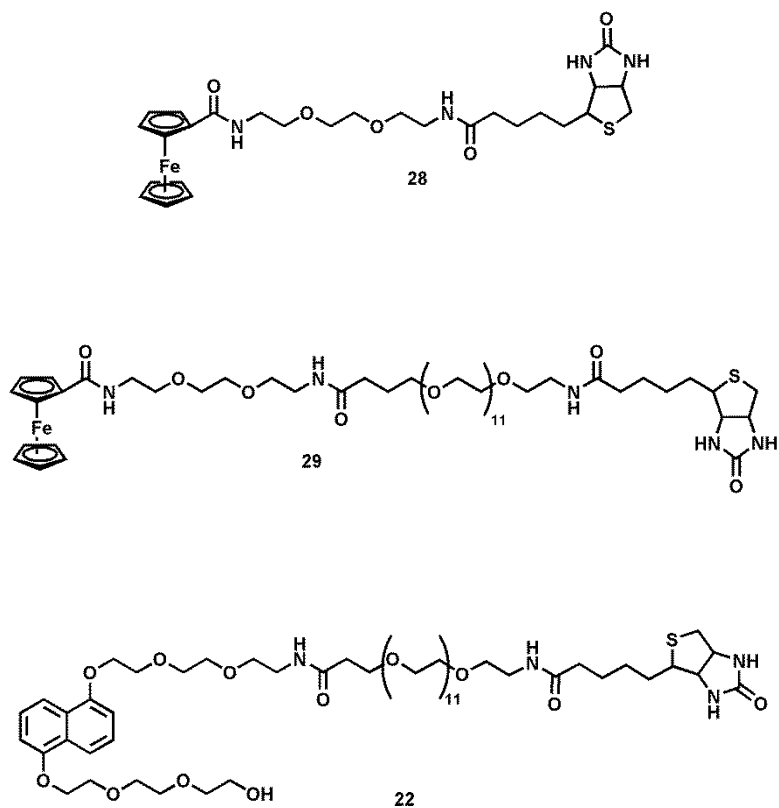


Figure 7.8. Functionalised biotin conjugates for investigation.

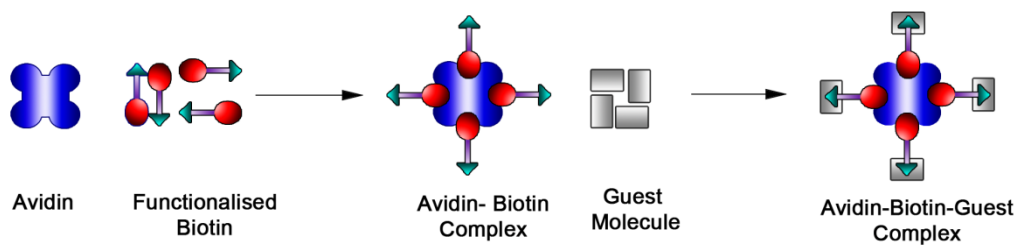
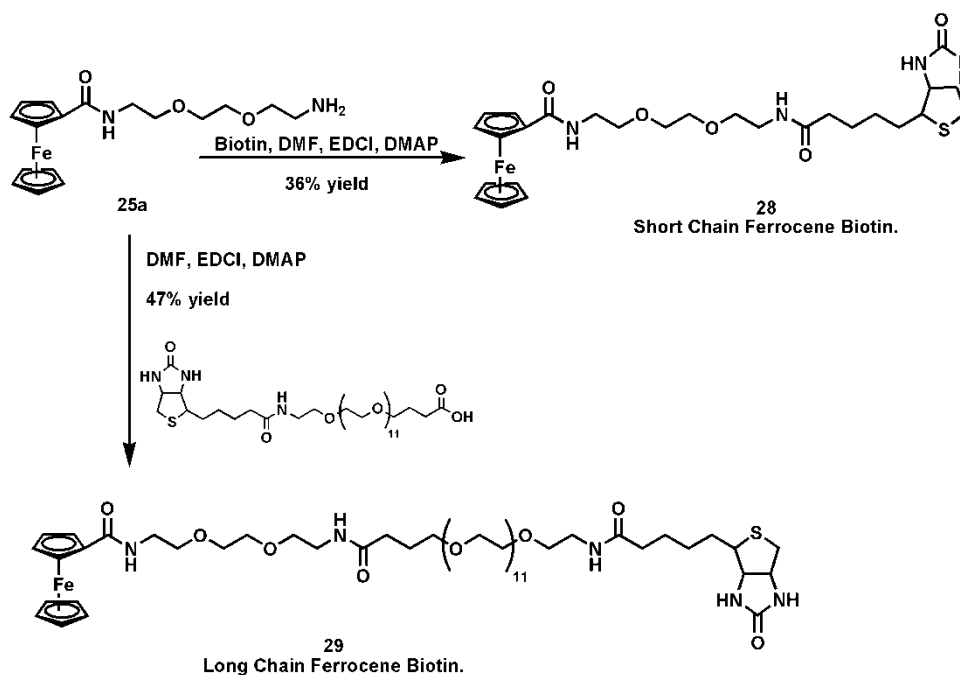


Figure 7.9. Illustrative schematic of the complexation of the functionalised biotins to avidin with additional complexation of a guest molecule.

7.3 Results and Discussion.

7.3.1 Synthesis of biotinylated ferrocene compounds **28** and **29**.

Starting with the ferrocene amine **25a**, the biotin conjugates were formed by EDCI couplings with either biotin or the long chain biotin derivative, O-[2-(biotinylamino)ethyl]-O'-[2-carboxyethyl] undecaethylene glycol in reasonable yields as indicated in Scheme 7.1.



Scheme 7.1. Synthesis of ferrocene biotin compounds **28** and **29** from ferrocene amine **25a**.

The EDCI coupling of **25a** with biotin to gain the biotinylated product **28** in a yield of 36% was fairly straightforward such that removal of impurities by column chromatography achieved the pure product as a glassy orange solid that had a tendency to stick to the sides of its container making manipulation for analysis slightly difficult. Solubility in aqueous media was low, and precipitation was an issue if the solutions were left for long periods. The reaction between **25a** and the long chain

biotin compound via an EDCI coupling similar to that of the reaction above, gave the ferrocene long chain biotin product **29** as a very greasy dark brown oil in 47% yield that did not require any purification after extraction in DCM. The oil was highly soluble in water, however, the consistency of the oil made handling the material non-trivial.

7.3.2 Analysis of the biotinylated conjugates.

7.3.2.1 UV-Vis Spectroscopy.

4'-Hydroxyazobenzene-2-carboxylic acid (HABA) can moderately bind to avidin at the proteins biotin binding site. The complex produced between HABA and avidin is a bright red colour that is lost upon removal of the HABA from the binding site.^[142] Biotin will competitively displace HABA from the avidin binding sites such that, upon complete decomplexation of the HABA from the avidin binding sites, the solution goes from bright red to pale yellow. As a result, the competitive binding of biotin to avidin can be monitored by UV-Vis experiments. This interaction was utilised to confirm the retention of biotin binding activity to avidin and its derivatives after modification with ferrocene in both compounds **28** and **29**. To a solution of neutravidin and HABA (3 mL) was added 10 μ L aliquots of 0.03 M aqueous solution of the required ferrocene biotin. Each aliquot corresponded to 1 molar equivalent of the biotin compound. After each addition an UV-Vis spectrum was ran. A total of 10 equivalents were added to the neutravidin HABA complex. The change in the absorbance at $\lambda = 500$ nm for ferrocene biotin compounds **28** and **29** are shown below in Figure 7.10 and Figure 7.11.

From the figures, it can be seen that the biotin moiety of **28** and **29** was still capable of displacing the HABA from the binding sites of the neutravidin. In the cases of **29**, after the 5th equivalent almost all HABA

had been displaced and the solutions had lost most of the red colour, and were dark yellow. By the 8th equivalent the solutions were very pale yellow and complete irreversible displacement had occurred.

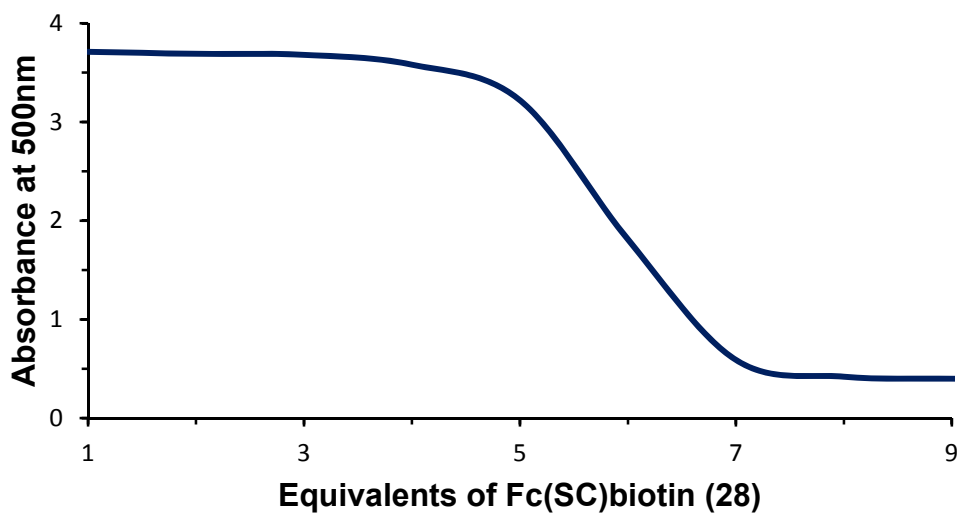


Figure 7.10. Changes in the absorbance at 500nm with increasing equivalents of 28 to HABA-Neutraavidin complex. Experiments were run at room temperature in water at a concentration of 10^{-3} M.

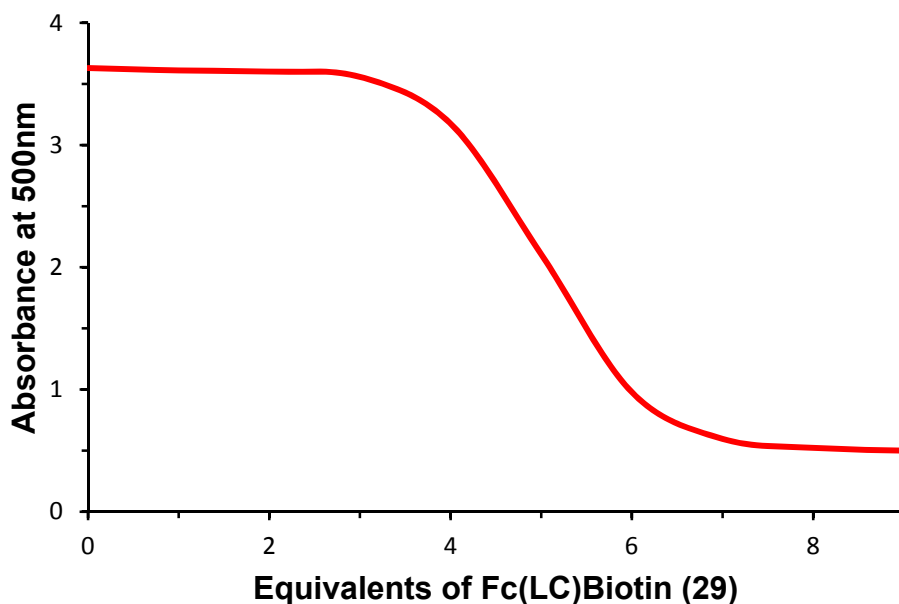


Figure 7.11. Changes in absorbance at 500 nm with increasing equivalents of 29 to the HABA –Neutraavidin complex. Experiments were run at room temperature in water at a concentration of 10^{-3} M.

The UV-Vis analysis of the naphthalene conjugate **22** with HABA and avidin showed that the compound also readily displaced the HABA from the avidin binding sites. By the fourth equivalent total displacement of the HABA had occurred. This indicates that the naphthalene substrate displaces the HABA more readily than that of the ferrocene conjugates. The results are shown in Figure 7.12.

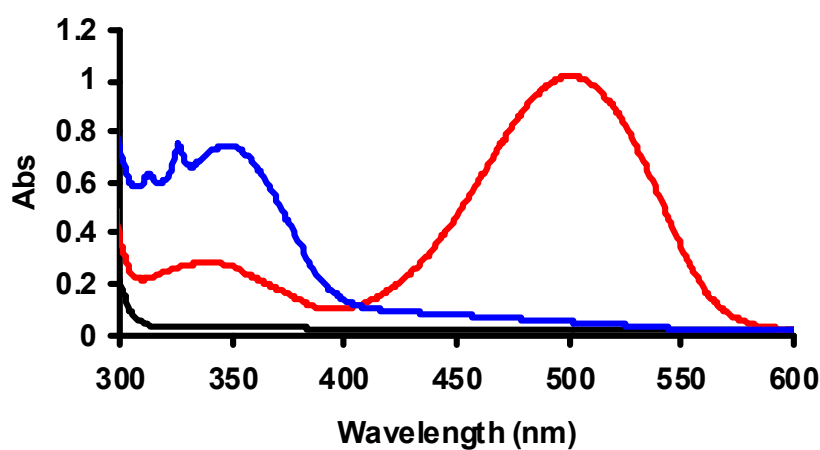


Figure 7.12. UV-Vis of naphthalene biotin into HABA/avidin. Black = avidin 10^{-5} M. Red = avidin with 4eq HABA. Blue = upon addition of 4eq of **22** into the HABA/avidin complex. Experiment run at room temperature.

Furthermore, the complex between **22** and CBPQT⁴⁺ was investigated by UV-Vis and fluorescence spectroscopy. As the complex formed the typical band for the pseudorotaxane formation was observed in the UV-Vis spectrum, while quenching of the naphthalene fluorescence was observed in the fluorescence emission spectrum. The results are shown in Figure 7.13 and Figure 7.14. Addition of avidin to the pseudorotaxane had no effect on the UV-Vis absorbance. The fluorescence spectrum for the complex between compound **22** and avidin was also recorded to investigate the effect on the fluorescence emission upon binding. The emission spectrum showed that upon complexation with avidin, there was very little effect on the fluorescence of the

naphthalene, indicating that quenching did not occur. The spectra produced are shown in Figure 7.14.

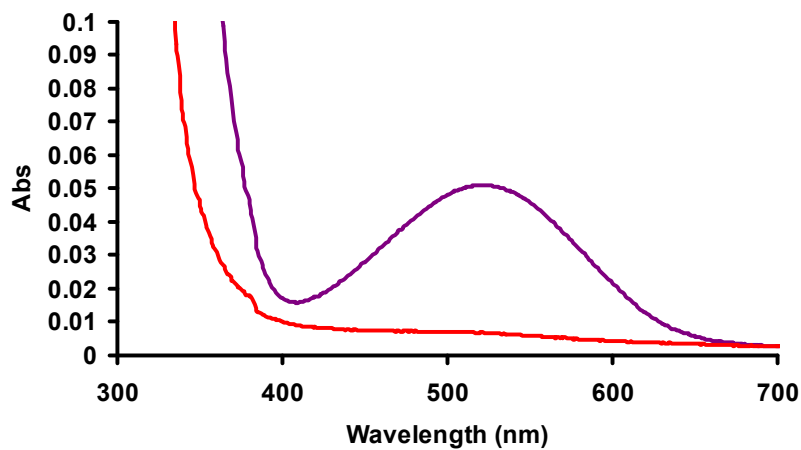


Figure 7.13 UV-Vis spectrum of 22 with CBPQT^{4+} . Red line = 22 (10^{-4} M). Blue line = 22 + CBPQT^{4+} Recorded at room temperature in water.

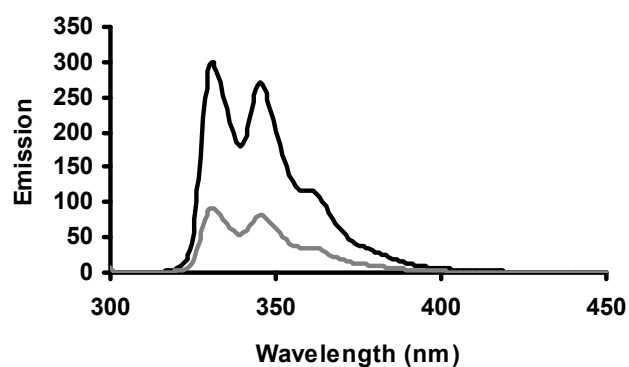


Figure 7.14. Fluorescence emission spectrum of 22 with CBPQT^{4+} . Black line = 22 (10^{-5} M). Grey line = 22 + CBPQT^{4+} . Run at room temperature in water.

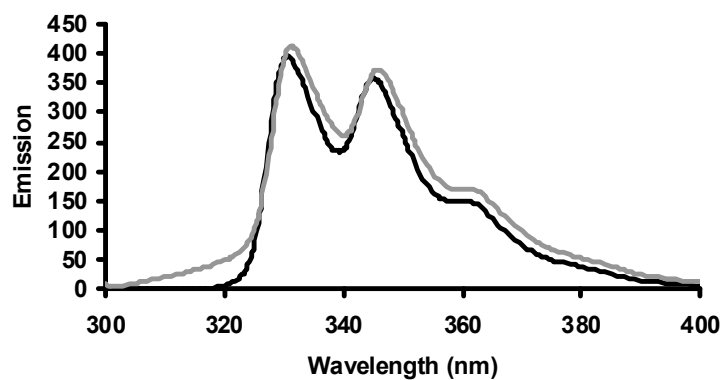


Figure 7.15. Fluorescence emission spectrum of 22 with avidin recorded at room temperature in water. Black line = 22 (10^{-5} M). Grey line = 22 + avidin.

7.3.2.2 ITC experiments.

To probe the binding interactions between neutravidin and the ferrocene biotin compounds, ITC was carried out in water. The interaction with β -cyclodextrin was also investigated. Table 7.1 below gives the details of each experiment carried out for compound **28**.

Experiment	Contents of cell	Contents of syringe
1	Water	Ferrocene SC Biotin (28) 0.7mM
2	Neutravidin 0.0125mM	Ferrocene SC Biotin (28) 0.7mM
3	Neutravidin / Fe SC Biotin (28) Complex (formed in expt 2)	β -cyclodextrin 0.7mM
4	Ferrocene SC Biotin 0.02mM	β -cyclodextrin 0.7mM
5	Ferrocene SC Biotin (28) 0.02mM (50°C)	β -cyclodextrin 0.7mM

Table 7.1. Experimental details for **28**, neutravidin, and β -cyclodextrin. All experiments unless otherwise indicated were carried out at 25°C.

Starting with the interaction between the short chain ferrocene biotin conjugate (**28**) and neutravidin, the investigation revealed a strong binding curve that gave the data shown in Table 7.2 from a single-set-of-sites binding model. The binding curve exhibited by the interaction between compound **28** and the β -cyclodextrin appeared to be purely dilution effects. The experiment was then repeated at 50°C in order to observe any weak interactions that could not be observed at the lower temperature. Again, the data recorded showed no binding interaction was observable. This may have been due a low isotherm form binding or that the binding was particularly weak. The raw data produced, and the analysed data for the short chain ferrocene biotin conjugate (**28**) with the neutravidin are shown in Figure 7.16 and Figure 7.17.

<i>N</i>	4.02
<i>K_a</i> (<i>M</i>⁻¹)	$1.32 \times 10^7 \pm 1.84 \times 10^6$
ΔH (cal mol⁻¹)	$-1.66 \times 10^4 \pm 100.2$
ΔS (cal mol⁻¹K⁻¹)	-23.07

Table 7.2. Thermodynamic data recorded for titration of 28 into neutravidin.

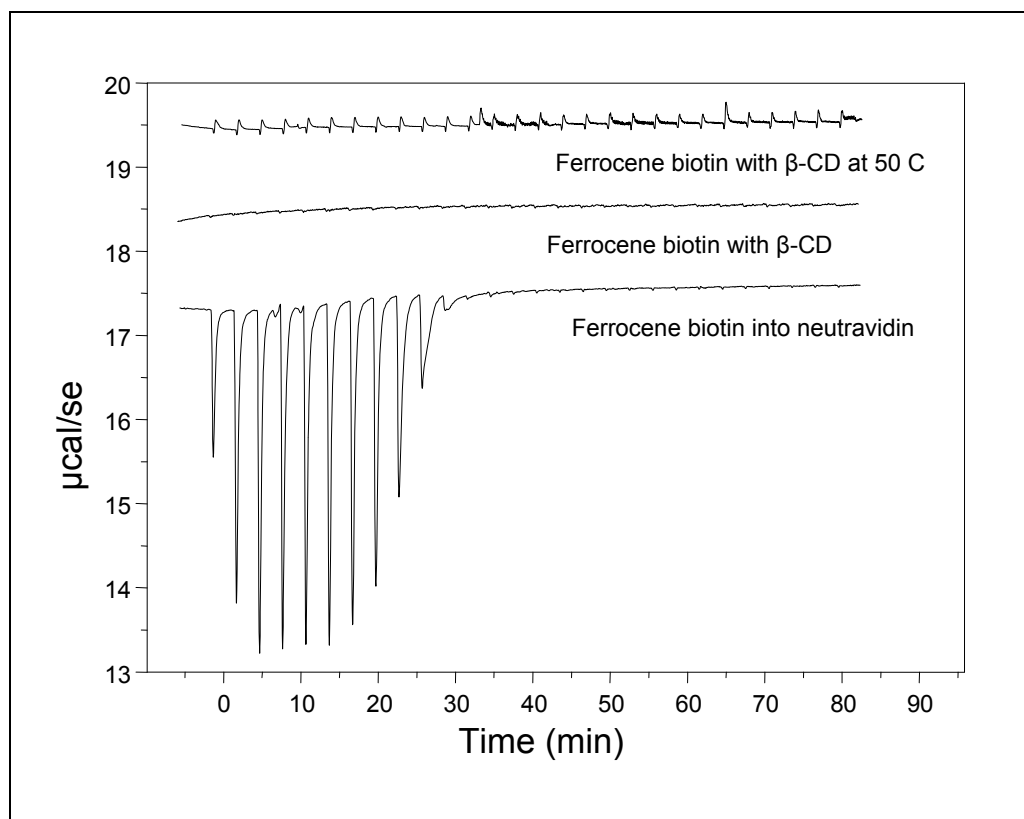


Figure 7.16. Raw ITC data collected for compound 28 with neutravidin and β-cyclodextrin.

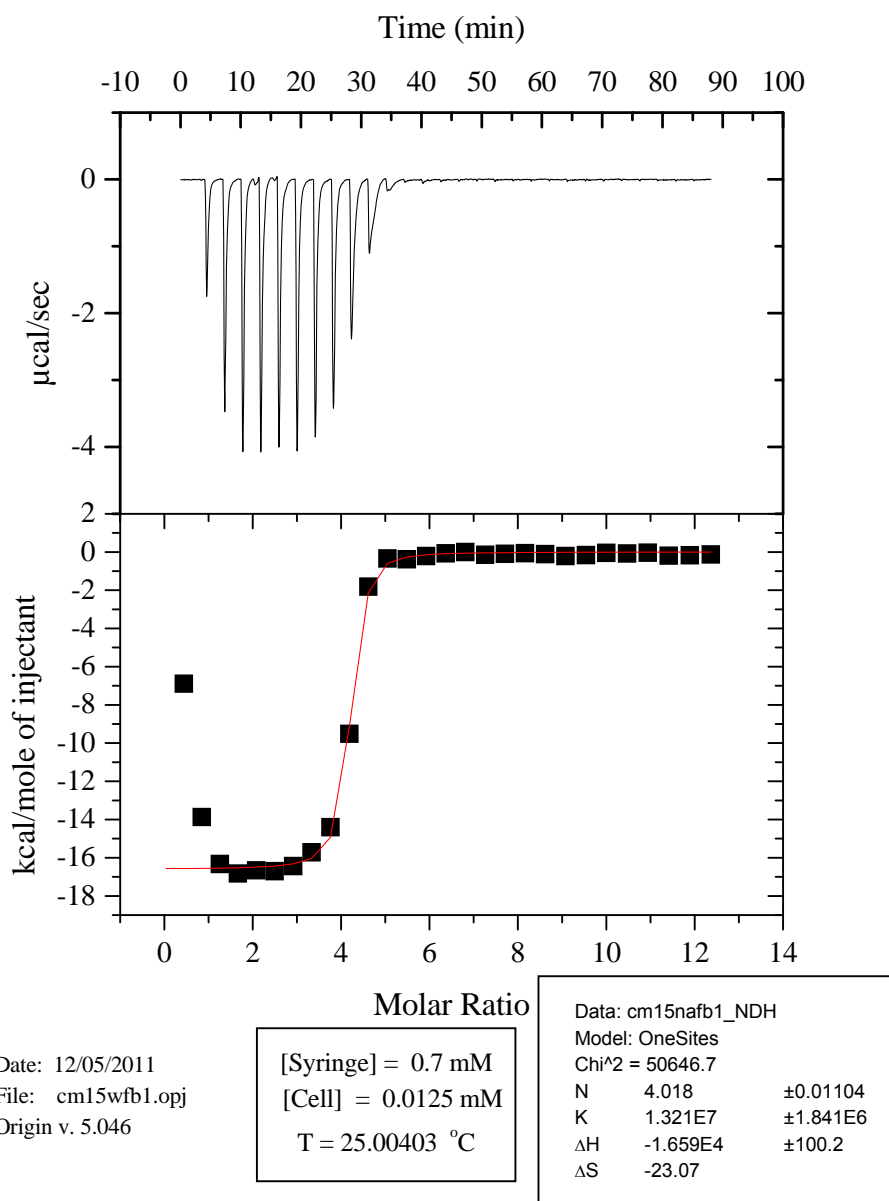


Figure 7.17. ITC data for the titration of 28 into neutravidin solution.

Table 7.3 gives the details of each experiment carried out for the long chain biotin compound. The ITC experiment with compound **29** with neutravidin gave a strong binding curve that gave the data shown in Figure 7.18, from a single-set-of-sites binding model. It can be noted that the K_a of these conjugates with neutravidin is significantly less than for

biotin to avidin, however the values are still high and in the range of 10^7 M^{-1} for the short chain ferrocene biotin conjugate **28** and 10^5 M^{-1} for the long chain ferrocene biotin conjugate **29**. The differences in K_a may be associated to the steric bulk of biotin conjugates, where the larger molecule has a lower K_a by almost two orders of magnitude. It may be that the larger molecule disrupts the change in conformation of the neutravidin protein that is required for binding.

The binding curves for the addition of β -cyclodextrin to the complex and to compound (**29**) only were very weak; however, by the subtraction of the dilution data for β -cyclodextrin into water we were able to fit the data when the binding stoichiometry N was kept at 1. The data for the interaction of β -cyclodextrin with compound (**29**) are shown in Table 7.4. From this data it can be observed that the binding is very weak, but in the range expected for ferrocene cyclodextrin which is typically 10^3 - 10^4 M^{-1} [31]. The analysed data for each experiment are shown in Figure 7.18.

Experiment	Contents of cell	Contents of syringe
1	Water	Ferrocene LC Biotin (29) 0.7 mM
2	Neutravidin 0.0125 mM	Ferrocene LC Biotin (29) 0.7 mM
3	Neutravidin / Fe LC Biotin (29) Complex from expt 2	β -cyclodextrin 0.7 mM
4	Ferrocene LC Biotin (29) 0.05 mM	β -cyclodextrin 0.7 mM
5	Water	β -cyclodextrin 0.7 mM

Table 7.3. Experimental details for **29**, neutravidin, and β -cyclodextrin.

All experiments were carried out at 25°C.

	29 into N_A	β-CD into 29/N_A	β-CD into 29
<i>N</i>	3.64 ± 0.0478	1.00	1.00
<i>K_a</i> (M⁻¹)	9.69 x10 ⁵ ± 1.63 x10 ⁵	404.7 ± 205.6	1283 ± 519.4
<i>ΔH</i> (calmol⁻¹)	-1.43 x10 ⁴ ± 299.2	-9.32 x10 ⁴ ± 4.50 x10 ⁴	-3890 ± 1327
<i>ΔS</i> (calmol⁻¹K⁻¹)	-20.91	-300.7	1.75

Table 7.4. Thermodynamic data recorded for the ITC of 29 with neutravidin and β-CD.

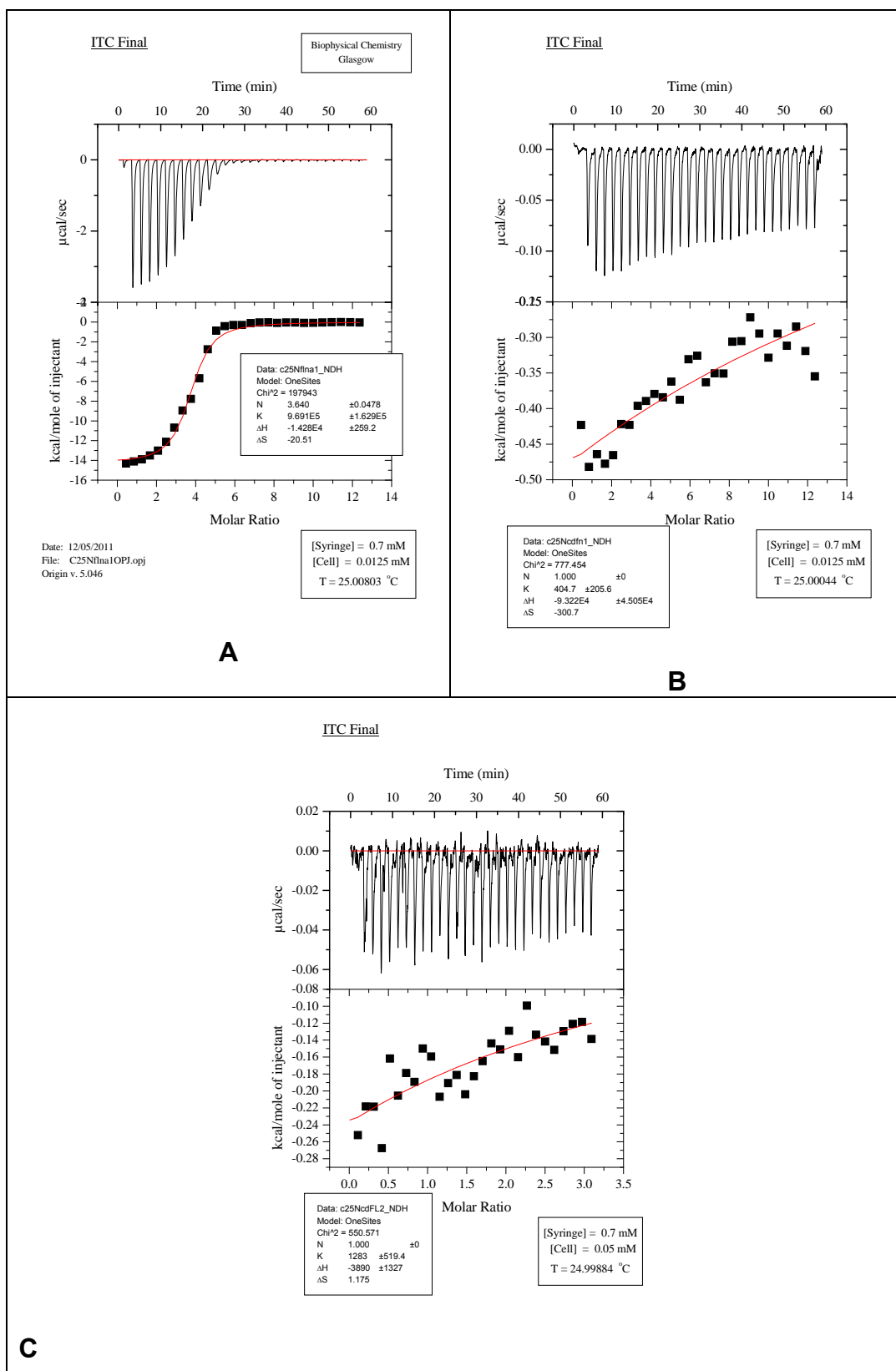


Figure 7.18. ITC titration data for A) 29 into neutravidin. B) addition of β -cyclodextrin to 29 / neutravidin. C) β -cyclodextrin into 29.

ITC analysis of the naphthalene biotin compound **22** with avidin, neutravidin and CBPQT⁴⁺ was carried out in water. The experiments were carried out to investigate the effect on the strength of binding K_a upon changing from avidin to neutravidin. The effect of chain length upon CBPQT⁴⁺ with the naphthalene biotin compound **22** was also investigated.

The interaction between **22** and avidin showed a strong interaction with a $K_a = 2.35 \times 10^7 \text{ M}^{-1}$. The interaction between **22** and neutravidin was lower with a $K_a = 4.7 \times 10^6 \text{ M}^{-1}$. The difference is attributed to the change in the protein used. It has been shown that the lower binding affinity observed for neutravidin is typical for avidin related proteins.^[148] The binding stoichiometry N for the two proteins with compound **22** was found to be 3 rather than the expected 4. However, this loss of a binding site is attributed to the oligomeric nature of conjugate. The interaction between compound **22** with CBPQT⁴⁺ was also strong where the $K_a = 2.05 \times 10^5 \text{ M}^{-1}$ showing that the affinity for the formation of the pseudorotaxane is reasonably unaffected by the presence of the biotin moiety. The thermodynamic data recorded for the interactions are shown in Table 7.5. The analysed data for each interaction are shown in Figure 7.19.

	avidin + 22	Neutravidin + 22	CBPQT⁴⁺ + 22
N	2.9 ± 0.01	3.2 ± 0.03	1.19 ± 0.01
$K_a (\text{M}^{-1})$	$2.35 \times 10^7 \pm 3.81 \times 10^6$	$4.69 \times 10^6 \pm 1.1 \times 10^5$	$2.05 \times 10^5 \pm 7142$
$\Delta H (\text{cal mol}^{-1})$	$-1.90 \times 10^4 \pm 123.4$	-1.91 ± 345.5	$-1.23 \times 10^4 \pm 95.36$
$\Delta S (\text{cal mol}^{-1} \text{K}^{-1})$	-29.9	-33.4	-16.8

Table 7.5. Thermodynamic data recorded for ITC titration experiments of **22** with avidin, neutravidin and CBPQT⁴⁺.

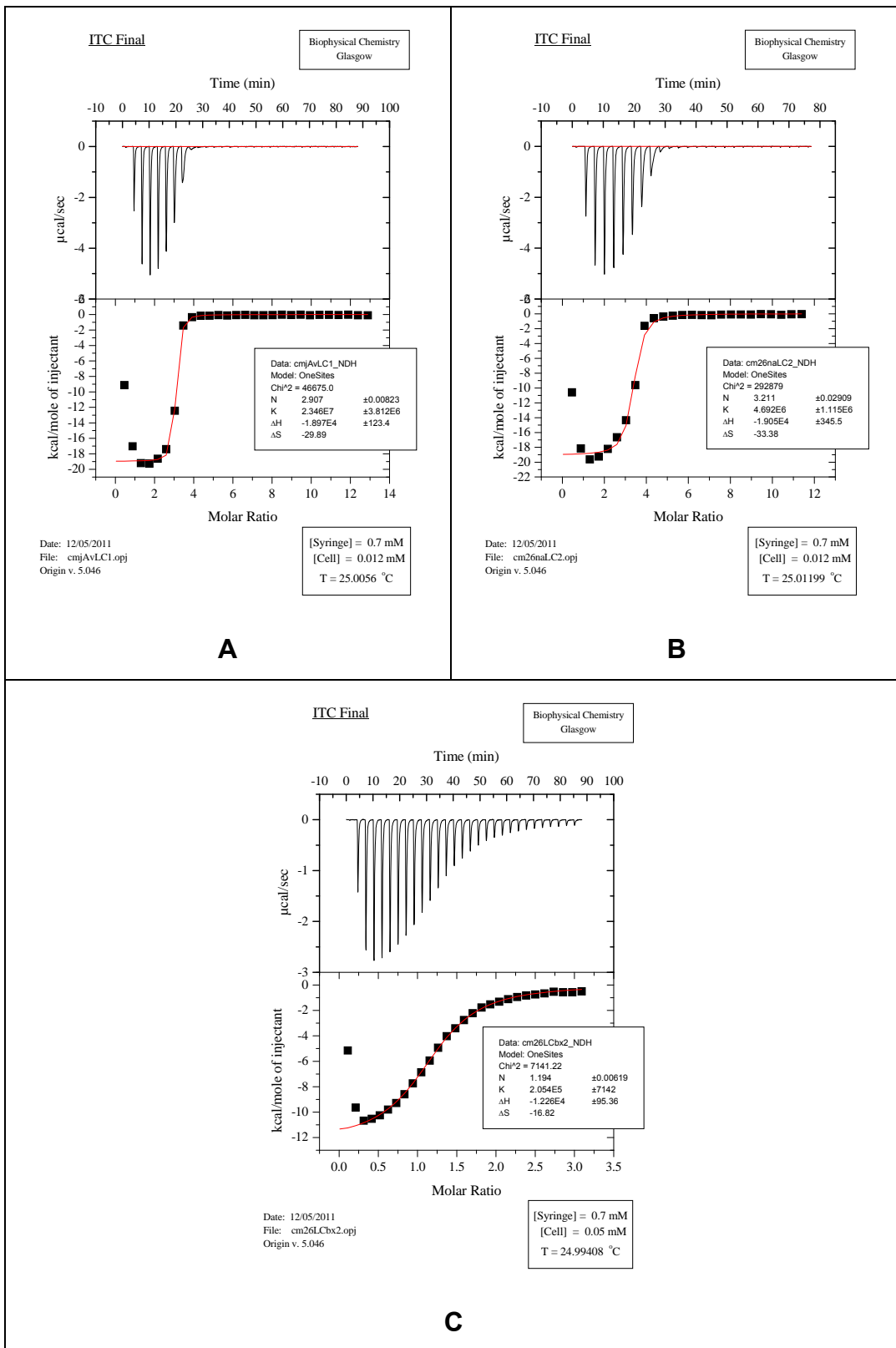


Figure 7.19. ITC graphs of A) 22 into avidin. B) 22 into neutravidin. C) CBPQT⁴⁺ into 22.

7.3.2.3 Cyclic Voltammetry.

For ferrocene to undergo the redox processes observed in a cyclic voltammetry experiment, it must be available to perform oxidation and reduction processes. When it has formed an inclusion complex with β -cyclodextrin it cannot participate in the redox chemistry and must exit the cavity of the β -cyclodextrin in order to do so. As the amount of β -cyclodextrin present in solution increases, the ferrocene does not leave the cavity of one β -cyclodextrin molecule long enough before re-entering another β -cyclodextrin cavity and so gradually becomes unable to perform the redox cycle. 0.5 mM solutions of the ferrocene biotin compounds with 0.1 M NaCl were used for the CV studies where up to 5 equivalents of β -cyclodextrin were added. The cyclic voltammograms were run after each equivalent of β -cyclodextrin was added. The results of the CV studies for the ferrocene biotin compounds **28** and **29** are shown in Figure 7.20 and Figure 7.21.

As the β -cyclodextrin was added the half wave potential $E_{1/2}$ shifted and the intensity of the signal was reduced as the redox activity of the ferrocene's were reduced. By the fourth equivalent the redox wave was completely diminished for both systems, and the ferrocene was completely saturated with β -cyclodextrin. This indicates that the ability of ferrocene to form inclusion complexes with β -cyclodextrin was uninhibited by the functional group attached.

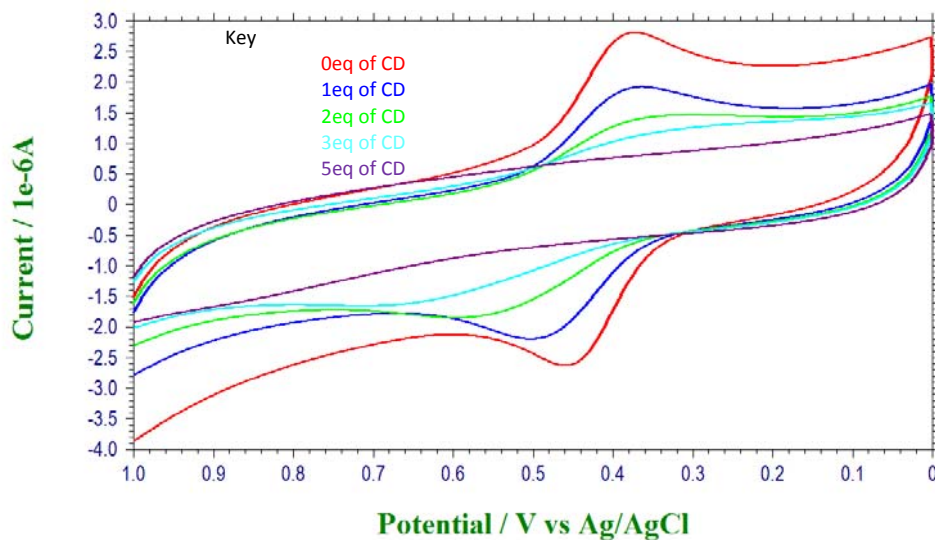


Figure 7.20. CV of compound 28 with increasing equivalents of β -cyclodextrin.

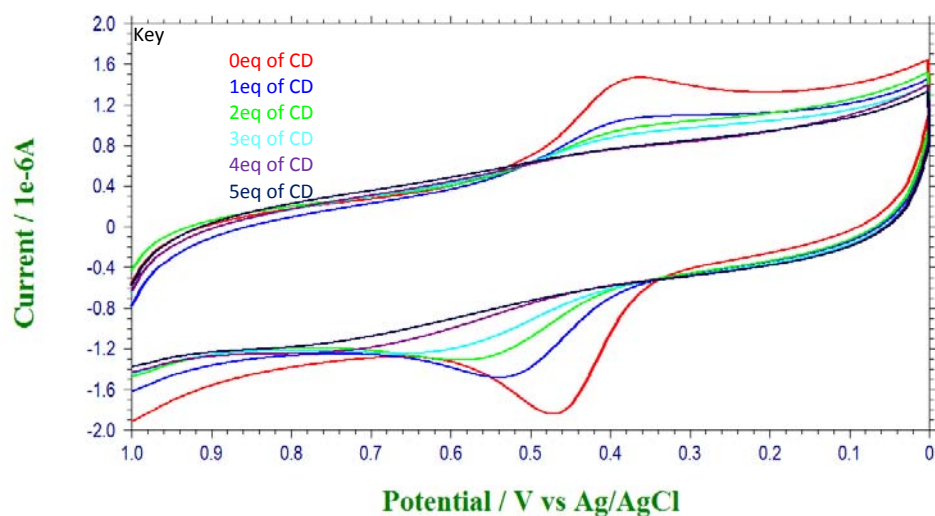


Figure 7.21. CV of compound 29 with increasing equivalents of β -cyclodextrin.

From the data produced in Figure 7.20 and Figure 7.21 it was observed that the redox activity was modulated with chain length such that the short chain system had an intensity of almost double that of the long chain system. The long chain system had a slightly higher $E_{1/2}$ than the short chain system, this would indicate that it was slightly more difficult for the long chain ferrocene compound to undergo the oxidation

reduction wave. The data recorded for these systems are shown in Table 7.6 and Table 7.7. The reduction in the intensity may be associated with dilution effects as the aliquots of β -cyclodextrin were added. The shift in the half wave potential upon addition of β -cyclodextrin was comparable to literature results.

Equivalents of β -Cyclodextrin	Half Wave Potential $E_{1/2}$	Intensity of Signal
0	+0.42 V	+2.63 E^{-6} \rightarrow -2.82 E^{-6} A
1	+0.43 V	+1.92 E^{-6} \rightarrow -2.19 E^{-6} A
2	+0.48 V	+1.40 E^{-6} \rightarrow -1.84 E^{-6} A
3	+0.49 V	+1.22 E^{-6} \rightarrow -1.62 E^{-6} A
4	N/A	N/A
5	N/A	N/A

Table 7.6. Intensity and $E_{1/2}$ of CVs collected for compound 28 and β -cyclodextrin.

Equivalents of β -Cyclodextrin	Half Wave Potential $E_{1/2}$	Intensity of Signal
0	+0.42 V	+1.46 E^{-6} \rightarrow -1.85 E^{-6} A
1	+0.46 V	+1.05 E^{-6} \rightarrow -1.49 E^{-6} A
2	+0.48 V	+9.70 E^{-7} \rightarrow -1.31 E^{-6} A
3	+0.50 V	+9.02 E^{-7} \rightarrow -1.20 E^{-6} A
4	N/A	N/A
5	N/A	N/A

Table 7.7. Intensity and $E_{1/2}$ of CVs collected for compound 29 and β -cyclodextrin.

7.3.2.4 ^1H NMR studies with β -cyclodextrin.

^1H NMR spectra recorded in D_2O were obtained for ferrocene biotin compounds with and without solvent suppression. Without solvent suppression, the signals for the compounds were swamped by the water and most of the detail was lost. By running with solvent suppression almost all signals were then visible. The ferrocene Cp ring resonances were diminished in intensity due to the overlap with the water signal. One equivalent of β -cyclodextrin was then added to each sample and the ^1H NMR spectra were re-run with and without solvent suppression. Upon addition of the β -cyclodextrin a slight shift of the Cp ring protons to the right was observed, indicating interaction with the cyclodextrin.

There was also a shift to the right for some of the aliphatic protons that were in close proximity to the ferrocene Cp rings. The shifts indicate that the ferrocene protons had become shielded by the cyclodextrin, which in turn would suggest that the inclusion complex had been formed. The additional shifts in the alkyl and biotinyl protons observed in both systems would indicate an increase in steric effects and or a change in structural conformation, suggesting that the cyclodextrin has interacted with the ferrocene moiety in such a way that the structural conformation in solution has changed. This change would also imply that the inclusion complex has been formed in both cases. Although the typical splitting of the Cp rings was not observed, this may be associated with the weak interaction that occurs, as observed by the ITC results, and that there is no saturation of the with β -cyclodextrin in the NMR sample. Addition of an excess of β -cyclodextrin may have produced the expected splitting pattern. The ^1H NMR spectra recorded with solvent suppression of the biotin compounds with the spectra recorded for the addition of β -cyclodextrin overlaid are shown in Figure 7.22 and Figure 7.23.

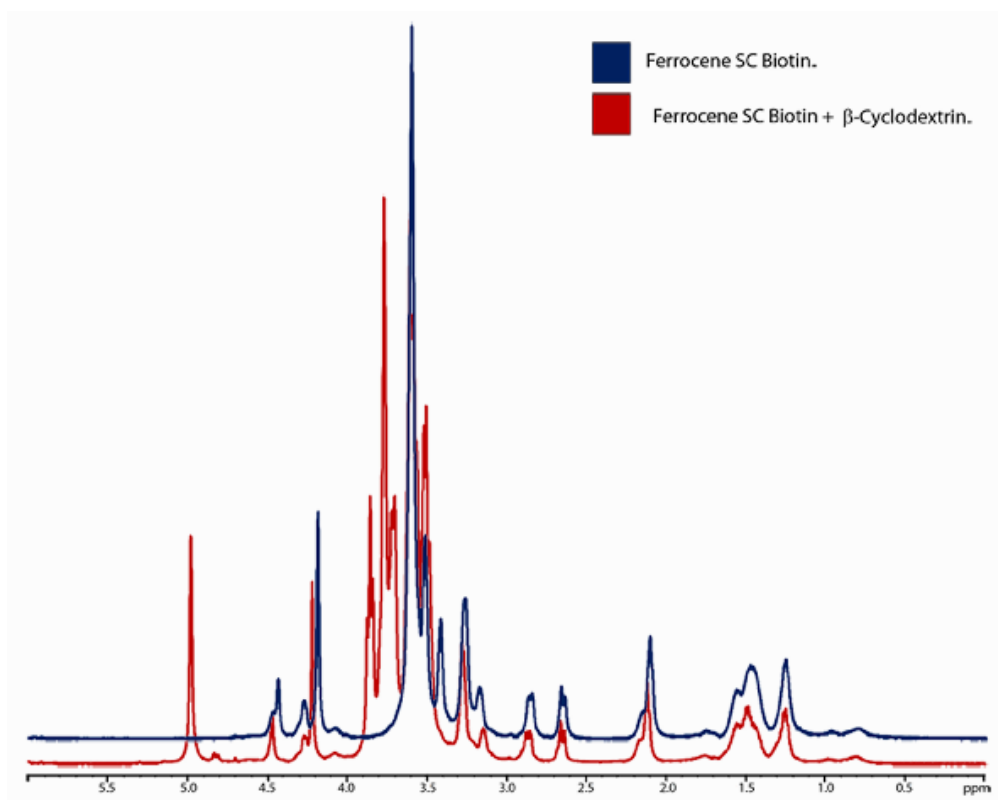


Figure 7.22. Spectra of the ferrocene SC biotin 28 with β -cyclodextrin added.

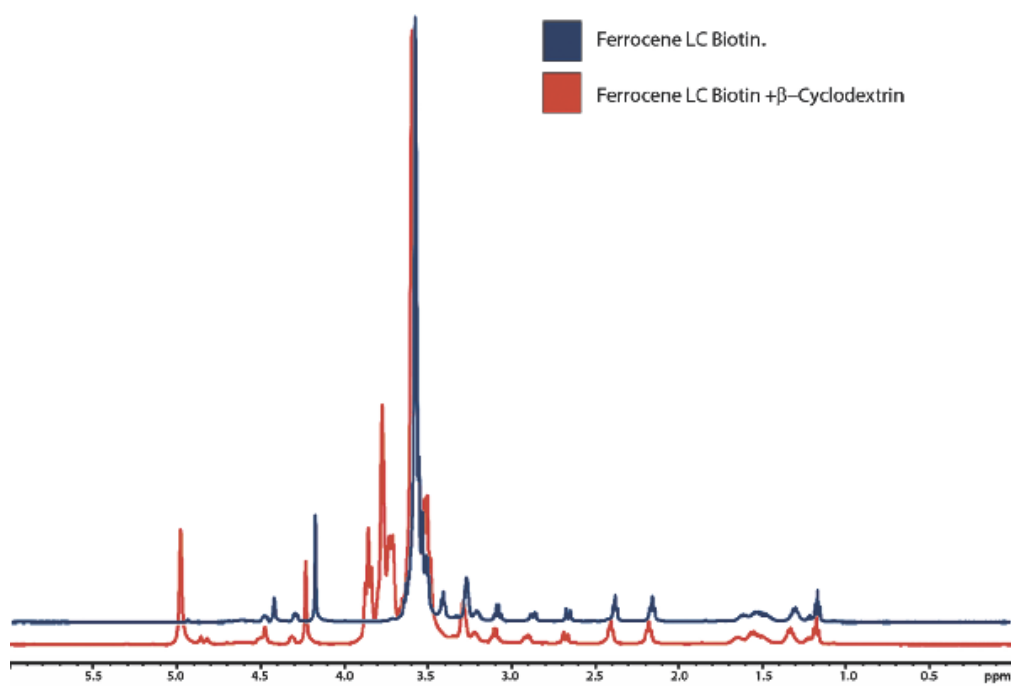


Figure 7.23. Spectra of the ferrocene LC biotin 29 with β -cyclodextrin added.

7.4. Conclusions and Future Work.

7.4.1. Conclusions.

Two ferrocene functionalised biotin conjugates **28** and **29** have been successfully synthesised and it has been shown that these conjugates will successfully displace HABA from the binding sites of avidin protein, neutravidin.

ITC experiments have shown that the K_a of binding between the avidin proteins and the conjugates is still strong, although reduced relative to native biotin avidin interactions. The interactions between β -cyclodextrin and the ferrocene moieties were investigated by ^1H NMR studies, where the changes in the proton shifts were recorded as β -cyclodextrin was added to aqueous solutions of each conjugate. The defined shifts indicated that the β -cyclodextrin formed inclusion complexes with the ferrocene moiety of the conjugates.

Cyclic voltammetry experiments showed that these conjugates retained their redox activity and that the addition of cyclodextrin modulated the redox behaviour exhibited by the ferrocene systems of these compounds.

A naphthalene functionalised biotin conjugate with a shorter tether had also been synthesised within Prof G Cooke's group for the investigation of its interactions with avidin, and neutravidin in addition to CBPQT⁴⁺. ITC showed that the conjugate had a high affinity for both avidin and neutravidin. UV-Vis and fluorescence spectroscopy showed that the interactions between CBPQT⁴⁺ and the naphthalene moiety were unaffected by both the biotin group and when complexed to avidin, where the pseudorotaxane formed was unhindered by the biotin and the avidin.

7.4.2. Future Work.

Further investigation of the effects of neutravidin on the redox activity of the conjugates by cyclic voltammetry experiments would have been pursued with more time available.

Additional investigation of the host-guest interactions could be performed where the use cucubit-[7]-uril could be used in place of β -cyclodextrin. This investigation could yield interesting results where the binding interactions could be measured by ITC, NMR and cyclic voltammetry.

8 Experimental.

8.1 General Experimental and Materials.

¹H NMR spectra were run on Bruker Avance 400MHz, and Bruker Avance 500MHz spectrometers. All NMR spectra used tetramethylsilane (TMS) as reference ($\delta = 0.0$ ppm)

MS spectra were obtained from the Mass Spectrometry laboratory in the Chemistry Department of the University of Glasgow. Measurements were run on a JEOL JMS 700 Mass Spectrometer [FAB, EI, CI, Accurate Mass] MALDI tof mass spectroscopy was obtained from the Mass Spectroscopy lab at the University of Strathclyde. The measurements were run on an AXIMA-CFR-MALDI TOF Mass Spectrometer.

Transmission IR spectra were recorded on Perkin-Elmer RX FT-IR system.

All melting points recorded are uncorrected.

Calorimetry experiments were run on a MicroCal VP-ITC Microcalorimeter. CT-DNA was supplied by Sigma-Aldrich and used as supplied. The synthetic Dickerson DNA was supplied by MWG-Biotech AG Sequence d(CGCGAATTCGCG)₂ lyophilised.

Cyclic Voltammetry experiments were carried out on a CH-Instruments Electrochemical Workstation.

UV-Vis Spectrometers used were Perkin-Elmer LAMBDA 25 UV-Vis Spectrometer and a THERMO HELIOS B UV-Vis Spectrometer.

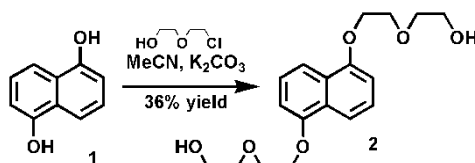
Fluorescence measurements were run on a Shimadzu Spectrophotometer RF-5301PC.

Microscopy work was carried out on a Leitz DMIRB with a Zeiss Axiocam attached.

All chemicals were supplied from Sigma Aldrich and were used without purification unless stated.

8.2 Synthesis.

1,5-Bis (2-(2-hydroxyethoxy)ethoxy) naphthalene (2).

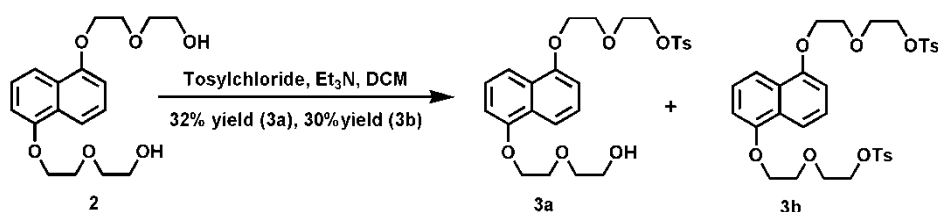


To a solution of 1,5-dihydroxynaphthalene (15 g, 0.094 mol) in acetonitrile (100 mL) was added first potassium carbonate (37.5 g, 0.28 mol), allowing the reaction mixture to stir for ~5 minutes. 2-(2-chloroethoxy)ethanol (30 mL, 0.28 mol) was then added slowly portionwise. The reaction mixture was heated under reflux at 80°C for one week. An additional equivalent of potassium carbonate (12.5 g) and 2-(2-chloroethoxy)ethanol (10 mL) was added and the reaction mixture was heated under reflux for a further two days. Once cool the reaction mixture was filtered washing with acetonitrile. The filtrate was evaporated to yield a very dark oily solid. This solid was taken up in DCM (250 mL) and water (250 mL). The DCM layer was removed and the aqueous layer was washed with DCM (3x 50 mL). The combined organic layers were then extracted with saturated potassium carbonate solution (2 x 100 mL) and saturated brine (1 x 100 mL). The organic layer was then dried over magnesium sulfate, filtered and evaporated *in vacuo* to yield a dark solid. The product was separated by flash silica column chromatography, eluting with a gradient of 0-100% EtOAc in DCM. The product was recovered in a 36% yield as a pale green solid. ^[10] ^[149]

¹H NMR in CDCl₃, 400 MHz, δ: 7.80 (2H, d, *J*=8.4Hz, 2x CH), 7.29 (2H, t, *J* = 8.0Hz, 2x CH), 6.79 (2H, d, *J* = 8.0Hz, 2x CH), 4.24 (4H, m, 2x CH₂), 3.94 (4H, m, 2x CH₂), 3.69 (8H, m, 4x CH₂), 1.86 (2H, br.s, 2x OH)
¹³C NMR in CDCl₃, 400 MHz, δ: 154.29 (QC), 126.77 (QC), 125.20 (CH),

114.63 (CH), 105.81 (CH), 72.61 (CH₂), 69.77(CH₂), 67.90(CH₂), 61.85 (CH₂), 60.42 (CH₂). IR (cm⁻¹) 3505(OH), 2929(CH₂), 2895(CH₂), 2866 (CH₂), 1596(Ar CH), 1513 (Ar CH), 1421 (Ar CH), 1399 (Ar CH), 1272 (Ar CH). Mass spectrum [M+H]⁺ = 337.3 Cl/ISO.

1-(2-(2-(toluene-4-sulfonyl)ethoxy)ethoxy)-5-(2-(2-hydroxyethoxy)ethoxy)naphthalene (3a).

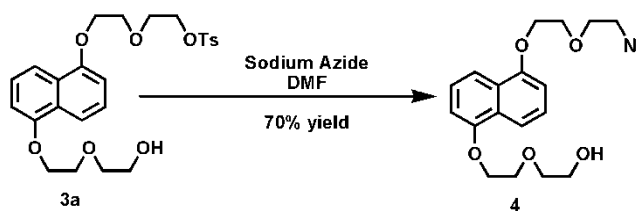


To a solution of **2** (2,050 mg, 6.1 mmol) in DCM (100 mL) was added triethylamine (0.95 mL, 6.71 mmol) followed by tosyl chloride portionwise (1,160 mg, 6.1 mmol). The reaction mixture was stirred at room temperature overnight. The solvent was then removed *in vacuo* to yield a dark brown oil. Separation of impurities by flash silica column chromatography using 100% ethyl acetate followed by a second purification by flash column chromatography eluting with pet ether and ethyl acetate in 25% step-wise gradient starting with 100% pet ether. The required product was obtained a pale solid in a 32% yield of **3a** and 30% yield of **3b**.^[150]

¹H NMR of **3a**, CDCl₃, δ: 7.89 (1H, d, *J* = 8.4Hz, CH), 7.85 (1H, d, *J* = 8.4Hz, CH), 7.83-7.79 (2H, m, 2x CH), 7.39 (2H, dt, *J*₁ = 8.4Hz, *J*₂ = 2.4Hz, 2x CH), 7.27 (2H, d, *J* = 8.6Hz, 2x CH), 6.88 (1H, d, *J* = 7.6Hz, CH), 6.83 (1H, d, *J* = 7.6Hz, CH), 4.35 (2H, t, *J* = 4.6Hz, CH₂), 4.27-4.21 (4H, m, 2x CH₂), 4.04 (2H, t, *J* = 4.8Hz, CH₂), 3.95 (2H, t, *J* = 4.8Hz, CH₂), 3.86(2H, t, *J* = 4.8Hz, CH₂), 3.84-3.76 (4H, m), 2.39 (3H, s, CH₃) IR

(cm^{-1}): 3509(OH), 2970, 2925, 2902, 2865, 1595, 1512, 1458, 1416, 1357, 1269, 1168, 1067. Mass spectrum = $[\text{M}+\text{H}]^+$ 491.2. ^1H NMR of **3b**, CDCl_3 , δ : 7.83 (2H, d, $J = 8.6\text{Hz}$, 2x CH), 7.78 (4H, d, $J = 8.1\text{Hz}$, 4x CH), 7.35 (2H, d, $J = 8.1\text{Hz}$, 2x CH), 7.25 (4H, d, $J = 8.3\text{Hz}$, 4x CH), 6.82 (2H, d, $J = 8.1\text{Hz}$, 2x CH), 4.24-4.20 (8H, m, 4x CH_2), 3.93 (4H, t, $J = 4.6\text{Hz}$, 2x CH_2), 3.84 (4H, t, $J = 4.6\text{Hz}$, 2x CH_2), 2.37 (6H, s, 2x CH_3) IR (cm^{-1}): 2949, 2920, 2907, 2884, 1596, 1514, 1415, 1346, 1271, 1163, 1067. Mass spectrum $[\text{M}+\text{H}]^+ = 644.8$.

1-(2-(2-(azido)ethoxy)ethoxy)-5-(2-(2-hydroxyethoxy)ethoxy)naphthalene (4).

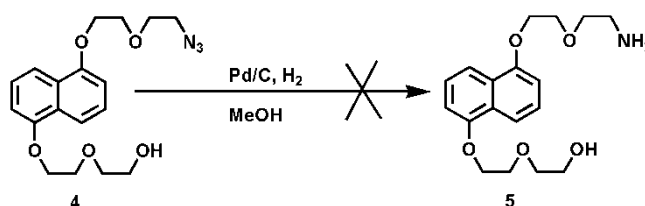


To a solution of **3a** (1,110 mg, 2.27 mmol) in DMF (30 mL) was added slowly sodium azide (340 mg, 5.22 mmol). The reaction mixture was heated gently to $\sim 55\text{-}60\text{ }^\circ\text{C}$ for 24 hours. The reaction was then partitioned between diethyl ether (50 mL) and water (50 mL). The organic layer was separated and then washed three times with water (3x 30 mL). The organic layer was then dried over magnesium sulfate, filtered and evaporated *in vacuo*. The resulting oil was purified by flash silica column chromatography eluting with 0-60% EtOAc DCM. The product was recovered as a pale oil in a 70% yield.^[151]

^1H NMR, CDCl_3 δ : 7.90 (1H, d, $J = 4.2\text{Hz}$, CH), 7.88 (1H, d, $J = 4.2\text{Hz}$, CH), 7.39 (2H, dt, $J_1 = 8.0\text{Hz}$, $J_2 = 2.5\text{Hz}$, 2x CH), 6.88 (2H, d, $J =$

8.1Hz, 2x CH), 4.34 (4H, t, $J = 5.0\text{Hz}$, 2x CH₂), 4.05-4.01 (4H, m, 2x CH₂), 3.86 (2H, t, $J = 5.0\text{Hz}$, CH₂), 3.84-3.75 (4H, m, 2x CH₂), 3.46 (2H, t, $J = 5.0\text{Hz}$, CH₂). ¹³C NMR CDCl₃ δ : 154.29 (QC), 126.7 (QC), 125.2 (CH), 125.1 (CH), 114.6 (CH), 105.8 (CH), 72.6 (CH₂), 70.4 (CH₂), 69.9 (CH₂), 69.81 (CH₂), 68.0 (CH₂), 61.9 (CH₂), 50.86 (CH₂). IR (cm⁻¹): 3488(OH), 2933, 2909, 2885, 2866, 2102(N₃), 1595, 1510, 1414, 1267. Mass spectrum [M+H]⁺ = 362.2.

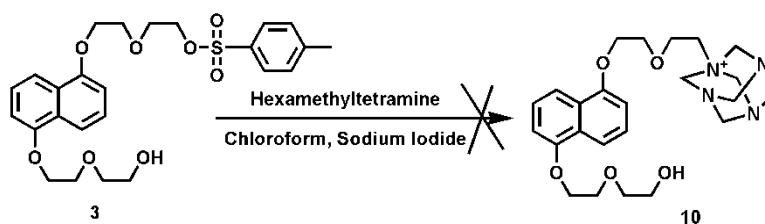
1-(2-(2-(amino)ethoxy)ethoxy)-5-(2-(2-hydroxyethoxy)ethoxy)naphthalene (5).



To a solution of **4a** (795 mg, 2.02 mmol), in methanol (50 mL) was added palladium on carbon (5 mol%, 147 mg). The reaction mixture was degassed and H₂ gas was introduced into the flask. The mixture was stirred for three and a half hours. After this time the mixture was filtered by vacuum under an atmosphere of nitrogen gas, and washed with acetone and methanol. Due to suck back of water into the vacuum flask, the filtrate was evaporated to remove the acetone and methanol. The resulting aqueous solution was extracted with DCM (50 mL), separated and then washed with DCM (3x 30 mL). The organic layers were combined, dried over magnesium sulfate filtered and evaporated *in vacuo* to yield a pale green oil. ¹H NMR in CDCl₃ showed significant impurities, the TLC showed no movement of the mixture. An acid/base extraction was carried out, taking the impure mixture up DCM washing first with 1 M

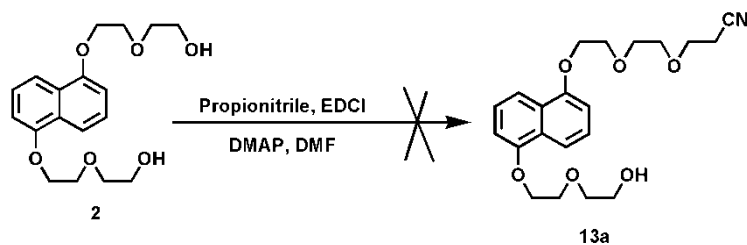
HCl. The organic layer was recovered, dried over magnesium sulfate, filtering and evaporating *in vacuo*. Mass spectrum $[M+H]^+ = 332.2$. The aqueous layer was then neutralised with saturated sodium bicarbonate solution, extracting with DCM. The organic layer was dried over magnesium sulfate, filtering and evaporating *in vacuo*. Mass spectrum $[M+H]^+ = 336.2$ $^1\text{H NMR}$ in CDCl_3 still showed significant impurities.

1-(2-(2-(*N*-hexamethylenetetrammonium)ethoxy)ethoxy)ethoxy)-5-(2-(2-hydroxyethoxy)ethoxy) naphthalene (10).^[152]



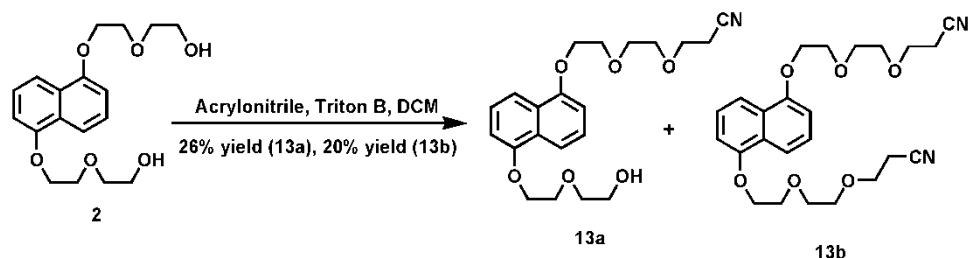
To a solution of hexamethylenetetramine (73 mg, 0.52 mmol) stirring at reflux in chloroform was added a solution of **3a** (212 mg, 0.43 mmol) in chloroform dropwise over a period of ~20 minutes. Once all of compound **3a** was added, the reaction mixture was heated under reflux for three hours. Once cool the reaction was sampled, $^1\text{H NMR}$ was run in CDCl_3 and a Mass Spectrum was run. $^1\text{H NMR}$ was inconclusive as there was a 1:1 mixture of hexamethylene tetramine and the naphthalene compound. Mass spectrum $[M+H]^+ = 490$ which relates to the starting material. Thin layer chromatography (TLC) showed one spot only. The reaction solvent was changed to 50:50 DMF chloroform and NaI (23 mg) and additional hexamethylenetetramine (50 mg) was added and the reaction mixture was heated to reflux for 24 hours. The mass spectrum showed starting material present only after this time.

1-(2-(2-(2-(cyano)ethoxy)ethoxy)ethoxy)-5-(2-(2-hydroxyethoxy)ethoxy) naphthalene (13a).



To a solution of **2** (500 mg, 1.48 mmol) in DMF (20 mL) was added sodium hydride (60% dispersion, 59 mg, 1.48 mmol). The reaction mixture changed colour from light yellow/green to cloudy green colour. Bromopropionitrile (198 mg, 1.48 mmol, 0.12 mL) was added dropwise. The solution became a more opaque colour and gradually became translucent over the course of 1 hour. TLC, mass spectrum and ^1H NMR showed no reaction.

1-(2-(2-(2-(cyano)ethoxy)ethoxy)ethoxy)-5-(2-(2-hydroxyethoxy)ethoxy) naphthalene (13a).^[83]



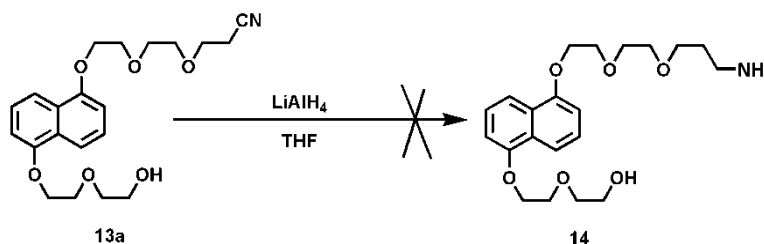
To a solution of **2** (1000 mg, 2.97 mmol) in DCM (30 mL) at 0°C was added first acrylonitrile (158 mg, 2.97 mmol, 0.2 mL), followed by TRITON B* (50 mg, 0.3 mmol, 0.12 mL) *([Benzyltrimethylammonium hydroxide] 40wt.% solution in water). The reaction mixture was stirred at 0°C for one hour then warmed slowly to room temperature where it was stirred for a further ten minutes. The reaction mixture was then added dropwise to saturated ammonium chloride solution (50 mL). An extraction in water / DCM (50 mL) was carried out. The aqueous layer was washed with DCM (3x 50 mL). The organic layer was then dried over magnesium sulfate, filtered and evaporated *in vacuo* to yield a yellow oil. The products were separated by flash silica column chromatography, eluting with 0-50% EtOAc in DCM followed by 7:1 EtOAc in acetone. The mono propionitrile naphthalene **13a** was recovered in a 26% yield as a pale oil (288 mg), while the bis propionitrile naphthalene **13b** was recovered in a 20% yield as a light brown oil (248 mg).

¹H NMR CDCl₃ Mono-alkylated product **13a**. δ : 7.86 (2H, d, *J* = 8.4Hz, 2x CH), 7.33 (2H, t, *J* = 8.0Hz, 2x CH), 6.76 (2H, t, *J* = 6.9Hz, 2x CH), 4.16 (4H, dt, *J*₁ = 4.3Hz, *J*₂ = 13Hz, 2x CH₂), 3.86 (4H, dt, *J*₁ = 4.3Hz, *J*₂ = 13Hz, 2x CH₂), 3.68 (4H, d, *J* = 3Hz, 2x CH₂), 3.62-3.54 (6H, m, 3x CH₂), 2.46 (2H, t, *J* = 6.2Hz, CH₂). ¹³C NMR, δ: 154.3 (QC), 126.7 (QC), 125.3 (CH), 118.2 (QC), 114.5 (CH), 105.8 (CH), 72.8 (CH₂), 70.8 (CH₂), 70.6 (CH₂), 69.8 (CH₂), 69.6 (CH₂), 67.8 (CH₂), 65.8 (CH₂), 61.6

(CH₂), 18.7(CH₂). IR (cm⁻¹): 3540(OH), 2937, 2875, 2175(CN), 1594, 1510, 1415, 1267. Mass spectrum [M+H]⁺ = 390.2

¹H NMR, CDCl₃ Bis-alkylated product **13b**. δ : 7.78 (2H, d, *J* = 8.4Hz, 2x CH), 7.27 (2H, t, *J* = 8.0Hz, 2x CH), 6.75 (2H, d, *J* = 8.0Hz, 2x CH), 4.83-4.20 (4H, m, 2x CH₂), 3.9-3.88 (4H, m, 2x CH₂), 3.69 (4H, d, *J* = 4.4Hz, 2x CH₂), 3.6-3.52 (8H, m, 4x CH₂), 2.46 (4H, t, *J* = 6.2Hz, 2x CH₂). IR (cm⁻¹): 2962, 2923, 2876, 2248(CN), 1593, 1511, 1416, 1266. Mass spectrum [M+H]⁺ = 443.2

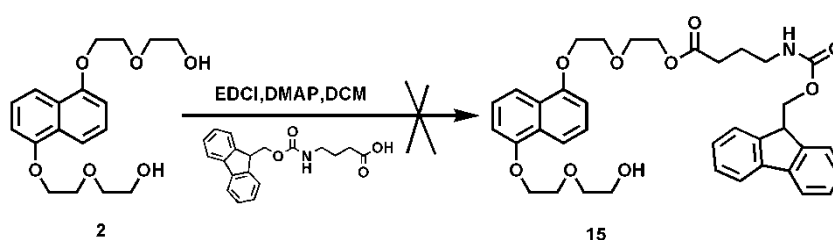
1-(2-(2-(3-aminopropoxy)ethoxy)ethoxy)-5-(2-(2-hydroxyethoxy)ethoxy) naphthalene (14).



To a flask containing mono propionitrile naphthalene **13a** (270 mg, 0.69 mmol) in THF (40 mL) was added lithium aluminium hydride (240 mg, 1.73 mmol). The reaction mixture was stirred at room temperature for 24 hours. After this time the mixture was cooled to 0°C and quenched with 10% sodium hydroxide solution (40 mL). The resulting suspension was filtered, and the aqueous layer was washed with DCM (3x 200 mL). The aqueous liquor was separated, and was washed with DCM (2 x 200 mL). The combined organic layers were washed with water (2x 200 mL) and brine (200 mL). The combined organic layer was concentrated under vacuum. Silica column chromatography eluting with initially 100% DCM, then 50% acetone in ethyl acetate, then flushing the

column with methanol failed to produce either the product or starting material. Repetition of the reaction showed that a retro-Michael reaction took place to give dialkoxynaphthalene **2** as the only product.

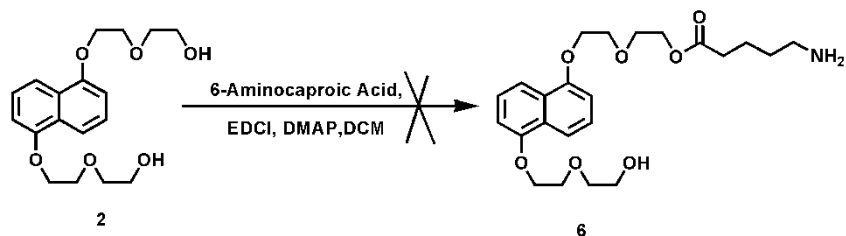
1-(2-(2-(N-(9-fluorenylmethoxycarbonyl)-gamma-butanoyl)oxyethoxy)ethoxy)-5-(2-(2-hydroxyethoxy)ethoxy) naphthalene (15).



To a solution of **2** (1,000 mg, 3.0 mmol) in DMF (40 mL) was added 4-(Fmoc-amino)-butyric acid (960 mg, 3.0 mmol), EDCI (570 mg, 3.0 mmol), and DMAP (360 mg, 3.0 mmol). The reaction mixture was stirred at room temperature for 24 hrs. The reaction was taken up in DCM (100 mL) and extracted three times with water (3x 50 mL). The organic phase was dried over magnesium sulfate, filtered and evaporated *in vacuo* to yield a pale yellow oil. The product was separated by flash silica column chromatography, eluting with a gradient of 0-100% EtOAc / pet ether. Column chromatography was not completely successful with EDCI by-products present on ^1H NMR.

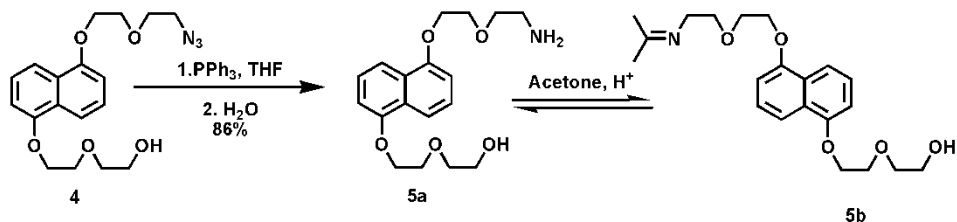
^1H NMR CDCl_3 , δ : 7.86 (2H, d, J = 9Hz, 2x CH), 7.75 (2H, d, J = 7.4Hz, 2x CH), 7.57 (2H, d, J = 7.4Hz, 2x CH), 7.40-7.28(6H, m, 6x CH), 6.81(2H, t, J = 6.8Hz, 2x CH), 4.39(2H, d, J = 10.3Hz), 4.29-4.23(6H, m), 4.18(1H, t, J = 6.7Hz), 3.81(2H, t, J = 4.5Hz), 3.77-3.75(2H, m), 3.73-3.70(2H, m), 3.13(1H, q, J = 4.8Hz), 2.31(2H, t, J = 7.2Hz), 1.77(2H, p, J = 6.9Hz) Mass spectrum $[\text{M}+\text{H}]^+ = 644.3$ the $[-\text{Fmoc M}+\text{H}]^+ = 423.2$ was also present in the mass spectrum.

Attempted Synthesis of 1-(2-(2-(6-aminohexanoyl)oxyethoxy)ethoxy)-5-(2-(2-hydroxyethoxy)ethoxy) naphthalene (6).



To a solution of dialkoxynaphthalene **2** (500 mg, 1.4 mmol) in DMF (50 mL) was added EDCI (268 mg, 1.4 mmol), DMAP (170 mg, 1.4 mmol) and 6-amino caproic acid (195 mg, 1.4 mmol). The reaction mixture was stirred at room temperature for 3 days, monitoring by TLC. As there was no reaction after 3 days, the mixture was heated under reflux for 16 hours. After this point there was still no reaction. The starting material was recovered by silica column chromatography.

1-(2-(2-(amino)ethoxy)ethoxy)-5-(2-(2-hydroxyethoxy)ethoxy)naphthalene (5).^[153]



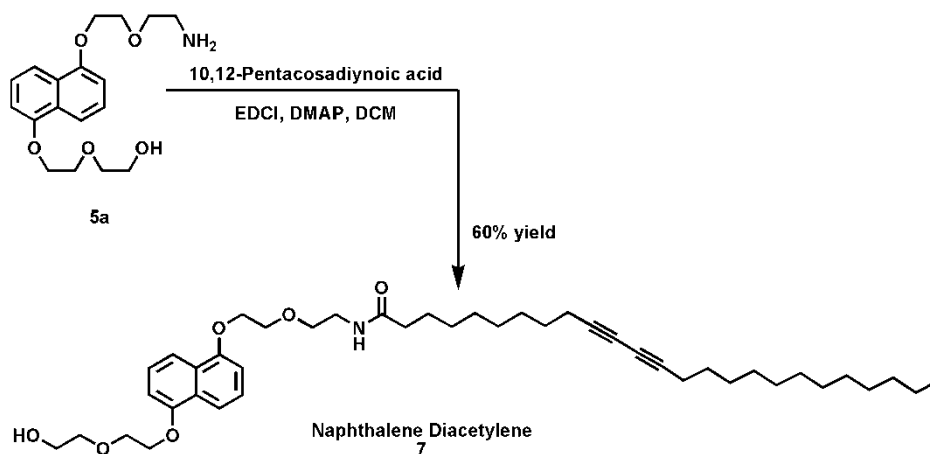
To a solution of **4a** (1,723 mg, 4.77 mmol), in dry THF (100 mL) was added triphenylphosphine (3,120 mg, 11.9 mmol). The reaction mixture was stirred at room temperature for 24 hrs. Water (1 mL) was added to the reaction mixture and allowed to stir for a further three hours. The solvent was then removed *in vacuo* to yield a pale oil. Flash silica column chromatography eluting with 0-97 % acetone in DCM with 3 % triethylamine held constant throughout the chromatography yielded the imine form (**5b**) of the product in an 86 % yield. Imine readily converts back to the amine **5a** in both mildly acidic and basic conditions.

¹H NMR of Naphthalene amine **5a**, CDCl₃: δ 7.88 (1H, d, J = 5.7Hz, CH), 7.86 (1H, d, J = 5.7Hz, CH), 7.38-7.31 (2H, m, 2xCH), 6.84 (2H, d, J = 7.6Hz, 2xCH), 4.29 (2H, t, J = 5.7Hz, CH₂), 4.28 (2H, t, J = 5.7Hz), 3.99 (2H, t, J = 4.5Hz, CH₂), 3.94 (2H, t, J = 4.5Hz, CH₂), 3.7-3.8 (4H, m, 2x CH₂), 3.63 (2H, t, J = 5.7Hz, CH₂), 2.89 (2H, t, J = 5.7Hz, CH₂), 1.98 (3H, broad s NH₂ and OH). ¹³C NMR CDCl₃: δ 154.4 (QC), 154.3 (QC), 126.83 (QC), 126.77 (QC), 125.2 (CH), 125.1 (CH), 114.7 (CH), 114.5 (CH), 105.8 (CH), 73.5 (CH₂), 72.7 (CH₂), 69.8 (CH₂), 69.6 (CH₂), 67.9 (CH₂), 61.8 (CH₂), 41.8 (CH₂). Mass Spectrum. [M+H]⁺ = 336.2 Exact mass (335.2) also found. IR (cm⁻¹): 3509 (OH), 3385 (NH₂), 3312, 2950, 2929, 2896, 2866, 1596, 1512, 1456, 1422, 1398, 1269.

¹H NMR of Naphthalene imine **5b**. CDCl₃: δ 7.86 (1H, d, J = 8.2Hz, CH), 7.86 (1H, t, J = 8.3Hz, CH) *overlapping signals, 7.38-7.31 (2H, m,

2xCH), 6.84 (2H, d, $J = 7.6\text{Hz}$, 2xCH), 4.33-4.24 (4H, m, 2xCH₂), 4.02-3.94 (4H, m, 2xCH₂), 3.88 (2H, t, $J = 6.2\text{Hz}$, CH), 3.76 (4H, dt, $J = 8.1\text{Hz}$, $J = 3.8\text{Hz}$, 2xCH₂), 3.44 (2H, t, $J = 6.2\text{Hz}$, CH), 2.03 (3H, s, CH₃), 1.85 (3H, s, CH₃). ¹³C NMR in CDCl₃ was very complicated with a mixture of the imine and amine present. ¹³C NMR CDCl₃: δ 207.0 (Acetone), 169.3 (QC), 154.4 (QC), 154.3 (QC), 126.84 (QC), 126.76 (QC), 125.2 (CH), 125.1 (CH), 125.0 (CH), 114.9 (CH), 114.7 (CH), 114.5 (CH), 114.4 (CH), 105.8 (CH), 105.75 (CH), 105.72 (CH), 73.5 (CH₂), 72.7 (CH₂), 71.9 (CH₂), 69.8 (CH₂), 69.6 (CH₂), 67.9 (CH₂), 61.8 (CH₂), 51.49 (CH₃), 41.8 (CH₂), 30.97 (CH₃), 29.3 (Acetone), 18.95 (CH₂). Mass spectrum = 375.2 and 335.2.

1-(2-(2-(10,12-pentacosadiynoylethoxy)ethoxy)ethoxy)-5-(2-(2-hydroxyethoxy)ethoxy) naphthalene (7).

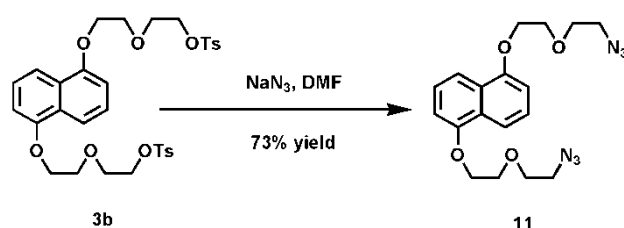


To a solution of the naphthalene amine **5** (1,290 mg, 3.85 mmol) in DCM (50 mL) was added sequentially EDCI (570 mg, 3.85 mmol), DMAP (470 mg, 3.85 mmol), and 10,12-pentacosadiynoic acid (1.44 g, 3.85 mmol). The reaction mixture was then stirred at room temperature for 3 days in the dark. The solvent was then removed *in vacuo* in the dark to yield pink/orange oily solid. Purification by silica column

chromatography, eluting with a 20 % stepwise gradient of 0-100% ethyl acetate in DCM gave the product as an off white solid in a 60% yield.

^1H NMR in CDCl_3 , δ : 7.87 (2H, t, $J = 8.1\text{Hz}$, 2x CH), 7.39-7.34 (2H, m, 2x CH), 6.87 (2H, d, $J = 7.6\text{Hz}$, 2x CH), 5.85 (1H, br t, $J = 5.3\text{Hz}$, NH), 4.34-4.29 (4H, m, 2x CH_2), 4.03-4.01 (2H, m, CH_2), 3.98-3.96 (2H, m, CH_2), 3.82-3.74 (4H, m, 2x CH_2), 3.7 (1H, d, $J = 5.1\text{Hz}$), 3.69 (1H, d, $J = 5.1\text{Hz}$), 3.52-3.48 (2H, m, CH_2), 2.26-2.21 (4H, m, 2x CH_2), 2.07-2.02 (3H, m), 1.55-1.45 (6H, m, 3x CH_2), 1.41-1.30 (5H, m), 1.26 (16H, s, 8x CH_2), 1.22-1.21 (5H, m), 0.9-0.87 (3H, m). ^{13}C NMR in CDCl_3 , δ : 173.14 (QC), 154.28 (QC), 154.27 (QC), 126.83 (QC), 126.76 (QC), 125.2 (CH), 114.71 (CH), 114.49 (CH), 105.82 (CH), 77.63 (QC), 77.47 (QC), 72.6 (CH_2), 70.15 (CH_2), 69.78 (CH_2), 69.57 (CH_2), 67.93 (CH_2), 67.78 (CH_2), 65.31 (QC), 65.23 (QC), 61.87 (CH_2), 39.13 (CH_2), 36.67 (CH_2), 31.92 (CH_2), 29.63 (CH_2), 29.49 (CH_2), 29.35 (CH_2), 29.11 (CH_2), 28.88 (CH_2), 28.77 (CH_2), 28.36 (CH_2), 28.30 (CH_2), 25.62 (CH_2), 22.69 (CH_2), 19.19 (CH_2), 14.12 (CH_3). IR (cm^{-1}): 3407 (OH), 3283, 2922, 2894, 2848, 1638(Amide), 1594, 1546, 1514, 1414, 1266. Mass spectrum $[\text{M}+\text{H}]^+ = 692.48$ Accurate Mass (691.48).

1,5-Bis (2-(2-(azido)ethoxy)ethoxy) naphthalene (11).

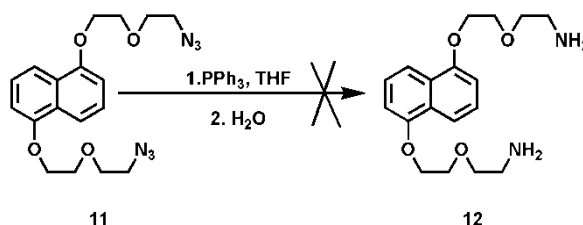


To a solution of **3b** (2,040 mg, 3.07 mmol) in DMF (30 mL) was added slowly sodium azide (920 mg, 14.12 mmol). The reaction mixture was heated gently to $\sim 55\text{-}60^\circ\text{C}$ for 24 hours. Once cool the reaction was then poured into diethyl ether (50 mL) and water (50 mL). The organic

layer was separated and washed with water (3x 30 mL). The organic layer was then dried over magnesium sulfate, filtered and evaporated *in vacuo*. The resulting oil was purified by flash silica column chromatography eluting with 0-60% EtOAc DCM. The product was recovered as a pale oil in a 73% yield (887 mg).

^1H NMR, CDCl_3 δ : 7.87 (2H, d, $J = 7.8\text{Hz}$, 2x CH), 7.36 (2H, t, $J = 7.7\text{Hz}$, CH), 6.86 (2H, d, $J = 8.2\text{Hz}$, 2x CH), 4.32 (4H, t, $J = 4.7\text{Hz}$, 2x CH_2), 4.01 (4H, t, $J = 4.7\text{Hz}$, 2x CH_2), 3.83 (2H, t, $J = 4.9\text{Hz}$, CH_2), 3.44 (4H, t, $J = 4.9\text{Hz}$, 2x CH_2). ^{13}C NMR CDCl_3 δ : 154.29 (QC), 126.7 (QC), 125.1 (CH), 114.7 (CH), 105.8 (CH), 70.4 (CH_2), 69.9 (CH_2), 68.0 (CH_2), 50.9 (CH_2). Mass Spectrum $[\text{M}+\text{H}]^+ = 387.4$. IR (cm^{-1}): 2947, 2922, 2876, 2102 (N_3), 2080 (N_3), 1590, 1508, 1414, 1269.

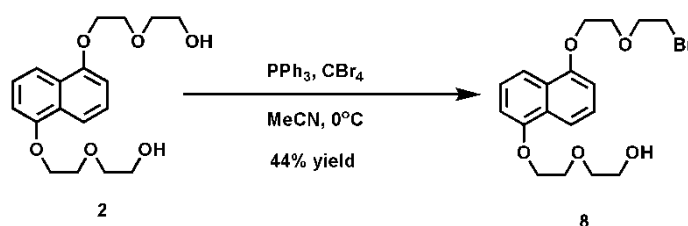
1,5-Bis (2-(2-(amino)ethoxy)ethoxy) naphthalene (12).^[153]



To a solution of **11** (880 mg, 2.3 mmol), in dry tetrahydrofuran (50mL) was added triphenylphosphine (1,500 mg, 5.75 mmol). The reaction mixture was stirred at room temperature for 24 hrs. Water (0.4 mL) was added to the reaction mixture and allowed to stir for a further three hours. The solvent was then removed *in vacuo* to yield a pale oil. The oil was taken up in DCM (100 mL) and 1.2 M hydrochloric acid (100 mL) was added. After separation the aqueous layer was washed with DCM (2x 100 mL). After the organic layer was removed, the hydrochloric

acid layer was neutralised with sodium bicarbonate. DCM was then added and the mixture was partitioned. The aqueous layer was washed with DCM (3x 100 mL). The organic fractions after neutralisation were combined and dried over MgSO₄, filtered and evaporated under reduced pressure to yield a white oily solid. Flash silica column chromatography eluting with 0-45 % acetone in DCM with 3 % triethylamine held constant throughout the chromatography failed to yield the required product.

1-(2-(2-(bromo)ethoxy)ethoxy)-5-(2-(2-hydroxyethoxy)ethoxy)naphthalene (8).^[154]

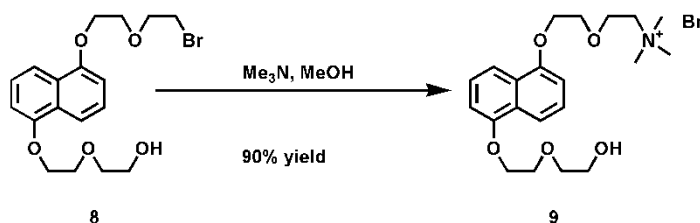


To a solution of the naphthalene diol **2** (1000 mg, 3.0 mmol), in acetonitrile (50 mL) at 0°C, under an atmosphere of nitrogen, was added carbon tetrabromide (990 mg, 3.0 mmol). The solution was stirred for 10 minutes, then triphenylphosphine (780 mg, 3.0 mmol) was added. The reaction mixture was slowly allowed to warm to room temperature and then stirred for a further 24 hours. The solvent was removed in vacuo to yield a dark red solid. Silica column chromatography eluting with 20% acetone in DCM gave the required product as a pale pink solid in a 44% yield.^[154]

¹H NMR (400 MHz, CDCl₃) δ 7.79 (d, J = 8.4 Hz, 2H), 7.29 (t, J = 8 Hz, 2H), 6.77 (d, J = 7.6 Hz, 2H), 4.23 (t, J = 4.6 Hz, 4H), 3.95-3.87 (m, 6H), 3.68 (m, 4H), 3.45 (t, J = 6 Hz, 2H). ¹³C NMR (400MHz, CDCl₃) δ: 154.28 (QC), 126.79 (QC), 125.23 (CH), 125.15 (CH), 114.75(CH), 114.61(CH), 105.86 (CH), 105.82 (CH), 72.61 (CH₂), 71.50 (CH₂), 69.79 (CH₂), 69.77 (CH₂), 67.97 (CH₂), 67.93 (CH₂), 61.73 (CH₂), 30.40 (CH₂).

IR (cm⁻¹): 3513 (OH) 2963, 2929, 2905, 2844, 1595, 1510, 1416, 1275, 1186. Mass spectrum [M+H]⁺ = 398.1 and 400.1 (⁷⁹Br and ⁸¹Br).

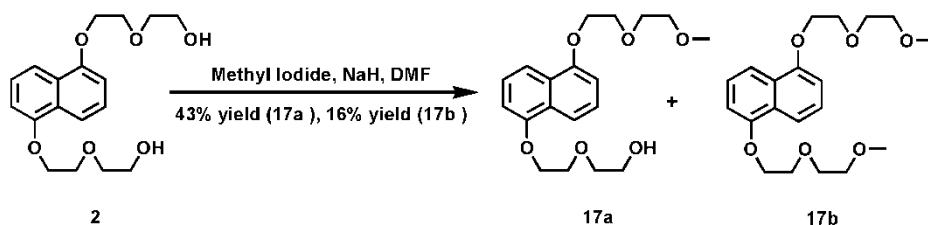
1-(2-(2-((trimethyl)ammonium)ethoxy)ethoxy)-5-(2-(2-hydroxyethoxy)ethoxy) naphthalene bromide (9).



To solution of the naphthalene bromide **8** (460 mg, 1.16 mmol) in methanol (70mL) was added dropwise trimethylamine (4.40 mL, 17.6 mmol). The reaction mixture was heated under reflux for 18 hours. After this time the reaction mixture was allowed to cool. The volume of methanol was reduced from 70 mL to 10 mL under reduced pressure. Diethyl ether (150 mL) was slowly added until total precipitation of the product had occurred. Vacuum filtration recovered the product as a white solid that was washed thoroughly with diethyl ether. The product was recovered in a 90% yield.

¹H NMR (400 MHz, MeOD) δ 7.85 (d, J = 8.4 Hz, 1H), 7.78 (d, J = 8.4 Hz, 1H), 7.35 (t, J = 7.4 Hz, 2H), 6.96 (d, J = 7.6 Hz, 1H), 6.95 (d, J = 7.6 Hz, 1H), 4.36-4.29 (m, 4H), 4.09-3.98 (m, 6H), 3.71 (s, 4H), 3.62 (t, J = 4.6 Hz, 2H), 3.16 (s, 9H). ¹³C NMR (400MHz, D₂O) δ: 126.08 (CH), 126.01 (CH), 114.60 (CH), 114.26 (CH), 107.54 (CH), 107.25 (CH), 72.00 (CH₂), 69.44 (CH₂), 69.21 (CH₂), 68.11 (CH₂), 67.98 (CH₂), 65.31 (CH₂), 64.56 (CH₂), 60.42 (CH₂), 53.78 (CH₃) IR(cm⁻¹): 3339, 3313, 3236, 3211, 2977, 2943, 2922, 2872, 2852, 2365, 2339, 1593, 1510, 1415, 1268, 1133. Mpt. 51-53 °C (dec). Mass Spectrum (ESI⁺): [M⁺] = 378.2.

1-(2-(2-methoxyethoxy)ethoxy),-5-(2-(2-hydroxyethoxy)ethoxy) naphthalene (17a).



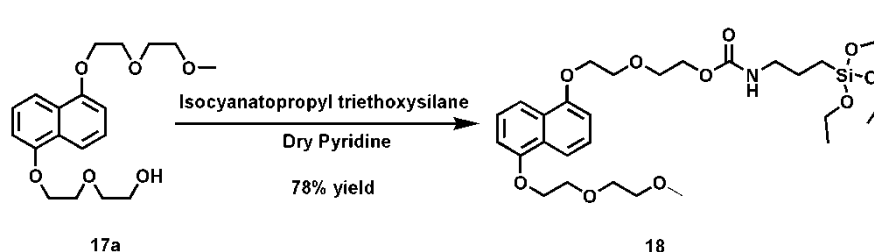
To a solution of **2** (2,960 mg, 8.8 mmol) in DMF (50 mL) was added sodium hydride (352 mg, 8.8 mmol, 60 % dispersion). The reaction mixture was stirred for five minutes. Methyl iodide (0.55 mL, 8.8 mmol) was then added and the reaction was stirred at room temperature for 24 hours. The mixture was taken up in ethyl acetate (200 mL) and washed thoroughly with water (3x 500 mL). The organics were dried over MgSO₄, filtered and evaporated to yield a dark oil. Flash silica column chromatography eluting with 0-100% EtOAc DCM recovered the products **17a** (1.08 g) and **17b** (411 mg) as oils in a 43% and 16% yield respectively. ^[13]

¹H NMR of **17a** in CDCl₃, δ : 7.87 (2H, t, *J* = 9.3 Hz, 2x CH), 7.36 (2H, t, *J* = 8.1 Hz, 2x CH), 6.85 (2H, d, *J* = 7.63Hz, 2x CH), 4.32 (4H, t, *J* = 4.24Hz, 2x CH₂), 4.01 (4H, t, *J* = 4.24Hz, 2x CH₂), 3.83 – 3.77 (4H, m, 2x CH₂), 3.77 – 3.73 (2H, m, CH₂), 3.61 (2H, t, *J* = 4.0Hz, CH₂), 3.41 (3H, s, CH₃). IR (cm⁻¹): 3461 (OH), 2975, 2918, 2897, 2875, 2806, 1592, 1509, 1413, 1353, 1263. Mass spectrum [M+H]⁺ = 350.17 Accurate Mass (350.17)

¹H NMR of **17b** in CDCl₃, δ : 7.87 (2H, d, *J* = 8.5Hz, 2x CH), 7.35 (2H, t, *J* = 7.8Hz, 2x CH), 6.85 (2H, d, *J* = 8.5Hz, 2x CH), 4.32 (4H, t, *J* = 5.0Hz, 2x CH₂), 4.02 (4H, t, *J* = 4.7Hz, 2x CH₂), 3.83 – 3.79 (4H, m, 2x CH₂), 3.63 – 3.59 (4H, m, 2x CH₂), 3.41 (6H, s, 2x CH₃). ¹³C NMR CDCl₃ δ: 154.3 (QC), 126.7 (QC), 125.1 (CH), 114.6 (CH), 105.6 (CH), 72.0

(CH₂), 70.9 (CH₂), 69.8 (CH₂), 67.9 (CH₂), 59.1 (CH₃). IR (cm⁻¹): 2975, 2918, 2896, 2876, 2806, 1592, 1510, 1413, 1353, 1264. Mass Spectrum, [M+H]⁺ = 364.19 Accurate Mass (364.19)

2-(2-(1-(2-(2-methoxyethoxy)ethoxy)naphthalen-5-yloxy)ethoxy)ethyl-3-(triethoxysilyl)propylcarbamate (18).^[155]

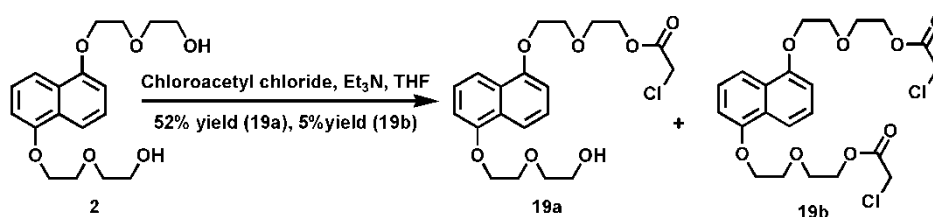


To a solution of the **17a** (1,080 g, 3.08 mmol) in dry pyridine (30 mL) was added isocyanatopropyl triethoxysilane (0.8 mL, 3.18 mmol). The reaction mixture was heated under reflux for 18 hours. Once cool, the pyridine was then removed *in vacuo*, to yield a dark oil. The silane product was purified by silica column chromatography, eluting with 0 – 60 % EtOAc DCM to gain the product as a yellow oil (1.45 g, 78%)

¹H NMR in CDCl₃, δ: 7.87 (1H, d, *J* = 8.2 Hz CH), 7.86 (1H, d, *J* = 8.2 Hz, CH), 7.35 (2H, t, *J* = 8.1 Hz, 2x CH), 6.84 (2H, d, *J* = 7.6 Hz, CH), 4.95 (1H, br s, NH), 4.34-4.24 (6H, m, 3x CH₂), 4.03-3.97 (4H, m, 2x CH₂), 3.81 (10H q, *J* = 6.7 Hz, 5x CH₂), 3.6 (2H, t, *J* = 4.3 Hz, CH₂), 3.41 (3H, s, CH₃), 3.16 (2H, q, *J* = 6.2 Hz, CH₂), 1.61 (2H, quintet, *J* = 7.6 Hz, CH₂), 1.22 (9H, t, *J* = 6.9 Hz, 3x CH₃), 0.61 (2H, t, *J* = 8.1 Hz, CH₂).
¹³C NMR in CDCl₃, δ: 156.39 (QC), 154.34 (QC), 154.30 (QC), 126.77 (QC), 126.75 (QC), 125.16 (CH), 125.06 (CH), 114.71 (CH), 114.59 (CH), 105.66 (CH), 105.63 (CH), 72.06 (CH₂), 70.93 (CH₂), 70.08 (CH₂), 69.88

(CH₂), 69.73 (CH₂), 67.91 (CH₂), 63.91 (CH₂), 59.16 (CH₃), 58.47 (CH₂), 43.47 (CH₂), 23.30 (CH₂), 18.32 (CH₃), 7.61 (CH₂). Mass spectrum failed to show the required mass ion. IR (cm⁻¹): 3475, 3398, 3363, 2924, 2874, 2827, 2360, 2341, 1666, 1593, 1508, 1412, 1265, 1065.

1-(2-(2-(chloroacetyloxy)ethoxy)ethoxy)-5-(2-(2-hydroxyethoxy)ethoxy) naphthalene (19a).^[137]



To a solution of **2** (500 mg, 1.48 mmol) in THF was added triethylamine (0.25 mL, 1.79 mmol) allowed to stir at room temperature for ~ twenty-five minutes. Chloroacetyl chloride (0.12 mL, 1.48 mmol) was added slowly dropwise. As the chloroacetyl chloride was added, HCl gas was evolved and the reaction mixture went cloudy. The reaction mixture was stirred at room temperature for one and a half hours under an atmosphere of N₂ gas. The solvent was removed *in vacuo* to yield a pale oil. The required product was separated by flash silica column chromatography eluting with 0-100 % EtOAc DCM. The monoalkylated and bis-alkylated products were recovered as waxy solids; **19a** in a 52 % yield and **19b** in a 5 % yield.

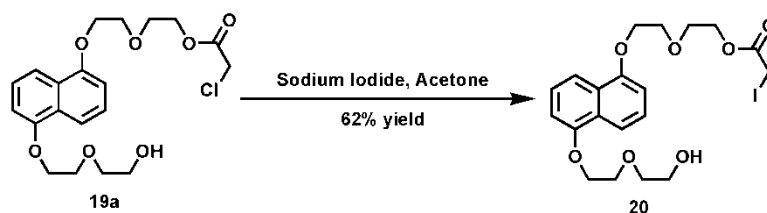
¹H NMR CDCl₃, bis-alkylated compound **19b**, δ : 7.78 (2H, d, *J* = 8.4Hz, 2x CH), 7.29 (2H, t, *J* = 8.0Hz, 2x CH), 6.78 (2H, d, *J* = 8.0Hz, 2x CH), 4.33 (2H, m, 2x CH₂), 4.24 (4H, q, *J* = 4.6Hz, 2x CH₂), 4.00 (2H, s, CH₂), 3.94 (4H, m, 2x CH₂), 3.82 (2H, m, 2x CH₂), 3.70 (4H, m, 2x CH₂)
¹³C NMR δ: 167.4 (QC), 154.3 (QC), 126.8 (QC), 125.2 (CH), 114.7 (CH), 105.8 (CH), 69.8 (CH₂), 69.1 (CH₂), 67.9 (CH₂), 65.3 (CH₂), 40.87 (CH₂).

IR (cm⁻¹): 2951, 2928, 2883, 1743 (C=O), 1594, 1512, 1415, 1330, 1269.

Mass spectrum [M+H]⁺ = 412.1

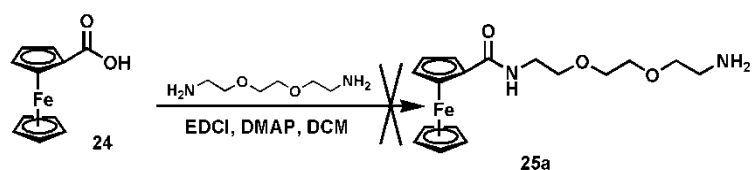
¹H NMR CDCl₃, mono-alkylated compound **19a**, δ : 7.79 (2H, m, 2x CH), 7.30 (2H, t, J = 8.0Hz, 2x CH), 6.78 (2H, m 2x CH), 4.33 (4H, m, 2x CH₂), 4.24 (4H, m, 2x CH₂), 4.04 (4H, s, 2x CH₂), 3.94 (4H, m, 2x CH₂), 3.82 (4H, m, 2x CH₂) ¹³CNMR δ: 167.4 (QC), 154.3 (QC), 126.7 (QC), 125.2 (CH), 114.6 (CH), 105.8 (CH), 72.7 (CH₂), 69.8 (CH₂), 69.7 (CH₂), 69.0 (CH₂), 67.9 (CH₂), 65.3(CH₂), 61.8 (CH₂), 40.90 (CH₂). IR (cm⁻¹): 3514 (OH), 2961, 2929, 2903, 2883, 2865, 1747 (C=O), 1595, 1512, 1417, 1328, 1270. Mass spectrum [M+H]⁺ = 488.1

1-(2-(2-(iodoacetyloxy)ethoxy)ethoxy)-5-(2-(2-hydroxyethoxy)ethoxy)naphthalene (20).



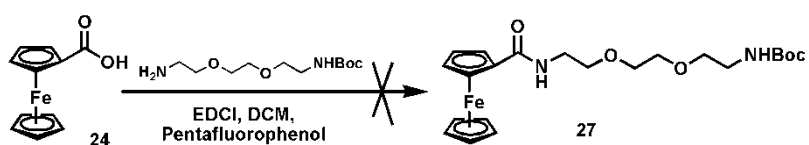
To a solution of **19a** (632 mg, 1.5 mmol) in acetone (20 mL) was added sodium iodide (390 mg, 2.6 mmol). The reaction mixture was refluxed for 2 days. The solvent was then removed *in vacuo*. A dark yellow-red oil was produced in a 62% yield. Mass Spectrum [M+H]⁺ = 505.4.

N-(2-(2-(2-aminoethoxy)ethoxy)ethylamido) ferrocene (25a).



To ferrocene-carboxylic acid (500 mg, 2.16 mmol) in DMF (100 mL) was added EDCI (414 mg, 2.16 mmol), 2,2'-(ethylenedioxy)diethylamine (0.32 mL, 2.16 mmol), and DMAP (264 mg, 2.16 mmol). The reaction mixture was then stirred at room temperature for 3 days. The mixture was filtered, and the solid was washed with DCM. The solution was concentrated and subjected to flash silica column chromatography. Eluting with 0-100% acetone in DCM failed to yield either the starting material or the product.

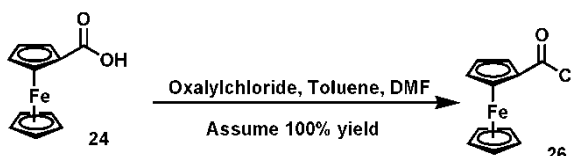
Attempted Synthesis of N-(2-(2-(2-(N-tert-Butylcarbonylamino)ethoxy)ethoxy)ethylamido) ferrocene (27).



To ferrocene carboxylic acid (930 mg, 4 mmol) in DCM (100 mL) was added EDCI (770 mg, 4 mmol) followed by pentafluorophenol (740 mg, 4 mmol). The reaction mixture was stirred at room temperature for two hours. After this time N-Boc-2,2'-(ethylenedioxy)diethylamine (1,000 mg, 4 mmol) was added. The reaction mixture was then stirred at room temperature for 16 hours. The solvent was removed *in vacuo* to yield a

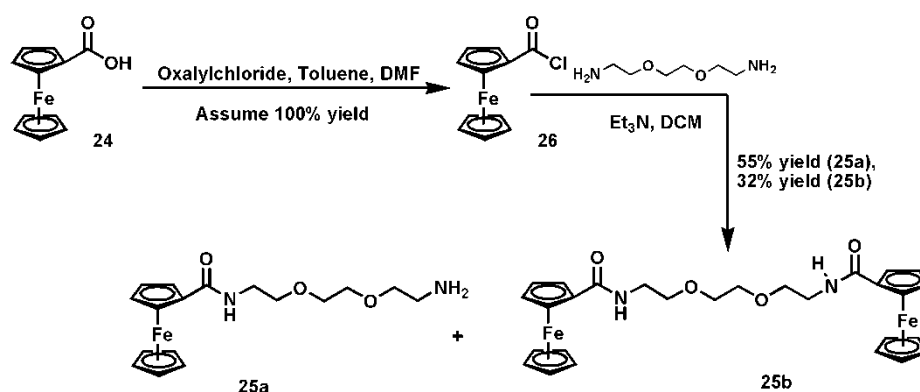
dark brown oil. Flash silica column chromatography eluting with 0-97 % acetone DCM with 3 % triethylamine failed to yield the product.

Ferrocene Acid Chloride Formation (26).^[94]



To a solution of ferrocene-carboxylic acid (1,000 mg, 4.35 mmol) in dry toluene (100 mL) was added dropwise, oxalyl chloride (0.55 mL, 6.1 mmol). Two drops of DMF were added and the reaction mixture was heated reflux under at 60°C for one hour. The mixture was allowed to cool and the solvent was removed *in vacuo* to yield a dark red solid. The solid was taken up into DCM and impurities were precipitated out by the addition of hexane. The mixture was filtered, and washed with hexane. The liquid was collected and solvent was removed *in vacuo* to yield a dark red oil. The product was taken on to react with ethylenedioxy bis(ethylamine) with no further analysis or purification. Assumed 100% yield.

N-(2-(2-(2-aminoethoxy)ethoxy)ethylamido) ferrocene (**25a**).^[94]

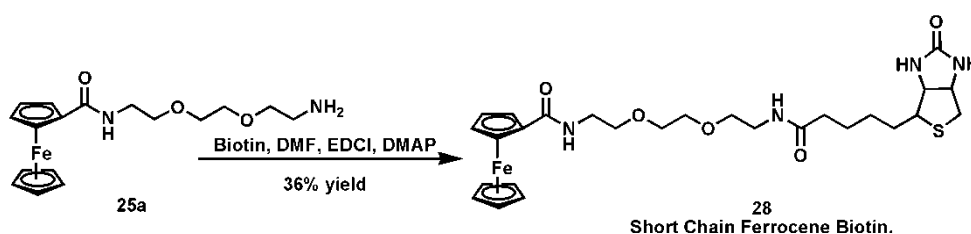


To a solution of 2,2'-(ethylenedioxy) bis(ethylamine) (1.2 mL, 8.7 mmol) and triethylamine (1.2 mL, 8.7 mmol) in DCM (125 mL) was added the ferrocene acid chloride **26** (1,080 g, 4.35 mmol) in DCM (125 mL), *via* a pressure equalising dropping funnel over a period of 30 minutes. The reaction mixture was allowed to stir for 16 hours at room temperature. The reaction mixture was poured water (150 mL), and the organic layer was separated, then washed with water (3x 100 mL). The organic layer was then collected and the solvent was removed *in vacuo*. Flash silica column chromatography eluting with 0-20 % MeOH in DCM with 3 % triethylamine yielded products **25a** (870 mg) and **25b** (405 mg) in a 55 % and 32 % yield respectively.

^1H NMR of ferrocene amine **25a** in CDCl_3 , δ : 6.53 (1H, br s, NH amide), 4.73 (2H, s Cp ring, 2x CH), 4.33 (2H, s, Cp ring, 2x CH), 4.20 (5H, s, Cp ring 5x CH), 3.69-3.63 (6H, m, 3x CH_2), 3.59 (2H, t, $J = 5\text{Hz}$, CH_2), 3.54 (2H, t, $J = 4.5\text{Hz}$, CH_2), 2.90 (2H, t, $J = 5\text{Hz}$, CH_2), 1.69 (2H, br s, NH_2)* overlaps with H_2O signal. ^{13}C NMR of ferrocene amine **25a** in CDCl_3 , δ : 170.38(QC), 73.29(QC), 70.38(CH), 70.27(CH_2), 70.20(CH_2), 69.78(CH), 68.22(CH), 41.71(CH_2), 39.31(CH_2), 30.98(CH). IR (cm^{-1}): 3384, 3321, 3074, 2929, 2914, 2893, 2884, 2850, 1643, 1629, 1542, 1103. Mass spectrum $[\text{M}+\text{H}]^+ = 361.2$

^1H NMR of ferrocene dimer **25b** in CDCl_3 , δ : 6.17 (2H, br s, 2x NH amide), 4.67 (4H, s, 2x Cp ring, 4x CH) 4.34 (4H, s, 2x Cp ring, 4x CH), 4.22 (10H, s, 2x Cp ring, 10x CH), 3.69 (4H, s, 2x CH_2), 3.66 (4H, t, $J = 5\text{Hz}$, 2x CH_2), 3.60(4H, t, $J = 5.4\text{Hz}$, 2x CH_2) Mass spectrum $[\text{M}+\text{H}]^+ = 573.1$

N-(2-(2-(2-(biotinoylamino)ethoxy)ethoxy)ethylamido) ferrocene (**28**).

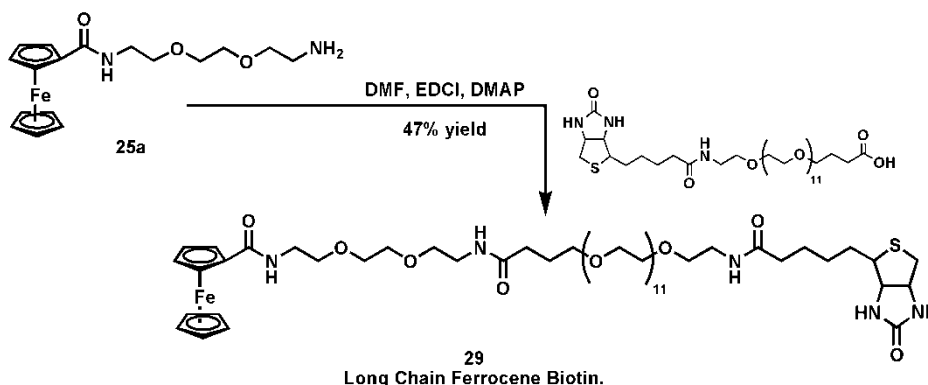


To a solution of **25a** (500 mg, 1.38 mmol) in DMF (30 mL) was added biotin (337 mg, 1.38 mmol), EDCI (204 mg, 1.38 mmol), and DMAP (168 mg, 1.38 mmol). The reaction mixture was stirred at room temperature for 48 hours. The crude reaction mixture was taken up in DCM (100 mL) and extracted with water (150 mL). The aqueous layer was washed with DCM (3x 100 mL) then the organic layers were combined and washed with brine (2x 100 mL). The organics were dried over MgSO_4 , filtered and evaporated to yield a dark oil. The product was purified by silica column chromatography, eluting with a 10 % stepwise gradient of 0 to 50 % methanol in ethyl acetate to gain the product as an orange glassy solid in a 36% yield.

Mass Spectrum $[\text{M}+\text{H}]^+ = 587.20$ Accurate mass (587.2). ^1H NMR in CDCl_3 , δ : 6.57 (1H, t, $J = 5.0\text{Hz}$, NH), 6.44 (1H, t, $J = 5.1\text{Hz}$, NH), 6.34 (1H, s, NH), 5.29 (1H, s, NH), 4.74 (2H, s, 2x CH Cp ring), 4.51 (1H, br t, $J = 6.0\text{Hz}$, CH biotin), 4.34 (2H, s, 2x CH Cp ring), 4.33-4.29 (1H, m, CH

biotin), 4.21 (5H, s, 5x CH Cp ring), 3.70-3.63 (6H, m, 3xCH₂), 3.62-3.55 (4H, m, 2xCH₂), 3.52-3.39 (2H, m, CH₂), 3.17-3.13 (1H, m, CH biotin), 2.91 (1H, dd, $J_1 = 4.6\text{Hz}$, $J_2 = 12.8\text{Hz}$, CH biotin), 2.76 (1H, d, $J = 12.7\text{Hz}$, CH biotin), 2.21 (2H, t, $J = 7.4\text{Hz}$, CH₂), 1.73-1.61 (4H, m, 2x CH₂), 1.44(2H, h, $J = 7.5\text{Hz}$, CH₂). ¹³C NMR in CDCl₃, δ : 173.3 (QC), 170.62 (QC), 164.02 (QC), 76.07 (QC), 70.51 (CH), 70.25 (CH₂), 70.21 (CH₂), 70.06 (CH₂), 69.95 (CH), 69.82(QC), 68.29 (CH), 61.79 (QC), 60.22(QC), 55.59(CH), 40.49(CH₂), 39.43(CH₂), 39.09 (CH₂), 36.00 (CH₂), 28.21 (CH₂), 28.11 (CH₂), 25.61 (CH₂). IR (cm⁻¹): 3277, 3108, 3092, 3081, 2932, 2912, 2895, 2886, 2853, 1702(C=O), 1641, 1629, 1540, 1105 CHN: 52.25/ 52.14 (55.29), 6.30/6.38 (6.53), 8.70/8.74 (9.55)

N-(2-(2-(2-(O-(2-(biotinoylamino)ethyl)-O'-(2-carboxethyl)undecaethyleneglycol)ethoxy)ethoxy)ethyl)amido ferrocene. (Ferrocene LC biotin) (29).

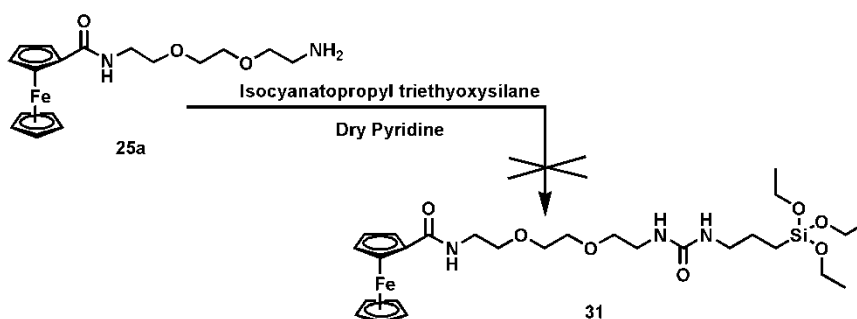


To ferrocene amine **25a** (56 mg, 0.15 mmol), in DCM (5mL) was added EDCI (34.5 mg, 0.18mmol), and DMAP (1.5 mg, 0.01 mmol). The mixture was stirred for 5 minutes under an atmosphere of nitrogen. O-[2-(biotinylamino)ethyl]-O'-[2-carboxyethyl] undecaethylene glycol (100 mg, 0.12 mmol) was added to the stirring mixture. The reaction was

then stirred for 24 hours at room temperature under an inert atmosphere. The crude mixture was diluted to 25 mL with DCM and then washed with water (1x 20 mL) and brine (2x 20 mL). The organic layer was separated and dried over sodium sulfate, filtered and evaporated to yield the product as a dark brown oil in a 47 % yield.

^1H NMR (500MHz, CDCl_3) δ : 6.73 (2H, br q, $J = 7\text{Hz}$, 2xNH), 6.41 (1H, br t, $J = 5.2\text{Hz}$, NH), 6.21 (1H, s, NH), 5.40 (1H, s, NH), 4.71 (2H, t, $J = 2\text{Hz}$, Cp ring), 4.50 (1H, br t, $J = 7.2\text{Hz}$, CH biotin), 4.33 (2H, s, 2xCH Cp ring), 4.32-4.29 (1H, m, CH biotin), 4.20 (5H, s, 5xCH Cp ring), 3.73 (2H, t $J = 6\text{Hz}$, CH_2), 3.68-3.60 (49H, m, Alkyl), 3.59-3.54 (7H, m, Alkyl), 3.48-3.40 (4H, m, 2x CH_2), 3.17-3.11(1H, m, CH biotin), 2.90 (1H, dd, $J = 6.25\text{Hz}$, $J = 8.3\text{Hz}$, CH biotin), 2.75 (1H, d, $J = 14\text{Hz}$, CH biotin), 2.47 (2H, t, $J = 5.8\text{Hz}$), 2.25-2.20 (2H, m CH_2), 1.79-1.71(1H, m, CH alkyl), 1.71-1.62 (3H, m 3xCH alkyl), 1.48-1.42 (2H,m, CH_2). Mass Spectrum : $\text{M}^+ = 1186.7$ FAB NOBA. CHN: 49.41/49.32 (54.68), 7.36/7.31 (7.73), 5.11/5.11 (5.90)

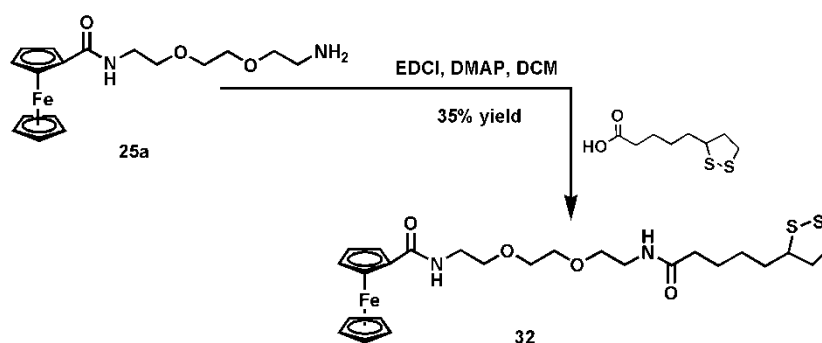
1-(2-(2-(2-(ferrocenoylamino)ethoxy)ethoxy)ethyl)-3-(3-(triethoxysilyl)propyl)urea (31).^[155]



To a solution of the ferrocene amine **25a** (500 mg, 3.08 mmols) in dry pyridine (30 mL) was added isocyanatopropyl triethoxysilane (0.8 mL,

3.18 mmols). The reaction mixture was heated to reflux for 18 hours. Once cool the pyridine was then removed *in vacuo*, to yield a dark oil. Column Chromatography failed to recover either the product or the starting material.

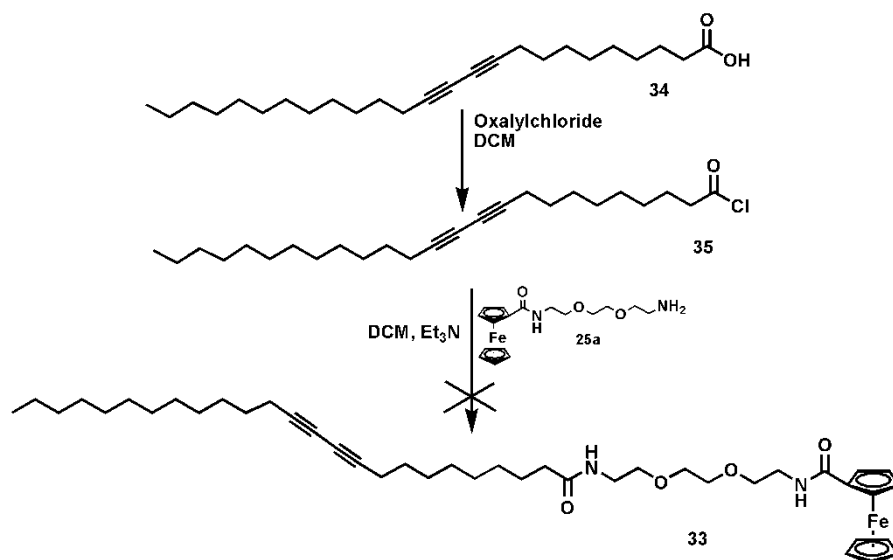
N-(2-(2-(2-(thioctinoylamino)ethoxy)ethoxy)ethylamido) ferrocene (32).



To a solution of **25a** (510 mg, 1.4 mmol) in DCM (50 mL) was added EDCI (210 mg, 1.4 mmol), DMAP (172 mg, 1.4 mmol), and thioctic acid (292 mg, 1.4 mmol). The reaction mixture was stirred at room temperature for 48 hours. The crude reaction mixture was taken up in DCM (100 mL), extracted with water (150 mL). The aqueous layer was separated and washed with DCM (3x 100 mL) then the organic layers were combined and washed with brine (2x 100 mL). The organics were dried over MgSO₄, filtered and evaporated to yield a dark oil. The product was purified by silica column chromatography, eluting with 100% petroleum ether followed by a 10% step-wise gradient of 0 to 60% acetone in ethyl acetate to afford **32** as a glassy orange solid in a 35% yield.

Mass Spectrum. $M^+ = 548.15$ Accurate Mass (548.14) ^1H NMR in CDCl_3 , δ : 6.48 (1H, t, $J = 5.3\text{Hz}$, NH), 6.31 (1H, t, $J = 4.9\text{Hz}$, NH), 4.69 (2H, t, $J = 1.88\text{Hz}$, 2x CH Cp ring), 4.32 (2H, t, $J = 2.0\text{Hz}$, 2x CH Cp ring), 4.18 (5H, s, 5x CH Cp ring), 3.65-3.60 (6H, m, 3x CH_2), 3.58-3.49 (5H, m), 3.42 (2H, br q, $J = 5.1\text{Hz}$, CH_2), 2.46-2.38 (1H, m, CH), 2.14 (2H, t, $J = 7.4\text{Hz}$, CH_2), 1.93-1.83 (1H, m, CH), 1.72-1.54 (4H, m, 2x CH_2), 1.49-1.34 (2H, m, CH_2) ^{13}C NMR in CDCl_3 , δ : 173.08 (QC), 170.69 (QC), 75.93 (QC), 70.54 (CH), 70.29 (CH_2), 70.25 (CH_2), 70.05 (CH_2), 69.82 (CH), 69.74 (QC), 68.24 (CH), 56.49 (CH), 40.27 (CH_2), 39.32 (CH_2), 39.14 (CH_2), 38.49 (CH_2), 36.32 (CH_2), 34.64 (CH_2), 28.91 (CH_2), 25.39 (CH_2). IR (cm^{-1}): 3275, 3110, 3093, 3082, 2934, 2911, 2895, 2888, 2851, 1705(C=O), 1641, 1632, 1543, 1104

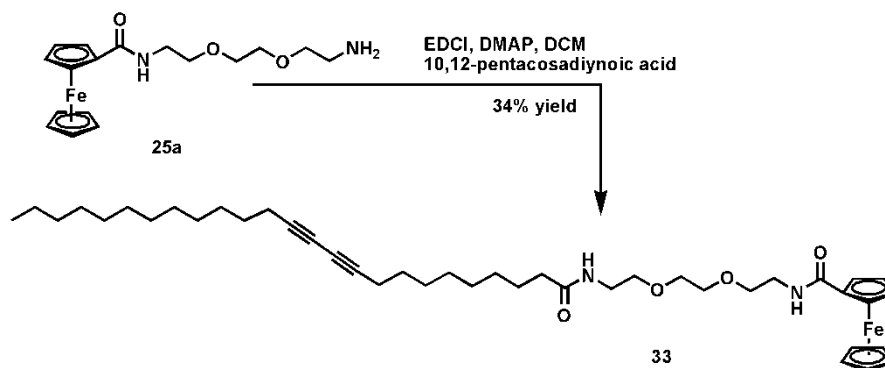
N-(2-(2-(2-(10,12-pentacosadynoylamino)ethoxy)ethoxy)ethylamido)ferrocene (33).^[107]



To a solution of 10,12-pentacosadiynoic acid (500 mg, 1.3 mmol) in dry DCM (50 mL) was added dropwise oxalyl chloride (0.2 mL,

1.3 mmol) followed by two drops of DMF. The reaction was then stirred for 3 hours in the dark. The solution was then added dropwise to a stirring solution of the ferrocene amine **25a** (396 mg, 1.1 mmol) and triethylamine (0.46 mL, 3.3 mmol) in DCM (50 mL). The reaction was then stirred in the dark for 16 hours. The solvent was then removed *in vacuo* to yield a black oily solid. ¹H NMR indicated that the product formed was not the desired compound.

N-(2-(2-(2-(10,12-pentacosadiynoylethoxy)ethoxy)ethylamido)ferrocene (33).

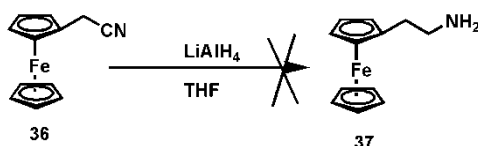


To a solution of the ferrocene amine **25a** (862 mg, 2.4 mmol) in DCM (50mL) was added sequentially EDCI (355 mg, 2.4 mmol), DMAP (292 mg, 2.4 mmol), and 10,12-pentacosadiynoic acid (897 mg, 2.4 mmol). The reaction mixture was then stirred at room temperature for 3 days in the dark. The solvent was then removed *in vacuo* in the dark to yield a dark oil. Purification by two silica column chromatographies, eluting with 100% ethyl acetate gave the product as an orange glassy solid in a 34% yield

Mass Spectrum. $[M+H]^+ = 716.3$ CHN: 70.22/70.40 (70.37), 9.07/9.09 (9.00), 4.05/4.06 (3.91) ¹H NMR in CDCl₃, δ : 4.68 (2H, t, $J =$

1.9Hz, 2x CH Cp ring), 4.34 (2H, t, $J = 1.9\text{Hz}$, 2x CH Cp ring), 4.19 (5H, s, 5x CH Cp ring), 3.67-3.62 (6H, m, 3x CH₂), 3.60-3.54 (4H, m, 2x CH₂), 3.45 (2H, q, $J = 5.3\text{Hz}$, CH₂), 2.23 (4H, t, $J = 6.8\text{Hz}$, 2xCH₂), 2.13 (2H, t, $J = 7.6\text{Hz}$, CH₂), 1.62-1.55 (2H, m), 1.54-1.46 (4H, m, 2x CH₂), 1.39-1.32 (4H, m), 1.31-1.26 (6H, m), 1.25 (16H, br. s), 0.89-0.85 (3H, m) ¹³C NMR in CDCl₃, δ : 173.24 (QC), 170.43 (QC), 77.61 (QC), 77.44 (QC), 70.45 (CH₂), 70.31 (CH₂), 70.28 (CH₂), 70.18 (CH₂), 70.06 (CH₂), 68.17 (CH₂), 65.31 (QC), 65.23 (QC), 39.29 (CH₂), 39.09 (CH₂), 36.69 (CH₂), 31.91 (CH₂), 29.47 (CH₂), 29.34 (CH₂), 29.24 (CH₂), 29.19 (CH₂), 29.09 (CH₂), 28.94 (CH₂), 28.86 (CH₂), 28.77 (CH₂), 28.35 (CH₂), 28.30 (CH₂), 25.67 (CH₂), 22.69 (CH₂), 19.20 (CH₂), 19.18 (CH₂), 14.13 (CH₃). IR (cm⁻¹): 3312, 3057, 2919, 2849, 1645, 1629, 1544, 1301, 1106.

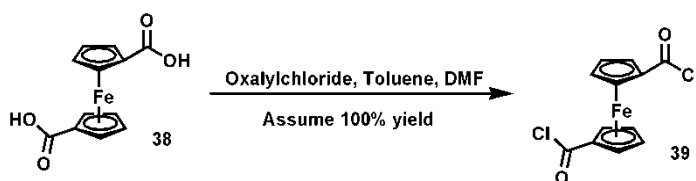
Ferrocene ethylamine (37).



To a solution of ferrocene acetonitrile (500 mg, 2.2 mmol) in dry tetrahydrofuran (100 mL) was added portionwise lithium aluminium hydride (60% dispersion, 614 mg, 4.4 mmol). The reaction mixture was stirred at room temperature for 2.5 hours. The reaction mixture was then cooled to 0°C in an ice bath and quenched with 15 % aq NaOH (100 mL), and filtered. The solution was extracted with DCM (100 mL), where the organic layer was washed with saturated brine solution (3x 75mL). The organic layer was dried over MgSO₄, filtered and the solvent was removed *in vacuo*. Flash silica column chromatography eluting with 0-

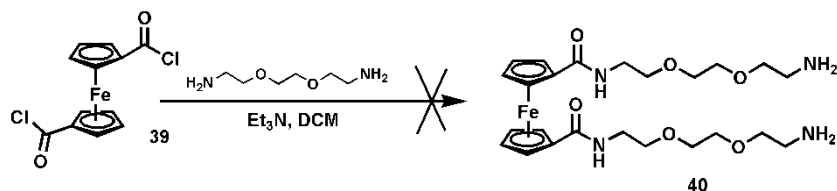
97% acetone in DCM with 3% triethylamine held constant throughout the chromatography failed to yield either starting material or product.

1,1'-Ferrocene dicarboxylic acid chloride Formation (39).^[156]



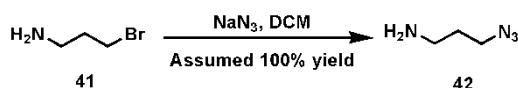
To a solution of ferrocene dicarboxylic acid (1,000 mg, 3.65 mmol) in dry toluene (100mL) was added dropwise, oxalyl chloride (0.98 mL, 11 mmol). DMF (10 mL) was added to aid solubility and as a catalyst. The reaction mixture was heated under reflux at 60°C for one hour. Once cooled, the solvent was removed *in vacuo* to yield a dark red solid that was taken on to react with ethylenedioxy bis(ethylamine) with no further analysis or purification. Assumed 100% yield.

1,1'-Bis(N-(2-(2-(2-aminoethoxy)ethoxy)ethylamido) ferrocene (40).^[156]



To a solution of 2,2'-(ethylenedioxy) bis(ethylamine) (2.2 mL, 14.6 mmol) and triethylamine (2 mL, 14.6 mmol) in DCM (100 mL) was added the ferrocene diacid chloride **39** (3,700 mg, 3.7 mmol) in DCM (200 mL) *via* a pressure equalising dropping funnel over a period of 30 minutes. The reaction mixture was allowed to stir for 16 hours at room temperature. The reaction mixture added to water (150 mL) and partitioned. The organic layer was separated and washed with water (3x 100 mL). The aqueous layer was evaporated under reduced pressure, and then washed with ethanol. It was found the residue was highly impure and failed to travel on TLC in any solvent.

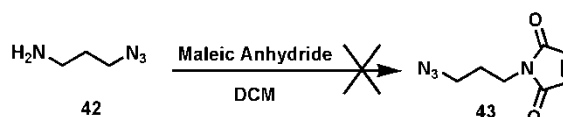
Synthesis of 1-Azido-propyl-3-amine (42).^[136]



To a solution of bromo propylamine (3,200 mg, 14.7 mmol) in 15mL distilled water was added dropwise a solution of sodium azide (2,900 mg, 44 mmol) in 10 mL water. The mixture was then refluxed for 20 hours and then allowed to cool. 50 mL DCM followed by potassium hydroxide (4,000 mg, 71 mmol) was then added and the mixture was

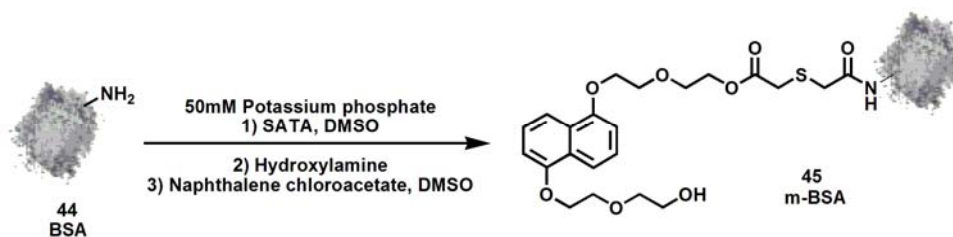
stirred at room temperature until the potassium hydroxide had fully dissolved. The biphasic system was then separated, and the aqueous layer was washed with DCM (25 mL). The organic layer was dried over magnesium sulfate, filtered and evaporated. The product was taken onto the next stage without any further treatment. Assumed 100% yield.

Synthesis of 1-Azido-propyl-3-maleimide (43).^[136]



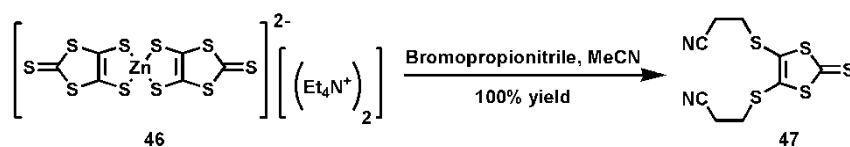
To a solution of **42** (1,470 mg, 14.7 mmol) in DCM (80 mL) at 0°C was added dropwise a solution of maleic anhydride (1,080 mg, 11 mmol). The reaction mixture was allowed to stir at 0°C for 2 hours, and then allowed to warm to room temperature overnight. The solvent was then removed *in vacuo* to yield an insoluble orange solid. After extensive heating and sonication a ¹H NMR in d₆-DMSO showed very impure product.

Naphthalene modified BSA (45).^[40]



To a solution of bovine serum albumin (110 mg) in 50 mM phosphate buffer (18 mL), pH = 7.2, was added a solution of N-succinimidyl-S-acetyl-thioacetate (SATA) (10 mg) in anhydrous DMSO (2 mL). The reaction mixture was stirred for 30 minutes. The crude mixture was then dialysed in 50 mM potassium phosphate (4x 1L). The dialysis tubing had a molecular weight cut off of 4000-6000g. The dialysed mixture was returned to the reaction flask and hydroxylamine (100 mg) was added. The reaction mixture was stirred for a further two hours and then re-dialysed in 50 mM potassium phosphate buffer (4x 1L). The mixture was returned to the reaction flask whereby a solution of **19a** (100 mg) in anhydrous DMSO (2 mL) was added. The reaction mixture was then stirred at room temperature for 24 hours. The reaction mixture went cloudy as the chloroacetate was added, the resulting suspension was centrifuged and the supernatant was collected. The solution was washed with ethyl acetate to remove any excess ligand. The aqueous layer was collected and dialysed in distilled water (6x 1L), to remove the potassium phosphate buffer. The aqueous solution was removed *in vacuo* to yield the modified BSA as a pale yellow glassy solid in a 14% yield.

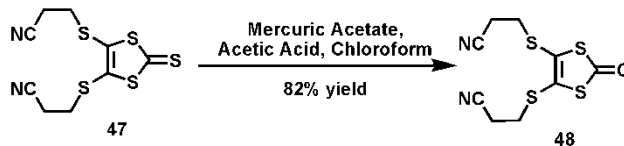
4,5-bis(2-cyanoethylthio)-1,3-dithiole-2-thione (47).^[95]



To a solution of bis(tetraethylammonium) bis(4,5-dimercapto-1,3-dithiole-2-thione) zincate salt **46** (5,000 mg, 7 mmol) in acetonitrile (100 mL) under reflux was added bromopropionitrile (2.9 mL, 35 mmol). The reaction mixture was heated to reflux for 1 hour. The mixture was then allowed to cool to room temperature overnight. The mixture was filtered and the solid was washed the acetonitrile (50 mL). The solvent was then removed *in vacuo*. The crude residue was then taken up in DCM (100 mL) and washed with water (1x 75 mL) and brine (3x 75 mL). The organic layer was separated, and dried over MgSO₄, filtered and evaporated to yield a yellow / orange solid. The solid was then taken up in toluene (100 mL) and petroleum ether (100 mL) was added to precipitate the product as a yellow solid (728 mg). The filtrate was evaporated to yield more crude material that was purified by silica column chromatography eluting with ethyl acetate, followed by 20% acetone in ethyl acetate, to yield the product as an oily solid. The greasy residue was then taken up in DCM and precipitated to yield the product as a yellow solid (1.5 g) total yield 100%

¹H NMR (400MHz, CDCl₃) δ: 3.19 (4H, t, *J* = 6.8 Hz), 2.83 (4H, t, *J* = 6.8 Hz). Mass Spectrum: [M]⁺ = 304.1

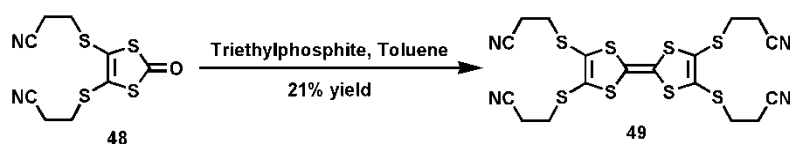
4,5-bis(2-cyanoethylthio)-1,3-dithiol-2-one (48).^[95]



To a solution of **47** (2.3 g, 0.007 mol) in chloroform (50 mL), was added mercuric acetate (6.2 g, 0.019 mol). The mixture was stirred for 5 minutes where by glacial acetic acid (15 mL) was added. As the mercuric acetate was added the solution went opaque, which then turned transparent yellow upon addition of the acetic acid. The reaction mixture was stirred under an atmosphere of N₂ gas for 16 hours. The mixture was filtered, and the solid was washed thoroughly with chloroform. The filtrate was extracted with 1.2 M aqueous sodium bicarbonate (200 mL) where the organic layer was washed with water (3x 150 mL). The organic layer was dried over MgSO₄, filtered and evaporated *in vacuo* to yield the product as a yellow solid (1.75 g) in 82% yield.

¹H NMR (400MHz, CDCl₃) δ : 3.16 (4H, t, *J* = 6.8 Hz), 2.82 (4H, t, *J* = 6.8 Hz). Mass Spectrum : [M]⁺ = 288.31

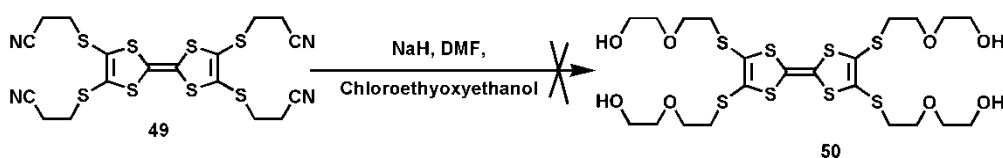
Tetra(2-cyanoethanethio) tetrathiafulvalene (**49**).^[95]



To a flask containing **48** (1.75 g, 0.006 mol), in toluene (125 mL) at reflux was added triethylphosphite (6.1 mL, 0.035 mol). The reaction mixture was stirred under reflux for 30 minutes. Once cool the mixture was cooled to 0°C and methanol (200 mL) was added to quench the reaction. The precipitate formed was then recovered by filtration and washed thoroughly with methanol. The filtrate was evaporated and purified by silica column chromatography eluting first with DCM to remove the triethylphosphite, then with 10-20% stepwise gradient of acetone in DCM to recover the product. The solid product and the material from the chromatograph were combined to give a 21% yield (346 mg)

¹H NMR (400MHz, CDCl₃) δ: 3.17 (8H, t, *J* = 6.8 Hz), 2.82 (8H, t, *J* = 6.8 Hz). Mass Spectrum : [M]⁺ 544.87

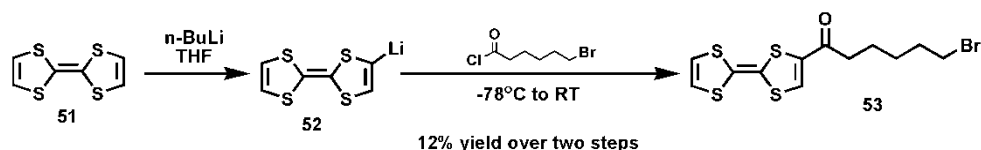
1-(Tetra(2,2'-ethoxy)-ethanethio) tetrathiofulvalene (**50**).



To a solution of **49** (364 mg, 0.64 mmol) in dry DMF (50 mL) was added sodium hydride (205 mg, 5.1 mmol). The mixture was stirred for 20

minutes at room temperature whereby the solution changed from orange to dark red/brown. 2-(2-Chloroethoxy) ethanol (2.1 mL, 19.2 mmol) was added dropwise. The mixture turned black/brown and heat was evolved. The reaction mixture was then stirred for 4 days at room temperature. Water (5 mL) was added cautiously to the reaction to quench the sodium hydride. The solvent was removed under reduced pressure to yield a dark oil. Silica column chromatography failed to yield either the starting material or product from the mixture.

4-(6-bromohexanoyl) tetrathiafulvalene (**53**).^[119]



To an oven dried flask containing tetrathiafulvalene (1,000 mg, 4.9 mmol) in dry diethyl ether (100 mL) under a N₂ atmosphere at -78° C was added n-butyl lithium (2.2 mL, 2.5 M in hexane, 5.4 mmol). The mixture turned from yellow to cloudy green as the lithiated species **43** was formed over a period of 1 hour. 6-Bromohexanoyl chloride (0.8 mL, 5.4 mmol) was added to the reaction mixture and stirred at -78°C under N₂ for 2 hours. As the reaction progressed, the solution turned dark red. The mixture was allowed to slowly warm to room temperature over 16 hours. The reaction mixture was quenched with water (100 mL) and extracted with diethyl ether (150 mL). The organic layer was washed with water (2x 100 mL) and brine (2x 100 mL), separated and dried over MgSO₄, filtered and evaporated under reduced pressure to yield the crude product as a dark red solid. The product was purified by silica column chromatography

eluting with a 10% step wise gradient of 0-100% DCM in petroleum ether, to yield the product as a dark red oil in a 12 % yield.

^1H NMR in CDCl_3 (400MHz) δ : 7.28 (1H, s, CH), 6.33 (2H, br. s, 2x CH), 3.41 (2H, t, $J = 6.6\text{Hz}$, CH_2), 2.70(2H, br.t, $J = 6.6\text{Hz}$, CH_2), 1.88 (2H, pent, $J = 7.1\text{Hz}$, CH_2), 1.70 (2H, pent, $J = 7.6\text{Hz}$, CH_2), 1.52-1.44 (2H, m, CH_2). ^{13}C NMR (400MHz) δ : 212.5(QC), 197.1(QC), 190.9(QC), 119.4(CH), 118.7(CH), 38.2(CH_2), 33.5(CH_2), 32.5 (CH_2), 27.7(CH_2), 23.5(CH_2) Mass Spectrum : M^+ 379.90 and 381.90 (^{79}Br and ^{81}Br) Accurate Mass (379.9 and 381.9)

4-(6-((trimethyl) ammonium)hexanoyl) tetrathiafulvalene bromide (54).

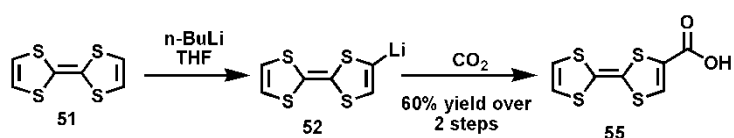


To a flask containing **53** (200 mg, 0.5 mmol) in methanol (50 mL) heated under reflux was added drop wise trimethylamine in ethanol (1 mL, 2.4 M in ethanol). The reaction mixture was stirred under reflux for 16 hours. Once cool, the crude mixture was concentrated under reduced pressure until the volume was 10 mL. Diethyl ether (200 mL) was added to precipitate a dark red / orange solid, which was washed with diethyl ether. The solid product was taken up in methanol and re-precipitated to yield the product as a dark red solid (179 mg, 78%).

^1H NMR in $\text{d}_4\text{-MeOH}$ (500MHz) δ : 7.85 (1H, s, CH), 6.53 (2H, s, 2x CH), 3.67-3.32 (2H, m, CH_2)*, 3.14 (9H, s, 3x CH_3), 2.85 (2H, t, $J = 7.25\text{Hz}$), 1.87-1.82 (2H, m, CH_2), 1.80-1.72 (2H, m, CH_2), 1.46-1.40 (2H, m, CH_2).* MeOD solvent signal overlapping CH_2 multiplet. ^{13}C NMR (500MHz) δ : 210.0(QC), 185.1(QC), 172.7(QC), 135.5(CH), 120.5(CH),

120.2(CH), 67.6(CH₂), 53.5(CH₃), 38.4 (CH₂), 26.8(CH₂), 24.9(CH₂), 23.7(CH₂). MS: [M⁺] = 360.0, 360.06 Accurate Mass. FAB, NOBA (360.06)

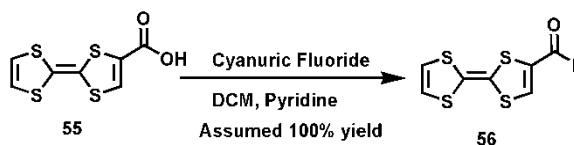
Tetrathiafulvalene carboxylic acid (**55**).^[96]



To an oven dried flask containing tetrathiafulvalene (1,000 mg, 4.9 mmol) under an inert atmosphere was added dry diethyl ether (100 mL) at -78°C in a carbon dioxide acetone bath. Butyl lithium (2.2 mL, 5.4 mmol, 2.5 M in hexane) was added dropwise to the solution and the mixture was then stirred for 1 hour at -78°C. Solid carbon dioxide (1 L) was then added and the reaction was stirred at -78°C for 3 hours and then allowed to slowly warm to room temperature over 12 hours. The mixture was filtered under gravity and washed with diethyl ether. The red solid was recovered and dissolved in water, acidifying with 2 M H₂SO₄ and stirred for 2 hours. The dark red precipitate was filtered by vacuum filtration. The product was then purified by column chromatography eluting with 100% THF to yield the impure product as a sticky red solid in a 60% crude yield.

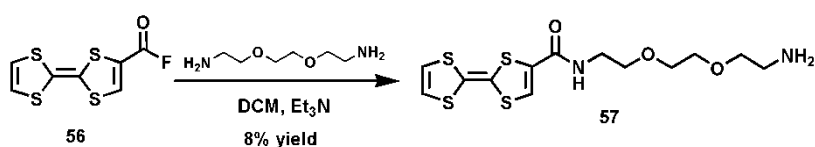
¹H NMR in d₆-acetone δ: 7.57 (1H, s), 6.67 (2H, s), 5.49 (br.s 1H)
MS – [M+H]⁺ = 248.37, Mpt 180-182°C (Literature Mpt : 182-184°C)^[96]

Tetrathiafulvalene acid fluoride (**56**).^[97]



To TTF carboxylic acid **55** (762 mg, 3.0 mmol) in dry dichloromethane (50mL) at 0°C was added pyridine (0.5 mL, 6.1 mmol) and cyanuric fluoride (0.5 mL, 6.1 mmol) under an atmosphere of N₂ gas. The reaction was stirred at 0°C for 2 hours under a N₂ atmosphere. Distilled water (100 mL) was added to quench the reaction, extracting with DCM / water, washing with water (3x 75 mL). The organic layer was collected and carefully evaporated to yield a dark red solid. The aqueous layers were neutralised with calcium oxide (aq) (1 L suspension) until the pH was basic. The product was taken on with assumed 100% yield with no further treatment.

N-(2-(2-(2-aminoethoxy)ethoxy)ethylamido) tetrathiafulvalene (**57**).

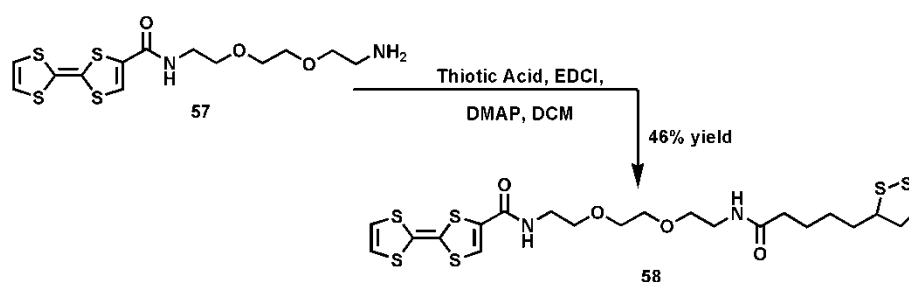


To a flask containing 2,2'-(ethylenedioxy) bis(ethylamine) (0.9 mL, 6.1 mmol) and triethylamine (0.9 mL, 6.2 mmol) in DCM (50mL) was added the **56** (767 mg, 3.0 mmol) in dichloromethane (100 mL) *via* a pressure equalising dropping funnel over a period of 1 hour. The reaction mixture was allowed to stir for 16 hours at room temperature. The reaction mixture was partitioned between dichloromethane (150 mL) and

water (150 mL). The organic layer was separated, and washed with water (3x 100 ml). The organics collected and the solvent was removed *in vacuo*. Flash silica column chromatography eluting with 0-20% methanol in DCM with 1% triethylamine, followed by a 5% stepwise gradient of 0-20% methanol in DCM with 1% triethylamine then flushed with 99% methanol. This yielded the product with excess 2,2'-(ethylenedioxy) bis(ethylamine) that ran with the **57** on the silica column. (83 mg impure material, 8 % yield)

^1H NMR in $\text{d}_4\text{-MeOH}$ (400MHz) δ : 7.18 (1H,s, CH), 6.40 (2H, s, 2x CH), 3.61-3.45 (8H,m, 4xCH₂)*, 3.40 (2H, t, J = 3.2 and 4.2Hz, CH₂), 3.01 (2H, t, J = 3.2 and 1,5Hz, CH₂). *contains additional Hs from 2,2'-(ethylene dioxy)bis(ethylamine). Mass Spectrum: $[\text{M}+\text{H}]^+$ 379.7.

N-(2-(2-(2-(thioctinoylamino)ethoxy)ethoxy)ethylamido) tetrathiafulvalene (58).



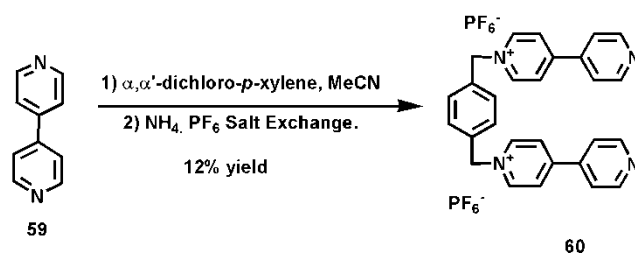
To a solution of compound **57** (83 mg, 0.22 mmol) in DCM (45 mL) / DMF (5 mL) was added EDCI (33 mg, 0.22 mmol), DMAP (27 mg, 0.22 mmol) and thiotic acid (45 mg, 0.22 mmol). The reaction mixture was stirred at room temperature for four days. The mixture was partitioned between DCM (100 mL) / water (100 mL), and the organic layer was washed with brine (3x 100 mL). The organic layer was separated and

dried over MgSO₄, filtered and the solvent was removed *in vacuo* to yield impure product as a dark oil. The crude material was purified by flash silica column chromatography eluting with 100% petroleum ether followed by 0-20% acetone in ethyl acetate to yield the product as an orange red oily solid (57 mg) in a 46 % yield.

¹H NMR in CDCl₃ (400MHz), δ: 7.19 (1H, s, CH), 6.36 (2H, s, 2xCH), 6.35 (1H, s, NH), 5.94 (1H, s, NH), 3.70-3.52 (12H, m, 6x CH₂), 3.51-3.48 (2H, m, CH₂), 3.23-3.10 (2H, m, CH₂), 2.48 (1H, hex, *J* = 6.2Hz, H from CH₂), 2.22 (2H, t, *J* = 7.4Hz, CH₂), 1.93 (1H, hex, *J* = 6.6Hz, H from CH₂), 1.71-1.66 (4H, m, 2x CH₂), 1.49-1.39 (1H, m, CH) It was found that the TTF moiety oxidised in CDCl₃ so a ¹³C NMR could not be run in this solvent.

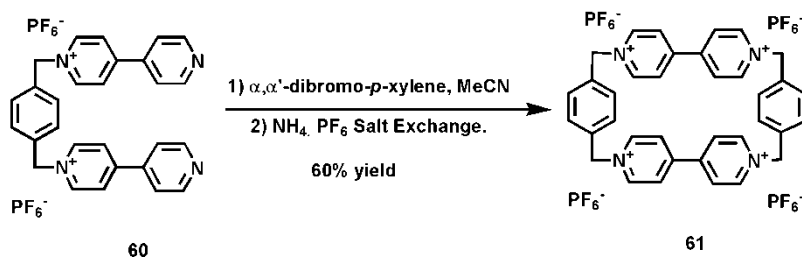
¹H NMR in d₄-MeOD (500MHz), δ: 7.30 (1H, s, CH), 6.53 (2H, d, *J* = 1.3Hz, 2x CH), 3.67-3.56 (10H, m, 5x CH₂), 3.47 (2H, t, *J* = 5.5Hz, CH₂), 3.39 (2H, t, *J* = 5.5Hz, CH₂), 3.20-3.17 (1H, m, H from CH₂), 3.14-3.10 (1H, m, H from CH₂), 2.48 (1H, hex, *J* = 6.4Hz, H from CH₂), 2.23 (2H, t, *J* = 7.4Hz, CH₂), 1.91 (1H, hex, *J* = 6.7Hz, H from CH₂), 1.78-1.61 (4H, m, 2x CH₂), 1.53-1.45 (1H, m, CH). ¹³C NMR in d₄-MeOD (500MHz), δ: 176.17 (QC), 161.85 (QC), 134.21(QC), 126.45 (CH), 120.50 (CH), 120.22 (CH), 114.21 (QC), 107.47 (QC), 71.37 (CH₂), 70.67 (CH₂), 70.41 (CH₂), 57.64 (CH), 41.35 (CH₂), 40.95 (CH₂), 40.34 (CH₂), 39.36 (CH₂), 39.89 (CH₂), 35.78 (CH₂), 29.92 (CH₂), 26.75 (CH₂). Mass spectrum: [M + Na]⁺ = 588.7 (FAB, NOBA)

1,1'-[1,4-phenylenebis-(methylene)] bis(4,4'-bipyridinium) bis(hexafluorophosphate) (60). [9]



To a solution of 4,4-dipyridyl (14.3 g, 0.09 mol) in dry acetonitrile (250mL) under reflux was added over a 3 hour period, a solution of α, α' -dichloro-*p*-xylene (6.7 g, 0.04 mol) in dry acetonitrile (200 mL). The reaction mixture was heated under reflux for 24 hours. As the reaction progressed it became cloudy and a yellow green precipitate formed. The mixture was allowed to cool, and the resulting precipitate was collected by filtration. The solid was washed with acetonitrile (50 mL) and diethyl ether (100 mL). The chloride salt of the product was taken up in water and precipitated with acetonitrile / diethyl ether mixtures. The product was then recrystallised from hot water with a final yield of 12% as a white solid. The product was then taken up into water (50 mL) and ammonium hexafluorophosphate (3.0 g, 17.8 mmol) was slowly added. The exchange reaction was stirred for 16 hours to allow full conversion to occur. The PF_6^- salt form of the product precipitated out as it formed as a white solid. ^1H NMR of chloride salt (D_2O , 400MHz) δ : 8.89 (4H, d, J = 6.6 Hz), 8.64 (4H, d, J = 5.7 Hz), 8.29 (4H, d, J = 6.6 Hz), 7.77 (4H, d, J = 5.9 Hz), 7.47 (4H, s), 5.79 (4H, s).

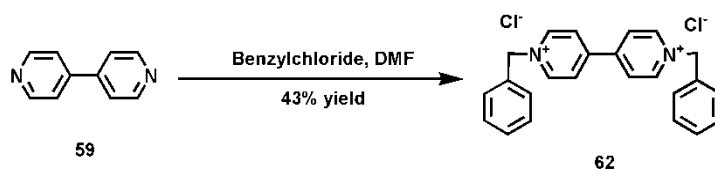
Cyclobis(paraquat-*p*-phenylene) Tetrakis(hexafluorophosphate)
(CBPQT⁴⁺) (61).^[9]



To a solution of **60** (706 mg, 1 mmol) in dry DMF (50 mL) was added α, α' -dibromo-*p*-xylene (264 mg, 1 mmol) and 1,5-Bis (2,2-methoxy ethoxy ethoxy) naphthalene (**17b**) (1,100 mg, 3 mmol). The reaction mixture was stirred at room temperature under an atmosphere of nitrogen for 5 days. The solvent was removed by reduced pressure to yield the crude product as a dark purple solid. The material was taken up into aqueous ammonium chloride (1 M, 100 mL) and was continuously extracted with DCM for two days. Once the layers had become colourless the aqueous layer was separated and the solvent removed *in vacuo*. The product was purified by silica column chromatography, eluting with 60% methanol: 30% water and 10% saturated ammonium chloride solution. The clean product was taken up in water and ammonium hexafluorophosphate was added until complete precipitation had occurred. The solid was collected by filtration and then washed with water and diethyl ether to recover the product as the PF_6^- salt in a 60% yield.^[9]

¹H NMR (400 MHz, CD₃CN) δ : 5.74 (s, 8H), 7.52 (s, 8H), 8.14-8.18 (m, 8H), 8.84-8.88 (m, 8H); ¹³C NMR (400 MHz, CD₃CN) δ : 65.7, 128.3, 131.4, 137.0, 146.2, 150.4

N,N'-dibenzyl-4,4'-dipyridinium dichloride (65).



To a solution of benzyl chloride (13.6 mL, 118 mmol) in DMF (30 mL) at 100° C was added dropwise a solution of 4,4'-bipyridine (500 mg, 3 mmol) in DMF. The reaction mixture was refluxed for 24 hours. The mixture was allowed to cool, collecting the precipitate formed by filtration, washing with hot diethyl ether (30 mL). The solid was re-crystallised from hot ethanol to remove a single impurity from the solid (533 mg) in a 43% yield

¹H NMR D₂O, δ : 8.95 (4H, d, *J* = 6.3 Hz, 4x CH), 8.32 (4H, d, *J* = 6.2 Hz, 4x CH), 7.33 (10H, s, 10xCH), 5.73 (4H, s, 2x CH₂). ¹³C NMR δ : 145.5 (QC), 130.1 (QC), 129.7 (CH Aryl), 129.2 (CH Aryl), 127.0 (CH Aryl), 126.1 (CH Aryl), 64.8 (CH₂ Alkyl). Mass spectrum : [M] = 338 (may be due to charge delocalisation)

9. References.

- [1] J. M. Lehn, *Science (Washington, D. C., 1883-)* **1993**, *260*, 1762-1763.
- [2] in *McGraw-Hill Dictionary of Scientific and Technical Terms*, 6th ed., McGraw-Hill Company Incorporated, **2002**, p. 183.
- [3] J.-M. Lehn, *Angewandte Chemie International Edition in English* **1988**, *27*, 89-112.
- [4] D. J. Cram, *Angewandte Chemie International Edition in English* **1988**, *27*, 1009-1020.
- [5] P. D. Beer, P. A. Gale, D. K. Smith, *Supramolecular Chemistry Oxford Chemistry Primer*, Oxford Science Publications, **1999**.
- [6] J. W. Steed, J. L. Atwood, *Supramolecular Chemistry*, 2nd ed., John Wiley and Sons Limited, **2009**.
- [7] J. Clayden, N. Greeves, S. Warren, P. Wothers, *Organic Chemistry*, 3rd ed., Oxford University Press, **2001**.
- [8] R. A. Kelln, J. R. Gear, *BioScience* **1980**, *30*, 110.
- [9] M. Asakawa, W. Dehaen, G. L'Abbé, S. Menzer, J. Nouwen, F. M. Raymo, J. F. Stoddart, D. J. Williams, *The Journal of Organic Chemistry* **1996**, *61*, 9591-9595.
- [10] P. L. Anelli, P. R. Ashton, N. Spencer, A. M. Z. Slawin, J. F. Stoddart, D. J. Williams, *Angew. Chem.-Int. Edit. Engl.* **1991**, *30*, 1036-1039.
- [11] Y.-L. Zhao, A. K. Shveyd, J. F. Stoddart, *Tetrahedron Letters* **2011**, *52*, 2044-2047.
- [12] R. Wolf, M. Asakawa, P. R. Ashton, M. Gomez-Lopez, C. Hamers, S. Menzer, I. W. Parsons, N. Spencer, J. F. Stoddart, M. S. Tolley, D. J. Williams, *Angew. Chem., Int. Ed.* **1998**, *37*, 975-979.
- [13] P. R. Ashton, R. Ballardini, V. Balzani, S. E. Boyd, A. Credi, M. T. Gandolfi, M. Gomez-Lopez, S. Iqbal, D. Philp, J. A. Preece, L. Prodi, H. G. Ricketts, J. F. Stoddart, M. S. Tolley, M. Venturi, A. J. P. White, D. J. Williams, *Chem.--Eur. J.* **1997**, *3*, 152-170.
- [14] M. Hmadeh, A. C. Fahrenbach, S. Basu, A. Trabolsi, D. Benítez, H. Li, A.-M. Albrecht-Gary, M. Elhabiri, J. F. Stoddart, *Chemistry – A European Journal* **2011**, *17*, 6076-6087.
- [15] Y. Liu, A. H. Flood, J. F. Stoddart, *J. Am. Chem. Soc.* **2004**, *126*, 9150-9151.
- [16] D. Philp, A. M. Z. Slawin, N. Spencer, J. F. Stoddart, D. J. Williams, *Journal of the Chemical Society, Chemical Communications* **1991**, 1584-1586.
- [17] Y. Liu, A. H. Flood, P. A. Bonvallet, S. A. Vignon, B. H. Northrop, H.-R. Tseng, J. O. Jeppesen, T. J. Huang, B. Brough, M. Baller, S. Magonov, S. D. Solares, W. A. Goddard, C.-M. Ho, J. F. Stoddart, *J. Am. Chem. Soc.* **2005**, *127*, 9745-9759.
- [18] P. L. Anelli, P. R. Ashton, R. Ballardini, V. Balzani, M. Delgado, M. T. Gandolfi, T. T. Goodnow, A. E. Kaifer, D. Philp, a. et, *J. Am. Chem. Soc.* **1992**, *114*, 193-218.
- [19] P. R. Ashton, V. Balzani, J. Becher, A. Credi, M. C. T. Fyfe, G. Mattersteig, S. Menzer, M. B. Nielsen, F. M. Raymo, J. F. Stoddart, M. Venturi, D. J. Williams, *J. Am. Chem. Soc.* **1999**, *121*, 3951-3957.
- [20] V. V. Strelets, I. A. Mamedjarova, M. N. Nefedova, N. I. Pysnograeva, V. I. Sokolov, L. Pospisil, J. Hanzlik, *Journal of Electroanalytical Chemistry* **1991**, *310*, 179-186.
- [21] A. Harada, Y. Hu, S. Yamamoto, S. Takahashi, *Journal of the Chemical Society, Dalton Transactions* **1988**, 729-732.
- [22] W. Zhang, M. Chen, G. W. Diao, *Electrochim. Acta* **2011**, *56*, 5129-5136.

- [23] A. Harada, *Accounts of Chemical Research* **2001**, *34*, 456-464.
- [24] M. R. de Jong, J. F. J. Engbersen, J. Huskens, D. N. Reinhoudt, *Chemistry – A European Journal* **2000**, *6*, 4034-4040.
- [25] G. J. Ashwell, B. Urasinska, C. Wang, M. R. Bryce, I. Grace, C. J. Lambert, *Chemical Communications* **2006**, 4706-4708.
- [26] M. E. N.P.R.A. Silva, A. J. L. Pombeiro, J. J. R. Fraústo da Silva, R. Herrmann, N. Deus, R. E. Bozak, *Journal of Organometallic Chemistry* **1994**, *480*, 81-90.
- [27] M. Elango, R. Parthasarathi, G. K. Narayanan, A. M. Sabeelullah, U. Sarkar, N. S. Venkatasubramanian, V. Supramanian, P. K. Chattaraj, *Journal of Chemical Sciences* **2005**, *117*, 61-65.
- [28] S. R. Bayly, P. D. Beer, G. Z. Chen, in *Ferrocenes*, John Wiley & Sons, Ltd, **2008**, pp. 281-318.
- [29] P. D. Beer, P. A. Gale, G. Z. Chen, *Journal of the Chemical Society-Dalton Transactions* **1999**, 1897-1909.
- [30] A. Harada, S. Takahashi, *Journal of Inclusion Phenomena* **1984**, *2*, 791-798.
- [31] W. S. Jeon, K. Moon, S. H. Park, H. Chun, Y. H. Ko, J. Y. Lee, E. S. Lee, S. Samal, N. Selvapalam, M. V. Rekharsky, V. Sindelar, D. Sobransingh, Y. Inoue, A. E. Kaifer, K. Kim, *J. Am. Chem. Soc.* **2005**, *127*, 12984-12989.
- [32] R. Isnin, C. Salam, A. E. Kaifer, *The Journal of Organic Chemistry* **1991**, *56*, 35-41.
- [33] M. V. Rekharsky, T. Mori, C. Yang, Y. H. Ko, N. Selvapalam, H. Kim, D. Sobransingh, A. E. Kaifer, S. Liu, L. Isaacs, W. Chen, S. Moghaddam, M. K. Gilson, K. Kim, Y. Inoue, *Proc. Natl. Acad. Sci. U. S. A.* **2007**, *104*, 20737-20742.
- [34] Y. Chen, Y.-M. Zhang, Y. Liu, *Israel Journal of Chemistry* **2011**, *51*, 515-524.
- [35] Q. Liu, W. Ye, N. Hu, H. Cai, H. Yu, P. Wang, *Biosensors and Bioelectronics* **2010**, *26*, 1672-1678.
- [36] T. M. Canh, *Biosensors, Vol. 1*, Chapman and Hall, **1993**.
- [37] P. Arora, A. Sindhu, N. Dilbaghi, A. Chaudhury, *Biosensors & bioelectronics* **2011**, *28*, 1-12.
- [38] M. G. Baek, R. C. Stevens, D. H. Charych, *Bioconjugate Chemistry* **2000**, *11*, 777-788.
- [39] D. J. Ahn, J.-M. Kim, *Acc. Chem. Res.* **2008**, *41*, 805-816.
- [40] K. Kam-Wing Lo, J. Shing-Yip Lau, D. Chun-Ming Ng, N. Zhu, *Journal of the Chemical Society, Dalton Transactions* **2002**, 1753-1756.
- [41] B. Geiger, A. Bershadsky, R. Pankov, K. M. Yamada, *Nat Rev Mol Cell Biol* **2001**, *2*, 793-805.
- [42] K. Burridge, M. ChrzanowskaWodnicka, *Annu. Rev. Cell Dev. Biol.* **1996**, *12*, 463-518.
- [43] K. Burridge, G. Nuckolls, C. Otey, F. Pavalko, K. Simon, C. Turner, *Cell Differentiation and Development* **1990**, *32*, 337-342.
- [44] G. McPhee, M. Dalby, M. Riehle, H. Yin, *Medical and Biological Engineering and Computing* **2010**, *48*, 1043-1053.
- [45] A. Curtis, C. Wilkinson, *Biomaterials* **1997**, *18*, 1573-1583.
- [46] S. Affrossman, M. Stamm, *Macromolecules* **1998**, *31*, 6280-6288.
- [47] S. Affrossman, G. Henn, S. A. O'Neill, R. A. Pethrick, M. Stamm, *Macromolecules* **1996**, *29*, 5010-5016.
- [48] B. G. Keselowsky, D. M. Collard, A. J. A. J. García, *Biomaterials* **2004**, *25*, 5947-5954.
- [49] C. D. W. Wilkinson, M. Riehle, M. Wood, J. Gallagher, A. S. G. Curtis, *Materials Science and Engineering: C* **2002**, *19*, 263-269.

- [50] B. G. Keselowsky, D. M. Collard, A. J. Garcia, *Proc. Natl. Acad. Sci. U. S. A.* **2005**, *102*, 5953-5957.
- [51] N. Faucheux, R. Schweiss, K. Lützwow, C. Werner, T. Groth, *Biomaterials* **2004**, *25*, 2721-2730.
- [52] M. Mrksich, G. M. Whitesides, *Annu. Rev. Biophys. Biomol. Struct.* **1996**, *25*, 55-78.
- [53] X. Jiang, R. Ferrigno, M. Mrksich, G. M. Whitesides, *J. Am. Chem. Soc.* **2003**, *125*, 2366-2367.
- [54] M. N. Yousaf, B. T. Houseman, M. Mrksich, *Angew. Chem.-Int. Edit.* **2001**, *40*, 1093-+.
- [55] W.-S. Yeo, M. N. Yousaf, M. Mrksich, *J. Am. Chem. Soc.* **2003**, *125*, 14994-14995.
- [56] C. D. Hodneland, M. Mrksich, *J. Am. Chem. Soc.* **2000**, *122*, 4235-4236.
- [57] A. Chandekar, S. K. Sengupta, J. E. Whitten, *Applied Surface Science* **2010**, *256*, 2742-2749.
- [58] A. Velázquez-Campoy, H. Ohtaka, A. Nezami, S. Muzammil, E. Freire, *Isothermal Titration Calorimetry*, John Wiley & Sons, Inc., **2001**.
- [59] T. Wiseman, S. Williston, J. F. Brandts, L. N. Lin, *Anal. Biochem.* **1989**, *179*, 131-137.
- [60] support@microcalorimetry.com/VP_ITC_Manual.
- [61] support@microcalorimetry.com/Tutorial_Guide.
- [62] T. Wiseman, S. Williston, J. F. Brandts, L.-N. Lin, *Analytical Biochemistry* **1989**, *179*, 131-137.
- [63] D. H. Evans, K. M. Oconnell, R. A. Petersen, M. J. Kelly, *Journal of Chemical Education* **1983**, *60*, 290-293.
- [64] C. M. A. Brett, A. M. O. Brett, *Electrochemistry: Principles, Methods and Applications*, Oxford University Press, **1993**.
- [65] S. P. Kounaves, *Handbook of Instrumental Techniques for Analytical Chemistry*, Tufts University, Department of Chemistry.
- [66] S. Shippy, M.-J. Lu, *Cyclic Voltammetry: An Example of Voltaic Methods*, **2007**.
- [67] Malvern.co.uk.
- [68] http://en.wikipedia.org/wiki/Ultraviolet%E2%80%93visible_spectroscopy.
- [69] D. H. Williams, I. Fleming, *Spectroscopic Methods in Organic Chemistry 5th edition*, McGraw-Hill, London, **1995**.
- [70] http://en.wikipedia.org/wiki/Fluorescence_spectroscopy.
- [71] <http://scienceworld.wolfram.com/physics/Fluorescence.html>.
- [72] <http://www.bioch.ox.ac.uk/aspsite/services/equipmentbooking/biophysics/introfluor.pdf>.
- [73] A. D. C. Parenty, L. V. Smith, K. M. Guthrie, D.-L. Long, J. Plumb, R. Brown, L. Cronin, *J. Med. Chem.* **2005**, *48*, 4504-4506.
- [74] A. D. C. Parenty, K. M. Guthrie, Y.-F. Song, L. V. Smith, E. Burkholder, L. Cronin, *Chem. Commun. (Cambridge, U. K.)* **2006**, 1194-1196.
- [75] M. Janovská, M. Kubala, V. Šimánek, J. Ulrichová, *Analytical and Bioanalytical Chemistry* **2009**, *395*, 235-240.
- [76] Z. Dvorak, I. Sovadinova, L. Blaha, J. P. Giesy, J. Ulrichova, *Food Chem. Toxicol.* **2006**, *44*, 1466-1473.
- [77] A. D. C. Parenty, L. V. Smith, A. L. Pickering, D.-L. Long, L. Cronin, *J. Org. Chem.* **2004**, *69*, 5934-5946.
- [78] K. M. Guthrie, A. D. C. Parenty, L. V. Smith, L. Cronin, A. Cooper, *Biophys. Chem.* **2007**, *126*, 117-123.

- [79] L. V. Smith, A. D. C. Parenty, K. M. Guthrie, J. Plumb, R. Brown, L. Cronin, *ChemBioChem* **2006**, *7*, 1757-1763.
- [80] G. J. T. Cooper, A. G. Boulay, P. J. Kitson, C. Ritchie, C. J. Richmond, J. Thiel, D. Gabb, R. Eadie, D.-L. Long, L. Cronin, *J. Am. Chem. Soc.* **2011**, *133*, 5947-5954.
- [81] C. Ritchie, G. J. T. Cooper, Y.-F. Song, C. Streb, H. Yin, A. D. C. Parenty, D. A. MacLaren, L. Cronin, *Nat Chem* **2009**, *1*, 47-52.
- [82] G. J. T. Cooper, L. Cronin, *J. Am. Chem. Soc.* **2009**, *131*, 8368-8369.
- [83] P. A. Wender, J. C. Horan, *Org. Lett.* **2006**, *8*, 4581-4584.
- [84] H.-R. Tseng, S. A. Vignon, J. F. Stoddart, *Angewandte Chemie International Edition* **2003**, *42*, 1491-1495.
- [85] H. R. Drew, R. M. Wing, T. Takano, C. Broka, S. Tanaka, K. Itakura, R. E. Dickerson, *Proc. Natl. Acad. Sci. U. S. A.* **1981**, *78*, 2179-2183.
- [86] M. Bria, G. Cooke, A. Cooper, J. F. Garety, S. G. Hewage, M. Nutley, G. Rabani, P. Woisel, *Tetrahedron Letters* **2007**, *48*, 301-304.
- [87] A. Credi, M. Montalti, V. Balzani, S. J. Langford, F. M. Raymo, J. Fraser Stoddart, *New Journal of Chemistry* **1998**, *22*, 1061-1065.
- [88] V. Balzani, A. Credi, M. Venturi, in *Molecular Devices and Machines*, Wiley-VCH Verlag GmbH & Co. KGaA, **2008**, pp. 401-451.
- [89] A. Hakura, Y. Tsutsui, H. Mochida, Y. Sugihara, T. Mikami, F. Sagami, *Mutation Research/Genetic Toxicology* **1996**, *371*, 293-299.
- [90] Scientific Committee on Consumer Products.
- [91] J. Sánchez-Cortés, K. Bähr, M. Mrksich, *J. Am. Chem. Soc.* **2010**, *132*, 9733-9737.
- [92] M. Mohorcic, I. Jerman, M. Zorko, L. Butinar, B. Orel, R. Jerala, J. Friedrich, *J. Mater. Sci.-Mater. Med.* **2010**, *21*, 2775-2782.
- [93] L. Cardoso, M. Araujo, A. Goes, L. Pacifico, R. Oliveira, S. Oliveira, *Microbial Cell Factories* **2007**, *6*, 1.
- [94] S. Mehdipour-Ataei, S. Babanzadeh, *Applied Organometallic Chemistry* **2007**, *21*, 360-367.
- [95] N. Svenstrup, K. M. Rasmussen, T. K. Hansen, J. Becher, *Synthesis* **1994**, *1994*, 809,812.
- [96] J. Garín, J. Orduna, S. Uriel, A. J. Moore, M. R. Bryce, S. Wegener, D. S. Yufit, J. A. K. Howard, *Synthesis* **1994**, *1994*, 489,493.
- [97] G. Cooke, V. M. Rotello, A. Radhi, *Tetrahedron Letters* **1999**, *40*, 8611-8613.
- [98] G. Cooke, J. F. Garety, S. G. Hewage, G. Rabani, V. M. Rotello, P. Woisel, *Chemical Communications* **2006**, 4119-4121.
- [99] S. Okada, S. Peng, W. Spevak, D. Charych, *Acc. Chem. Res.* **1998**, *31*, 229-239.
- [100] W. Spevak, J. O. Nagy, D. H. Charych, *Adv. Mater. (Weinheim, Ger.)* **1995**, *7*, 85-89.
- [101] M. A. Reppy, B. A. Pindzola, *Chem. Commun. (Cambridge, U. K.)* **2007**, 4317-4338.
- [102] Z. Yuan, C.-W. Lee, S.-H. Lee, *Angewandte Chemie International Edition* **2004**, *43*, 4197-4200.
- [103] J. Lee, H. Jun, J. Kim, *Advanced Materials* **2009**, *21*, 3674-3677.
- [104] X. Sun, T. Chen, S. Huang, L. Li, H. Peng, *Chemical Society Reviews* **2010**, *39*, 4244-4257.
- [105] D. Charych, Q. Cheng, A. Reichert, G. Kuziemko, M. Stroh, J. O. Nagy, W. Spevak, R. C. Stevens, *Chemistry & Biology* **1996**, *3*, 113-120.
- [106] X. Yu, Y. Luo, W. Wu, Q. Yan, G. Zou, Q. Zhang, *European Polymer Journal* **2008**, *44*, 3015-3021.
- [107] E.-K. Ji, D. J. Ahn, J.-M. Kim, *Bull. Korean Chem. Soc.* **2003**, *24*, 667-670.

- [108] http://www.sigmaaldrich.com/catalog/ProductDetail.do?lang=en&N4=C2485|SIGMA&N5=SEARCH_CONCAT_PNO|BRAND_KEY&F=SPEC.
- [109] A. Cifuentes, J. L. Bernal, J. C. Diez-Masa, *Analytical Chemistry* **1997**, *69*, 4271-4274.
- [110] <http://www.thefreedictionary.com/surfactant>.
- [111] F. Z. Sosa, S. C. Padron, S. C. Mahugo, R. J. J. Santana, *TrAC, Trends Anal. Chem.* **2004**, *23*, 469-479.
- [112] M. Sharon, L. L. Ilag, C. V. Robinson, *J. Am. Chem. Soc.* **2007**, *129*, 8740-8746.
- [113] A. J. Hagen, T. A. Hatton, D. I. C. Wang, *Biotechnol. Bioeng.* **1990**, *35*, 955-965.
- [114] T. R. Kommuru, B. Gurley, M. A. Khan, I. K. Reddy, *International Journal of Pharmaceutics* **2001**, *212*, 233-246.
- [115] B.-H. Sohn, J.-M. Choi, S. I. Yoo, S.-H. Yun, W.-C. Zin, J. C. Jung, M. Kanehara, T. Hirata, T. Teranishi, *J. Am. Chem. Soc.* **2003**, *125*, 6368-6369.
- [116] S. I. Yoo, B.-H. Sohn, W.-C. Zin, S.-J. An, G.-C. Yi, *Chem. Commun. (Cambridge, U. K.)* **2004**, 2850-2851.
- [117] Y. He, T. P. Lodge, *J. Am. Chem. Soc.* **2006**, *128*, 12666-12667.
- [118] Y. He, Z. Li, P. Simone, T. P. Lodge, *J. Am. Chem. Soc.* **2006**, *128*, 2745-2750.
- [119] M. R. Bryce, G. Cooke, A. S. Dhindsa, D. Lorcy, A. J. Moore, M. C. Petty, M. B. Hursthouse, A. I. Karaulov, *Journal of the Chemical Society, Chemical Communications* **1990**, 816-818.
- [120] J. S. Nowick, O. Khakshoor, M. Hashemzadeh, J. O. Brower, *Organic Letters* **2003**, *5*, 3511-3513.
- [121] J. Louisy, F. Delattre, J. Lyskawa, A. Malfait, C. E. Maclean, L. Sambe, N. Zhu, G. Cooke, P. Woisel, *Chemical Communications* **2011**, *47*, 6819-6821.
- [122] J. M. Chalker, G. J. L. Bernardes, Y. A. Lin, B. G. Davis, *Chem.--Asian J.* **2009**, *4*, 630-640.
- [123] M. Kato, M. Mrksich, *J. Am. Chem. Soc.* **2004**, *126*, 6504-6505.
- [124] G. Zaupa, P. Scrimin, L. J. Prins, *J Am Chem Soc* **2008**, *130*, 5699-5709.
- [125] H. Greg T, in *Bioconjugate Techniques (Second Edition)*, Academic Press, New York, **2008**, pp. 1-168.
- [126] K. L. Heredia, H. D. Maynard, *Org. Biomol. Chem.* **2007**, *5*, 45-53.
- [127] K. L. Heredia, D. Bontempo, T. Ly, J. T. Byers, S. Halstenberg, H. D. Maynard, *J. Am. Chem. Soc.* **2005**, *127*, 16955-16960.
- [128] X. F. Han, L. Soblosky, M. Slutsky, C. M. Mello, Z. Chen, *Langmuir* **2011**, *27*, 7042-7051.
- [129] D. S. Dime, Toronto Research Chemicals Inc., North York, Ontario, **1997**.
- [130] Y. J. Zhao, Y. Q. Zhai, Z. G. Su, G. H. Ma, *Polym. Adv. Technol.* **2010**, *21*, 867-873.
- [131] <http://www.medicinenet.com/neutropenia/article.htm>.
- [132] H. Greg T, in *Bioconjugate Techniques (Second Edition)*, Academic Press, New York, **2008**, pp. 169-212.
- [133] M. L. Nielsen, M. Vermeulen, T. Bonaldi, J. Cox, L. Moroder, M. Mann, *Nat. Methods* **2008**, *5*, 459-460.
- [134] E. S. Boja, H. M. Fales, *Analytical Chemistry* **2001**, *73*, 3576-3582.
- [135] N. Lundell, T. Schreitmüller, *Analytical Biochemistry* **1999**, *266*, 31-47.
- [136] B. Karlen, B. Lindeke, S. Lindgren, K. G. Svensson, R. Dahlbom, D. J. Jenden, J. E. Giering, *J. Med. Chem.* **1970**, *13*, 651-657.
- [137] J.-M. Barbe, G. Canard, S. Brandes, R. Guillard, *Eur. J. Org. Chem.* **2005**, 4601-4611.
- [138] T. T. Goodnow, M. V. Reddington, J. F. Stoddart, A. E. Kaifer, *J. Am. Chem. Soc.* **1991**, *113*, 4335-4337.

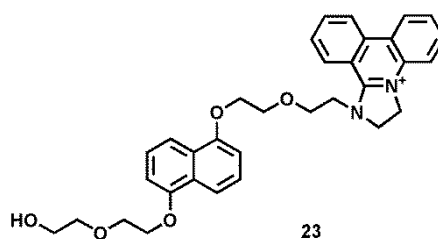
- [139] M. Kuragaki, M. Sisido, *Bull. Chem. Soc. Jpn.* **1997**, *70*, 261-265.
- [140] R. P. Haugland, W. W. You, *Vol. 418*, **2007**, pp. 13-23.
- [141] A. Chilkoti, P. S. Stayton, *J. Am. Chem. Soc.* **1995**, *117*, 10622-10628.
- [142] S. Repo, T. A. Paldanius, Vesa P. Hytönen, T. K. M. Nyholm, Katrin K. Halling, J. Huuskonen, Olli T. Pentikäinen, K. Rissanen, J. P. Slotte, T. T. Airene, T. A. Salminen, Markku S. Kulomaa, Mark S. Johnson, *Chemistry & Biology* **2006**, *13*, 1029-1039.
- [143] F. J. Munoz, A. Rumbero, J. V. Sinisterra, J. I. Santos, S. Andre, H.-J. Gabius, J. Jimenez-Barbero, M. J. Hernaiz, *Glycoconjugate J.* **2008**, *25*, 633-646.
- [144] Y. Mori, K. Minamihata, H. Abe, M. Goto, N. Kamiya, *Organic & Biomolecular Chemistry* **2011**, *9*, 5641-5644.
- [145] Y. P. Timalisina, J. Branen, D. E. Aston, K. Noren, G. Corti, R. Schumacher, D. N. McIlroy, *Journal of Applied Physics* **2011**, *110*.
- [146] S. T. Caldwell, G. Cooke, A. Cooper, M. Nutley, G. Rabani, V. Rotello, B. O. Smith, P. Woisel, *Chemical Communications* **2008**, 2650-2652.
- [147] P. R. Ashton, M. Gomez-Lopez, S. Iqbal, J. A. Preece, J. F. Stoddart, *Tetrahedron Lett.* **1997**, *38*, 3635-3638.
- [148] V. Hytonen, J. Maatta, T. Nyholm, O. Livnah, Y. Eisenberg-Domovich, D. Hyre, H. Nordlund, J. Horha, E. Niskanen, T. Paldanius, T. Kulomaa, E. Porkka, P. Stayton, O. Laitinen, M. Kulomaa, *J Biol Chem* **2005**, *280*, 10228 - 10233.
- [149] D. B. Amabilino, P. R. Ashton, M. S. Tolley, J. F. Stoddart, D. J. Williams, *Angew. Chem.-Int. Edit. Engl.* **1993**, *32*, 1297-1301.
- [150] C. P. Collier, J. O. Jeppesen, Y. Luo, J. Perkins, E. W. Wong, J. R. Heath, J. F. Stoddart, *J. Am. Chem. Soc.* **2001**, *123*, 12632-12641.
- [151] O. Š. Miljanić, W. R. Dichtel, S. I. Khan, S. Mortezaei, J. R. Heath, J. F. Stoddart, *J. Am. Chem. Soc.* **2007**, *129*, 8236-8246.
- [152] in *Organic Synthesis Collections, Vol. 43*, Organic Synthesis Collections, **1963**, p. 6; in *Organic Synthesis Collection, Vol. 5*, Organic Synthesis Collection, **1973**, p. 121.
- [153] A. Faust, B. Waschkau, J. Waldeck, C. Hoeltke, H.-J. Breyholz, S. Wagner, K. Kopka, W. Heindel, M. Schaefer, C. Bremer, *Bioconjugate Chem.* **2008**, *19*, 1001-1008.
- [154] A. Star, Y. Liu, K. Grant, L. Ridvan, J. F. Stoddart, D. W. Steurman, M. R. Diehl, A. Boukai, J. R. Heath, *Macromolecules* **2003**, *36*, 553-560.
- [155] L. L. Crowe, K. M. Solntsev, L. M. Tolbert, *Langmuir* **2007**, *23*, 6227-6232.
- [156] L. Deng, L. Wang, J. Huo, Q. Tan, Q. Yang, H. Yu, H. Gao, J. Wang, *The Journal of Physical Chemistry B* **2008**, *112*, 5333-5337.

Appendices

Appendix 1.

Experimental Procedures for the synthesis of the functionalised DIPs **23** and **30**.

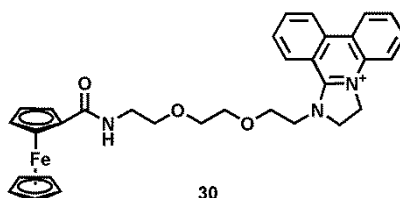
1-[2-(2-{5-[2-(2-Hydroxy-ethoxy)-ethoxy]-naphthalen-1-yloxy}-ethoxy)-ethyl]-2,3-dihydro-1H-imidazo[1,2-f]phenanthridin-4-ylum; bromide (23).



To a solution of **5a** (100 mg, 0.30 mmol, 1.0 eq) in 5% Na₂CO₃ (aq) (10 mL) and EtOAc (10 mL) was added of 5-(2-bromoethyl)-phenanthridinium bromide 110 mg, 0.30 mmol, 1.0 eq) and the reaction stirred under N₂ for 2 hrs. The reaction mixture was transferred to a separating funnel and layers were separated, the organic layer was washed with water (1 × 10 mL) and brine (1 × 10 mL). NBS (53 mg, 0.30 mmol, 1.0 eq) was added to the EtOAc solution and the reaction was stirred for 10 min, upon which a sticky brown residue formed on the reaction vessel walls. The Mother liquor was decanted off and acetone was added to the sticky residue, upon sonication a brown suspension formed which was collected by filtration to yield the product as a beige powder (**23**) (18 mg, 0.029 mmol, 9.7%). ¹H NMR (DMSO, 400 MHz) δ: 8.77 (d, 1H, *J*=8.0 Hz), 8.67 (d, 1H, *J*=8.0 Hz), 8.63 (d, 1H, *J*=8.0 Hz), 8.05 (t, 1H, *J*=8.0 Hz), 7.80 (t, 1H, *J*=8.0 Hz), 7.72 (t, 1H, *J*=8.0 Hz), 7.60 (t, 1H, *J*=8.0 Hz), 7.55 (d, 1H, *J*=8.0 Hz), 7.46 (m, 2H), 7.27 (t, 1H, *J*=8.0

Hz), 7.06 (t, 1H, $J=8.0$ Hz), 6.92 (d, 1H, $J=8.0$ Hz), 6.75 (d, 1H, $J=8.0$ Hz), 4.69 (t, 1H, $J=5.2$ Hz), 4.52 (t, 2H, $J=10.6$ Hz), 4.32 (t, 2H, $J=10.6$ Hz), 4.29 (t, 4H, $J=4.2$ Hz), 4.13 (m, 4H), 4.03 (m, 2H), 3.87 (m, 2H), 3.58 (m, 4H); ^{13}C NMR (CDCl_3 , 100 MHz) δ : 154.27 (C), 154.01 (C), 135.37 (C), 135.04 (CH), 132.7 (C), 132.48 (C), 131.36 (CH), 128.70 (CH), 128.45 (CH), 126.23 (C), 126.36 (C), 125.46(CH), 125.09 (CH), 124.96 (CH), 123.44 (CH), 123.28 (CH), 120.27 (C), 115.59 (CH), 114.43 (CH), 113.75 (CH), 105.65 (CH), 105.3 (CH), 72.69 (CH_2), 70.14 (CH_2), 69.69 (CH_2), 67.74 (CH_2), 67.51 (CH_2), 67.12 (CH_2), 61.79 (CH_2), 51.77 (CH_2), 51.45 (CH_2), 46.56 (CH_2). IR (KBr, cm^{-1}) 3327 (w), 2870 (w), 1575 (s), 1415 (m), 1265 (s), 1066 (s), 773 (s); MS (FAB) m/z (%) 539.3 (M^+) (100); HRMS (FAB) for (M^+) calcd 539.2546, obsd 539.2551.

1-{2-[2-(2-ferrocenoylamino-ethoxy)-ethoxy]-ethyl}-2,3-dihydro-1H-imidazo[1,2-f]phenanthridin-4-ylum bromide (30).



To a solution of **25a** (868 mg, 2.32 mmol, 1.0 eq) in DMF (100 mL) was added Triethylamine (970 μL , 6.97 mmol, 3.0 eq) followed by 5-(2-Bromo-ethyl)-phenanthridinium bromide (1.702 g, 4.64 mmol, 2.0 eq) and the reaction was stirred under N_2 for 3 days. The reaction mixture was added to Et_2O (400 mL) and the precipitate was filtered under vacuum, washing the residue thoroughly with Et_2O . Trituration of the residue with acetone and drying under vacuum afforded a pale brown powder (**30**), (1.118 g, 1.61 mmol, 69.4%). Mpt 180-183 $^\circ\text{C}$ (degrad); ^1H NMR (CDCl_3 , 400 MHz) δ : 8.61 (d, 1H, $J=8.0$ Hz), 8.59 (d, 1H, $J=8.0$ Hz), 8.42 (d, 1H, $J=8.0$ Hz), 8.05 (t, 1H, $J=8.0$ Hz), 7.78 (t, 2H, $J=8.0$ Hz), 7.61 (t, 1H,

$J=8.0$ Hz), 7.49 (d, 1H, $J=8.0$ Hz), 7.14 (brd, 1H), 4.89 (t, 2H, $J=11.2$ Hz), 4.84 (s, 3H), 4.82 (t, 2H, $J=11.2$ Hz), 4.52 (t, 2H, $J=4.5$ Hz), 4.17 (s, 5H), 4.15 (s, 3H), 3.81 (m, 2H), 3.71 (m, 4H), 3.58 (dt, 2H, $J=5.0, 5.6$ Hz); ^{13}C NMR (CDCl_3 , 100 MHz) δ : 171.03 (C), 154.08 (C), 135.56 (C), 135.41 (CH), 132.72 (C), 131.71 (CH), 129.09 (CH), 128.18 (CH), 125.78 (CH), 123.79 (CH), 123.47 (CH), 120.34 (C), 115.75 (CH), 115.48 (C), 75.76 (C), 70.85 (CH_2), 70.39 ($2\times\text{CH}$), 70.31 (CH_2), 69.87 (CH_2), 69.77 ($5\times\text{CH}$), 68.41 ($2\times\text{CH}$), 68.15 (CH_2), 51.54 (CH_2), 51.41 (CH_2), 46.70 (CH_2), 39.19 (CH_2); IR (cm^{-1}) 3319 (w), 2862 (w), 1624 (s), 1602 (s), 1579 (s), 1545 (s), 1313 (m), 1122 (s), 1033 (m); MS (FAB) m/z (%) 564.1 (M^+) (100); Anal. Calcd for $\text{C}_{32}\text{H}_{34}\text{BrFeN}_3\text{O}_3$ C, 59.65; H, 5.32; N, 6.52; Found C, 58.75; H, 5.27; N, 6.49; HRMS (FAB) for $(\text{C}_{32}\text{H}_{34}\text{BrFeN}_3\text{O}_3)^+$ calcd 564.1950, obsd 564.1953.

Appendix 2.

Standard procedures for using analytical equipment.

Isothermal Titration Calorimetry.

The calorimetric experiments were performed in aqueous media, at 25°C. Typically the cell contained the macromolecule at a concentration of ~0.05 mM relative to the binding sites available. The syringe contained ~0.7 mM solutions of the ligand required. The solutions were thoroughly degassed prior to use to remove air bubbles from solution as they cause interference in the spectrum when present.

Cyclic Voltammetry.

Voltammetry experiments were performed in aqueous media using 0.01 mM solutions of the conjugates with 0.1 M NaCl as the supporting electrolyte. Cyclic voltammograms (CV) were recorded using a CH Instrument Inc (Austin, TX, USA.), 440a EC Analyser, employing a glassy carbon (GC) electrode (diameter 3.1 mm). Voltammograms were referenced against an Ag / AgCl electrode.

UV-Vis Spectroscopy.

UV-Vis absorbance measurements were run on samples with a concentration of 10^{-3} to 10^{-5} M. For UV-Vis spectroscopy using a Perkin-Elmer LAMBDA 25 UV-Vis spectrometer, the use of two paired quartz cuvettes was required. Initially both cuvettes were filled with the solvent used and a background scan was run. After this the solvent was replaced with the sample required, and the UV-Vis spectrum recorded. The data collected was analysed using excel.

Fluorescence Spectroscopy.

Fluorescence emission measurements were run on samples with a concentration of 10^{-5} to 10^{-7} M. The sample in a clear quartz cuvette is run, where the excitation wavelength chosen is the λ_{Max} found from the UV-Vis. The spectrum recorded is saved as a txt file that can be opened in excel for analysis.

Appendix 3.

Cell Culture Protocols.

DMEM Complete.

400 mL DMEM Dulbeccos Modified Eagles.

100 mL Medium 199.

5 mL Sodium Pyruvate.

10 mL Antibiotic.

50 mL Foetal Bovine Serum.

Trypsin / Versine.

20 mL Versine.

0.5 mL Trypsin.

Fixative.

10 mL Formaldehyde.

90 mL PBS.

2 g Sucrose.

Directions for 24 well plate.

Remove media then wash cells with PBS (2x ~1 mL / well).

Add fixative (~0.5 mL / well) and leave for 20 minutes.

Rinse with PBS (2x ~1 mL / well).

Store at 4°C in PBS until use.

Appendix 3 continued

Permeablising buffer.

10.3 g Sucrose.

0.29 g NaCl.

0.06 g MgCl₂·6H₂O.

0.47 g HEPES in 100 mL PBS.

0.5 mL Triton X.

Adjust to pH 7.2.

Directions for 24 well plate.

After fixing.

Remove PBS and add permeablising buffer (~0.5 mL / well) and leave to soak for 20 minutes.

Wash with PBS (2x 1 mL / well).

Store at 4°C in PBS until use.

Appendix 3 continued.

MTT.

Thiazoyl Blue Tetrazolium Bromide. 0.5 mg/ml in PBS.

Store in the dark at 4°C.

Directions for a 24 well plate.

Seed cells into plate and incubate until suitable confluency has been reached. (in triplicate for treatment group and control)

Add treatment and incubate for the desired time period.

Wash with PBS (2x ~1 mL) to remove media and treatment material.

Add 300 µL MTT per well.

Incubate at 37°C for 1.5 hours.

Remove MTT and add 150 µl DMSO, leave for 10 minutes.

Pipette into 96 well plate.

Place in plate reader at 550 nm.

Appendix 3 continued.

Coomassie Blue.

1.25 g Coomassie 'Bright' blue R-250.

50 mL Glacial acetic acid.

225 mL Methanol.

225 mL Reverse osmosis water.

Mix together the coomassie blue, methanol, acetic acid and water, allow to stand for 30 minutes and then filter through a No. 1 filter paper.

Directions for 24 well plate.

After fixing.

Add coomassie blue solution (1 mL / well) and leave to soak for 20 minutes.

Remove stain.

Wash with destain (10% glacial acetic acid, 10% methanol in water.) and leave 5 minutes per wash (3x 1 mL / well).

Rinse with water (3x ~1 mL / well).

Store in PBS at 4°C.

Appendix 3 continued

Staining with antibodies.

Rinse cells with PBS x1.

Fix cells for 15 minutes at 37°C.

Remove fixative add permeablising buffer and incubate at 5 minutes.

Remove buffer and add PBS/BSA and incubate for 5 minutes at 37°C.

Remove buffer and add primary antibody with phalloidin. Wrap in foil and incubate at 37°C for 1 hour.

Remove antibody and wash with PBS/Tween x3.

Remove PBS/Tween and add secondary antibody. Wrap in foil and incubate at 37°C for 1 hour.

Remove antibody and wash with PBS/Tween x3.

Remove PBS/Tween and add. Wrap in foil and incubate for 30 minutes.

Remove streptavidin-FITC and wash with PBS/Tween x3.

Place a small drop of vectorshield-DAPI on a labelled microscope slide and invert the coverslip onto the drop of vectorshield.

Seal with a drop of clear nail varnish.

Store in foil at 4°C until required for viewing under a microscope.

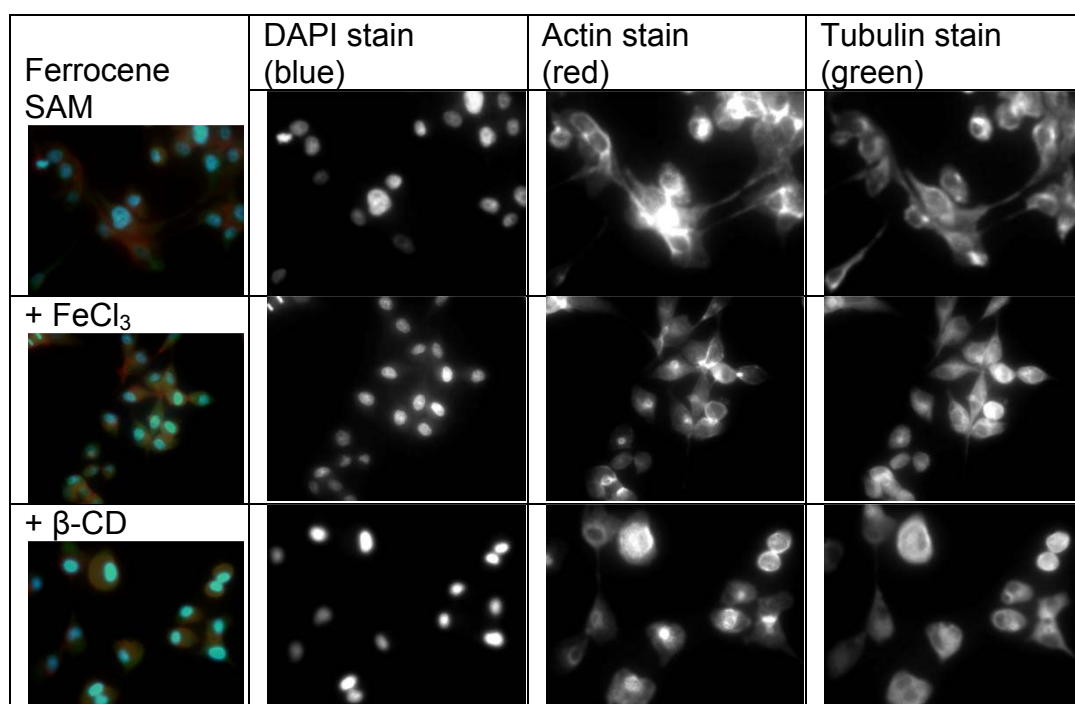
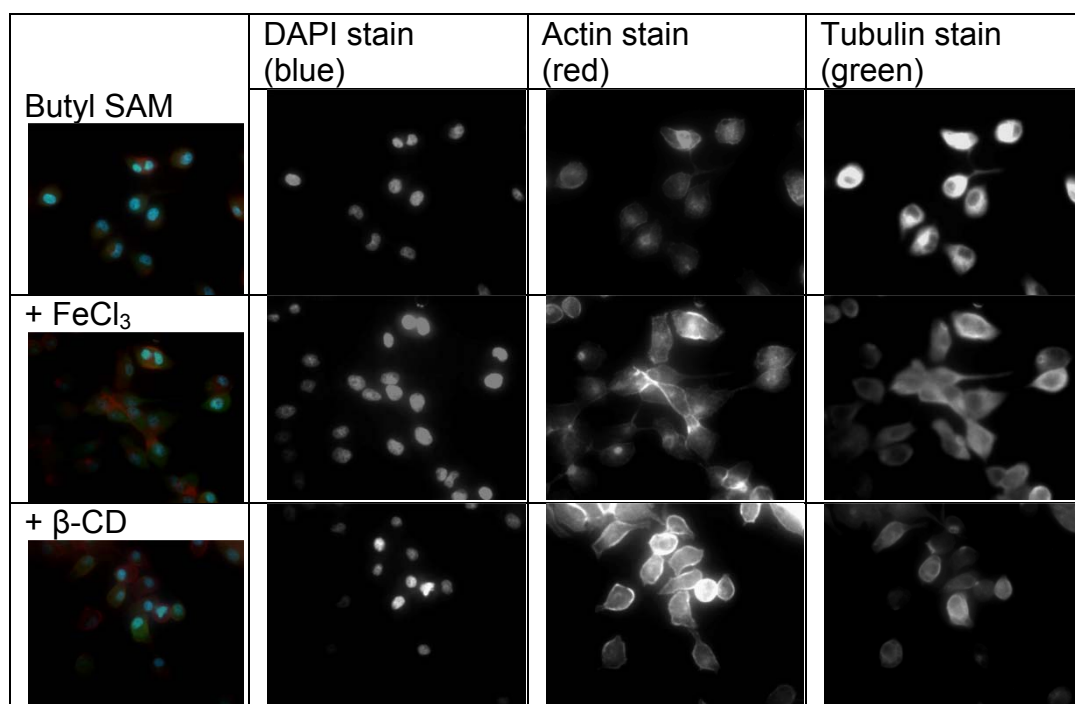
Appendix 4.

Glass cleaning with Caro's Acid.

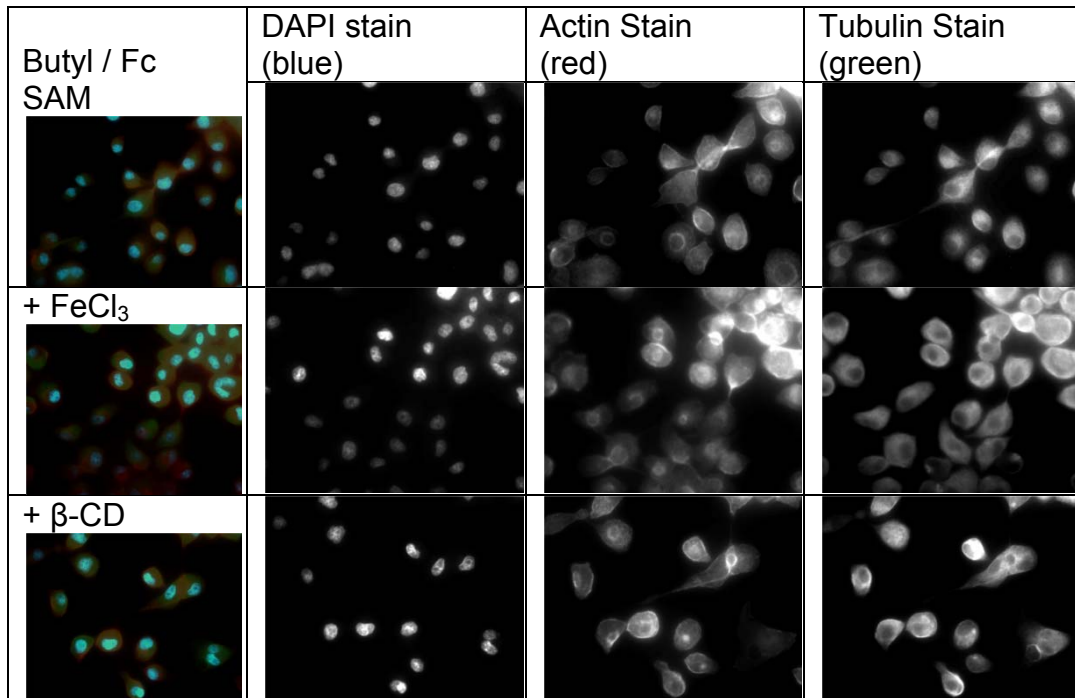
The Caro's acid was made from hydrogen peroxide (20 mL) added to fuming sulfuric acid (40 mL). As the peroxide was added the acidic mixture started to boil and persulfuric acid was formed and oxygen was given off. It was at this point that the coverslips were carefully added. This highly acidic species reacted with any organic residue on the glass. Once the solution had cooled, after around 20 minutes, the acid was decanted off carefully into continuously running water. The coverslips' were then rinsed with distilled water to remove any residual acid. They were then soaked for a further 10 minutes in distilled water, whereby 10 mL 5M NaOH was added the solution and after mixing briefly, the mixture was left to stand for 20 minutes in order to allow the NaOH to react with the now cleaned glass surface so as to increase the number of hydroxyl sites on the glass. The coverslips were then rinsed thoroughly with water, air dried and stored at 80°C for 1 hour.

Appendix 5.

Monochromatic images from antibody cell staining experiments in § 3.3.4.



Appendix 5 continued.



Cite this: *Chem. Commun.*, 2011, **47**, 6819–6821

www.rsc.org/chemcomm

COMMUNICATION

Surfactant-mediated control of CBPQT⁴⁺–dialkoxynaphthalene complexation†Jeremie Louisy,^{ab} François Delattre,^c Joel Lyskawa,^b Aurélie Malfait,^b Catherine E. Maclean,^a Léna Sambe,^b Ning Zhu,^{bd} Graeme Cooke^{*a} and Patrice Woisel^{*b}

Received 28th January 2011, Accepted 11th April 2011

DOI: 10.1039/c1cc10571j

The addition of the surfactant SDS to an aqueous solution containing 1–2 results in the disassembly of the latter via the simultaneous incorporation of 1 into a micelle and the precipitation of 2 by an anion exchange reaction.

Pseudorotaxane-based host–guest assemblies have attracted a great deal of attention as functional building blocks for the creation of molecular machines.¹ In these systems, facile and reversible control over the relative motion of the components is required for the development of systems with bespoke properties and applications. The electron-deficient cyclophane cyclobis(paraquat-*p*-phenylene)² (CBPQT⁴⁺) has emerged as an important host system for the fabrication of pseudorotaxanes with tuneable complexation properties. A range of stimuli have been employed to control the assembly/disassembly of pseudorotaxanes of this type including: redox reactions,³ acid/base reactions,⁴ photochemical processes,⁵ and alkali metal complexation.⁶ In addition, the tetracationic nature of CBPQT⁴⁺ allows the solubility and assembly properties⁷ to be tuned by varying the nature of the counter anion.

In this communication, we describe a CBPQT⁴⁺-based pseudorotaxane assembly that has the propensity to be controlled in aqueous media by the addition of a surfactant (Fig. 1).⁸ The pseudorotaxane is comprised of an electron rich 1,5-dialkoxynaphthalene unit incorporating an ammonium moiety (1) and CBPQT⁴⁺ (2). The ammonium moiety of compound 1 was introduced to promote micelle formation with an anionic surfactant molecule such as sodium dodecyl sulfate (SDS). Previous studies have demonstrated that cationic alkylammonium derivatives allow the self-assembly

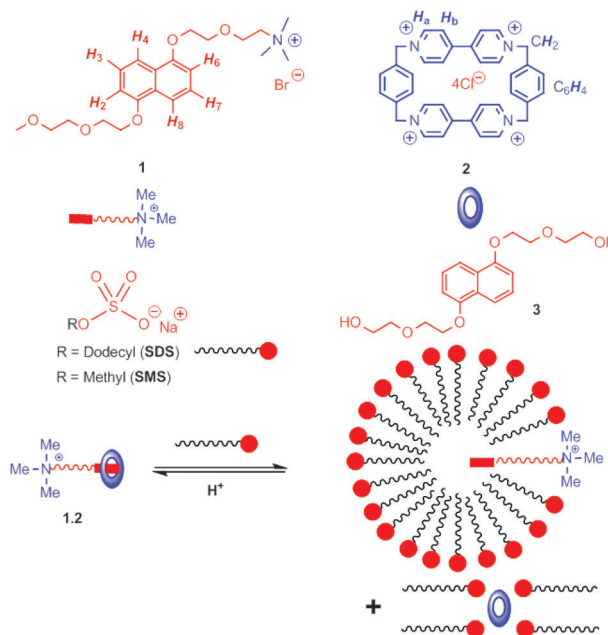


Fig. 1 The SDS-mediated complexation between 1 and 2.

of mixed micelles with SDS, due to attractive electrostatic interactions.⁹

The synthesis of compound 1 is outlined in the ESI†. The complexation between 1 and 2 was established by comparing the ¹H NMR spectra of 1 and 2 and their equimolar admixture (Fig. 2). As shown in Fig. 2b, proton resonances belonging to the CBPQT⁴⁺ and naphthalene units of the complex show broad signals and display noticeable chemical shift changes that are characteristic of a pseudorotaxane-based complex.¹¹ It is particularly noteworthy that a dramatic chemical shift change for resonances belonging to protons H₄ and H₈ ($\Delta\delta \approx 5.5$ ppm) of 1 occurred during the formation of pseudorotaxane 1.2.

Host–guest binding was also investigated by UV-vis spectroscopy (see ESI†). Addition of aliquots of 2 to a solution containing 1 immediately resulted in the formation of a purple coloured solution and the appearance of a broad absorption band $\lambda = \sim 520$ nm in the UV-vis spectrum. This colour change is indicative of complex formation between the 1,5-dialkoxynaphthalene moiety of 1 and 2.⁵ A binding constant (K_a) of $7.8 \times 10^3 \text{ M}^{-1}$ was determined in water using

^a GCPOC, WestCHEM, School of Chemistry, University of Glasgow, Glasgow, G12 8QQ, UK. E-mail: Graeme.Cooke@glasgow.ac.uk

^b Université Lille Nord de France, Unité matériaux et Transformations, UMR-CNRS 8207, Université des Sciences et Technologies de Lille, C6 59655 Villeneuve d'Ascq Cedex, France. E-mail: patrice.woisel@ensc-lille.fr

^c UCEIV (Unité de Chimie Environnementale et Interactions sur le Vivant), EA 4492, Université du Littoral Côte d'Opale, Av. M. Schumann 59140 Dunkerque, France

^d Department of Polymer Science and Engineering, Key Laboratory of Macromolecular Synthesis and Functionalization of the Ministry of Education, Zhejiang University, Hangzhou 310027, China

† Electronic supplementary information (ESI) available: Synthesis of 1 and characterisation of micelles. See DOI: 10.1039/c1cc10571j

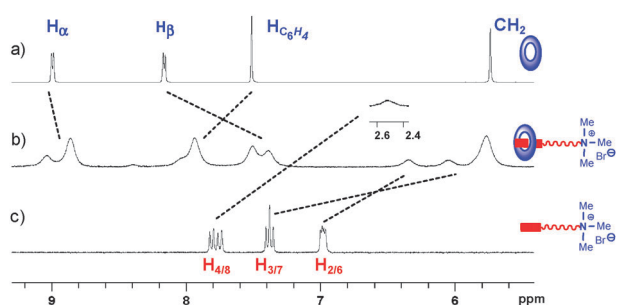


Fig. 2 Partial ^1H NMR spectra of (a) **2** (1 mM); (b) **1:2** (1/1 molar ratio) and (c) **1**. Recorded in D_2O at 25°C .

ITC (see ESI \dagger). This value is significantly lower than that obtained for complex **2:3** ($K_a = 1.1 \times 10^6 \text{ M}^{-1}$),¹¹ and is likely due to coulombic repulsion between the tetracationic **2** and the ammonium group of **1**.

The ability of **1** to be incorporated into micelles of SDS was first investigated using fluorescence spectroscopy by exploiting the intrinsic fluorescence properties of the naphthalene unit. Fig. 3 clearly shows the influence of increasing SDS concentration on the fluorescence emission of **1**. In particular, a gradual decrease in the relative fluorescence intensity of the naphthalene moiety¹² with increasing surfactant concentration was observed until a value of around 4 mM was reached. At this concentration an abrupt change in the fluorescence intensity of **1** was observed, suggesting the onset of micelle formation. It should be noted that this observed CMC is lower than the CMC of pure SDS (8.2 mM),¹³ indicating that **1** promotes the micellization of SDS.⁹

The incorporation of **1** into micelles of SDS was also investigated by ^1H NMR spectroscopy (see ESI \dagger). The addition of SDS to a solution of **1** induced upfield shifts in the resonances of all protons (for $\text{H}_{2/6}$ see Fig. 4, for others see ESI \dagger) above the CMC, indicating a change in their environment. In addition, a plateau was reached at a SDS concentration of 14 mM, suggesting a complete incorporation of SDS at this concentration. To demonstrate the importance of both the ammonium unit of **1** and hydrophobic alkyl chain of SDS in the micellization process, fluorescence experiments were undertaken with compounds **1** and **3** upon the addition of sodium methyl sulfonate (SMS) and SDS, respectively (see ESI \dagger). In both cases, no significant variation in the

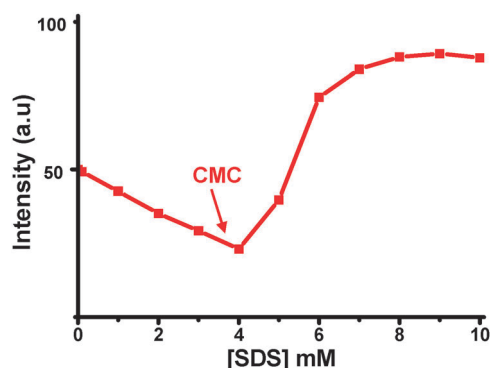


Fig. 3 Graph showing the variation in the fluorescence emission intensity of **1** (3.6 mM) as a function of SDS concentration. $\lambda_{\text{ex}} = 295 \text{ nm}$. $\lambda_{\text{em}} = 329 \text{ nm}$. Recorded in H_2O at 25°C .

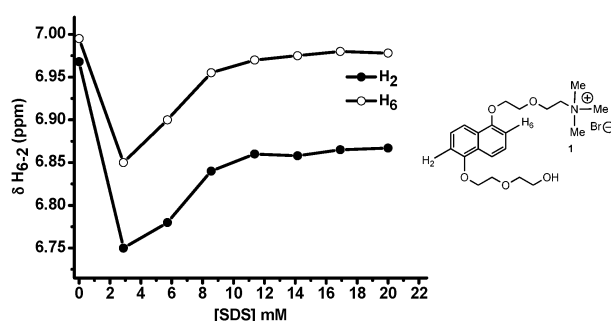


Fig. 4 Graph showing the effect of SDS concentration on the chemical shift of protons H_2 and H_6 of **1**.

relative intensity of fluorescence emission was observed upon the addition of SMS to **1** and SDS to **3**, indicating that no micellization occurred under the conditions investigated.

With complexation confirmed for **1:2** and the ability of **1** to be incorporated into a SDS-based micelle, we next investigated whether the micellization process could be used as a tool to control the assembly of pseudorotaxane **1:2**. As shown in Fig. 5, addition of SDS to a solution of **1:2** resulted in an immediate change in turbidity and a complete disappearance of the characteristic purple colour of the complex, suggesting the dethreading of the pseudorotaxane. This was confirmed by removing the white precipitate from the solution by centrifugation and by analysing the supernatant by UV-vis and ^1H NMR spectroscopies. The UV-vis spectrum of the supernatant (see ESI \dagger) did not display the typical broad absorption band at $\lambda = \sim 520 \text{ nm}$ for the pseudorotaxane. Furthermore, the ^1H NMR spectra of the supernatant indicated that compound **1** was incorporated inside SDS micelles (see Fig. 5b) and that proton resonances associated with **2** were absent. The ^1H NMR spectrum of the precipitate recorded in $\text{DMSO}-d_6$ (see Fig. 5d) showed the characteristic resonances of the tetracationic cyclophane associated with four dodecyl sulfate anions (DS^-). Inspection of the integration of the NMR signals indicated that the four Cl^- counter-ions of **2** were exchanged by 4DS^- , giving the water insoluble **2** (4DS^-).

To obtain further insight on the dethreading process, we have studied the behaviour of pseudorotaxanes **1:2** and **2:3** upon the addition of SMS and SDS, respectively, using ^1H NMR and UV-vis spectroscopies (see ESI \dagger). While the addition of SMS into a solution **1:2** showed the persistence of the absorption band at $\sim 520 \text{ nm}$ characteristic of pseudorotaxane architecture, the addition of SDS to a solution containing **2:3** resulted in the disappearance of colour in the liquid phase and the formation of a purple precipitate presumably of the pseudorotaxane **2:3** (4DS^-) (see ESI \dagger). These results demonstrate that the presence of the ammonium unit of **1** and the hydrophobic alkyl chain of the surfactant are needed to disrupt pseudorotaxane **1:2**.

Finally, we have investigated whether it is possible to reform complex **1:2** following SDS addition. We reasoned that the addition of a strong acid, such as HCl ,¹⁴ would result in the conversion of SDS to dodecyl sulfonic acid thereby allowing reformation of the water soluble form of **2** (4Cl^-), and thus complex **1:2**. To test this hypothesis, the addition of HCl to a

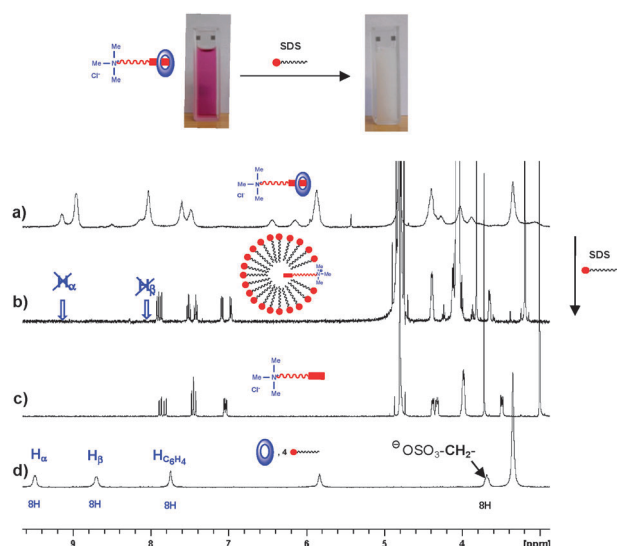


Fig. 5 Partial ^1H NMR spectra of (a) **1-2**; (b) **1-2** + SDS (supernatant); (c) **1** recorded in D_2O ; (d) precipitate from **1-2** + SDS recorded in $\text{DMSO}-d_6$ ($\sim 10^{-4}$ M) at 40°C .

solution of **1**, **2** and SDS was monitored by UV-vis spectroscopy and clearly showed the reappearance of the characteristic purple colour of the pseudorotaxane and a corresponding absorption band centred around $\lambda = \sim 520$ nm (see ESI†). Comparison of the absorbance values at 520 nm for solutions of **1-2** and **1** + **2** + SDS + HCl, when recorded at equal concentration, suggests that the acidification process results in a near complete re-assembly of the pseudorotaxane when a pH value of 1.0 was reached (Fig. 6).

In conclusion, we have shown that compounds **1** and **2** have the ability to form a pseudorotaxane in aqueous media. Upon the addition of SDS to the solution containing the pseudorotaxane, complexation is disrupted by the simultaneous precipitation of **2** by an anion exchange reaction and the sequestering of **1** by incorporation into SDS based micelles. Furthermore, we have shown that the complex between **1** and **2** can be reformed by acidifying the media. Further work in our laboratory will develop analogues of the systems described here in endeavours to extend this methodology to biological applications such as drug delivery.

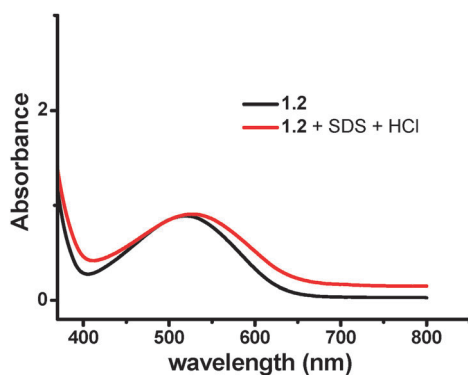


Fig. 6 UV-vis spectra of **1-2** (2.7 mM) (black curve) and **1-2** (2.7 mM) + SDS + HCl conc (red curve). Recorded at 25°C .

We thank the EPSRC and Agence Nationale de la Recherche (ANR-09-JCJC-0032-01) for funding. CEM thanks the University of Glasgow for the award of a Kelvin-Smith Scholarship.

Notes and references

- For representative reviews on molecular machines: (a) E. R. Kay, D. A. Leigh and F. Zerbetto, *Angew. Chem., Int. Ed.*, 2007, **46**, 72; (b) V. Balzani, A. Credi and M. Venturi, *Chem. Soc. Rev.*, 2009, **38**, 1542; (c) J.-P. Collin, C. Dietrich-Buchecker, P. Gavina, M. C. Jimenez-Molero and J.-P. Sauvage, *Acc. Chem. Res.*, 2001, **34**, 477; (d) A. Harada, *Acc. Chem. Res.*, 2001, **34**, 456; (e) M. Venturi, A. Credi and V. Balzani, *Molecular Devices and Machines—A Journey into the Nanoworld*, Wiley-VCH, Weinheim, 2003; (f) V. Sindelar, S. Silvi, S. E. Parker, D. Sobransingh and A. E. Kaifer, *Adv. Funct. Mater.*, 2007, **17**, 694; (g) A. Trabolsi, M. Hmadeh, N. M. Khashab, D. C. Friedman, M. E. Belowich, N. Humbert, M. Elhabiri, H. A. Khatib, A.-M. Albrecht-Gary and J. F. Stoddart, *New J. Chem.*, 2009, **33**, 254; (h) K. Kim, *Chem. Soc. Rev.*, 2002, **31**, 96; (i) V. Balzani, A. Credi, F. M. Raymo and J. F. Stoddart, *Angew. Chem., Int. Ed.*, 2000, **39**, 3448; (j) V. Balzani and J. F. Stoddart, *Acc. Chem. Res.*, 1998, **31**, 405; (k) Y. H. Ko, E. Kim, I. Hwang and K. Kim, *Chem. Commun.*, 2007, 1305.
- B. Odell, M. V. Reddington, A. M. Z. Slawin, N. Spencer, J. F. Stoddart and D. J. Williams, *Angew. Chem., Int. Ed. Engl.*, 1988, **27**, 1547.
- (a) W. Devonport, M. A. Blower, M. R. Bryce and L. M. Goldenberg, *J. Org. Chem.*, 1997, **62**, 885; (b) V. Balzani, A. Credi, G. Matternsteig, O. W. Matthews, F. M. Raymo, J. F. Stoddart, M. Venturi, A. J. P. White and D. J. Williams, *J. Org. Chem.*, 2000, **65**, 1924; (c) M. Asakawa, P. R. Ashton, V. Balzani, A. Credi, G. Matternsteig, O. A. Matthews, M. Montalti, N. Spencer, J. F. Stoddart and M. Venturi, *Chem.—Eur. J.*, 1997, **3**, 1992; (d) P. R. Ashton, V. Balzani, J. Becher, A. Credi, M. C. T. Fyfe, G. Matternsteig, S. Menzer, M. B. Nielsen, F. M. Raymo, J. F. Stoddart, M. Venturi, A. J. P. White and D. J. Williams, *J. Am. Chem. Soc.*, 1999, **121**, 3951.
- O. A. Matthews, F. M. Raymo, J. F. Stoddart, A. J. P. White and D. J. Williams, *New J. Chem.*, 1998, **22**, 1131.
- R. Ballardini, V. Balzani, M. T. Gandolfi, L. Prodi, M. Venturi, D. Philp, H. G. Ricketts and J. F. Stoddart, *Angew. Chem., Int. Ed. Engl.*, 1993, **32**, 1301.
- M. Asakawa, S. Iqbal, J. F. Stoddart and N. D. Tinker, *Angew. Chem., Int. Ed. Engl.*, 1996, **35**, 976.
- For representative examples see: (a) J. Bigot, D. Fournier, J. Lyskawa, T. Marmin, F. Cazaux, G. Cooke and P. Woisel, *Polym. Chem.*, 2010, **1**, 1024; (b) K. Tanabe and T. Kato, *Chem. Commun.*, 2009, 1864; (c) R. C. Ahuja, P.-L. Caruso, D. Möbius, D. Philp, J. A. Preece, H. Ringsdorf, J. F. Stoddart and G. Wildberg, *Thin Solid Films*, 1996, **284–285**, 671; (d) B. W. Laursen, S. Nygaard, J. O. Jeppesen and J. F. Stoddart, *Org. Lett.*, 2004, **6**, 4167.
- For representative examples of pseudorotaxane-like non-polymeric micelles see: (a) Y. Suzuki, T. Taira and K. Osakada, *Bull. Chem. Soc. Jpn.*, 2010, **83**, 378; (b) Y. Suzuki, T. Taira, D. Takeuchi and K. Osakada, *Org. Lett.*, 2007, **9**, 887; (c) K. D. Zhang, G. T. Wang, X. Zhao, X. K. Jiang and Z.-T. Li, *Langmuir*, 2010, **26**, 6878; (d) Y. Murakami, J.-I. Kikuchi, T. Ohno, O. Hayashida and M. Kojima, *J. Am. Chem. Soc.*, 1990, **112**, 7672.
- (a) J. S. Nowick, J. S. Chen and G. Noronha, *J. Am. Chem. Soc.*, 1993, **115**, 7636; (b) A. Malliaris, W. Binana-Limbele and R. Zana, *J. Colloid Interface Sci.*, 1986, **110**, 114.
- A. Star, Y. Liu, K. Grant, L. Ridvan, J. F. Stoddart, D. W. Steuerman, M. R. Diehl, A. Boukai and J. R. Heath, *Macromolecules*, 2003, **36**, 553.
- M. Bria, G. Cooke, A. Cooper, J. Garety, S. G. Hewage, M. Nutley, G. Rabani and P. Woisel, *Tetrahedron Lett.*, 2007, **48**, 301.
- M. Sakar and S. Poddar, *J. Colloid Interface Sci.*, 2000, **221**, 181.
- P. Mukerjee and K. J. Mysels, Critical Micelle Concentrations of Aqueous Surfactant Systems; National Standard Reference Data Series 36; National Bureau of Standards, U.S. Government Printing Office: Washington, DC, 1971; NSRDS-NBS 36.
- H. Topallar and B. Karadag, *J. Surfactants Deterg.*, 1998, **1**, 49.